UNIVERSITÀ DEGLI STUDI
DI MODENA E REGGIO EMILIA

Dottorato di ricerca in Models and Methods for Material and Environmental Sciences

Ciclo XXXI

Deformation processes of shallow subduction megathrusts: insights from field and microstructural analysis

Candidato: **Anna Cerchiari**

Relatore: Prof.ssa Francesca Remitti

Correlatore: Dott.ssa Silvia Mittempergher

Coordinatore del Corso di Dottorato: Prof.ssa Maria Giovanna Vezzalini

Index

Abstract

The largest earthquakes recorded on Earth (M_w>8) occur along low-dipping megathrusts at subduction plate margins. Shallow (< 5 km of depth) megathrusts are characterized by a spectrum of slip behaviors, including large earthquakes, tsunami earthquakes, slow slip and tremors. The physical and chemical processes controlling this complex behavior are still poorly constrained and, to investigate them, the study of fossil analogues exhumed by orogenic uplift represents an approach complementary to scientific drilling and geophysical investigations.

This project has been aimed at studying in detail outcrops of megathrust fossil faults by means of field, microstructural and geochemical analyses, with a particular focus on tectonic veins, to shed some light on the processes controlling fault slip style. I investigated two thrust fault zones, belonging to different fossil subduction complexes, to compare in detail the observed structural features and infer deformation mechanisms, helping to link the geological record to processes operating on active subduction margins.

The Sestola Vidiciatico tectonic Unit (SVU) in the Northern Apennines of Italy has been interpreted as a field analogue for the shallow portion (4-5 km, 150 °C maximum temperature) of subduction megathrusts. Throughout a multi-scale structural analysis of the SVU basal thrust cropping out in Vidiciatico (BO) and laser ablation-inductively coupled plasma-mass spectrometry (LA-ICP-MS) analyses performed on vein samples, the megathrust deformation history and interrelated fluid/stress variations during the seismic cycle have been reconstructed. Based on obtained results, the SVU basal thrust can be characterized as a weak fault, which progressively localized deformation to a cm-scale shear zone and which underwent a cyclical shifting of the principal σ_1 and σ_3 stresses, producing interrelated changes in permeability, fluid pressure and composition.

The fault zone cropping out in SW Llŷn Peninsula, NW Wales (UK), is related to the ~ 600-500 Ma Pacific-type subduction-accretion Mona Complex. Meso- and microstructural analyses, fluid inclusion microthermometry and EBSD microscopy suggest that the fault zone deformed at conditions correspondent to the brittle-ductile transition, at T ≤ 300 °C. This occurred with a cyclical shifting from brittle to ductile deformation, mainly controlled by strain rate variations coupled with overpressured fluid pulses, producing repeated transient embrittlement. At low strain rate, the presence of fluid promoted hydrolitic weakening in vein crystals, thus facilitating the onset of low temperature quartz plasticity in high dislocation density regions. At higher strain rate, deformation lo-

calized in thin shear zones where fluid overpressures counteracted the principal stress, allowing dilatant fracturing to occur more easily and producing new shear veins.

The study results are consistent with what has been observed in several other fossil examples and with some of the recent data obtained from active subduction margins, and suggest that: i) the updip transition to the seismogenic zone is gradual, can vary in depth and is strongly controlled by the lithification state depending on lithologies involved. The downdip limit is similarly transitional, influenced by strain rate variations and the developing of fluid overpressures; ii) along shallow megathrusts shear occurs on localized weak faults sustaining low shear stress, low differential stress and cyclical high (up to supra-lithostatic) fluid pressures; iii) cyclical intermittent slip along megathrust faults is strongly related to the alternating activation of fluid circuits with different amplitude, geometry and source.

This works shows that a multidisciplinary approach to the study of tectonic veins, involving field, microstructural and geochemical investigations, is a powerful tool to obtain information on the interrelations between fluid flow and deformation, enriching our knowledge of megathrust seismic behavior.

Riassunto

I maggiori terremoti registrati sulla Terra (Mw>8) si verificano lungo i piani di contatto poco inclinati dei margini di subduzione di placca, i cosiddetti “megathrust”. Queste superfici sono caratterizzate a bassa profondità (meno di 5 km) da una gamma di stili di scivolamento lungo il piano, che include grandi terremoti (alcuni causa di tsunami), Slow Slip Events e tremori. I processi fisici e chimici alla base di questa molteplicità di comportamenti sismici sono ancora poco conosciuti, per cui, nell’ottica di comprenderli, lo studio di analoghi fossili, esumati in seguito a processi orogenetici, rappresenta un approccio complementare alle perforazioni oceaniche e alle tecniche di indagine geofisica.

Questo progetto ha avuto come obiettivo lo studio di dettaglio di affioramenti di megathrust fossili, per mezzo di indagini sul campo, microstrutturali e geochimiche focalizzate in particolare sulle vene tettoniche, in modo da fare luce sui meccanismi che controllano lo stile di scivolamento lungo il piano di faglia. Sono stati analizzate due zone di thrust appartenenti a complessi di subduzione fossili differenti, per confrontare e descrivere dettagliatamente le strutture osservate e fornire informazioni sui collegamenti tra record geologico e processi attivi ai margini di subduzione.

L’Unità tettonica Sestola Vidiciatico (USV) negli Appennini Settentrionali, Italia, è stata interpretata come un analogo della porzione più superficiale (4-5 km, T massima = 150 °C) dei megathrust. Attraverso un’analisi strutturale multiscala del thrust alla base della USV affiorante a Vidiciatico (BO) e tramite spettrometrie di massa in laser ablation su campioni di vene, è stata ricostruita la storia deformativa del thrust e le variazioni correlate del campo di stress e della circolazine dei fluidi durante il ciclo sismico. Sulla base dei risultati ottenuti, il thrust basale della USV è stato caratterizzato come una faglia debole, che ha progressivamente localizzato la deformazione in una shear zone alla scala del cm ed è stata interessata da uno scambio ciclico tra le orientazioni degli stress principali massimo e minimo. Questo ha provocato variazioni di permeabilità, pressione e composizione dei fluidi, correlate tra loro.

La zona di faglia che affiora nella Penisola di Llŷn sudorientale, in Galles del Nord (UK), fa parte di un complesso di subduzione-accrezione risalente a ~600-500 Ma. Analisi meso- e microstrutturali, dati da microtermometria delle inclusioni fluide e EBSD suggeriscono che la zona di faglia sia stata deformata in corrispondenza della transizione fragile-duttile, a una temperatura prossima a 300 °C. Questo è avvenuto tramite un passaggio ciclico da deformazione fragile a duttile e viceversa, controllato principalmente da variazioni di strain rate accoppiate a sovrappressioni dei

fluidi, che hanno prodotto un embrittlement transitorio della zona di faglia. A bassa strain rate, la presenza di fluidi causava hydrolitic weakening dei cristalli di vena, permettendo l’innesco della plasticità del quarzo a bassa temperatura. Ad alta strain rate, la deformazione si localizzava in sottili shear zone dove la sovrappressione dei fluidi controbilanciava lo stress principale, permettendo più facilmente l’aprirsi di fratture dilatanti e la produzione di nuove vene di taglio.

I risultati di questo studio concordano con quanto è stato osservato in altri esempi fossili e con dati recenti provenienti dai margini di subduzione attivi, e suggeriscono che: i) il limite superiore della zona sismogenetica è graduale, può variare in profondità ed è fortemente controllato dalla litologia. Il limite inferiore è, analogamente, transizionale, influenzato da variazioni di strain rate e sovrappressioni dei fluidi; ii) lungo la parte superficiale dei megathrust, il taglio avviene su faglie deboli e localizzate, a bassi stress differenziali e cicli di alta pressione dei fluidi; iii) lo scivolamneto sismico intermittente lungo le faglie di un megathrust é fortemente correlato all’attivazione di circuiti di fluidi di diversa ampiezza, geometria e con diversa sorgente.

Questo lavoro mostra che un approccio multidisciplinare allo studio delle vene tettoniche, che coinvolga indagini meso-, micro-strutturali e geochimiche, è uno strumento utile ad ottenere informazioni sulle correlazioni tra circolazione di fluidi e deformazione e a progredire nella conoscenza del comportamento sismico dei megathrust.

Chapter 1. Introduction

In continent-ocean subduction zones around the world, over the 90% of global seismic energy is released through devastating earthquakes. These represent the greatest natural hazard for coastal populations, even more for their potential to trigger terrestrial or submarine landslides and tsunamis.

Even if long-term cyclicity has been recognized for great earthquakes (M_w > 7.0, McCann et al., 1979), the historic record length is very limited and one of the major challenges in facing these destructive events is that, to date, no effective methods exist to predict their occurrences on a short time-scale.

Monitoring techniques applied to areas where recent great earthquakes occurred (Mw > 9.0, e. g. the 2004 Indonesian Sumatra-Andaman and the 2011 Japanese Tohoku-oki earthquakes) suggest that pore pressure conditions, together with fault and wall rock permeability, porosity and elastic moduli vary systematically immediately after earthquakes and in the interseismic period, but observations are still too sparse and limited to make reliable predictions about the pre-earthquake conditions.

1.1. What is a megathrust?

Subduction earthquakes occur on contact surfaces called megathrusts, which accommodate the relative movement between the overriding and underthrusting plates (Fig. 1.1) (Bilek and Lay, 2018). Megathrusts are more conveniently described as shear zones, composed by multiple parallel rupture surfaces, "fault strands" (Rowe et al., 2013) accommodating most of the strain of the relative plate motion in a tectonic mélange evolving through time (Fig. 1.2): progressive shear deforms rocks accordingly to their rheological properties, determined by lithology, lithification state and fluid content, while pressure and temperature increase constantly as subduction progresses (Fisher and Byrne, 1997; Fagereng and Sibson, 2010; Kimura et al., 2012; Rowe et al., 2013; Fagereng et al., 2018). Measurements of the thickness of subduction thrust faults from active and ancient examples observed by ocean drilling and field studies in accretionary wedges (Rowe et al., 2013) suggest that all simultaneously active fault strands are encompassed in a thickness reaching ∼100–350 m at ∼1–2 km below seafloor and maintained down to a depth of ∼15 km. Inside this thickness, each fault

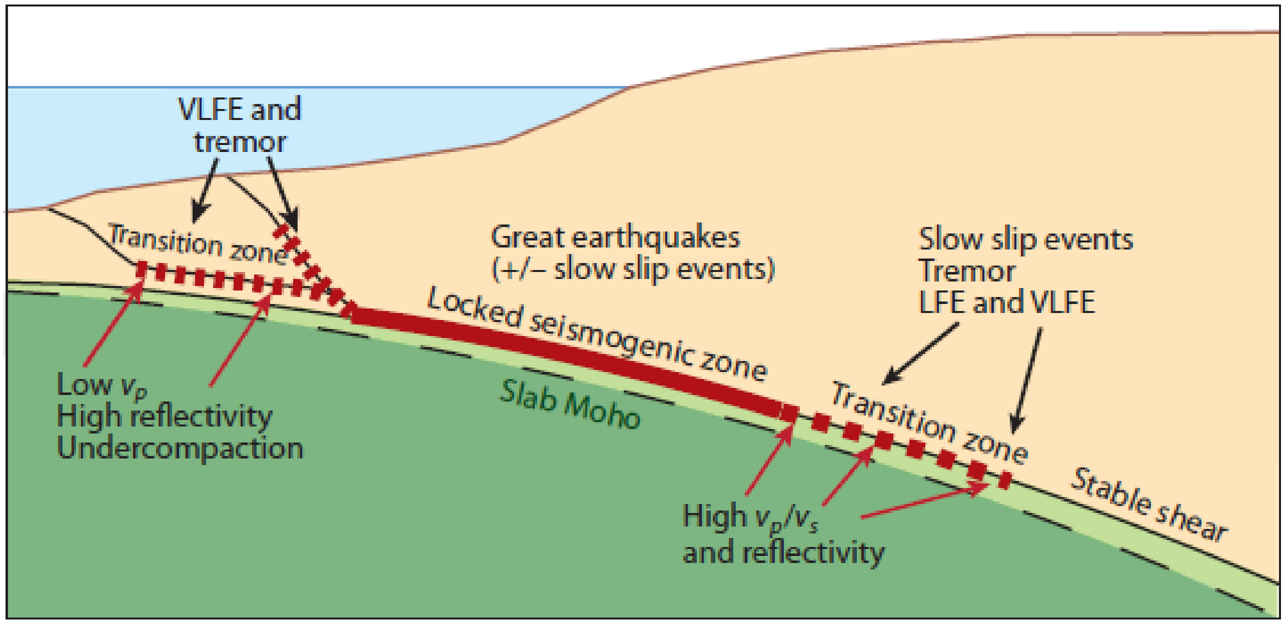

Figure 1.1. *Schematic cross section of a subduction zone, showing the locations of the different types of slip observed along the megathrust plane at the seismogenic zone updip and downdip ends (red dashed line). As indicated, VLFE and tremors can occur on splay faults within the upper plate (Ito and Obara, 2006; Obana and Kodaira, 2009). The red line indicates the classical extension of the locked seismogenic zone, where great earthquakes typically rupture. LFEs, VLFEs, tremors and slow slips are accompanied at both shallow and deep levels by peaks in Vp/Vs, indicative of the presence of high fluid pressure. From: Saffer and Tobin (2011).*

strand is 5-35 m thick, and contains or is bounded by 1-20 cm thick sharp faults representing earthquake slip surfaces or other discrete slip events (Fig. 1.2). The total fault zone thickness corresponds to the minimum structural thickness encompassing all simultaneously active strands, and generally it does not match with that of the whole mélange (Fig. 1.2b). In fact, as shear migrates through time and new fault strands activate, a greater thickness of sheared rock or mélange may be accumulated, making difficult to distinguish for each fault the respective total thickness. Moreover, mélange may form by flattening and volume loss rather than high shear strain (Fagereng, 2013), or may result from structural overprint on an already present sedimentary mélange (Cowan, 1978; Vannucchi et al., 2008; Wakabayashi, 2011; Festa et al., 2019). This is a problem when deriving the décollement thickness from seismic reflection images: the active fault zone cannot be distinguished from the cumulative thickness of sheared rock that may include previously underplated sediments (Fig. 1.2), and moreover the highest resolution of seismic reflection data is similar to the fault strand thickness, so that thinner features are not imaged (Rowe et al., 2013). For these reason, looking at single fault strands belonging to ancient plate boundary fault zones cropping out on-land and analysing structural crosscutting relationship is particularly useful to discern the progressive deformation phases and the succession of different fault strands active through time.

While seismic (or, more generally, transient) deformation is accommodated by faults in strands, interseismic (continuous) deformation is thought to be distributed in stratally disrupted rocks surrounding the fault strands (Rowe et al., 2013). The resulting heterogeneous rock assemblage displays strong internal contrasts in rheology and fluid transport properties, inferred to play a significant role in controlling the seismic behavior typical of shallow megathrusts settings, which is rather complex (Fagereng & Sibson, 2010; Wei et al., 2012). Geodetic and seismological data have indeed showed that the strain along a megathrust plane is released with slip rate varying in space and time (Fig 1.1). The range of slip behaviors comprises: seismic failure with high energy releases, caused by slips that last seconds to minutes; low- or very low-frequency earthquakes (LFEs or VLFEs, Shelly et al., 2007; Shapiro et al., 2018); episodic tremor and slip (including Slow Slip Events, SSEs), in the order of days and weeks, (Obara, 2002; Rogers e Dragert, 2003; Gomberg et al., 2004; Brown et al., 2009; Wallace et al., 2009); continuous aseismic creep, which proceeds at the plate convergence rate (Schwartz e Rokosky, 2007; Peng e Gomberg, 2010; Fagereng, 2011).

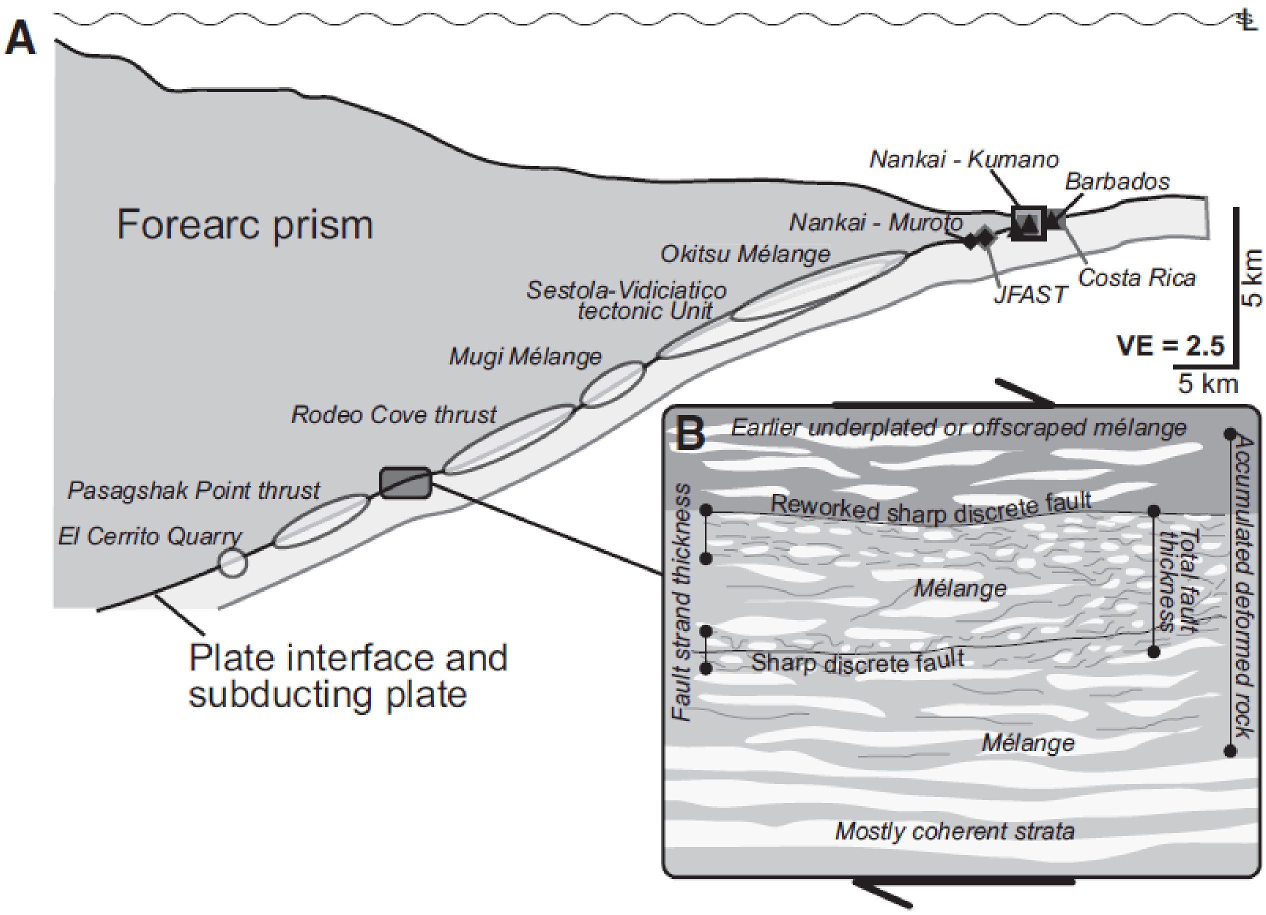

Figure 1.2. *a) Cross section of subduction zone with depth (b. s. f.) of representative subduction plate boundary fault zone examples studied by Rowe et al. (2013). VE is vertical exaggeration. Filled symbols are observations from ocean drilling; ellipses are data from on-land geological observations including depth uncertainty range. b) Schematic representation of characteristic total fault zone and fault strand thicknesses at~ 10 km depth. The thickness of the deformed mélange rocks does not correspond to the total fault thickness. From: Rowe et al. (2013).*

The seismogenic zone is defined as that portion of a megathrust that produces earthquakes through stick-slip sliding (Brace and Byerlee, 1966; Dixon and Moore, 2007). The simplified "stick-slip" frictional model predicts that stress and strain "stick" (i.e., accumulate) during the interseismic period and fail dramatically slipping during seismic events. The part of a fault zone with stick-slip behavior is said to be dominated by "unstable" or "conditionally stable" frictional slip (Scholz, 1998), where unstable regions are velocity-weakening, i.e. frictional strength decreases as slip velocity increases (Marone and Saffer, 2007). Other parts of the fault are instead dominated by stable frictional failure producing asesimic creep, and therefore they are considered as velocity strengthening, e.g. frictional strength increases as slip velocity increases, precluding earthquake nucleation.

For a megathrust, the seismogenic zone as defined above has traditionally been considered as encompassed between the 100-150 °C at the updip end and the 350-450 °C at the downdip end. The upper and lower portions are generally thought to be aseismic. This temperature range corresponds roughly to depths of 5-10 km for the updip and 40-50 km for the downdip (Dixon and Moore, 2007).

The temperature limits of the seismogenic zone have been defined by comparing thermal models to the depth extent of earthquake ruptures and their aftershocks (Currie et al., 2002; Hyndman and Wang, 1993; Hyndman et al., 1995, 1997; Oleskevich et al., 1999; Peacock et al., 1996). They are inferred to correspond to thermally-activated geological processes (Sibson, 1984; Tse and Rice, 1986; Vrolijk, 1990; Tichelaar and Ruff, 1993; Hyndman et al., 1997; Oleskevich et al., 1999; Moore and Saffer, 2001). For the updip limit, the main mechanism invoked is the dehydration reaction of smectite to illite coupled to diagenetic processes, such as sediment cementation by clay, carbonates, zeolites and quartz, becoming efficient at ~150°C, promoting an increase in normal stress and a transition to the velocity-weakening frictional regime (Moore and Saffer, 2001, Fagereng et al., 2018). As pointed out by Moore et al. (2007), this is further favoured by the fact that, at T > 150°C, quartz is velocity-weakening (Blanpied et al., 1995) and most efficiently mobilized by pressure solution (Rimstidt and Barnes, 1980). Fagereng et al. (2018) highlighted as the 150 °C transition to velocity-weakening seismic behaviour may correspond to the passage from unlithified to lithified sediments, at least in quartz-rich sediments. A change in quartz frictional properties is similarly inferred to mark the 350 °C lowest value for downdip limit of the seismogenic zone (Fagereng et al., 2018). Becoming velocity-strenghtening (Blanpied et al., 1995), quartz deforms well by crystal plastic flow (Hirth et al., 2001), allowing ductile deformation mechanisms to overcome brittle rupturing (the so called "brittle-ductile transition"). Hyndman et al. (1997) proposed that serpentinization of the forearc mantle, caused by the upward infiltration of fluids derived from the subducting slab intersecting the forearc mantle, could control the downdip limit of the seismogenic zone. The serpentinization process transforms dry, strong olivine + pyroxene ultramafic rocks into weak, hydrous mineral assemblages consisting of serpentine minerals, metasomatic talc and brucite, promoting stable sliding and aseismic behaviour (Tichelaar and Ruff, 1993; Hyndman et al., 1997; Peacock and Hyndman, 1999).

The classic determination of the thermally-controlled updip and downdip limit as presented above is, nevertheless, subjected to a varying degree of uncertainty, depending on the chosen thermal model and the precise thermal effects on seismic coupling and seismic style. Therefore, the limits of the seismogenic zone are actually still debated (Hyndman, 2007; Fagereng and Ellis, 2009).

Infact, not only thermal effects influence the frictional stability/instability transitions, which can vary both in space and time (Dixon and Moore, 2007). Seismic and geodetic data suggest that seismogenic zones are not fully locked and slip at some fraction of the plate convergence rate during the interseismic period (McNally and Minster, 1981; Norabuena et al., 1998, 2004). This behavior is modeled as patches of frictionally unstable fault surface remaining locked for the most of the seismic cycle and failing during seismic intervals, surrounded by stable portions subjected to creep (Bilek and Lay, 2002). The resulting fault surface is therefore generally “partially locked”, with unstable patches representing frictional “asperities” (Dixon and Moore, 2007). Transient slip events at or near the seismogenic zone imply that locking and frictional properties are transitional and vary with time. Tremors, slow-slip events and low-frequency earthquakes are both shallow and deep located along the subduction interface, at the updip and downdip ends of the seismogenic zone. Very low-frequency earthquakes can locate very shallowly outboard of the locked seismogenic zone and in the accretionary prism, consistently with the occurrence of VLFE along major splay faults in the upper plate accretionary prism (Ito and Obara, 2006; Obana and Kodaira, 2009) (Fig. 1.1). These varying slip modes occur at conditions between those allowing steady aseismic creeping and those favouring stick-slip behavior, marking the transition to seismogenesis (Saffer and Wallace, 2015). They also indicate that conditonally stable behavior of the megathrust extends out of the seismogenic zone, blurring the localization of the updip and downdip limits and showing that fault zone stability is transitional. Moreover, recent great earthquakes have occured in the updip region of the seimogenic zone, previously labeled as aseismic.

This is the case of the M_w 9.1 Tohoku-oki earthquake, which on 11th March 2011 ruptured with hypocenter at 29 km depth and propagated up to the trench, causing a devastating tsunami along the northeastern coast of Japan (Fig. 1.3) (Fujiwara et al., 2011; Chester et al., 2013; Sun et al., 2017). A coseismic slip of ~60 m took place near the trench (Fujiwara et al., 2011; Kodaira et al., 2012), well above the estimated position of the 150°C isotherm limit, which marks the updip limit of the seismogenic zone.

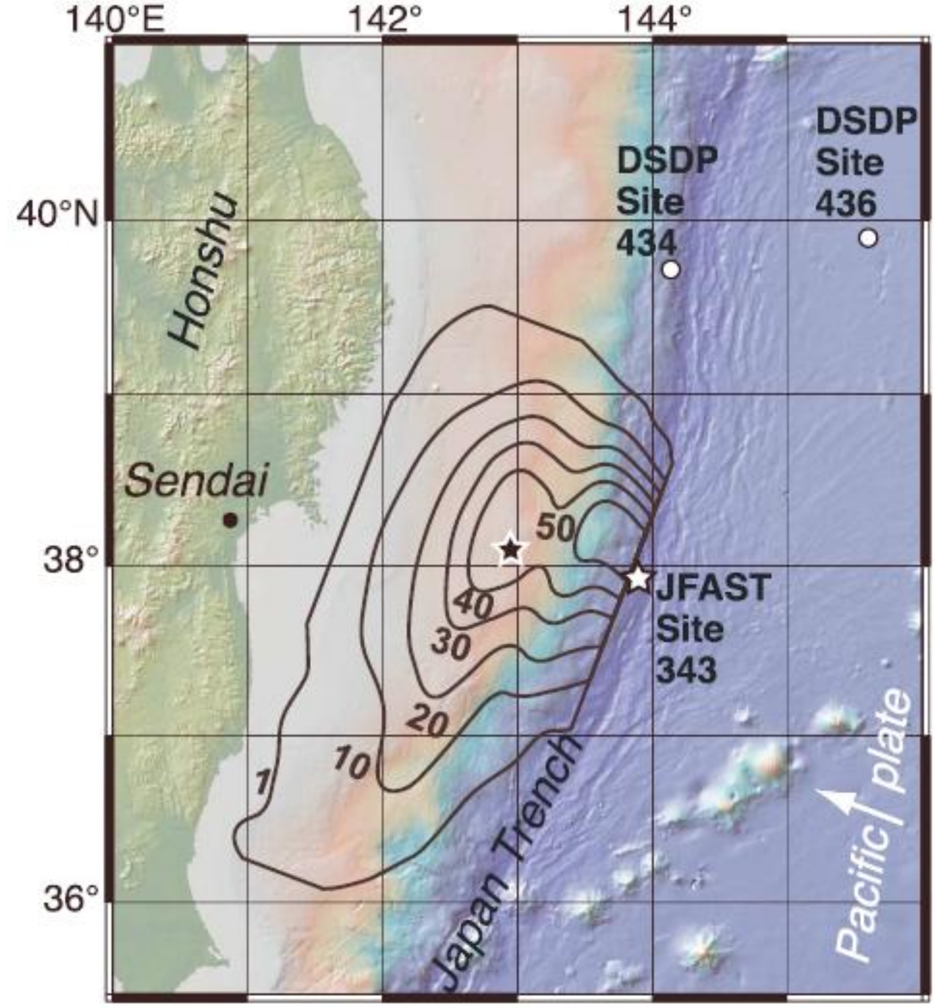

Figure 1.3. The map shows the extent of the 2011 Tohoku-oki earthquake rupture, along the eastern coast of Honshu, Japan. Slip amount in meters is contoured. White arrow shows the convergence direction between the Pacific Plate and the Japan Trench. White star indicates the location of IODP Expedition 343 JFAST drilling site. From: Kirkpatrick et al. (2015).

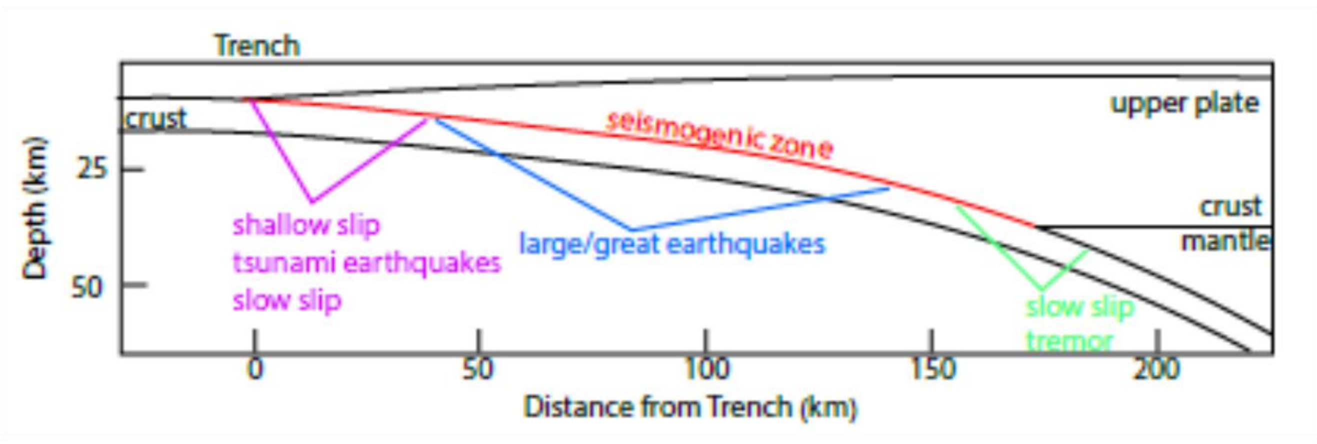

Figure 1.4. Updated schematic cross section of a subduction zone, showing the locations of different slip styles. Following the recently observed seismic slips at shallow depth, the seismogenic zone has been extended updip along the megathrust to the trench. From: Bilek and Lay (2018).

The transient character of frictional locking above the megathrust suggested by slow slip events, tremors, low- or very-low-frequency earthquakes and the shallow propagation of great earthquakes has ultimately challenged the understanding of the factors controlling rupture nucleation and slip mechanics, forcing the geological community to revise the definition of “seismogenic zone” (Fig. 1.4). The definition of the updip and downdip limits is currently under debate. This works offers a contribution, describing and interpreting the geological record of two fossil megathrust analogues, deformed at conditions compatible with the classical updip and downdip ends of the seismogenic zone.

1.2. Megathrust weakness

Subduction megathrusts have been recognized for many years as weak surfaces, operating in condition of low shear stresses (<20MPa, Bird, 1978; Lamb, 2006; Seno, 2009; Duarte et al., 2015) and active circulation of fluids (Saffer & Tobin, 2011). Weakness of the fault plane is interpreted as promoted mainly by the presence of low-friction minerals and the occurrences of fluid overpressures (pore fluid factors $\lambda_v = P_f/\sigma_v > 0.9$, where P_f is the fluid pressure and σ_v is the vertical stress, Sibson, 2013), that significantly lower the effective friction coefficient of the megathrust. Also in this case, the Tohoku-oki earthquake confirmed the previous interpretations and observations. During IODP JFAST Japan Trench Fast Drilling Project immediately following the 2011 Tohoku-oki earthquake, sediments were cored from the interpreted plate margin: they consist of clays very rich in smectite, that have been proved to be able to deform at various rates, ranging from seismic to the order of slow slip events, consistent with the pattern of slip behaviors observed in the area (Ikari, 2015a and 2015b).

The velocity-weakening behavior of the Tohoku-oki megathrust fault stands further out from recent studies on the focal mechanisms of the 2011 earthquake and aftershocks. They suggest that a nearly complete stress drop caused by the mainshock was associated to the switching of σ_1 and σ_3 in most of the forearc (Ide et al., 2011; Hasegawa et al., 2011; Hasegawa et al., 2012; Sibson, 2013), thus implying a low differential stress and a dynamic weakening of the megathrust.

Geophysical investigations have also highlighted the relation between Tohoku-Oki megathrust weakness and high fluid pressure values. Yamamoto et al. (2014), using Vp/Vs ratio as a fluid pressure proxy, found significant Vp/Vs heterogeneity in the shallow megathrust zone of the 2011 Tohoku-oki rupture, suggesting high fluid pressures in the very near-trench area of high coseismic slip and downdip of the hypocenter.

Tohoku-oki is not an isolated case: several major active megathrusts around the world display evidence of weakness. Tobin and Saffer (2009) used seismic velocity data to quantify fluid pressure and effective normal stress along and beneath the megathrust within the updip region of Nankai subduction zone, offshore southwestern Japan. They found remarkable and progressively increasing with depth fluid overpressure, reflecting a substantial underconsolidation of the sediment. At the trench, total pore pressure is ~5 MPa, close to hydrostatic, while at to 20 km depth along the megathrust it reaches ~32 MPa, accounting for more than 75% of the lithostatic load. These almost undrained conditions correspond to only small increases in the effective stress, a globally low shear stress (for most of the transect, <4 MPa) and an effective friction coefficient μ of 0.1, implying weakness of the plate interface, strongly controlled by fluid overpressure buildup. Near-lithostatic pore fluid pressure is inferred to account also for Cascadia megathrust weakness (Wang et al., 1995), which is suggested based on almost absent frictional heating along the plate interface computed from heat flow measurements and on the low value of tectonic stress acting on the megathrust obtained from earthquake focal mechanism solutions. Megathrust weakness is invoked as necessary to allow margin-normal subduction when the stress regime and orientations are not favourable, as happening at Cascadia, Nankai (where margin-parallel compression is dominant, Wang, 2000) and Hikurangi margin (where a strong component of vertical motion is present, McGinty et al., 2000).

Despite the evidences presented above, the distribution and complete extent of weakness on the plate interface are still poor understood. In fact, average stress drop for great earthquakes is always rather low (~4 MPa, Allman and Shearer, 2009) and accounts for only a small fraction of the average fault strength. This imply partitioning in the frictional behaviour of the megathrust, with parts of the faults undergoing large dynamic weakening and peak shear stress drops (up to ~50 Mpa, Allman and Shearer, 2009), and other parts experiencing much less weakening or even strengthening (Gao and Wang, 2014). Changes in the frictional properties along the plate interface can result also from variations in topography, and this can affect the mode of slip behaviour. This stems from the observation that rough subducting seafloor promotes mainly creeping and small or moderate earthquakes on megathrusts, in contrast with Mw 9 or greater earthquakes all occurring in presence of smooth interfaces. This is assessed by Gao and Wang (2014), who compared the thermally derived friction coefficients of the mostly creeping Hikurangi margin (New Zealand) and the Tohoku-oki one. Their analysis completely contrast with the common assumption that faults producing great earthquakes are stronger than those that creep (Scholz and Campos, 1995), upon which megathrusts locked to build up stress for future great earthquakes are described as “strongly coupled”.

Based on these considerations, investigating the relationship between megathrust stress state, frictional properties and slip modes and how they are determined and controlled is of primary importance in geotectonics nowadays.

1.3. The role of fluids in promoting megathrust weakness

Fluids in subduction zones are involved in numerous processes, where they play a fundamental role. These include heat loss from the solid Earth, transfer of volatiles to and from subduction zones, formation of fractures and mineral deposition, rock alteration and stress accumulation and release resulting in earthquakes and landslides.

Despite its importance, fluid flow in the plate interface region is yet poorly known. Characteristic rates of fluid transport have not been defined, nor how these vary with location and flow direction. The lateral and depth extent, distribution, and geometry of flow paths, and the temporal evolution of fluid flow systems are poorly constrained.

Fluids enter the shallow seismogenic zone either within the pore space of the subducting material, or bound in hydrous minerals crystalline structure and are released either through compaction in the shallowest 5–7 km depth or in dehydration reactions at corresponding higher pressures and temperatures (Saffer and Tobin, 2011; Bilek and Lay, 2018). The fluids move flowing through fault-fracture meshes and permeable strata within the megathrust and overriding plate (Carson and Screaton, 1998). If they are trapped by low-permeability sediments, they are subject to overpressurization, with consequent reduction of the effective normal stress on the megathrust (Hubbert and Rubey, 1959; Saffer and Bekins, 2002), following the classical Coulomb criterion for shear failure:

$$\tau = C + \mu_i \sigma'_n = C + \mu_i (\sigma_n - Pf) \qquad (1)$$

where τ and σ_n are, respectively, resolved shear and normal stresses on the failure plane, σ'_n is the effective normal stress, C is the cohesive strength, μ_i is the coefficient of internal friction and Pf is the pore fluid pressure (Anderson, 1950). Indeed, borehole-based studies indicate that even within ~1–4 km of the trench, pore pressures in the underthrusting sediment are typically more than 60–70% of the lithostatic load (λ = 0.68–0.97, where λ is the ratio of pore fluid pressure Pf to vertical stress σ_v, corrected for weight of overlying seawater) (e.g., Becker et al. 1997, Screaton et al. 2002; Saffer 2003, Saffer and Tobin, 2011). Results from analyses of seismic reflection data show that these elevated pore fluid pressures extend to at least 20–30 km from the trench. Field observations of mineral veins and orientations of faults and fractures from exhumed ancient megathrusts imply fluid pressures significantly above hydrostatic, reaching, or even transiently exceeding, lithostatic pressure values (Byrne and Fisher, 1990; Fagereng et al., 2010; Ujiie et al., 2018).

Fluid overpressure is involved in processes occurring at the plate interface on multiple time-scales (Faulkner et al., 2018). Reduction of the effective normal stress and consequent lowering of the shear stress produced by the persistence of elevated pore pressure within the fault contribute to long-term weakening and slip on misoriented weak faults. On intermediate timescales, episodic tremor and slip and slow earthquakes have been related to high pore fluid pressure (Fig. 1.1) (Rubin, 2008; Frank et al., 2015).

On shorter timescales, the instability developing in an earthquake rupture is generally interpreted as produced by a lowering of the fault rock friction coefficient (see Equation 1). This is evaluated in terms of rate-and-state friction (van den Ende et al., 2018), following the most widely used law formulated by Dieterich (1979) and Ruina (1983):

$$\mu(V, \theta) = \mu^* + a \ln\left(\frac{V}{V*}\right) + b \ln\left(\frac{V*\theta}{Dc}\right) \tag{2}$$

where μ* is a reference coefficient of friction measured at sliding velocity V*, while the parameters a and b are proportionality constants thought to represent material properties. Dc is the characteristic slip distance, over which the evolution towards the new steady-state takes place. At steady-state, the formulation of the coefficient of friction (Dieterich, 1979; Ruina, 1983) is simplified as:

$$\mu_{ss}(V) = \mu^* + (a - b) \ln\left(\frac{V}{V*}\right) \tag{3}$$

The new parameter (a−b) describes the velocity-dependence of μ at steady-state, with positive values (i.e. a>b) resulting in velocity-strengthening, and negative values resulting in velocity-weakening behavior. Ruina (1983) showed that a material characterized by a negative (a−b), thus velocity-weakening, is effectively prone to frictional instabilities, i.e. to stick-slip behavior. Seismogenic faults should accordingly have negative (a−b) values (Fig. 1.5).

The rate-and-state friction law (RSF) thus predicts that small changes in the friction coefficient due to variations in slip velocity give rise to the onset of instability, and describes well a wide range of laboratory data. Anyway, it presents also some important limitations: first of all, it is not able to capture the full extent of frictional behaviors observed in experiments (from velocity-strengthening to velocity-weakening continuously and vice versa) with only a single set of parameters. To solve this problem, the classical RSF framework has been modified and extended, (Okubo, 1989; Shibazaki and Iio, 2003; Noda and Shimamoto, 2012; Noda, 2016), but the rearranged RSF relations remain rather empirical and do not explain thouroughly many important question, such as the dependence of RSF parameters on the imposed normal stress, or the presence of reactive fluids (van den Ende et al., 2018). Moreover, in the RSF framework most experiments are constructed assuming a near steady-state fault behavior, thus greatly limiting the comparison with natural faults, involved in seismic cycles with diverse transient phases.

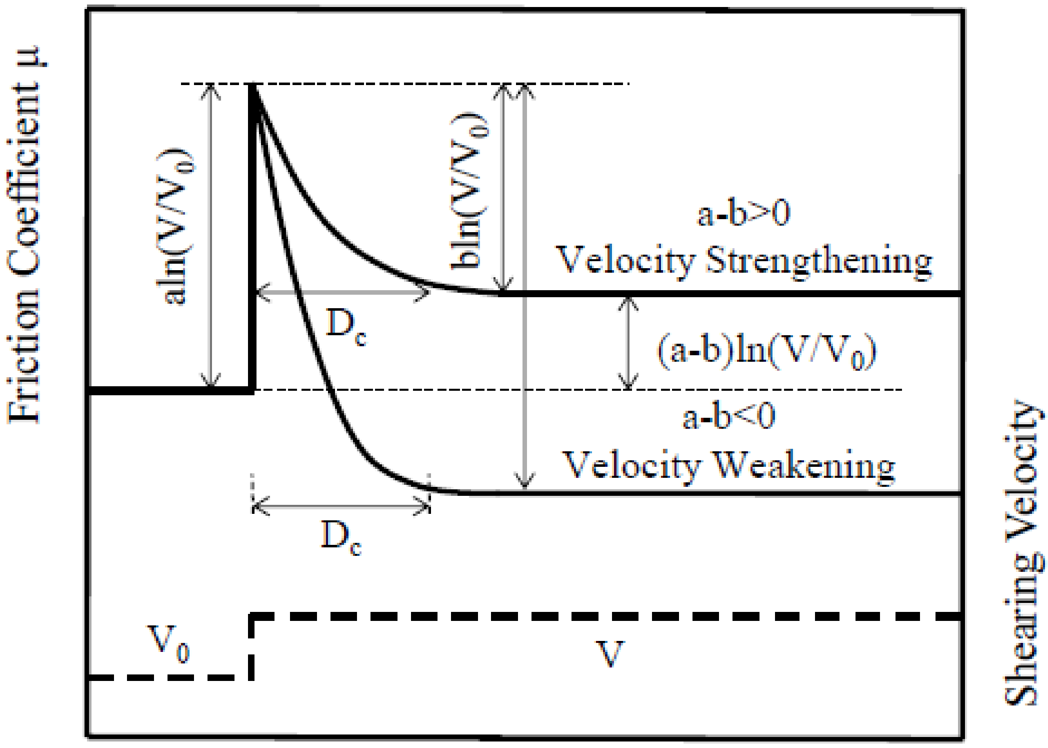

Figure 1.5. *Schematic diagram for rate-and-state friction law, showing the dependence of the friction coefficient μ from the shear displacement distance D and from changes in shear velocity. See text for definition of the parameters. From: An et al. (2018).*

For these reasons, recent studies have started to evaluate the role of fluid pressure in promoting instability along thrust planes, as even small changes in pore fluid pressure from compaction, dilation, or thermal effects can produce first-order changes in the apparent friction coefficient via modifications of the effective normal stress (Lockner and Byerlee, 1994; Segall & Rice, 1995; Bizzarri and Cocco, 2006; Samuelson et al., 2009; Noda and Lapusta, 2010; Garagash, 2012). The influence of pore fluid pressure on thrust mechanics depends on how efficiently the fault zone can produce pore fluid overpressure transients and on how it can drain away excess pore fluid pressure (Faulkner et al., 2018). Therefore, the determination of fault zone hydraulic properties, as the permeability, becomes essential.

The tectonic mineral veins coating faults and fractures in exhumed fault zones crystallized from fluids circulating in interconnected permeable networks, leading to consider the study of tectonic veins in megathrust fossil analogues very promising to investigate fluid interplay in faulting dynamics.

1.4. The study of fossil megathrust field analogues

Modern subduction megathrusts have been extensively investigated during International Ocean Discovery Program (IODP) / Ocean Drilling Program (ODP) expeditions over the last 50 years, with great improvements in the understanding of their architecture, fluid-transport properties and lithological composition (Saffer & Tobin, 2011). However, because of the extremely challenging conditions of operating in several kilometer-deep oceanic trenches, scientific drilling is limited in depth, and cores offer just one-dimensional insights on the internal architecture of faults. Moreover, the acoustic transparency and the small scale of features within fault zones (meters to tens of meters), well below standard seismic resolution, allow only large-scale imaging of the active megathrust faults by means of seismic reflection surveys. Therefore, field-based studies of fossil subduction zones are the only method to investigate the mesoscale architecture of megathrusts. Detailed studies on exhumed subduction-related shear zones worldwide, taken as megathrust field analogues, have provided useful information about the 3D arrangement of the deformation structures and the possible geological record of the seismic cycle.

The widespread occurrence of different fracture sets filled with mineral veins in fossil megathrust-related tectonic mélanges testifies for an active fluid circuit, cyclically subjected to pressure rises and drops, triggered also by permeability changes related to fracturing and fracture healing by precipitation of hydrothermal minerals (e.g. Sibson, 1992; 2013; 2017). Tectonic veins thus represent a valuable archive of information on both the orientations of the paleostresses and the physicochemical characteristics of fluids circulating in the fault zone through time. Several studies have explored these aspects in tectonic veins, for example reconstructing stress changes and inversions during deformation history from detailed meso- and microstructural description of the structures (Fisher et al., 1995; Fagereng et al., 2010; Meneghini and Moore, 2007; Ujiie et al., 2018), or inferring the characteristics of fluid source and circulation patterns from trace element abundances and isotope signatures retained in vein crystals (Yamaguchi et al., 2011; Yamaguchi et al., 2012; Lacroix et al., 2014). The coupling of geochemical and structural analysis applied to tectonic vein appears as a powerful tool to explore the interplay between fluids and strain during the seismic cycle.

1.5. Purpose of the study

The following chapters describe meso- and microstructural studies conducted on two fault strands belonging to field analogues of megathrust-related shear zone: the basal thrust of the Sestola Vidiciatico tectonic Unit, in the Northern Apennines of Italy, (Chapter 2, see also Mittempergher et al., 2018 and Cerchiari et al., submitted) and the SW Lleyn Peninsula fault zone, in NW Wales, UK (Chapter 3).

The first aim of the study is to analyze the structural architecture and understand how deformation operated from the meso-to the microscale in these fossil fault strands. A particular focus has been dedicated to the analysis of tectonic veins, diffusely present in both outcrops as witnesses of the presence of an active fluid flow during the whole thrust fault activity.

The second objective of the study is to compare what have been observed in the two different outcrops, to identify common operating processes and compare them to the dynamics of active megathrusts, explored during the participation in the Core-Log-Seismic-Investigation at Sea (CLSI@Sea) Workshop. This took place from 12 January to 7 February 2018 onboard the drilling vessel Chikyu, during the IODP Expedition 380 in the Nankai Through subduction zone, off south-western Japan (Cerchiari et al., 2018). The workshop allowed participants to examine existing core, log, and seismic data previously acquired during the IODP Nankai Trough Seismogenic Zone Experiment (NanTroSEIZE), to address the role of the deformation front of the Nankai accretionary prism in tsunamigenic earthquakes and slow slip in the shallow portion of the subduction interface. A brief review of the CLSI@Sea Workshop outcomes is given in Chapter 4, together with a summary of the state-of-the-art knowledge about the Nankai subduction zone. Chapter 5 compares and discuss the data collected from the study of the fossil and active examples, aiming particularly at addressing three outstanding questions, arising from the above introduced themes:

1. The geological processes and structures characterising the updip and downdip limits of the seismogenic zone;

2. The weakness of megathrusts faults and how it is influenced by fluids;

3. The interplay between fluid circulation and the seismic cycle along megathrusts.

Chapter 2. The SVU basal thrust in the Northern Apennines of Italy

After a brief introduction to the geologic context (paragraph 2.1) and the investigation methods (paragraph 2.2), this chapter presents, subdivided in four sections, the study of a fault strand (*sensu* Rowe et al., 2013) at the base of the Sestola Vidiciatico tectonic Unit (SVU), the Northern Apennines fossil interplate shear zone (Vannucchi et al., 2008). In Section 2.a, the internal structure of the fault strand (Fig. 2.1 and 2.2) is firstly described, as observed on outcrop and in microscale samples. In Section 2.b, the fault strand deformation history is reconstructed based on the structural arrangement. Section 2.c presents the results of trace element geochemical analyses on calcite tectonic veins. Finally, in Section 2.d, the state of stress in the fault strand zone is determined based on structural relations between the veins (paragraph 2.d.1), subsequently geochemical and structural analyses are integrated, to infer the characteristics of fluid circulation patterns during the fault strand activity and their implications in the earthquake cycle (paragraph 2.d.2).
The data presented in this Chapter have been partly already published (Mittempergher et al., 2018, for what concerns Sections 2.a and 2.b), partly submitted for publication (Cerchiari et al., submitted, with regards to Sections 2.c and 2.d).

2.1. Geological setting

The Northern Apennines developed as a result of the convergence between the European plate and the Adriatic microplate (which was part of the African plate). The process started in the Late Cretaceous with the closure of the former oceanic basin between the two plates and the consequent oceanic crust subduction, up to Cenozoic continental collision and related crustal thickening (Boccaletti et al., 1971; Coward and Dietrich, 1989; Vai and Martini, 2001 and reference therein). Frontal offscraping and underplating during Late Cretaceous-Eocene subduction and the related accretion on the overriding plate originated the Ligurian accretionary complex (e.g., Principi and Treves, 1984; Bortolotti et al., 2001; Marroni et al., 2010). The Sestola Vidiciatico tectonic Unit (SVU hereafter) has been interpreted as the plate boundary shear zone developed in the early-middle Miocene between the overthrusting Ligurian paleo-accretionary complex and the underthrusting Tuscan

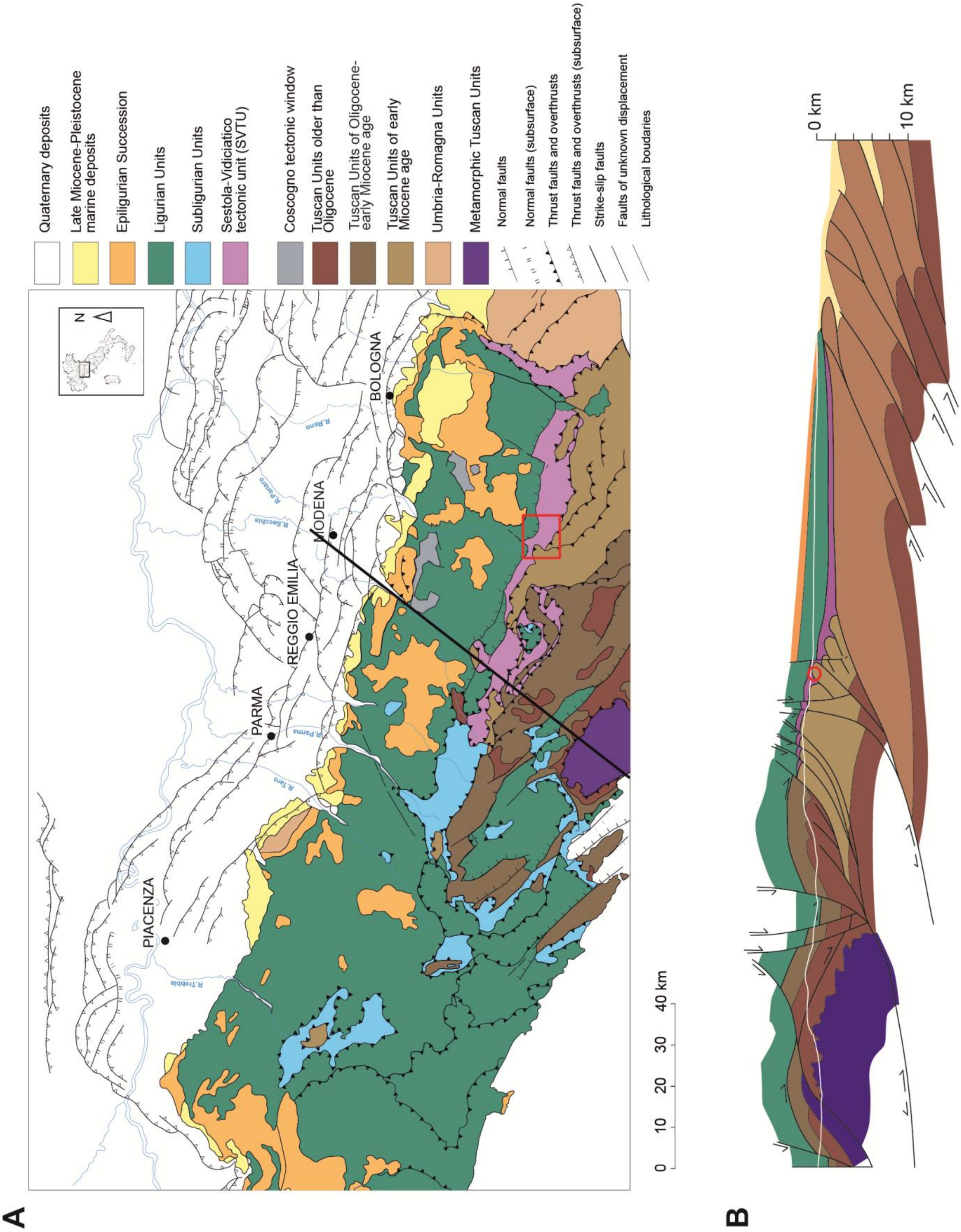

Figure 2.1. *Geological map of the Northern Apennines reported from Vannucchi et al. (2008). The Sestola-Vidiciatico tectonic Unit (SVU) is the interplate shear zone represented in pink, bounded between the Ligurian accretionary prism of the European upper plate (green) and the footwall foredeep turbidites of the Adriatic lower plate (brown). The approximate location of the studied outcrop is outlined in red, both in map and cross-section.*

/Umbrian Units of the Adriatic continental margin (Vannucchi et al., 2008 and reference therein, Fig. 2.1). The SVU is a regional-scale shear zone, 200 km-long parallel to the Northern Apennine chain and about 200 m-thick. It is a tectonic mélange (Festa et al., 2019), composed by blocks of different sizes, from cm to km, of three main sources (Vannucchi et al, 2008):

- Blocks, hm to km sized and aged from Early Cretaceous to middle Eocene, of 1) oceanic dark-gray shales with interbedded sandstone and micritic carbonate turbidites, 2) varicolored shales, 3) marl and calcareous turbidites. Age, lithological character and deformation style of these deposits imply that they are blocks mainly coming from the frontal and younger part of the overlying Ligurian accretionary prism (Landuzzi, 1994; Bettelli, 2002; Bettelli and Boccaletti, 2002; Plesi, 2002). Some of these blocks are interpreted as deriving from the more internal, older portions of the base of the oceanic accretionary prism (Vannucchi et al., 2008).
- hm- to km-sized blocks of shaly, marly and sandy turbidites deposited on the accretionary prism lower slope (Bettelli and Panini, 1992; Remitti, et al., 2007; Lucente and Pini, 2008; Remitti et al. 2013). Their ages span from late Eocene to middle Miocene (Cibin et al., 2001; Bettelli, 2002; Bettelli and Boccaletti, 2002; Plesi, 2002; Landuzzi, 2004; Botti et al., 2004). In some cases these blocks, though deformed, preserve complete basin sections with their original substratum (Landuzzi, 1994; Bettelli, 2002; Bettelli and Boccaletti, 2002; Plesi, 2002) and are interpreted as representing the infill of satellite or wedge-top basins formed on top of the foredeep developed in the frontal part of the prism. A minor component of marly slope sediments has been correlated with the deposits cropping out at the top of the oceanic accretionary prism (Cibin et al., 2011; Landuzzi, 2004).
- Extensive debris flow deposits, reworking material coming from the more external, and partly younger, thrust units of the oceanic accretionary prism (Landuzzi, 1994; Bettelli, 2002; Bettelli and Boccaletti, 2002; Lucente and Pini, 2008).

Material incorporated in the SVU has been removed from the actively forming frontal prism of the upper plate through gravitational and tectonic processes, resulting in contemporaneous frontal and basal erosion through the simultaneous activity of a roof and basal décollement (Vannucchi et al., 2008).

The different blocks described are arranged in superimposing slices, bounded by several thrust faults cutting through the SVU and including the basal and upper décollements (Vannucchi et al., 2008; Remitti et al., 2012). Vitrinite reflectance, illite crystallinity and apatite fission track data suggest that the SVU and the footwall rocks reached maximum temperatures around 120-150 °C, corresponding to ~4-5 km of burial depth with a 30 °C/km geothermal gradient (Reutter, 1981; Botti et al, 2004; Vannucchi et al., 2008; Thomson et al., 2010).

Although the SVU has been thoroughly described at the regional scale (e.g., Vannucchi et al., 2008;

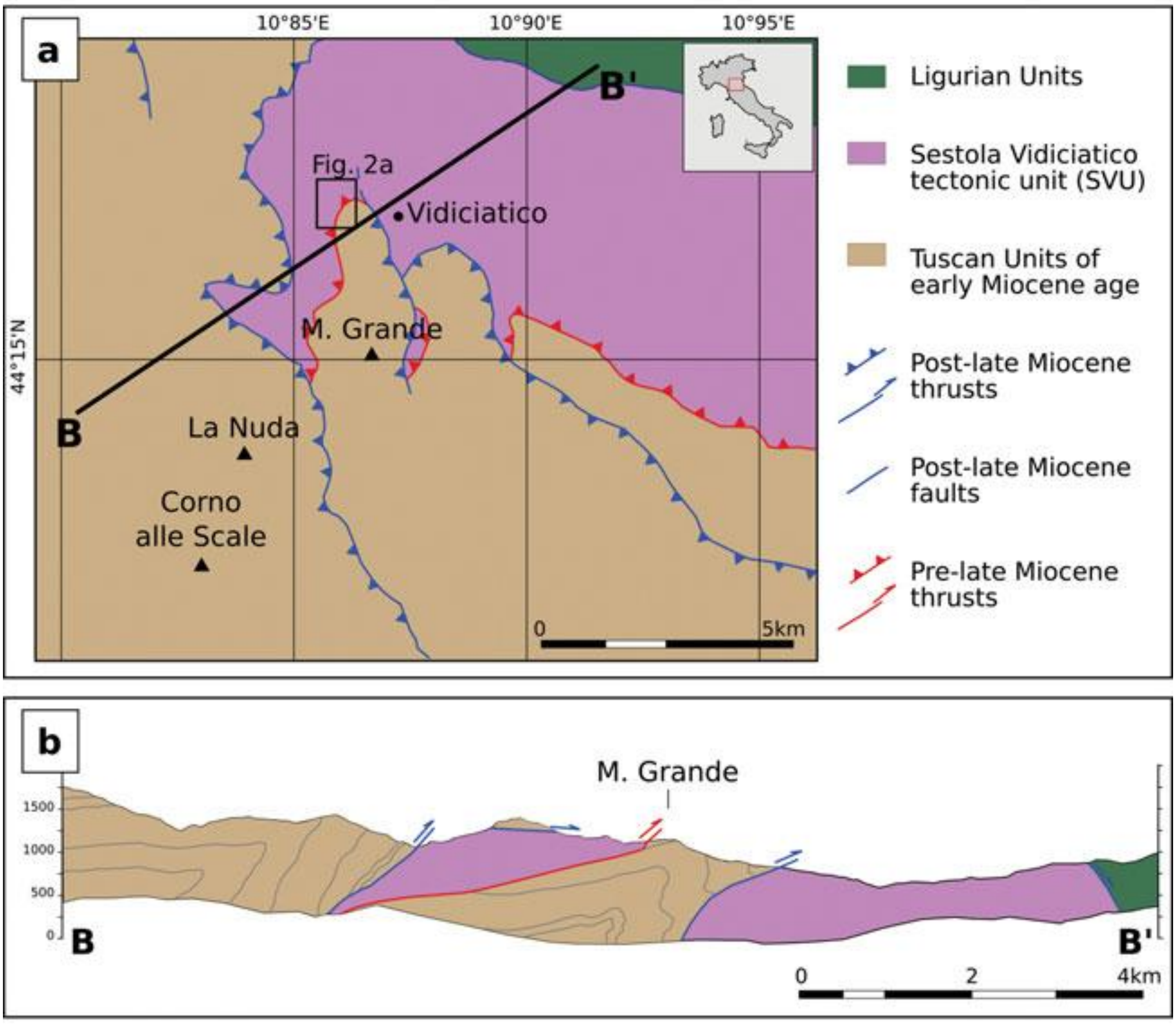

Figure 2.2. *Simplified structural map (a) and geological cross-section (b), showing that Vidiciatico outcrop (in the black box) has not been involved in post-Miocene thrusting. From Mittempergher et al. (2018).*

Vannucchi et al., 2012; Remitti et al., 2013), the SVU basal contact has not yet been studied in detail. Field observations have been focused mainly on fault strands within the SVU, while the basal and upper thrusts have been investigated at a larger scale. The upper thrust is generally bad exposed, while the lower thrust crops out more frequently and is directly accessible. Marking the contact between the foredeep turbidites on the lower plate and the whole of the SVU, it represents the first limit between the plates and records deformation from the beginning of subduction to subsequent superimposing phases.

This work is a first contribution to the exploration of the SVU basal thrust, upon direct observations of a fault strand cropping out in Vidiciatico (BO) (see Mittempergher et al, 2018; Cerchiari et al., submitted).

At the regional scale, the basal thrust is characterized by a ramp-and-flat architecture and is crosscut by post-late Miocene thrust faults (Fig. 2.2). These segmented the basal thrust in portions without

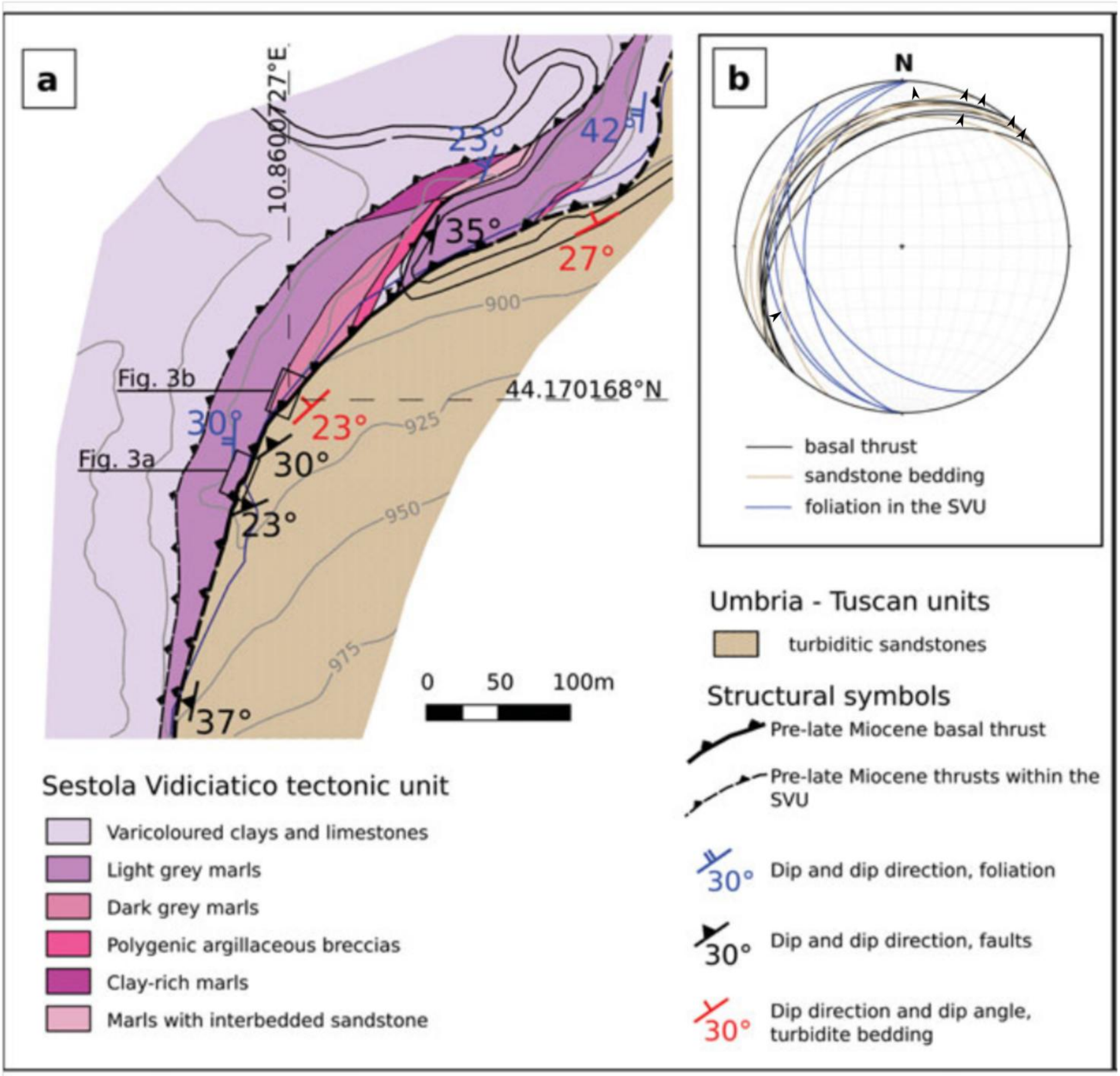

Figure 2.3. *Geological and structural framework of the Vidiciatico outcrop. a) Interpreted geology of the study area. For purpose of simplicity, lithological subdivisions not referring to official formation names have been introduced (see Geological Setting). b) Stereoplot of the orientations of the SVU basal thrust (black), the footwall turbidite bedding (light brown) and the tectonic foliation planes in the SVU marls (blue). Equiareal, lower hemisphere projection. From Mittempergher et al. (2018).*

further deforming them internally, as it is the case for the outcrop in Vidiciatico (Bettelli et al., 2002; Plesi et al. 2002; Botti et al. 2011).

The SVU basal thrust fault strand in Vidiciatico is ~1 m-thick and separates the SVU from the foredeep sandstone turbidites belonging to the underthrusting Adriatic plate (Umbria-Tuscan Domain) (Figs. 2.3 and 2.4). The footwall turbidite beds are sandy and pelitic-sandy (S/P >>1), Burdigalian in age (Botti et al., 2011). Accordingly to official cartography at the 1:50000 scale, (Botti et al., 2011) the SVU here is composed of Oligocene to Miocene marls (e.g. Marmoreto Marls, Poggialto Formation, Civago Marls), sedimentary breccias of uncertain age (Polygenic Argillaceous Breccias) and slices of Varicolored Shale and Limestones of pre-middle Eocene age. In Figure 2.3, a geological map at the scale 1:2000 of Vidiciatico outcrop area, drawn based on field survey data (paragraph 2.2), shows that the contacts between lithological units are in some cases clearly tectonic and bounded by a thrust fault (e.g., the upper contact between varicoloured clays and limestones and light grey marls in Fig. 2.3.a), while in other cases the nature of contacts is undetermined, possibly being also originally stratigraphic with a component of subsequent mechanical reworking (simple black lines in Fig. 2.3.a). The main orientation of the basal thrust fault strand is parallel to footwall bedding, strikes from N to E and kinematic indicators (calcite slickenfibers) show a main tectonic transport direction toward the NNE (Fig. 2.3.b). It currently dips of ∼20° toward WNW, thus resembling a normal fault. This is the result of a late tilting, related to the exhumation phase, and the thrust orientation during pre-late Miocene subduction is unknown. Nevertheless, the cutoff relationships of the basal thrust with the footwall bedding range from 0° to 20-30° at the regional scale, suggesting a ramp-and flat geometry (Landuzzi, 1994; Vannucchi et al., 2010). In particular, the Vidiciatico basal thrust fault thrust is nearly parallel to the footwall turbidite beds, therefore it should correspond to a flat portion of the contact (Figs. 2.3.b and 2.4).

2.2 Methods

Several fieldtrips were performed from 2015 to 2018 to measure in detail the orientations and the geometrical relationships of the structural elements in the field and to accomplish repeated sampling with specific targets. The 1:2000 geological map of the study area (Fig. 2.3.a) was constructed based on field surveys and the 1: 10000 scale map already available at http://geoportale.regione.emilia-romagna.it/it/mappe/informazionigeoscientifiche/geologia/carta-geologica-1-10.000. The map is drawn according to the lithological variations within the SVU, but it does not refer to official geological formation names, whose attribution was uncertain due to the lack of specific biochronological constraints. The main structure orientations were displayed using equiareal, lower hemisphere stereographic projections, constructed with the aid of Stereonet 9 software (Allmendinger et al., 2012, Fig. 2.3.b). From samples collected in the field, 47 polished thin sections with a 30 μm thickness were obtained, suitable for optical, cathodoluminescence microsco-

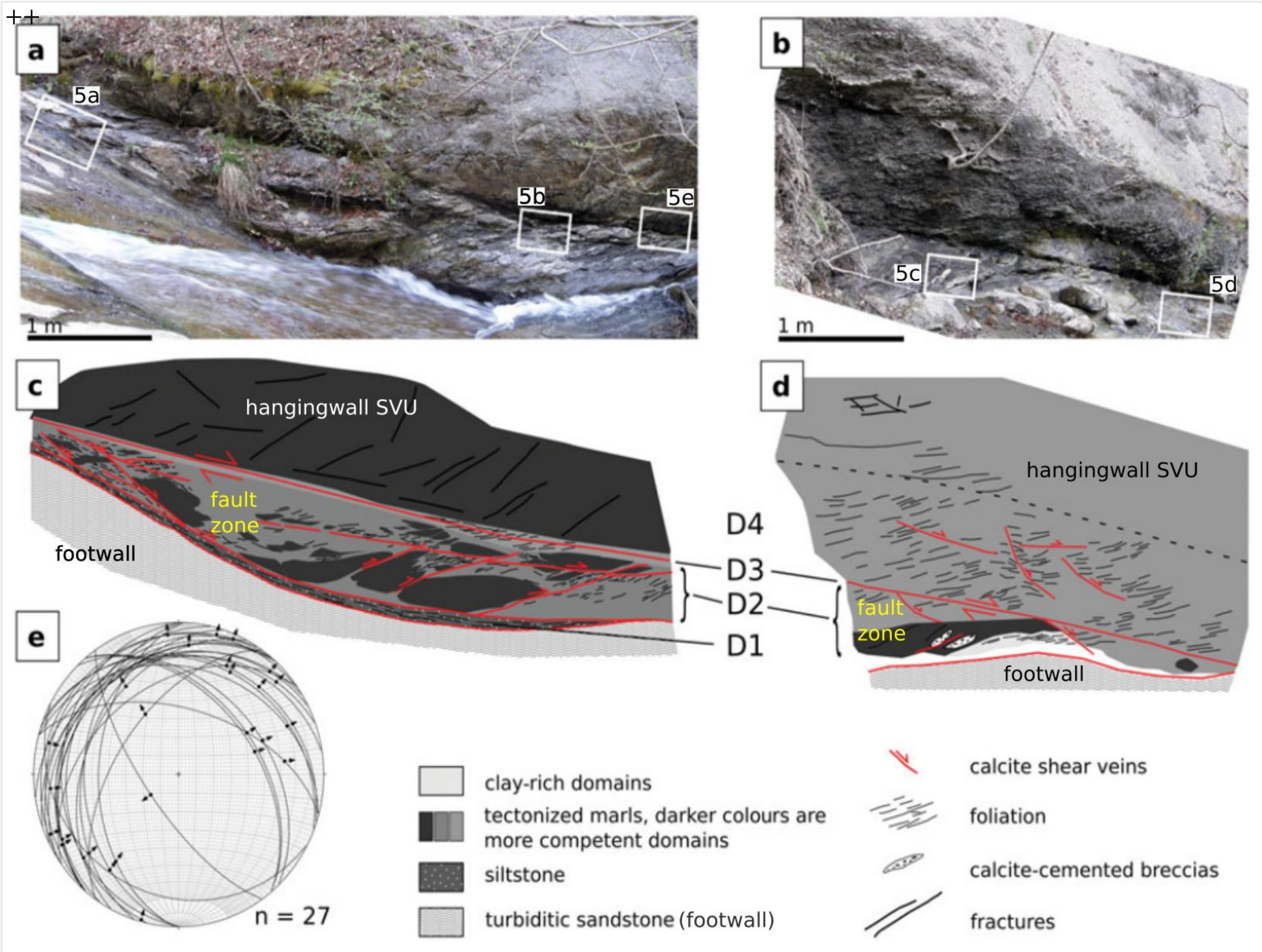

Figura 2.4. *Structure of the basal thrust in Vidiciatico. a) and b) Mesoscale photographs of two outcrops of the basal thrusts. White squares indicate the localizations of Figs. 2.5.a-e. c) and d) Sketches of the main interpreted structural features correspondent to the outcrops in a) and b). e) Stereoplot of calcite shear veins in the basal thrust shear zone, with the slip vectors inferred from the slickensides. Equiareal, lower hemisphere projection. From Mittempergher et al. (2018).*

pe and, properly gold-coated, also for Scanning Electron Microscope imaging coupled with Energy Dispersive X-Ray Spectroscopy. Two 100 µm-thick thin sections and three 0.5 cm-thick rock slices were derived from samples of calcite veins and the relative wall rock, for the Rare Earth Element (REE) determination with Laser Ablation Inductive Coupled Plasma Mass Spectrometry (LA-ICP-MS). The equipment has been provided by the Centro Interdipartimentale Grandi Strumenti (CIGS) at Modena University, Italy, except for the cathodoluminescence microscope, held by the Department of Earth Sciences at the University of Turin, Italy. The scanning electron microscope is a Field Emission Gun FEI Nova Nano-SEM 450 apparatus, equipped with a Quantax-200 X-Flash 6 detector for EDS.

Element concentrations obtained from the X-Ray EDS microanalysis were used to determine vein calcite composition and to calibrate spectrometer analysis: calcium fractions were measured for every vein to normalize each mass spectrum to its base peak. For the REE mass spectrometry a 213 nm Nd:YAG laser ablation system (NewWave Research) coupled to a quadrupole ICP-MS (Thermo Fisher Scientific X-SeriesII) was used. Carbonate specimens were analysed with a laser spot size of 80 µm, a frequency of 10 Hz, a fluence of ~6 J/cm^2 and a He flux of 0.6 L/min. Before each analysis, the sample surface was carefully pre-ablated to remove possible contaminants. Several spot analyses were collected per sample, through the direct laser ablation of the 100 µm-thick thin section or rock slice. Raw ICP counts were normalized and corrected using ^{43}Ca as internal standard and NIST612 as reference material, with mass fractions from Jochum et al. (2007) (georem.mpch-mainz.gwdg.de). Relative standard deviation was always better than 10%.

REEs in whole rocks were measured in powders obtained by microdrilling of the rock slices. About 100 mg of powder were rinsed several times with MilliQ water, dried overnight and dissolved with a HF-HNO_3 mixture. Solutions were properly diluted and analysed using a quadrupole ICP-MS X-SeriesII at CIGS of the University of Modena and Reggio Emilia. Data were acquired for ^{139}La, ^{140}Ce, ^{141}Pr, ^{146}Nd, ^{147}Sm, ^{153}Eu,^{157}Gd, ^{159}Tb, ^{163}Dy, ^{165}Ho, ^{166}Er, ^{169}Tm, ^{172}Yb, ^{175}Lu and calibrated using a multi-element standard solution of different concentrations (from 1 ppb to 1000 ppb) combined with ^{115}In as an internal standard. Precisions were typically better than 5% RSD (relative standard deviation).

Section 2.a. Structure of the SVU basal thrust

In the studied fault strand, the turbidite sequences of the footwall appear not much affected by tectonic deformation. At the mesoscale, meter-spaced planar shear calcite veins dipping at medium to high angle toward NNE cut the sandstone beds with only slight normal offset, the orientations of the beds being rather constant and parallel to the orientation of thrust faults. At the microscale, only primary sedimentary structures are recognizable (as planar and convolute lamination, Fig. 2.6.a). The contact between the turbidites and the SVU (i. e. the SVU basal thrust fault strand) is marked by a less than 5 m-thick fault zone. A thin (a few cm), discontinuous shear calcite vein parallel to the footwall beds, separates them from a 30 cm-thick interval of dark grey siltstones at the base of the fault strand (Fig. 2.5.a, paragraph 2.a.1). Here, a planar, mm-spaced foliation parallel to the contact is visible at the mesoscale, together with sparse mm-thick extensional veins between foliation planes. A 3 to 5 cm-thick discontinuous calcite shear vein marks the contact with overlying grey marls (Fig. 2.5.a-e, paragraph 2.a.2), with more competent sandstone or limestone layers boudinaged to form lens-shaped lithons. The less competent, more pelitic portions of the marls are

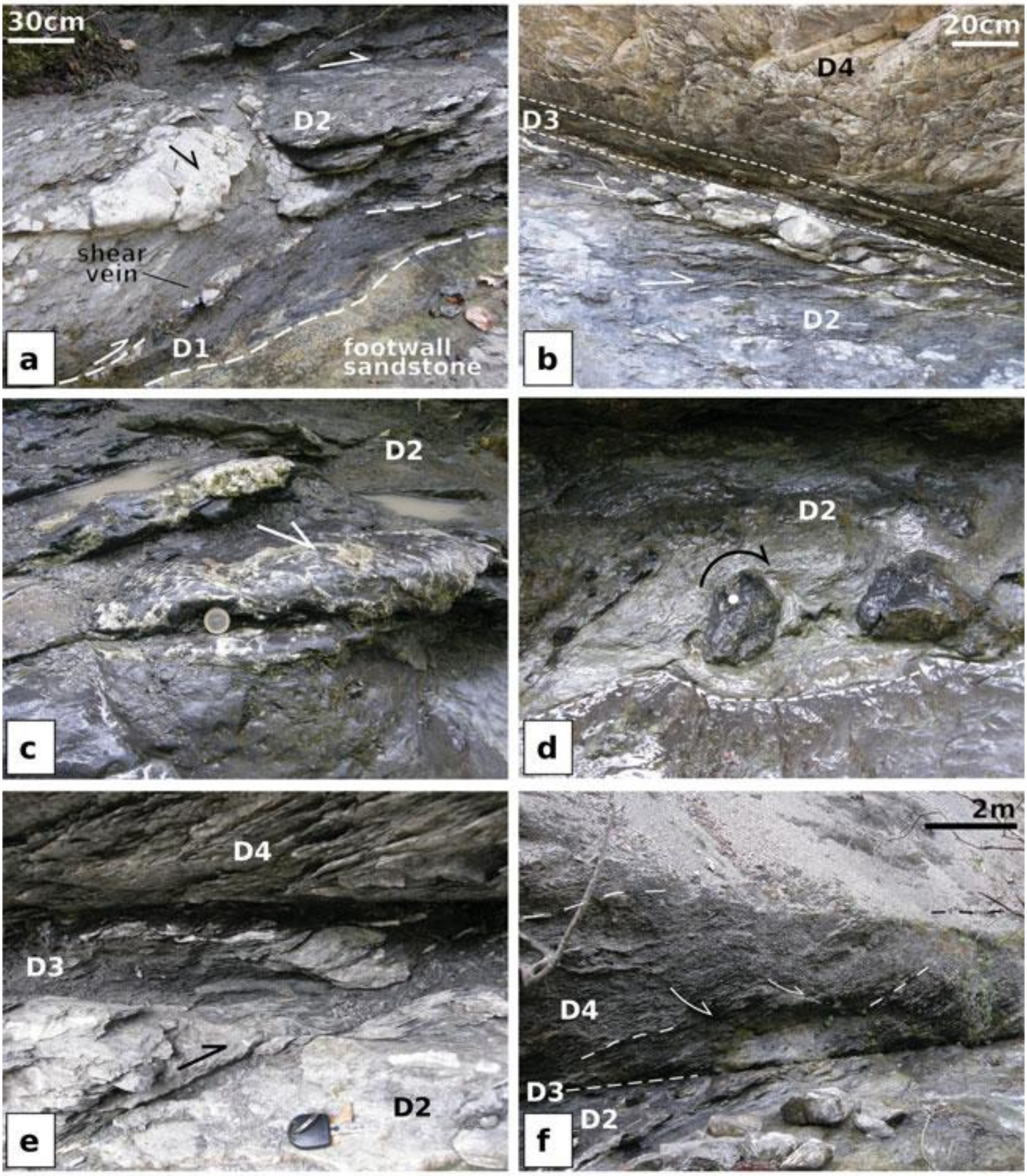

Figure 2.5. *Mesoscale structures of the fault zone. a) Close up of footwall, D1 and D2, with relative thrust contacts. D1 is composed by dark siltstone, D2 consists of foliated light gray marls including harder lithons bounded by shear calcite veins. (b) Close up of the contacts between D2, D3 and D4. The latter consists of fractured competent carbonate-rich light gray marls. c) Detail of a hard lithon tail embedded in D2, showing angular wall rock fragments cemented by calcite crystals in a breccia. d) Detail of rounded hard blocks of sandstone-rich limestone, embedded within foliated marls in D2. The arrow shows the rotation of the block inferred from the deflection of marl foliation. e) Detail of the internal texture of D3, showing the pervasive foliation and boudinage of calcite shear veins. f) Details of the outcrop in Figure 2.4b, showing the D4 foliation deflected due to shear along D3. Modified from Mittempergher et al. (2018).*

affected by a scaly cleavage, where centimetric, lens-shaped scales (similar to the "scaly lithons", as defined in Pini, 1999) are formed by the intersection of two subparallel sets of discontinuous cleavage planes (Fig. 2.4.f). The scale sides are polished, with striations coated by thin iron oxide layers, suggesting slip with a normal shear sense along the scale sides, with a component of flattening normal to the scaly cleavage mean direction (i. e. the alignment direction of the scales). This is oriented at about 30° to the main thrust (Figs. 2.3.b and 2.4). Fault strand marls are cut by several calcite shear veins, a few cm thick, subparallel to the thrust faults or fracturing more competent lithons and bounding their edges (Fig. 2.4). Shear veins always bear slickenfibers with variable orientations, but overall consistent with the main NNE main sense of transport (Fig. 2.4.e). Marls are abruptly cut by the main thrust fault cropping out in the fault strand, formed by a pervasively foliated 20-30 cm-thick interval marked at the top by a shear vein. This is thin (2-3 cm-thick), but very sharp and continuous for tens of meters (Fig. 2.5.b, e, f, paragraph 2.a.3). Above the main thrust, the transition from the fault zone to the hangingwall SVU is gradual, and marked by the decrease in intensity of fractures and shear veins, and by a steeper (~40° inclined) scaly cleavage (Fig. 2.5.b, f).

Four structural domains (D1 to D4, Figs. 2.4.c-d and 2.5) have been recognized based on their different deformation styles both at the meso- and microscale (Mittempergher et al., 2018).

2.a.1 Domain 1 (D1)

Domain 1 represents the basal part of the fault strand, immediately above the footwall, and consists of a 30 cm-thick horizon of laminated dark gray siltstone, separated from both the footwall sandstones and the overlying layer D2 by a few cm-thick calcite shear veins. Internally, D1 is deformed by a pervasive and closely spaced (less than 1 mm) foliation subparallel to the sedimentary lamination and to the shear veins bounding the layer (Fig. 2.5.a). The shear veins have crack-and-seal texture (Ramsay, 1980), with calcite growth increments marked by trails of inclusions of the wall rock. Individual increments are oriented at 20 to 40° to the vein walls (Fig. 2.6.b). The siltstone shows alternating coarse and fine, clay-rich laminae, spaced less than 1 cm between each other (Fig. 2.6.c). The clastic component includes quartz, feldspar, mica and biotite lamellae, illite and calcareous bioclasts, and the cement consists in calcite. The sedimentary lamination is crosscut by deformation bands, shear calcite veins and extensional calcite veins. Deformation bands form an angle of about 30°–40° to the main thrust orientation, are spaced apart about 10–20 mm and are characterized by the reorientation of mineral grains without fracturing. The alignment of mica lamellae to the shear bands and their asymmetry within the bounded volume (Fig. 2.6.d) indicate a dextral component of movement, synthetic with the main transport direction of the thrust. Thin (< 1 mm), discontinuous shear calcite veins are found parallel to the sedimentary lamination and locally infill the shear bands

with opaque calcite, which contains small inclusions of sediment particles (Fig. 2.6.e). Shear veins show a mutual crosscutting relationship with extensional veins oriented at 80–90° to the sedimentary lamination, up to 10 mm thick (Fig. 2.6.c, e). The extensional veins perpendicular to the lamination have irregular, wavy interfaces to the wall rock and include crack-and-seal increments traced by wall rock inclusions (Fig. 2.6.e). Calcite veins are draped (if shear veins) or truncated (if extensional veins) by layer-parallel dark dissolution seams, suggesting layer-perpendicular compaction after veining (Fig. 2.6.e). In the siltstone, preferentially oriented phyllosilicate lamellae define a microscale layer-parallel foliation. It wraps around hard quartz and feldspar clasts, which are strongly corroded, while calcite is precipitated in microcracks and pressure shadows (Fig. 2.6.f).
These features suggest that the wavy and anastomosing geometry of calcite extensional veins can be partly due to general compaction of the layer through pressure-solution processes. The extensional veins are crosscut by shear veins, as the one which separates D1 from D2 (Fig. 2.5.a). However, some evidences of fault-perpendicular extensional veins crosscutting the shear veins suggest that extensional and shear veins formed cyclically during the thrust activity (Fig. 2.6.b).

2.a.2. Domain 2 (D2)

Domain 2 is a 50–80 cm-thick layer of strongly deformed marls with variable content of clay, carbonate and silt. The marls show a penetrative fabric consisting of rhombohedral lithons, whose long axis is oriented at low angle of ~20° to the main thrust orientation in the above Domain 3 (D3, see paragraph 2.a.3). Surfaces bounding the lithons are polished and striated, with local millimeter-scale calcite fibers, suggesting that they acted as slip surfaces. The size of lithons in marls varies from a few millimeters to some decimeters (Figs. 2.4 and 2.5), being larger in relatively competent, carbonate-rich domains. They become smaller with the increase of clay content, forming flattening surfaces visible at the mesoscale as a scaly cleavage, often draped and deflected around decimeter-scale competent lithons (Fig. 2.5.e, f). In clay-rich domains, centimeter-scale synthetic shear bands form a typical S-C’ fabric, deflected around hard carbonate clasts. At the meter scale, the marls are cut by several sharp calcite shear veins, parallel or at low angle of about 20° to D3 main thrust and synthetic with its top to the NE sense of transport (Fig. 2.4e). The shear veins are laminated and have mesoscopic striped-bedded crack-and-seal texture (Koehn and Passchier, 2000) but, in correspondence of dilational jogs along the fault plane, they include also breccias of angular clasts of the wall rock dispersed in a matrix of euhedral calcite crystals (Fig. 2.5.c).
At the microscale, the inner part of more competent, carbonate-rich lithons is substantially undeformed and preserves sedimentary structures like bioturbation or calcareous bioclasts (Fig. 2.7.a, b). The surfaces bounding the lithons are lined by curvilinear and weakly anastomosing dark dissolu-

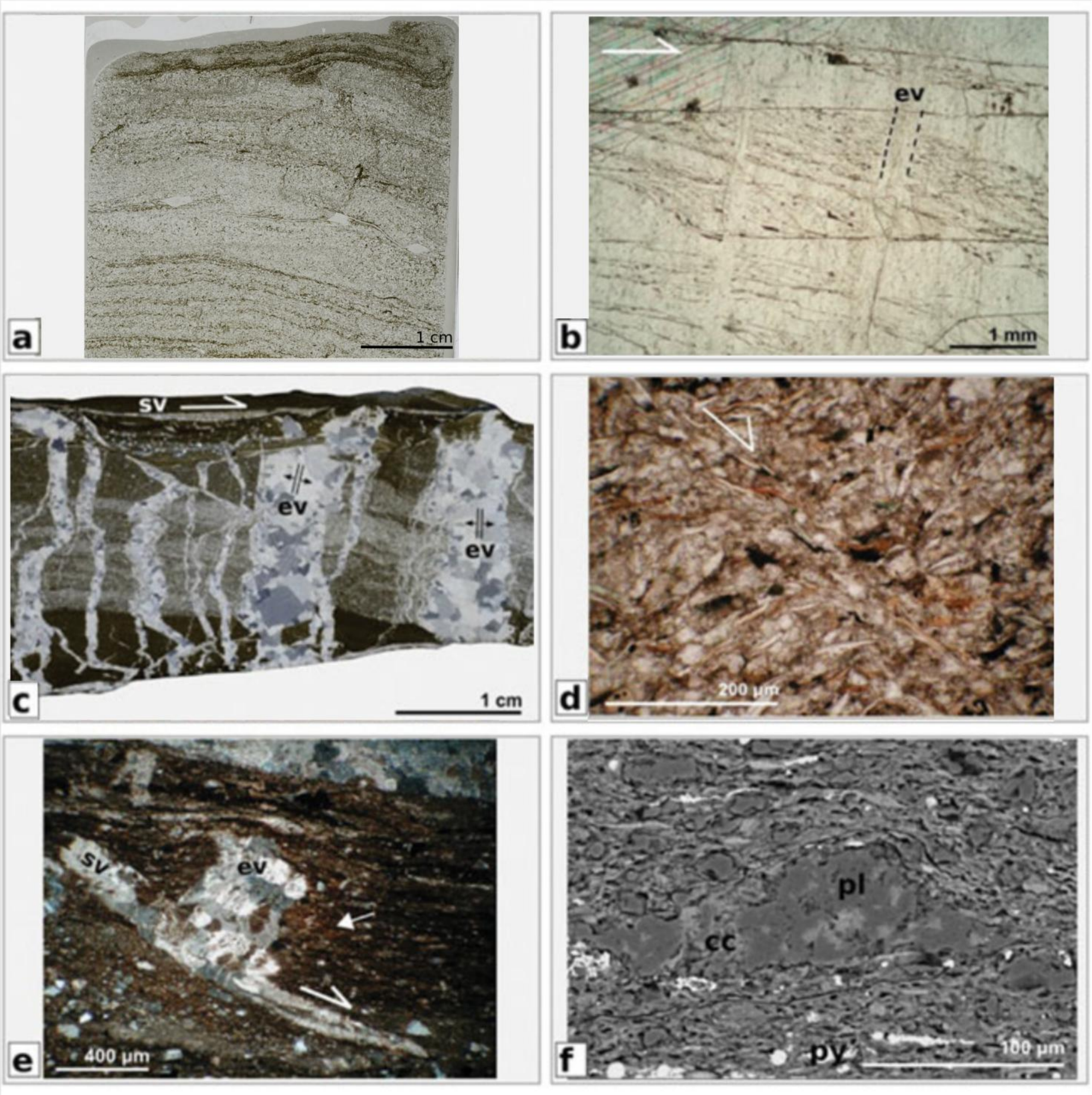

__Figure 2.6.__ Microstructures of D1. a) Photomicrograph showing the undisturbed primary structure of footwall turbidites, with lamination and bioturbation. b) Crack-and-seal calcite shear vein bounding the top of D1. The crack-and-seal increments are cut at high angle by two extensional veins. Plane polarized micrograph. c) Overview of anastomosing extensional veins (ev) perpendicular to the layer, cutting a discontinuous shear vein (sv), thus suggesting layer-perpendicular compaction. Cross polarized thin section scan. d) Shear band within the siltstone, showing displacement of grains without fracturing and alignment of phyllosilicate lamellae along the plane. Plane polarized micrograph. e) Crack-and-seal extensional vein (ev) associated with a partially dissolved shear vein (sv), acting as hard object during general layer-perpendicular shortening. The dark dissolution seams in the siltstone are draped around the veins, bypassing the shaded area on the right of the vein (arrow). Cross polarized micrograph. f) Internal texture of the siltstone, showing evidence of pressure-solution flattening and deposition of calcite (cc) in pressure shadows, represented by microcracks in a plagioclase (pl) clast, and smearing of pyrite (py) parallel to the dissolution seams. Back Scattered Electron image. Modified from Mittempergher et al. (2018).

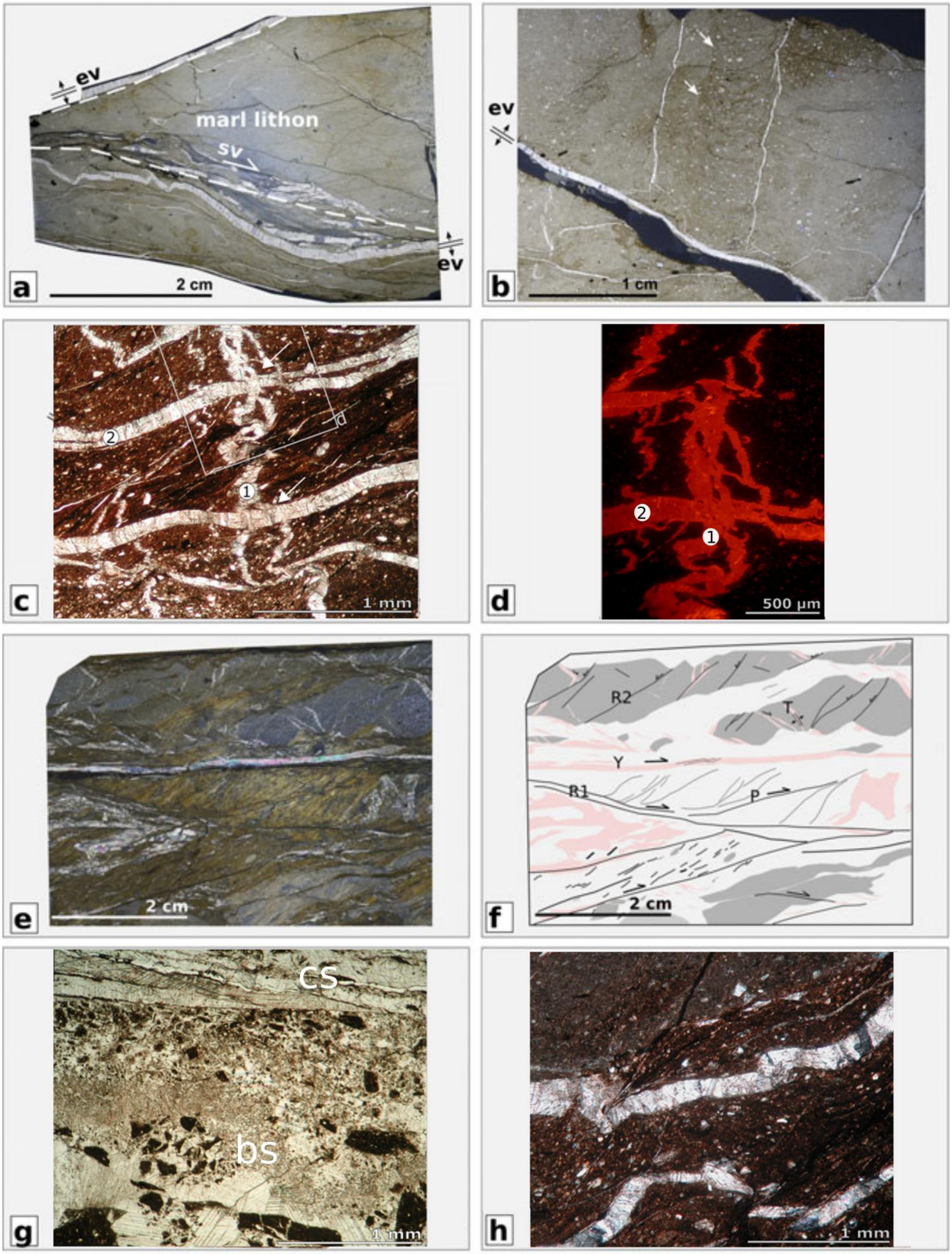

(Caption in the following page)

Figure 2.7. *Microstructures of D2. a) Deformation in a marl lithon. The internal part is not deformed and, at the boundaries (hatched white lines), is lined by several veins and dark dissolution seams. Both shear veins (sv) and extensional veins (ev) are emplaced along the lithon boundaries. Cross polarized thin section scan. b) Detail of the inner undeformed part of a marl lithon, bounded by an extensional vein (ev) preserving bioturbation structures and bioclasts (white arrows). Cross polarized micrograph. c) Mutually crosscutting (arrows) fault-perpendicular (1) and fault-parallel (2) extensional veins in a clay-rich domain. Fault perpendicular extensional veins are shortened and folded. The rectangle shows the location of figure (d). Plane polarized light micrograph. d) Optical cathodoluminescence image of the area highlighted in c). Calcites filling fault-parallel and fault-perpendicular extensional veins have the same orange-reddish luminescence. e) and f) Deformation in clay-rich domains. Interpretative sketch in f), where light pink is calcite, light gray corresponds to more competent layers or clasts, thick black lines are shear bands and thin black lines the foliation planes. Thin section scan, cross polarized light. g) The texture of a shear vein, with the upper part formed by crack-and-seal hybrid shear increments (cs = crack-and-seal shear vein) and the lower part represented by a breccia, with angular wall rock clasts dispersed in a calcite matrix (bs = breccia shear vein). Plane polarized light micrograph. h) Detail of fault-parallel extensional veins in a clay-rich domain. The veins are folded and shortened both at high angle and at low angle to their direction. Plane polarized light micrograph. Modified from Mittempergher et al. (2018).*

tion seams, with non-sutured surfaces typical of relatively phyllosilicate-rich lithologies (Logan and Semeniuk, 1976) (Fig. 2.7.a). The dark seams are enriched in preferentially oriented phyllosilicate lamellae, suggesting that a slight shearing occurred along these surfaces. Several calcite shear and extensional veins are localized around lithons (Fig. 2.7.a, b). Shear veins (Fig. 2.7.g) are filled by elongated blocky calcite crystals growing along parallel shear microtransforms (*sensu* Fagereng et al., 2010). They correspond to crack-and-seal increments defined by wall rock inclusion bands oriented 20° to 40° to the microtransforms. This structure characterizes the veins as hybrid shear, i. e. veins opened on shear surfaces with a dilatant component (Ramsay, 1980; Ramsay and Huber, 1983; Bons et al., 2012).

The breccia intervals along the shear veins are composed of fragments sourced from the wall rock and/or preexistent veins, dispersed in a calcite matrix (Fig. 2.7.g). Clasts/matrix proportions are variable, just as fragments dimension and aspect ratio. Calcite has always blocky crystals with growth at the margins uninterrupted by the contact with wall rock clasts. The lack of clast rotation or evidence for shearing, together with their location inside dilational jogs, suggests that these veins correspond to implosion breccias (Sibson 1985; Sibson, 1986; Sibson, 1987), up to tens of cm in both thickness and length. The exact mechanics, kinetics and tectonic significance of this type of breccias are still unclear.

Extensional veins have trends that, even if wavy and anastomosing, are generally subparallel to dissolution seams bounding the lithons. They are sealed by blocky to fibrous calcite crystals perpendicular to the vein boundaries (Fig. 2.7.a, b), with evidences for antitaxial growth. Fracturing and boudinage affect more competent lithons or early-stage calcite veins (Fig. 2.7.e, f).

In less competent, clay-rich domains, the preferred orientation of phyllosilicate lamellae forms, coherently with the mesoscale observation, a penetrative foliation, displaced by an array of Y, R1, R2, T and P shear bands (*sensu* Logan et al. 1992), locally lined by thin calcite shear veins (Fig. 2.7.e, f). The clay foliation is crosscut by several generations of thin extensional veins, oriented at high angle to the fault zone or with anastomosing trajectories often subparallel to the foliation planes (Fig. 2.7.c, d, h) The anastomosing, fault parallel extensional veins are sealed by fibrous calcite crystal perpendicular to the vein walls, and crosscut the phyllosilicate foliation and the shear veins. The fault-perpendicular extensional veins have blocky to elongated blocky crystals and they are folded and truncated by layer-parallel dark dissolution seams, suggesting, also here, compaction normal to the fault (Fig. 2.7.c). Also fault-parallel extensional veins are in many cases gently folded, and locally dislocated by micro-thrust faults (Fig. 2.7.h), suggesting a minor component of fault-parallel shortening. Fault-parallel and fault-perpendicular extensional veins mutually cut each other and are sealed by calcite with the same orange luminescence (Fig. 2.7.c, d), suggesting that they were contemporaneous and crystallized from the same fluid.

2.a.3. Domain 3 (D3)

Domain 3 is the main thrust, represented by a 20–30 cm-thick shear zone, separating D2 from D4 and marked at the top by a 2-3 cm-thick calcite shear vein, very sharp and continuous for tens of

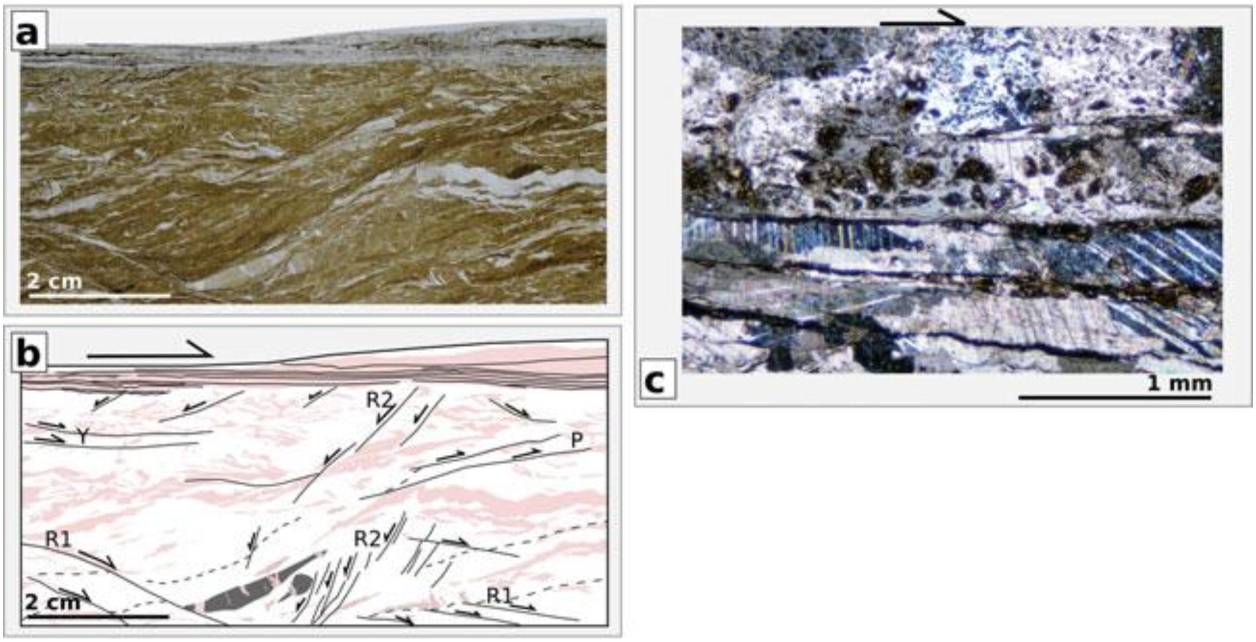

Figure 2.8. *Microstructure of D3. a) The top D3 vein, cutting the strongly deformed clay-rich domain below it. Plane polarized thin section scan. (b) Drawing of a) highlighting the deformation structures: light pink for calcite veins, light gray for competent layers and clasts, thick black lines marking the shear bands and hatched black lines lining the foliation planes. c) Detail of shear calcite veins lining the upper boundary of D3, showing both crack-and-seal shear and breccia shear textures. From Mittempergher et al. (2018).*

meters (Fig. 2.4). Adjacent to the main shear vein, D3 shows a structural fabric similar to D2 clay-rich domains, but with a higher degree of deformation: this is shown by a close spaced mesoscopic foliation involving also deformed fragments of calcite veins (Fig. 2.5.b, e) and, at the microscale, by the abundance of calcite shear and extensional veins, which are folded, boudinaged and reoriented and whose crystals are intensely twinned (Fig. 2.8.a, b). Secondary shear bands adjacent to the main shear vein are both synthetic and antithetic to its shear sense inferred from calcite slickenfibers (Fig. 2.8.a, b). They are thus compatible with flattening of the sediments perpendicular to the fault plane. The main shear vein actually consists of multiple parallel shear veins separated by thin layers of clay or carbonaceous material and, as D3 shear veins, cemented by crack-and-seal elongated-blocky calcite crystals, locally passing to dilational jogs with breccia infill (Fig. 2.8.c).

2.a.4. Domain 4 (D4)

Domain 4 is the 3 m thick damage zone that marks the transition from D3 to the hanging wall. It consists in either more calcareous light gray (Fig. 2.4.a) or less calcareous dark gray marls (Fig. 2.4.b). Light gray marls are rather competent and cut by shear fractures, spaced some centimeters to some decimeters apart, which define elongate rhombohedra with flattening planes at about 40° from D3 (Fig. 2.5.b, e). Dark gray marls are instead cut by a pervasive scaly foliation defined by sub-centimetric flattened lithons. The penetrative tectonic fabric in dark gray marls is deflected in a way consistent with shearing along D3 and is cut by thin synthetic shear veins either parallel or at ~30° to D3 (Figs. 2.4 and 2.5.f).

Section 2.b. Interpreted deformation history of the fault zone

Based on the observed fault strand structural arrangement, three main stages of evolution have been reconstructed and summarized in Fig. 2.9.

2.b.1. First stage: pre-lithification soft-sediment deformation

The first stage has been recorded only in D1 siltstone, where the inter-particle rearrangement without fracturing or deformation of the grains is typical of independent particulate flow (Borradaile, 1981; Knipe, 1986) (Fig. 2.6.d). This process should have involved overthrust sediments shortly after their deposition, i. e. at shallow depth along the SVU basal thrust. The thin, discontinuous shear veins in the deformation bands suggest, with their internal dirty appearance, that they developed in not completely lithified sediments (Maltman, 1994). This indicates a gradual transition to dilatant brittle deformation with the increasing grade of cementation of the siltstone, at very shallow depth and temperatures typical of carbonate diagenesis. Similar calcite veins that formed at early diagenetic conditions have been documented in other outcrops of the Apennines (Labaume et al., 1991) and in similar shallow subduction settings, such as the Palaeogene accretionary complex of the central European Alps (Dielforder et al. 2015; Dielforder, et al., 2016).

2.b.2. Second stage: syn-lithification progressive embrittlement

Progressive lithification and embrittlement of the sediments led to a second stage of deformation, best expressed in D2. Strain has been accommodated in different ways, depending on the competence contrast of the components. The deformation is more brittle in carbonate-rich marls and localized along multiple thrust faults lined by shear veins (Fig. 2.4.a), Shear veins and pressure solution seams are localized along the anastomosing surfaces bounding competent lithons, which are not deformed internally (Fig. 2.7.a, b). The lack of intergranular deformation in marls suggests that they were already cemented when embedded within the SVU, unlike the D1 siltstones. Shearing, fluid flow and fluid-rock interactions in marls are likely driven by fracturing. In clay-rich domains, deformation is more diffuse and involves the development of pressure-solution seams (Fig. 2.7.c, e, f, h) and of a microscale tectonic fabric characterized by the preferred orientation of clay lamellae displaced by shear bands. This fabric is typical of phyllosilicate-rich gouges deformed by frictional sliding (e.g., Logan et al. 1992; Haines et al. 2009). The frictional strength of foliated clay-rich rocks with interconnected layers of phyllosilicates is lower than their non-oriented equivalent (Collettini et al. 2009; Tesei et al. 2012; Tesei et al., 2015), with friction coefficient in the order of 0.2-0.4, i.e. significantly lower than commonly inferred friction coefficients of 0.6 to 0.85 (Byerlee, 1978). Clay-rich domains are thus weak compared with calcareous competent lithons, and tend to accommodate strain at low differential stress, although they are only locally present within D2. The emplacement of calcite shear veins in clay-rich domains documents episodic dilatancy and embrittlement (Fig. 2.7.e, f). Deformation structures suggest that, during this second stage, D1 likely experienced only limited shear strain and a preponderant flattening: shear veins are crosscut by extensional veins perpendicular to the layer (Fig. 2.6.b), while pressure-solution foliation planes are parallel to the layer. This D1 flattening during the second stage of deformation is coherent with a progressive localization of the shear strain in the overlying D2, which produces a strain decoupling across the shear vein separating D1 from D2.

2.b.3. Third stage: post-lithification localized intense deformation

The last stage of deformation concentrates in D3, which cuts all the D2 brittle and ductile structures. It corresponds to the maximum depth and temperature reached by the thrust (Fig. 2.9) and it is similar to what is described in D2, showing a combination of shear veins with frictional sliding and pressure solution in clay-rich domains. Nevertheless, deformation in D3 is much more pervasive, due to the strong localization of shear strain in a relatively thin domain (Fig. 2.8.a, b). D4, the hanging wall damage zone, displays deformation structures compatible with shearing along D3, i.e. synthetic shears in light grey marls (Fig. 4.a, c) and a foliation at 30–40° to D3 crosscut by synthetic shears in dark grey marls (Fig. 4.b, d). In D2, latest deformation structures consist of extensional veins, either perpendicular, or, most frequently, having anastomosing trends roughly parallel to the thrust.

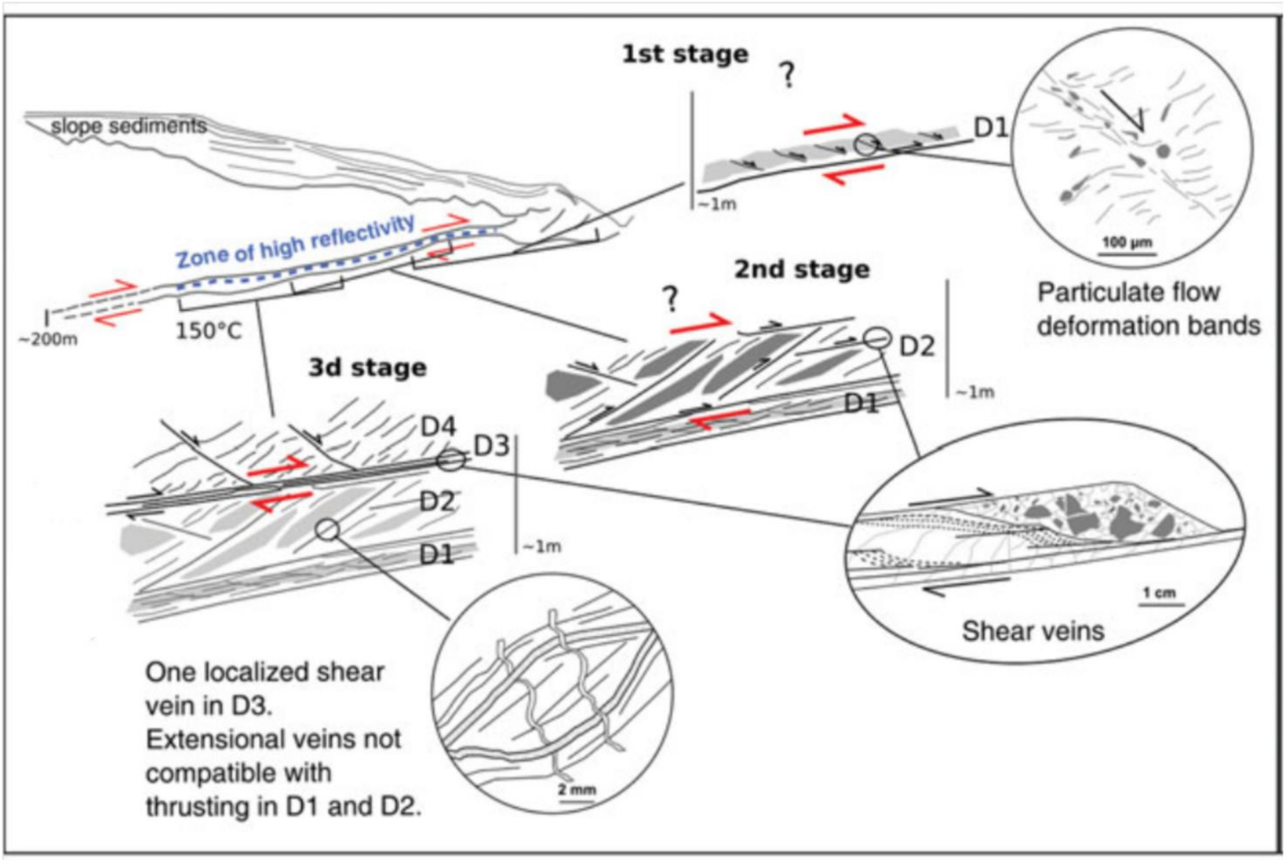

Figure 2.9. *Sketch showing the spatial and temporal evolution of the studied fault zone as a comparison for a megathrust, drawn based on Ranero et al. (2008). The zone of high fluid pressure is shown as estimated on the basis of high amplitude seismic reflectivity along megathrusts. The three phases of deformation of the studied fault zone at the base of the SVU (Section 2.b) are transitional and partly overlapped, and represent different faulting stages as occurred with increasing depth. From Mittempergher et al. (2018).*

The three interpreted deformation phases suggest a progressive concentration of the deformation up the 20–30 cm thickness of D3. Localization to a thin slipping zone is generally associated with seismic slip (e.g., Sibson, 2003), and the observed thinning of the active shear zone might be related with the progressive transition to the seismogenic zone of active megathrusts (e.g., Oleskevich et al., 1999). Alternatively, deformation might have concentrated in D3 planar and continuous shear zone to overcome and by-pass a geometric irregularity, such as a ramp, located NE from Vidiciatico and not cropping out. A similar reduction of fault plane irregularities and of perturbing effects generated by geometric heterogeneities is generally associated with increasing displacement accumulated by the fault (e.g., Sagy et al., 2007).

The progressive localization of the deformation to D3 is also associated with the long-term deactivation of the structural domains below it, where the shear component of strain is overprinted by thrust-parallel flattening with perpendicular extensional veining and pressure-solution, more evident in D1, but recognizable also in D2. Similar strain decoupling across actively shearing décollements has been measured in magnetic susceptibility studies in cores from the basal décollement of active megathrusts, as the one of the Barbados accretionary prism (Housen et al. 1996) and of the Japan Trench prism (Yang et al. 2013). Strain decoupling, likely responding to stress decoupling, suggests that the basal thrust of the SVU was weak.

This condition could have been favoured by fluid overpressures, as suggested by the calcite vein structures and geometry in the fault strand: extensional veins in D2 have fibrous structure typical of mode I extensional veins (e.g. Bons et al., 2012), and a dilatant character whatever their orientation. Such characteristics suggest extension nearly independent on the orientation, thus reflecting local, transient low differential stress and high fluid pressure, episodically higher than lithostatic. These conditions are also consistent with the hybrid opening of the shear veins and the lack of wear products like cataclasite or gouge in the fault strand zone (e. g. Cox, 2010).

The relations between the different types of calcite veins in the whole fault strand are complex. As previously noted, fault-parallel and fault-perpendicular extensional veins appear as contemporaneous, mutually cutting each other (Fig. 2.7.c, d). Both sets of extensional veins are crosscut by shear veins (Fig. 2.6.b). However, some evidences of fault-perpendicular veins crosscutting the shear veins suggest that extensional and shear veins should have formed cyclically during the thrust activity.

Nevertheless, the fault-perpendicular extensional veins could only form in a state of stress (with a high-angle σ_1) that is not kynematically compatible with that required to form the fault-parallel extensional veins (with a low-angle σ_1) consistent with movement along the thrust. This implies field stress changes during the fault strand evolution and determines the creation of characteristic struc-

turally controlled fluid pathways and permeability modifications, which can or cannot be associated to changes in the fluid intake.
To obtain information about the characteristic of fluids that circulated in the fault strand and precipitated in fractures during the second and third stages of deformation, geochemical analyses were performed on samples of the different calcite veins (Section 2.c).

Section 2.c. Geochemical analyses on tectonic calcite veins

2.c.1. Geochemical data

Based on the detailed structural analysis described in the previous sections, the following representative samples of the different vein types and crosscutting veining phases have been selected. For simplicity, hybrid shear veins with crack-and-seal growth and with breccia infill are referred to hereafter as “crack-and-seal shear veins” and “breccia shear veins”, respectively. The analysis included:

- three shear vein samples: (i) from the D3 main thrust, cutting through the whole fault strand (Sample AC26-shear, Fig. 2.10), (ii) from a parallel smaller thrust in D2 (Sample AC15-shear, Fig. 2.11, with crack-and-seal shear veins and breccia shear veins) and (iii) from a low-angle shear fracture in D2 (Sample MC3, breccia shear vein, Fig. 2.13);
- three extensional vein samples, all from D2: (i) 2 mm-thick extensional fault-parallel veins (Sample AC3a2-ext, Fig. 2.12), (ii) a < 1mm-thick fault-parallel extensional vein, cut by later MC3-breccia (Sample MC3-ext, Fig. 2.13), and (iii) fault-parallel and fault-perpendicular extensional veins crosscutting each other, appearing all affected by pressure solution deformation (Sample AC19-ext, Fig. 2.14).
- five samples of the wall rock surrounding each selected vein (Samples AC3a.2-WR, AC15-WR, AC19-WR, AC26-WR and MC3-WR), suitable to compare trace element values between veins and related wall rocks.

Vein samples have been semi-quantitatively analysed for major elements. X-EDS microanalyses indicate that infilling is pure calcite for all the veins, with only very low percentage of $MgCO_3$ and $FeCO_3$ (<1%) (Fig. 2.15). In situ trace element analyses were conducted on vein thin sections or rock slices by laser ablation-inductively coupled plasma-mass spectrometry (LA-ICP–MS), with a series of spot analyses per sample. In shear veins, points were taken parallel to the slip direction and particular attention was paid in selecting points as far as possible from visible wall rock inclusions.

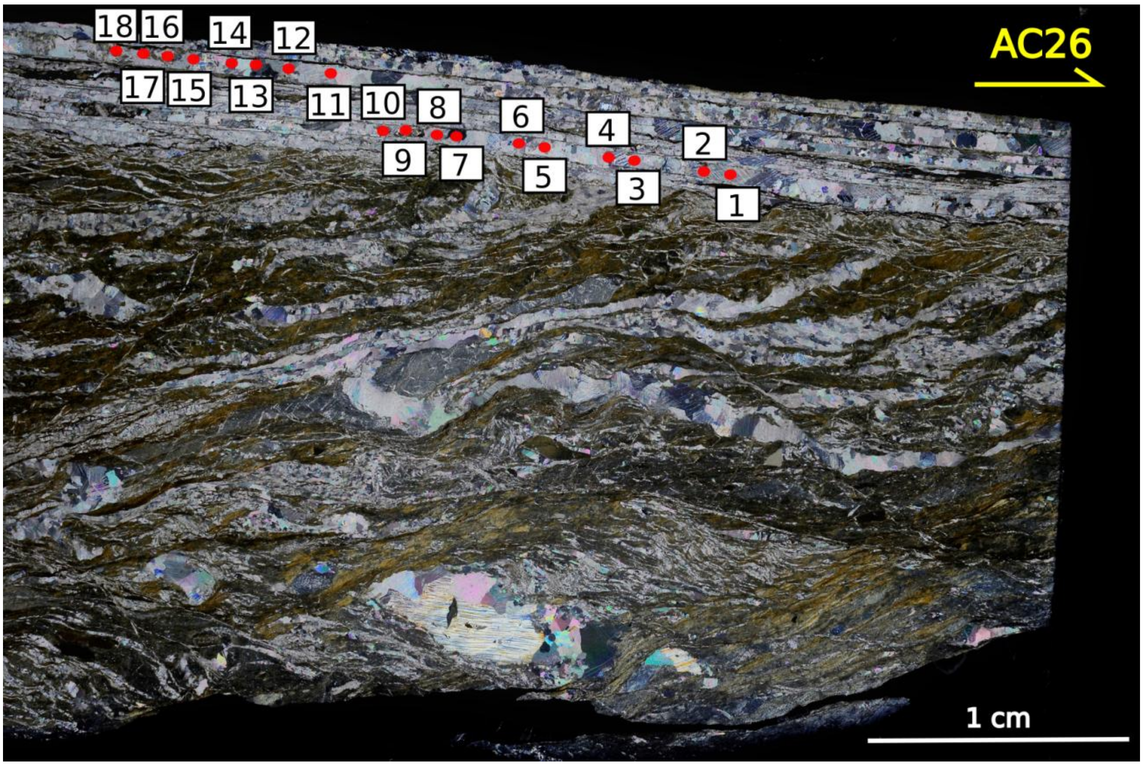

Figure 2.10. *AC26 sample cross polarized thin section scan. Crack-and-seal shear vein analyzed for REE content determination. Red points correspond to LA-ICP-MS spots. Labels correspond to spot numbers in Table 2.1 reporting analytical results. From Cerchiari et al., submitted.*

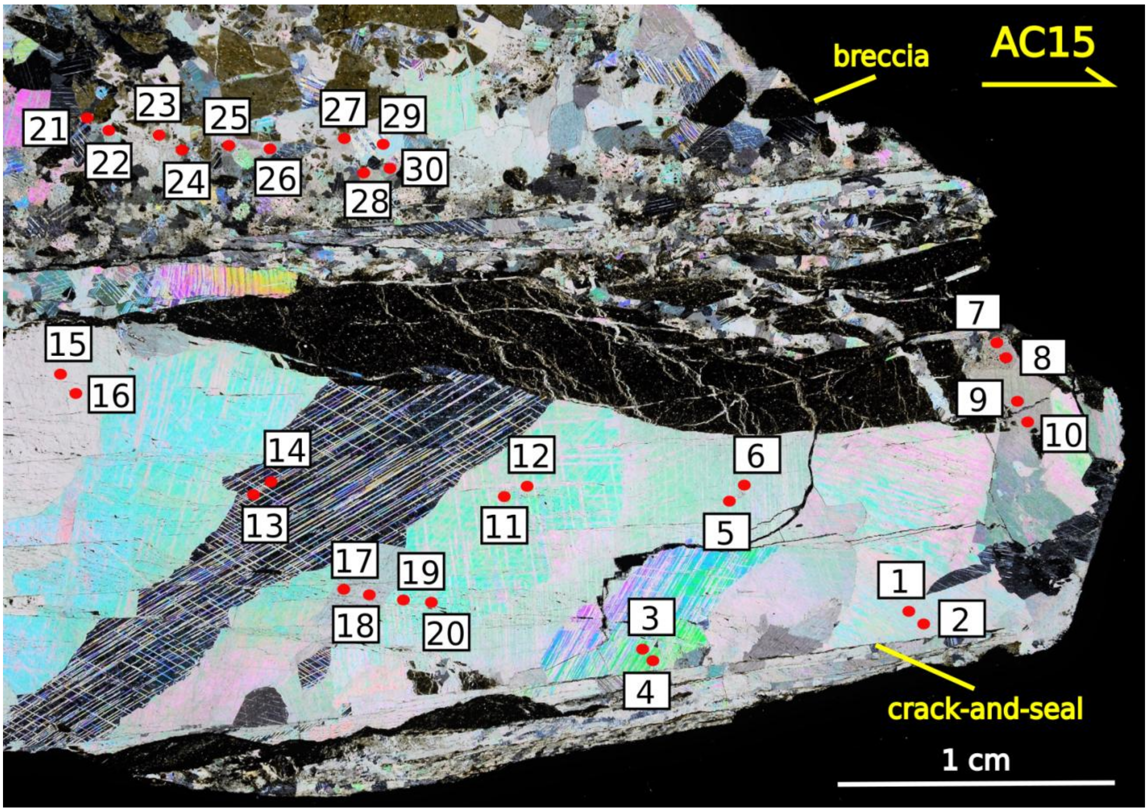

Figure 2.11. *AC15 sample cross polarized thin sections scan. Crack-and-seal shear and breccia shear veins analyzed for REE content determination. Red points correspond to LA-ICP-MS spots. Labels correspond to spot numbers in Table 2.1 reporting analytical results. From Cerchiari et al., submitted.*

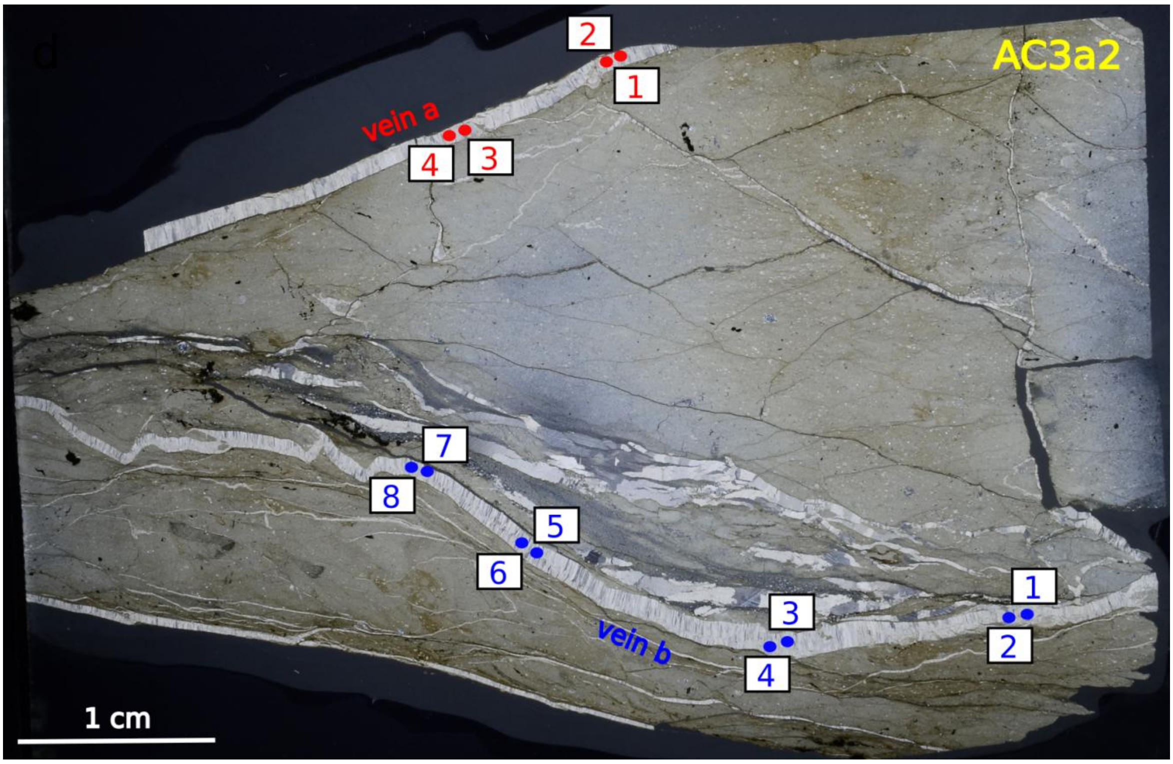

Figure 2.12. *AC3a2 sample cross polarized thin section scan. Fault-parallel extensional vein analyzed for REE content determination. Red and blue points correspond to LA-ICP-MS spots. Labels correspond to spot numbers in Table 2.1 reporting analytical results. from Cerchiari et al., submitted.*

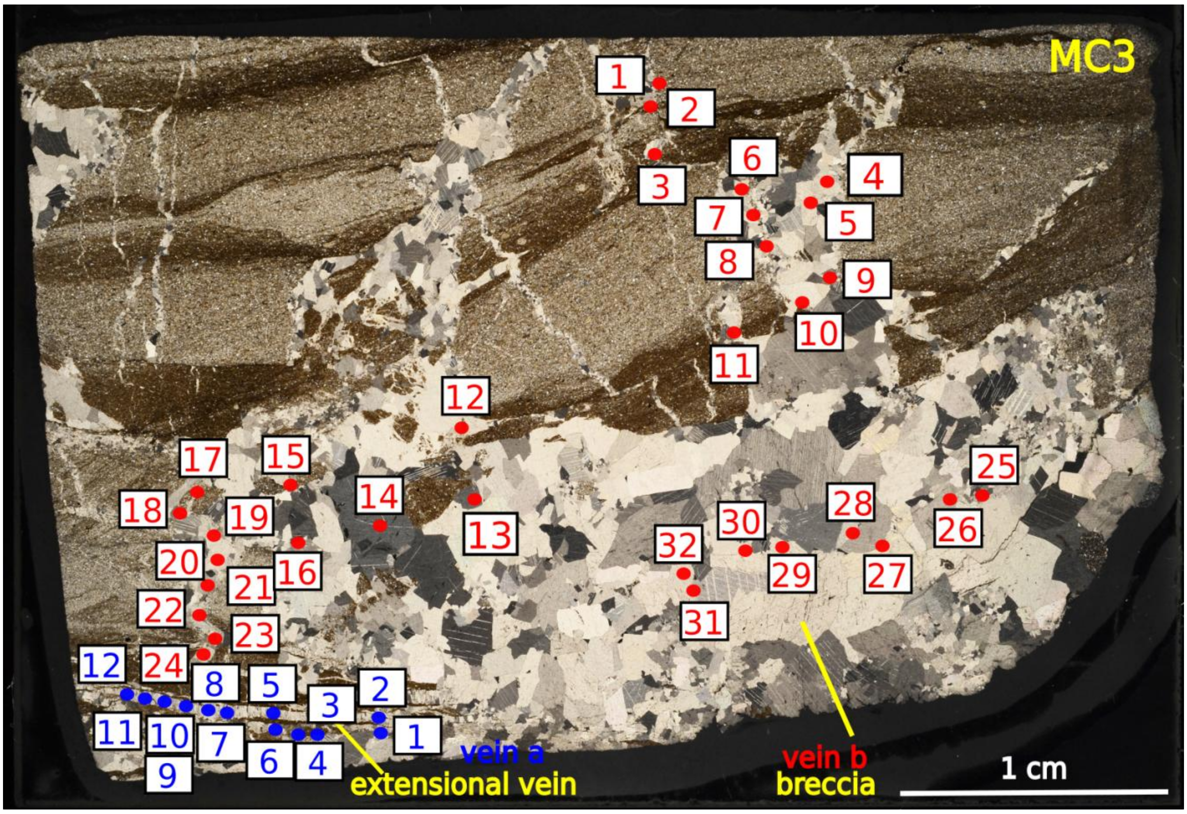

Figure 2.13. *MC3 sample cross polarized thin section scan. Fault-parallel extensional vein and shear breccia vein analyzed for REE content determination. Red and blue points correspond to LA-ICP-MS spots. Labels correspond to spot numbers in Table 2.1 reporting analytical results. From Cerchiari et al., submitted.*

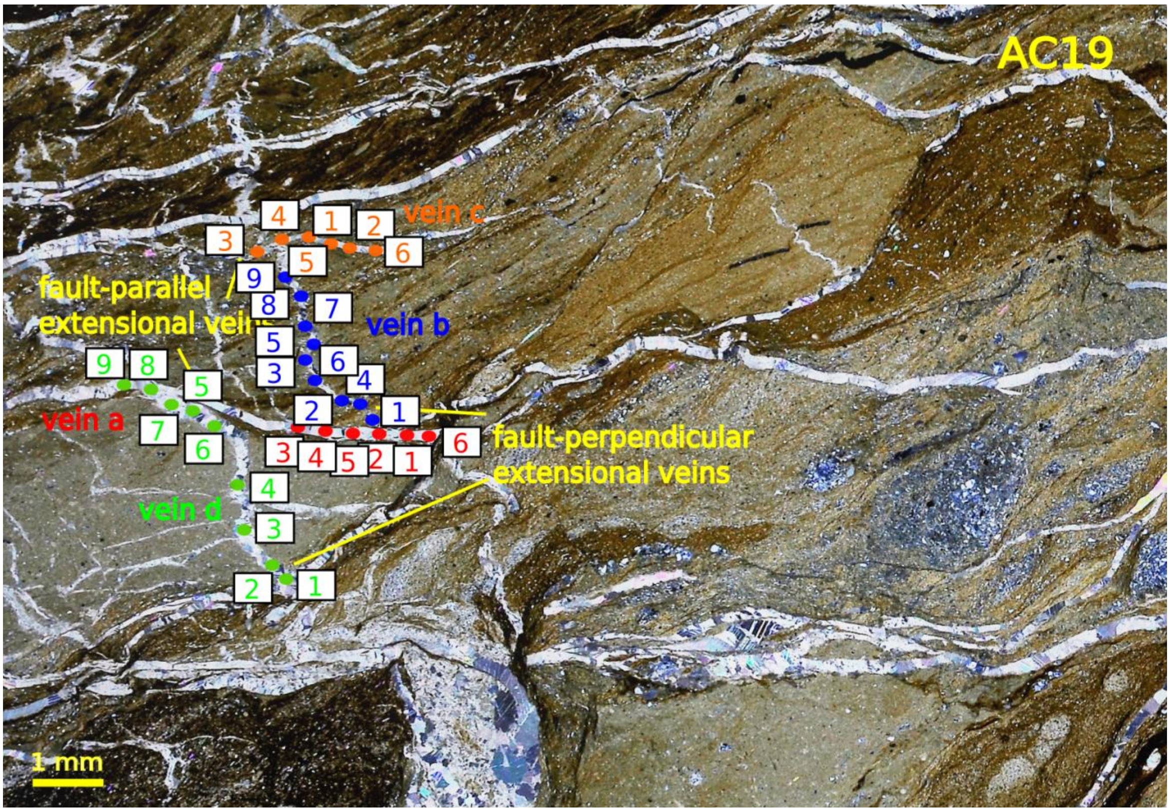

Figure 2.14. *AC19 sample cross polarized micrograph. Fault-parallel and fault-perpendicular extensional veins analyzed for REE content determination. Red, blue, orange and green points correspond to LA-ICP-MS spots. Labels correspond to spot numbers in Table 2.1 reporting analytical results. From Cerchiari et al., submitted.*

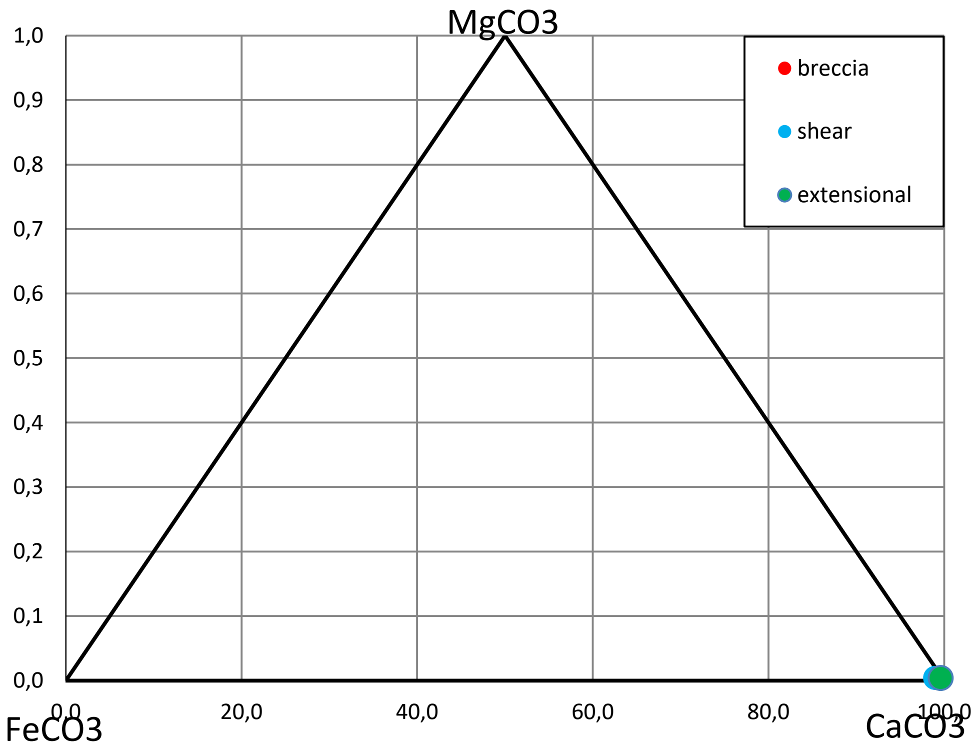

Figure 2.15. *Ternary plot of the vein carbonate composition, showing that the infilling is pure calcite for each vein type.*

A large range of trace elements was analysed and some of them were used to discern calcite contamination by wall-rock micro-inclusions. This was necessary due to the sampling limitations of the laser device, that make it hard to distinguish and avoid, during ablation, trails of inclusions in the shear veins and wall rock clasts in the breccias (Figs. 2.6.b and 2.7.g), or partial breaching of the wall rock for very thin extensional veins (e. g. “vein a” in Fig. 2.13). We measured anomalously high counts of Mg, Fe, Si or K (between 1000 and 70000 ppm) in calcites for AC26 shear vein and MC3 extensional vein and, since they are probable inclusions, we excluded them from the dataset.
The specific target of analysis was to determine REE distribution in the different vein types. In Table 2.1, REE abundances for crack-and-seal shear veins, breccia shear veins, fault-perpendicular extensional veins and fault-parallel extensional veins are reported. These data were plotted and obtained patterns were normalized to chondrite (using values reported by Taylor and McLennan, 1985), to eliminate spikes due to the Oddo-Harkins effect, i. e. the higher abundances of elements with even atomic number relative to those with odd atomic number due to the nucleosynthesis processes. The chondrite-normalized REE patterns are reported in Figure 2.16, according to the different vein types. Figure 2.17 shows the REE distribution pattern of each vein sample wall rock and of two reference standard shale compositions, the North American Shale Composite (NASC, Gromet et al., 1984) and the Post Archean Australian Shale (PAAS, Taylor and McLennan, 1985).
Considering all the veins, the range of REE abundances is very broad, overall spanning 1 or 2 orders of magnitude and up to 1 order of magnitude over a few hundred microns in a single vein. The greatest variations are recorded in shear veins, while the smallest ones are seen for fault-perpendicular extensional veins.
The crack-and-seal shear veins are characterized by a variable positive Eu anomaly and show patterns relatively flat, with variable depletion of HREEs and flat to strongly enriched LREEs. AC15 patterns have smaller Eu anomalies than those of AC26 (Figs. 2.16.a and 2.19). The Eu anomalies are plotted as histograms in Figure 2.19, for crack-and-seal shear veins, breccia shear veins and extensional veins. Following Gao & Wedepoh (1995), the Eu anomalies have been calculated as $Eu/Eu^* = Eu_N\sqrt{}Sm_N \text{ x } Gd_N$, where the subscript “N” indicates chondrite-normalized values. The red line marks the value of 0.9: for higher values the Eu anomaly is positive, for lower value is negative.
The REE patterns of the fault-parallel extensional veins (AC3.a2, MC3 and AC19) (Fig. 2.16.c) can be divided in three groups (Fig. 2.17). Group 1 patterns are strongly enriched in LREEs with respect to HREEs and present a strong negative Eu anomaly; Group 2 patterns have a variable enrichment in LREEs, flat Mid to Heavy REE trends and slightly negative Eu anomalies; Group 3 patterns have flat to slightly depleted LREE trends, with depleted HREEs, but less fractionated than Group 1.

Table 2.1. *Rare Earth Element LA-ICP-MS analyses on calcite veins and wall rocks (data in ppm). From Cerchiari et al., submitted.*

Sample	Vein Type	Spot #	La	Ce	Pr	Nd	Sm	Eu	Gd	Tb	Dy	Ho	Er	Tm	Yb	Lu
AC3a2	fault-parallel extensional	vein_a #1	41,9	93,5	9,16	39,48	7,18	1,24	5,50	-	4,25	0,65	1,53	0,18	1,06	0,13
AC3a2	fault-parallel extensional	vein_a #2	133	249	21,05	85,03	11,39	1,72	7,40	-	4,63	0,74	1,84	0,21	1,38	0,18
AC3a2	fault-parallel extensional	vein_a #3	77,2	191	18,24	82,12	16,75	3,01	13,50	-	9,33	1,37	2,86	0,30	1,80	0,20
AC3a2	fault-parallel extensional	vein_a #4	47,3	97,9	9,80	43,12	7,92	1,47	6,34	-	4,56	0,70	1,60	0,17	1,03	0,12
AC3a2	fault-parallel extensional	vein_b #1	73,7	136	12,34	52,81	9,45	1,58	7,06	-	5,55	0,91	2,02	0,22	1,32	0,17
AC3a2	fault-parallel extensional	vein_b #2	144	229	19,02	76,61	11,57	1,91	8,83	-	7,85	1,45	3,88	0,46	2,88	0,36
AC3a2	fault-parallel extensional	vein_b #3	155	234	18,95	71,93	9,98	1,48	6,58	-	4,79	0,83	1,97	0,22	1,29	0,17
AC3a2	fault-parallel extensional	vein_b #4	30,2	50,2	5,11	21,09	3,78	0,66	3,03	-	2,39	0,39	0,93	0,10	0,54	0,07
AC3a2	fault-parallel extensional	vein_b #5	107	188	16,38	70,74	11,84	1,95	8,60	-	5,66	0,87	1,95	0,18	1,03	0,12
AC3a2	fault-parallel extensional	vein_b #6	82	140	12,53	52,96	9,30	1,53	7,53	-	7,29	1,40	3,79	0,44	2,79	0,35
AC3a2	fault-parallel extensional	vein_b #7	102	189	16,55	67,81	12,40	1,98	9,49	-	8,31	1,38	3,42	0,38	2,48	0,29
AC3a2	fault-parallel extensional	vein_b #8	120	231	19,47	78,73	13,87	2,33	10,72	-	9,71	1,75	4,38	0,54	3,44	0,41
AC15	shear (crack-and-seal)	vein_a #1	4,17	11,24	1,70	8,66	2,61	1,13	2,47	-	2,80	0,51	1,52	0,16	0,93	0,12
AC15	shear (crack-and-seal)	vein_a #2	4,78	13,10	1,91	11,21	3,70	1,72	3,68	-	4,06	0,77	2,21	0,25	1,60	0,17
AC15	shear (crack-and-seal)	vein_a #3	0,92	1,99	0,26	1,40	0,41	0,13	0,40	-	0,36	0,08	0,22	0,04	0,18	0,02
AC15	shear (crack-and-seal)	vein_a #4	0,62	1,37	0,19	0,78	0,14	0,08	0,18	-	0,29	0,06	0,20	0,02	0,19	0,03
AC15	shear (crack-and-seal)	vein_a #5	0,51	1,19	0,16	0,92	0,23	0,14	0,28	-	0,26	0,07	0,17	0,02	0,14	0,02
AC15	shear (crack-and-seal)	vein_a #6	6,38	11,76	1,29	6,38	1,20	0,45	1,05	-	1,29	0,25	0,76	0,10	0,69	0,09
AC15	shear (crack-and-seal)	vein_a #7	5,46	13,30	1,90	10,54	2,70	1,65	3,25	-	3,27	0,65	1,76	0,19	1,07	0,12
AC15	shear (crack-and-seal)	vein_a #8	5,45	14,25	1,93	11,39	3,63	1,79	3,83	-	3,92	0,73	1,98	0,23	1,29	0,15
AC15	shear (crack-and-seal)	vein_a #9	6,77	18,75	2,61	14,79	4,44	1,67	3,96	-	3,70	0,66	1,87	0,23	1,36	0,16
AC15	shear (crack-and-seal)	vein_a #10	53,52	90,24	8,86	39,46	5,96	1,89	4,11	-	2,97	0,59	1,74	0,26	1,61	0,17
AC15	shear (crack-and-seal)	vein_a #11	0,58	1,46	0,23	1,02	0,23	0,12	0,33	-	0,35	0,07	0,25	0,03	0,23	0,03
AC15	shear (crack-and-seal)	vein_a #12	0,52	1,33	0,14	0,85	0,20	0,16	0,21	-	0,26	0,06	0,19	0,02	0,18	0,02
AC15	shear (crack-and-seal)	vein_a #13	6,36	15,08	1,86	9,30	2,25	0,77	2,18	-	2,44	0,46	1,36	0,16	1,11	0,12
AC15	shear (crack-and-seal)	vein_a #14	5,79	14,54	1,92	9,38	2,38	0,85	2,41	-	2,69	0,52	1,45	0,17	1,23	0,13
AC15	shear (crack-and-seal)	vein_a #15	5,46	14,18	1,84	8,97	2,43	0,99	2,56	-	2,73	0,52	1,51	0,18	1,23	0,14
AC15	shear (crack-and-seal)	vein_a #16	5,05	13,99	1,93	9,81	2,42	0,98	2,75	-	2,81	0,54	1,53	0,21	1,38	0,14
AC15	shear (crack-and-seal)	vein_a #17	6,27	14,83	2,05	10,88	3,01	1,19	3,46	-	3,77	0,78	2,23	0,25	1,52	0,20
AC15	shear (crack-and-seal)	vein_a #18	5,85	15,38	2,05	10,13	2,79	1,19	3,16	-	3,63	0,75	2,00	0,27	1,53	0,18
AC15	shear (crack-and-seal)	vein_a #19	4,82	12,08	1,64	8,67	2,35	1,02	3,11	-	3,24	0,70	1,83	0,21	1,45	0,16
AC15	shear (crack-and-seal)	vein_a #20	21,08	38,06	4,42	19,71	4,33	1,68	4,43	-	4,77	0,95	2,50	0,30	1,73	0,25
AC15	shear (breccia)	vein_a #21	2,88	6,51	0,97	5,61	1,41	0,68	1,58	-	1,40	0,26	0,64	0,08	0,41	0,05
AC15	shear (breccia)	vein_a #22	3,34	7,71	1,14	6,08	1,75	0,74	1,67	-	1,40	0,26	0,68	0,08	0,40	0,05
AC15	shear (breccia)	vein_a #23	6,12	16,72	2,28	11,78	3,25	1,19	3,10	-	2,99	0,55	1,55	0,18	1,14	0,13
AC15	shear (breccia)	vein_a #24	5,75	14,50	2,02	11,08	3,13	1,16	2,82	-	2,66	0,52	1,37	0,14	1,01	0,12
AC15	shear (breccia)	vein_a #25	3,82	8,53	1,29	6,90	1,85	1,02	1,93	-	1,88	0,32	0,85	0,10	0,52	0,05
AC15	shear (breccia)	vein_a #26	4,03	9,73	1,40	7,84	1,99	0,93	2,12	-	2,07	0,38	1,05	0,11	0,68	0,08
AC15	shear (breccia)	vein_a #27	2,26	3,93	0,59	3,34	0,89	0,73	1,09	-	0,92	0,18	0,47	0,04	0,25	0,02
AC15	shear (breccia)	vein_a #28	2,17	4,05	0,59	3,21	0,89	0,64	1,03	-	0,86	0,16	0,41	0,04	0,20	0,02
AC15	shear (breccia)	vein_a #29	3,42	7,47	1,06	5,85	1,65	0,79	1,63	-	1,54	0,29	0,84	0,09	0,53	0,05
AC15	shear (breccia)	vein_a #30	2,86	6,09	0,86	5,18	1,45	0,74	1,51	-	1,42	0,27	0,71	0,07	0,39	0,04

AC19	fault-perpendicular extensi	vein_b #1	8,79	26,12	4,56	28,84	10,86	3,20	10,57	1,69	9,89	1,82	4,40	0,51	3,09	0,33
AC19	fault-perpendicular extensi	vein_b #2	8,89	31,21	5,57	36,40	12,98	4,09	12,67	2,06	12,50	2,26	5,79	0,63	3,60	0,40
AC19	fault-perpendicular extensi	vein_b #3	13,81	42,75	7,21	43,75	14,50	4,07	14,43	2,21	13,23	2,51	6,25	0,69	4,07	0,44
AC19	fault-perpendicular extensi	vein_b #4	10,64	23,59	3,72	24,26	7,53	3,18	8,01	1,20	6,59	1,20	2,89	0,28	1,54	0,15
AC19	fault-perpendicular extensi	vein_b #5	8,29	22,10	3,68	23,99	8,52	2,97	8,62	1,29	8,04	1,38	3,33	0,32	2,00	0,22
AC19	fault-perpendicular extensi	vein_b #6	6,49	16,14	2,67	14,83	4,97	1,51	4,51	0,75	3,81	0,78	1,80	0,22	1,06	0,15
AC19	fault-perpendicular extensi	vein_b #7	9,61	28,25	4,89	31,53	11,62	3,29	11,66	1,94	11,31	1,95	5,05	0,58	3,28	0,38
AC19	fault-perpendicular extensi	vein_b #8	17,32	45,55	7,10	41,49	11,95	3,21	11,35	1,75	10,72	2,14	5,15	0,69	4,70	0,58
AC19	fault-perpendicular extensi	vein_b #9	13,14	35,60	6,08	38,51	13,40	3,95	14,00	2,17	12,91	2,37	5,89	0,66	3,77	0,43
AC19	fault-perpendicular extensi	vein_d #1	16,89	39,05	5,28	29,20	9,03	2,79	7,24	1,13	6,53	1,22	3,00	0,37	2,17	0,27
AC19	fault-perpendicular extensi	vein_d #2	21,67	50,59	7,72	46,89	13,42	3,85	11,54	1,77	10,57	1,93	4,87	0,52	3,39	0,37
AC19	fault-perpendicular extensi	vein_d #3	48,22	90,45	9,91	49,08	12,11	3,04	8,80	1,46	8,36	1,66	4,04	0,50	3,75	0,45
AC19	fault-perpendicular extensi	vein_d #4	11,06	35,99	6,04	38,64	13,72	4,19	14,09	2,29	13,85	2,56	6,28	0,79	4,36	0,53
AC19	fault-perpendicular extensi	vein_d #5	13,01	34,56	5,56	35,02	11,31	3,16	10,29	1,67	9,40	1,64	4,19	0,49	2,82	0,36
AC19	fault-perpendicular extensi	vein_d #6	13,60	37,83	5,78	37,43	10,88	3,07	10,37	1,54	8,90	1,60	4,15	0,51	2,87	0,36
AC19	fault-perpendicular extensi	vein_d #7	31,80	79,67	10,01	47,99	11,15	2,57	9,44	1,68	10,12	1,91	5,29	0,70	4,64	0,54
AC19	fault-perpendicular extensi	vein_d #8	31,51	91,12	14,19	75,31	20,85	5,20	17,20	2,94	17,39	3,14	8,25	1,00	6,18	0,84
AC19	fault-perpendicular extensi	vein_d #9	10,19	29,82	4,88	28,53	10,46	2,89	9,57	1,49	8,93	1,59	4,11	0,45	3,22	0,35
AC19	fault-parallel extensional	vein_a #1	11,51	30,42	4,96	29,91	8,79	2,67	8,16	1,31	7,75	1,46	3,81	0,44	2,81	0,33
AC19	fault-parallel extensional	vein_a #2	36,83	73,78	9,48	52,23	14,78	4,05	12,76	2,02	12,38	2,36	6,29	0,80	5,38	0,68
AC19	fault-parallel extensional	vein_a #3	23,28	58,18	8,05	46,14	13,14	3,46	11,41	1,85	10,87	2,13	5,49	0,65	4,92	0,56
AC19	fault-parallel extensional	vein_b #7	29,42	83,01	11,59	57,31	11,23	2,44	8,59	1,37	8,34	1,62	4,51	0,64	4,75	0,63
AC19	fault-parallel extensional	vein_b #8	8,79	26,76	4,22	23,59	6,77	1,72	6,15	0,97	6,12	1,18	3,12	0,36	2,29	0,30
AC19	fault-parallel extensional	vein_a #4	16,85	43,01	6,69	39,95	12,34	3,47	11,71	1,82	11,17	2,03	5,28	0,61	3,71	0,41
AC19	fault-parallel extensional	vein_a #5	13,11	39,01	6,46	38,39	13,06	3,68	12,98	2,05	12,59	2,27	5,80	0,66	4,07	0,48
AC19	fault-parallel extensional	vein_a #6	9,78	26,29	4,06	23,68	7,88	2,30	7,27	1,18	6,97	1,34	3,17	0,37	2,11	0,25
AC19	fault-parallel extensional	vein_c #1	11,13	32,63	4,96	26,75	6,91	1,51	6,03	0,96	6,39	1,17	3,31	0,44	2,84	0,34
AC19	fault-parallel extensional	vein_c #2	34,78	99,28	14,53	76,47	16,16	3,17	12,81	2,17	13,31	2,58	7,63	1,06	7,25	0,94
AC19	fault-parallel extensional	vein_c #3	19,58	54,74	7,62	41,09	8,36	1,81	6,66	1,08	6,68	1,33	3,98	0,53	4,00	0,56
AC19	fault-parallel extensional	vein_c #4	5,32	14,78	2,15	11,10	2,61	0,59	2,07	0,35	2,41	0,43	1,32	0,19	1,26	0,17
AC26	crack-and-seal shear	vein_a #1	0,80	1,93	0,29	2,17	0,98	1,29	0,93	-	0,61	0,11	0,24	0,03	0,08	0,01
AC26	crack-and-seal shear	vein_a #2	0,38	0,96	0,14	0,92	0,50	0,59	0,41	-	0,34	0,06	0,17	0,02	0,09	0,01
AC26	crack-and-seal shear	vein_a #3	1,72	4,03	0,64	3,97	1,63	2,72	1,49	-	1,23	0,17	0,43	0,04	0,23	0,02
AC26	crack-and-seal shear	vein_a #4	1,82	4,55	0,68	4,64	2,00	2,53	1,87	-	1,33	0,21	0,52	0,06	0,27	0,03
AC26	crack-and-seal shear	vein_a #5	0,10	0,23	0,04	0,19	0,06	0,14	0,10	-	0,11	0,02	0,05	0,01	0,05	0,01
AC26	crack-and-seal shear	vein_a #6	2,09	5,20	0,82	5,32	2,23	3,08	2,19	-	1,59	0,29	0,53	0,07	0,32	0,04
AC26	crack-and-seal shear	vein_a #7	2,29	5,08	0,77	4,87	2,15	3,32	2,34	-	1,61	0,25	0,55	0,06	0,28	0,03
AC26	crack-and-seal shear	vein_a #8	2,46	6,19	0,94	6,27	2,44	3,46	2,22	-	1,92	0,28	0,63	0,08	0,31	0,04
AC26	crack-and-seal shear	vein_a #9	16,73	35,60	4,16	21,01	7,36	3,09	5,42	-	5,15	1,01	2,89	0,40	3,13	0,39
AC26	crack-and-seal shear	vein_a #10	14,98	28,22	3,28	17,79	5,44	2,48	4,28	-	3,83	0,75	1,97	0,24	1,93	0,27
AC26	crack-and-seal shear	vein_a #11	2,48	3,66	0,54	3,01	1,39	1,39	1,21	-	0,89	0,15	0,37	0,03	0,25	0,03
AC26	crack-and-seal shear	vein_a #12	0,42	0,90	0,13	0,75	0,32	0,62	0,35	-	0,19	0,03	0,09	0,01	0,04	0,01
AC26	crack-and-seal shear	vein_a #13	0,94	1,60	0,21	1,58	0,59	0,93	0,47	-	0,41	0,07	0,17	0,01	0,06	0,01
AC26	crack-and-seal shear	vein_a #14	6,05	11,87	1,57	8,58	2,99	1,77	2,38	-	1,97	0,35	1,00	0,13	0,78	0,10
AC26	crack-and-seal shear	vein_a #15	0,80	1,76	0,29	1,75	0,53	1,02	0,74	-	0,42	0,07	0,18	0,01	0,09	0,01
AC26	crack-and-seal shear	vein_a #16	2,97	6,45	0,82	4,30	1,75	1,41	1,28	-	1,10	0,18	0,46	0,06	0,46	0,04
AC26	crack-and-seal shear	vein_a #17	2,00	6,15	0,56	3,61	1,52	1,08	1,19	-	1,19	0,22	0,52	0,07	0,35	0,04
AC26	crack-and-seal shear	vein_a #18	4,87	10,04	1,39	6,95	2,52	1,34	2,24	-	2,20	0,40	1,14	0,13	0,97	0,12

MC3	fault-parallel extensional	vein_a #1	59,95	104,10	10,54	40,27	5,99	1,57	5,35	-	5,65	1,20	3,94	0,53	4,14	0,51
MC3	fault-parallel extensional	vein_a #2	55,49	168,80	25,71	139,70	35,98	7,91	31,05	-	25,30	4,43	11,43	1,28	8,39	0,86
MC3	fault-parallel extensional	vein_a #3	11,78	30,65	4,37	24,38	7,84	2,35	7,41	-	7,58	1,27	3,55	0,47	2,78	0,34
MC3	fault-parallel extensional	vein_a #4	8,78	25,21	3,72	20,84	6,79	2,21	6,55	-	6,62	1,16	3,01	0,32	2,59	0,25
MC3	fault-parallel extensional	vein_a #5	15,54	36,25	5,09	24,95	5,48	1,77	5,51	-	5,66	1,07	3,07	0,39	2,27	0,30
MC3	fault-parallel extensional	vein_a #6	50,50	122,70	13,22	50,96	9,68	2,24	8,29	-	8,85	1,92	5,78	0,80	5,47	0,66
MC3	fault-parallel extensional	vein_a #7	60,81	154,70	17,11	70,04	11,99	3,28	10,70	-	11,48	2,60	8,16	1,11	7,44	0,87
MC3	fault-parallel extensional	vein_a #8	118,30	199,00	18,90	69,60	11,48	2,51	9,09	-	10,52	2,24	7,28	1,04	8,00	1,01
MC3	fault-parallel extensional	vein_a #9	125,50	205,20	19,01	71,69	11,86	2,63	10,62	-	12,18	2,56	8,13	1,22	8,96	1,14
MC3	fault-parallel extensional	vein_a #10	80,53	132,80	12,08	47,46	7,99	1,76	6,86	-	7,13	1,46	4,81	0,68	5,76	0,76
MC3	fault-parallel extensional	vein_a #11	56,42	128,80	14,08	57,50	9,83	2,48	8,55	-	9,25	1,88	5,90	0,81	5,19	0,62
MC3	fault-parallel extensional	vein_a #12	23,98	56,86	6,51	29,25	5,58	1,55	5,71	-	6,39	1,29	4,11	0,48	3,52	0,37
MC3	breccia	vein_b #1	35,04	73,91	9,57	43,84	10,28	2,55	8,66	-	9,28	1,98	5,43	0,72	4,60	0,61
MC3	breccia	vein_b #2	16,36	45,81	7,01	35,27	10,57	2,50	11,03	-	12,15	2,40	6,62	0,91	5,92	0,76
MC3	breccia	vein_b #3	17,73	53,36	8,21	42,93	13,17	3,23	13,85	-	15,70	3,20	8,46	1,18	7,71	0,92
MC3	breccia	vein_b #4	9,03	23,47	3,77	20,58	6,57	2,34	7,20	-	7,72	1,59	4,03	0,46	2,97	0,36
MC3	breccia	vein_b #5	10,27	29,51	4,75	25,45	8,09	2,54	9,07	-	9,81	2,05	5,44	0,70	4,22	0,55
MC3	breccia	vein_b #6	90,74	175,60	21,53	93,93	17,18	3,60	13,89	-	15,13	3,39	10,15	1,45	9,72	1,30
MC3	breccia	vein_b #7	20,19	44,34	6,04	28,82	7,35	2,15	6,67	-	6,89	1,45	4,06	0,50	3,05	0,37
MC3	breccia	vein_b #8	16,20	40,33	5,94	31,08	9,05	2,62	8,92	-	10,32	2,12	5,79	0,71	4,50	0,53
MC3	breccia	vein_b #9	10,35	28,92	4,53	24,65	7,63	2,37	8,48	-	9,37	1,95	5,44	0,73	4,03	0,52
MC3	breccia	vein_b #10	4,51	11,68	1,80	9,30	3,04	1,24	3,29	-	3,49	0,73	1,96	0,21	1,23	0,14
MC3	breccia	vein_b #11	7,60	18,71	2,85	16,08	4,72	1,85	5,53	-	5,78	1,24	2,97	0,38	2,28	0,28
MC3	breccia	vein_b #12	11,60	24,59	3,34	16,77	4,84	1,67	4,81	-	5,48	1,10	2,98	0,39	2,23	0,26
MC3	breccia	vein_b #13	9,78	22,48	3,20	15,93	4,37	1,41	4,57	-	5,29	1,10	2,83	0,37	2,43	0,29
MC3	breccia	vein_b #14	6,81	17,40	2,88	15,92	4,92	2,03	6,04	-	6,50	1,30	3,32	0,43	2,44	0,31
MC3	breccia	vein_b #15	8,62	19,41	2,80	14,39	3,96	1,39	4,18	-	4,46	0,93	2,53	0,33	1,89	0,23
MC3	breccia	vein_b #16	18,11	34,78	4,69	21,73	5,29	1,60	5,56	-	5,96	1,27	3,26	0,42	2,70	0,37
MC3	breccia	vein_b #17	10,53	22,83	3,06	16,20	4,54	1,67	4,87	-	5,10	1,00	2,64	0,32	1,98	0,23
MC3	breccia	vein_b #18	12,77	31,19	4,19	20,62	5,49	1,94	5,35	-	5,60	1,23	3,28	0,37	2,26	0,27
MC3	breccia	vein_b #19	11,59	27,91	3,78	18,80	5,02	1,91	5,09	-	5,23	1,11	2,97	0,37	2,11	0,25
MC3	breccia	vein_b #20	11,05	24,86	3,33	16,16	4,17	1,74	4,20	-	4,23	0,92	2,39	0,32	1,64	0,18
MC3	breccia	vein_b #21	9,98	21,25	2,88	14,72	4,01	1,80	4,34	-	4,12	0,95	2,34	0,28	1,61	0,20
MC3	breccia	vein_b #22	22,50	47,43	6,29	27,91	7,22	2,05	6,33	-	6,78	1,44	3,80	0,52	3,23	0,39
MC3	breccia	vein_b #23	11,23	23,36	3,05	15,56	4,22	1,64	4,67	-	4,75	0,94	2,60	0,32	1,83	0,24
MC3	breccia	vein_b #24	17,22	34,55	4,50	22,34	5,93	1,96	5,77	-	6,23	1,27	3,47	0,48	2,49	0,27
MC3	breccia	vein_b #25	2,10	4,38	0,63	3,53	1,03	0,79	1,43	-	1,36	0,26	0,65	0,08	0,43	0,05
MC3	breccia	vein_b #26	3,20	6,72	1,03	5,63	1,86	0,96	1,70	-	1,85	0,36	1,02	0,13	0,66	0,06
MC3	breccia	vein_b #27	0,61	1,02	0,13	0,83	0,29	0,21	0,30	-	0,29	0,05	0,12	0,01	0,05	0,01
MC3	breccia	vein_b #28	0,62	0,95	0,20	0,84	0,32	0,36	0,35	-	0,35	0,06	0,14	0,02	0,04	0,00
MC3	breccia	vein_b #29	1,75	3,34	0,48	2,71	0,88	0,59	0,89	-	0,87	0,20	0,54	0,06	0,34	0,03
MC3	breccia	vein_b #30	4,80	9,75	1,26	7,27	1,93	1,05	2,14	-	2,20	0,43	1,13	0,13	0,82	0,06
MC3	breccia	vein_b #31	4,37	8,99	1,16	6,41	1,71	0,89	1,73	-	1,80	0,37	1,02	0,12	0,61	0,07
MC3	breccia	vein_b #32	4,79	9,71	1,26	7,41	1,75	0,94	1,71	-	1,76	0,32	0,79	0,10	0,56	0,07
Sample	**Type**	**Sr**	**La**	**Ce**	**Pr**	**Nd**	**Sm**	**Eu**	**Gd**	**Tb**	**Dy**	**Ho**	**Er**	**Tm**	**Yb**	**Lu**
AC3a2	whole rock	347	26,1	50,5	5,56	20,0	4,10	0,930	4,21	nd	3,32	0,610	1,94	0,230	1,83	0,210
AC15	whole rock	247	13,6	27,6	3,23	13,9	3,32	0,850	3,45	nd	2,60	0,461	1,26	0,155	1,04	0,140
AC19	whole rock	nd	18,66	38,16	5,34	23,83	6,03	1,32	5,56	0,8	4,43	0,83	2,88	0,31	2,00	0,290
AC26	whole rock	129	25,8	48,6	4,93	17,7	3,15	0,800	3,31	nd	2,21	0,417	1,26	0,161	1,10	0,150
MC3	whole rock	840	18,4	38,8	4,76	18,3	3,91	1,02	4,10	nd	3,52	0,685	1,97	0,258	1,66	0,230

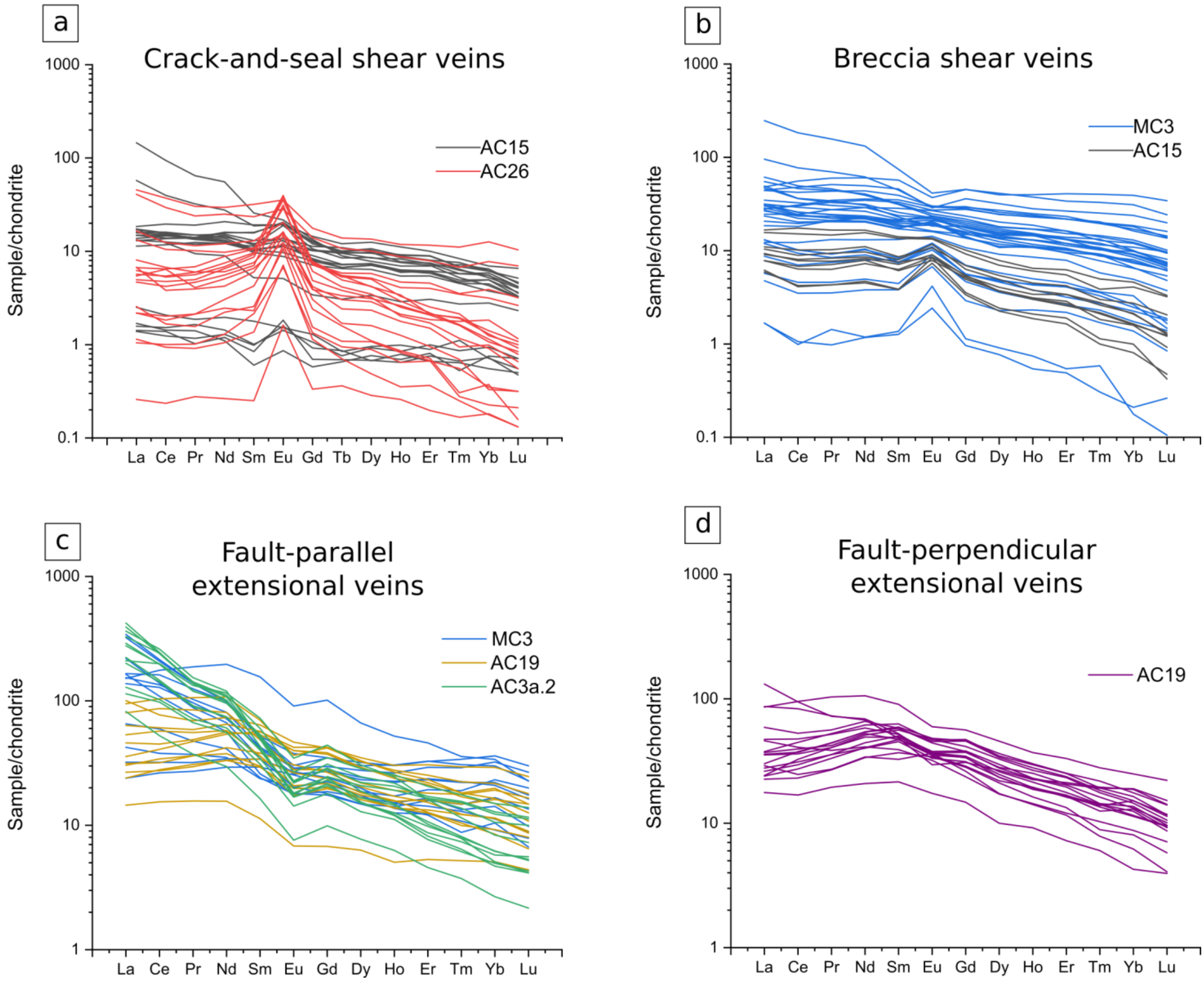

Figure 2.16. *REE distribution plots normalized to chondrite (Taylor & McLennan, 1985) for: a) crack-and-seal shear veins, separated by sample; b) breccia shear veins, separated by sample; c) extensional veins subparallel to the fault zone orientation, separated by sample; d) fault-perpendicular extensional veins in sample AC19. From Cerchiari et al., submitted.*

They have small to absent Eu anomalies. Group 1 patterns are present exclusively in sample AC3.a2. Group 2 and 3 patterns are present indistinctly in MC3 and AC19.

Fault-perpendicular extensional veins belong only to sample AC19 and their REE patterns are indistinguishable from those of Groups 2 and 3 fault-parallel extensional veins (Fig. 2.16.d).

Most of the breccia shear veins REE patterns resemble those of AC15 shear veins with crack and seal texture, but they have a variable Eu anomaly ranging from positive to slightly negative (Figs. 2.16.b and 2.19).

Wall rock REE patterns show trends consistent with those of typical sedimentary rocks, with a negative Eu anomaly (McLennan, 1989; Plank & Langmuir, 1998) (Fig. 2.17).

The normalization factor of REE patterns was then changed from chondrite to wall rock: this means that, for each type of vein, the correspondent wall rock contribution has been subtracted to the

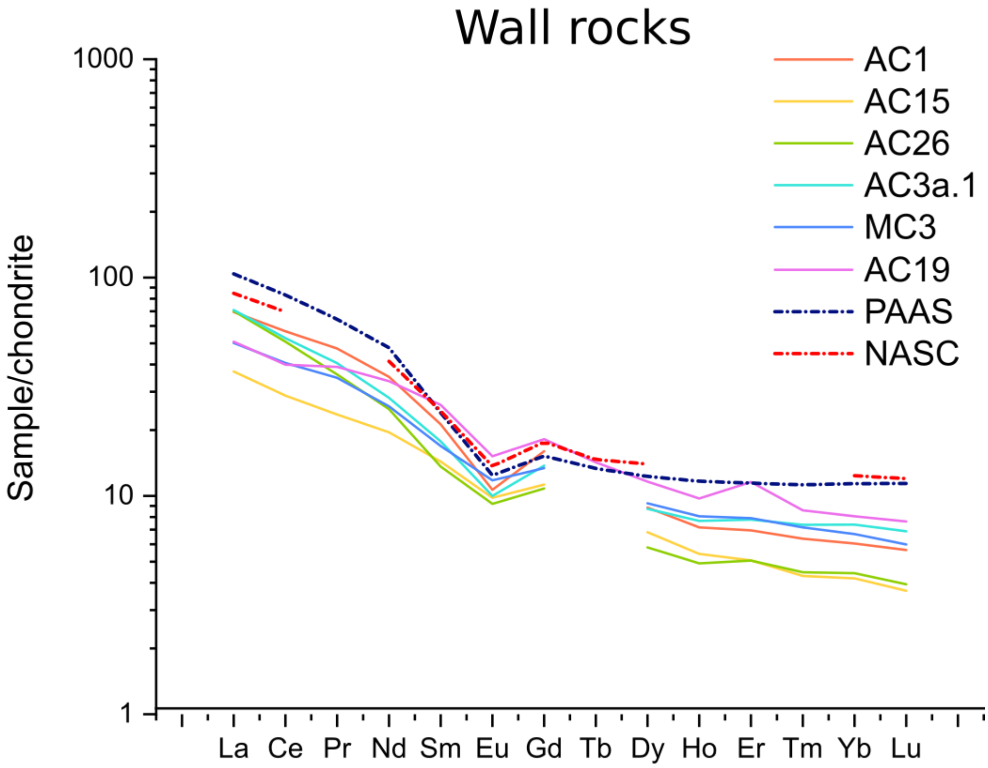

Figure 2.17. *REE distribution plots normalized to chondrite for vein sample wall rocks, North American Shale Composite (NASC, Gromet et al., 1984) and Post Archean Australian Shale (PAAS, Taylor & McLennan, 1985). From Cerchiari et al., submitted.*

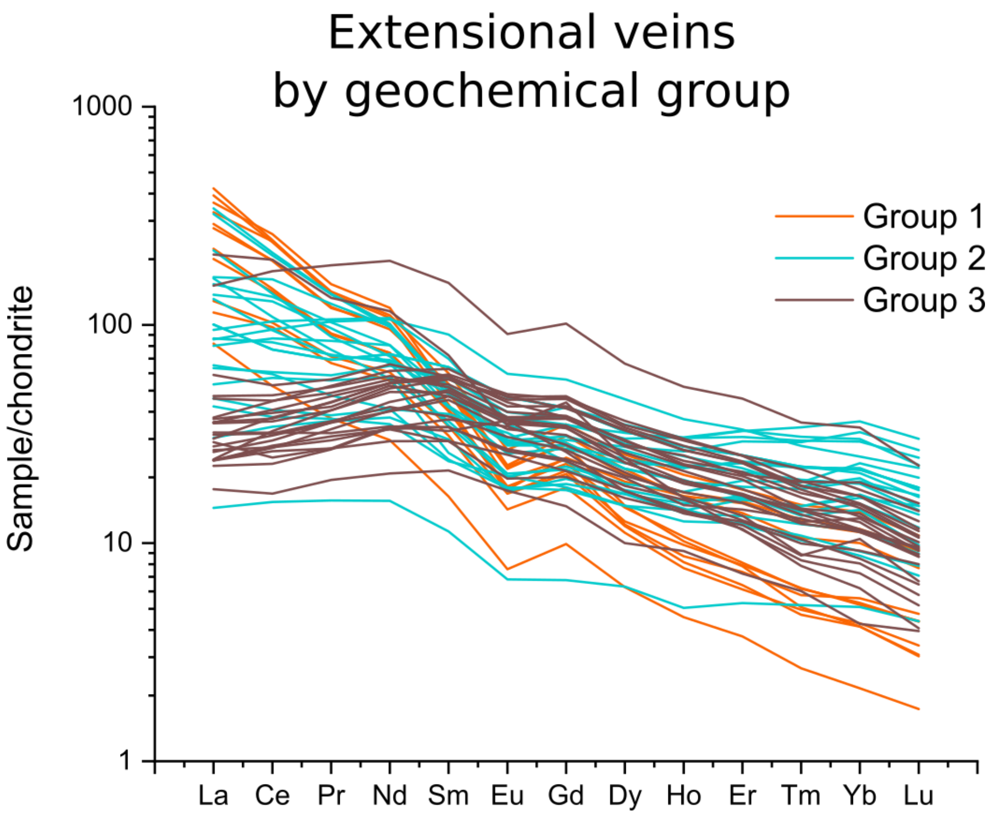

Figure 2.18. *REE distribution plots normalized to chondrite for extensional veins, separated by geochemical group. From Cerchiari et al., submitted.*

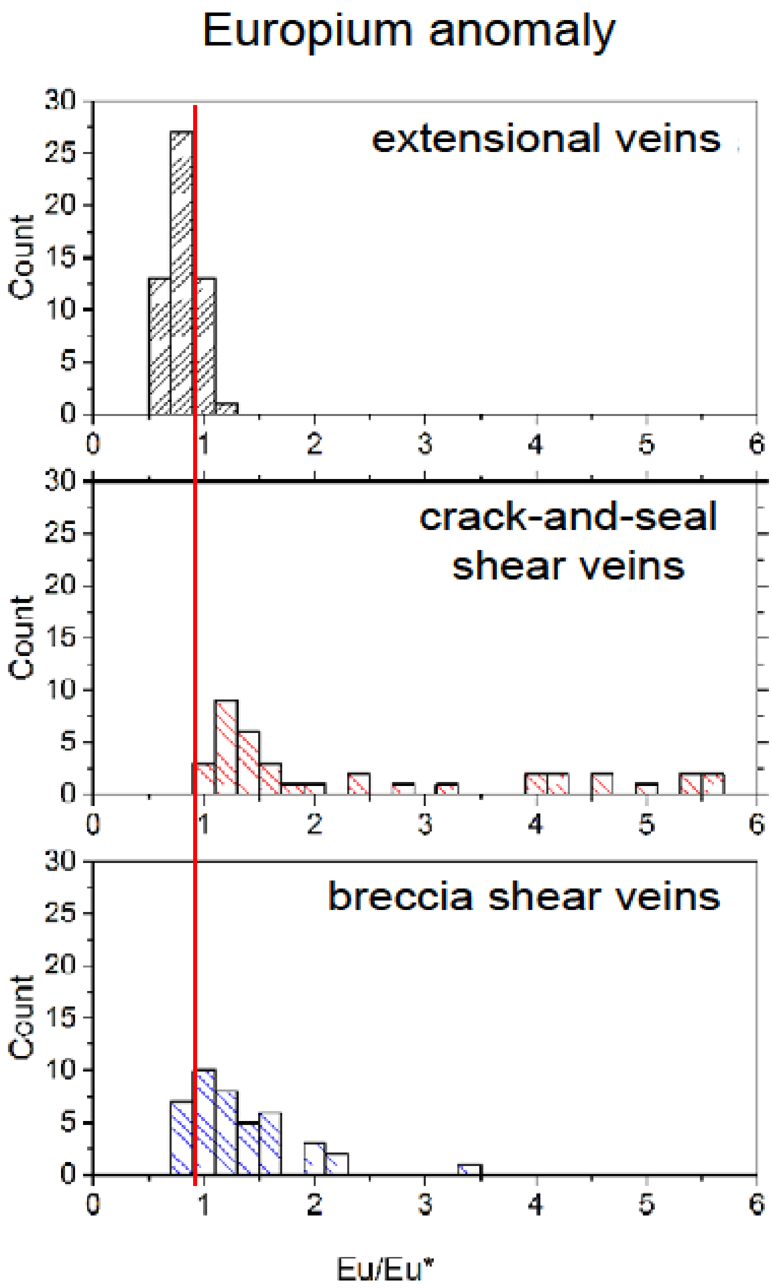

***Figure 2.19**. Histograms of Eu/Eu* Europium anomalies (Gao & Wedepohl, 1995) in crack-and-seal shear veins, breccia shear veins and extensional veins. The red line marks the value of 0.9: for higher values the Eu anomaly is positive, for lower value is negative. From Cerchiari et al., submitted.*

measured total amount of REE. Doing this, eventual anomalies originally present in the wall rock should disappear from the normalized patterns of the veins. The wall rock-normalized plots for each vein type are reported in Figure 2.20.

The overall REE abundances are scaled down (Fig. 2.20). The crack-and-seal shear veins maintain the positive Eu anomaly (Fig. 2.20.a). The breccia shear veins also keep their positive or negative

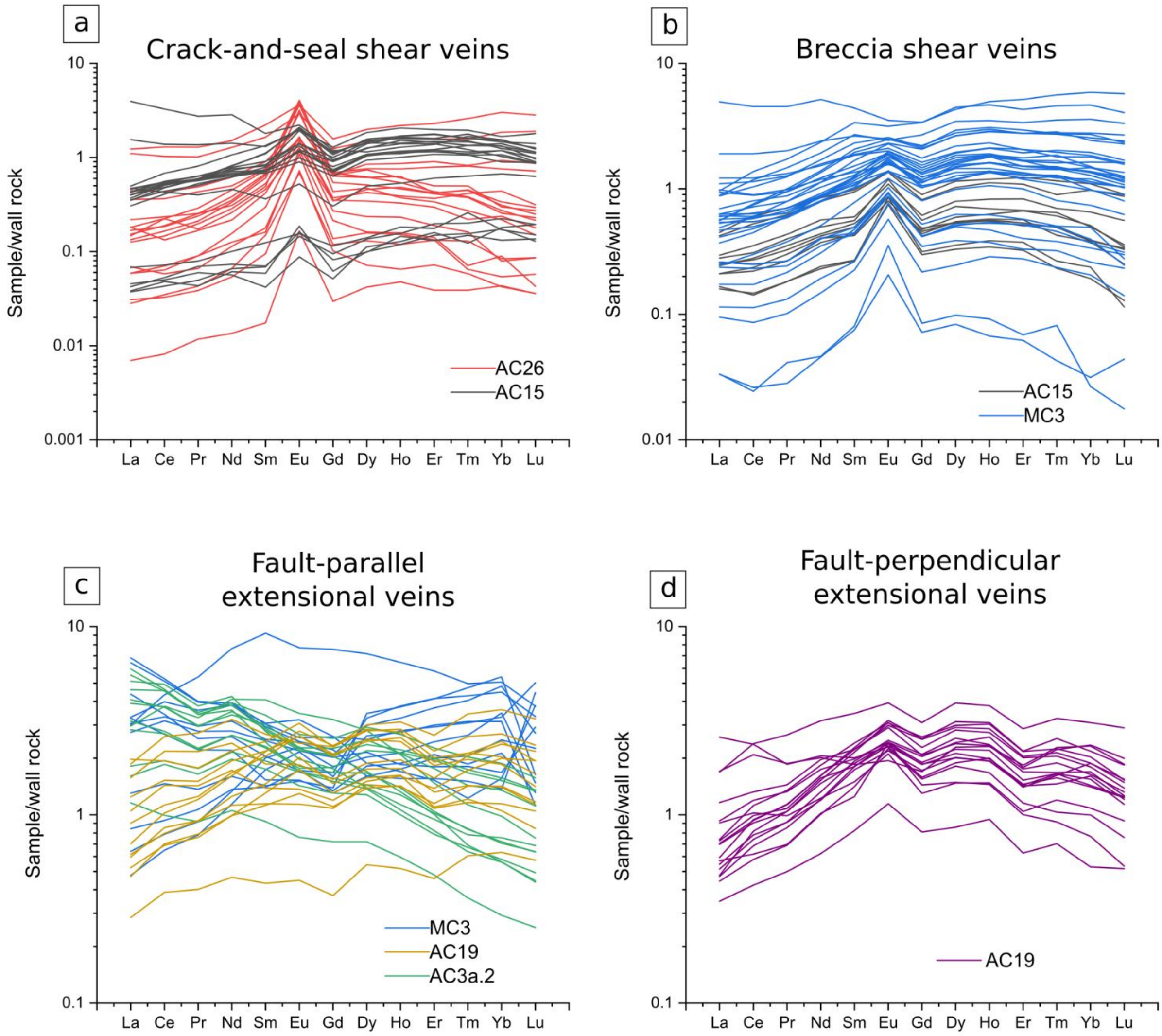

Figura 2.20. *REE distribution plots normalized to the relative wall rock, for a)crack-and-seal shear veins, separated by sample; b) breccia shear veins, separated by sample; c) fault-parallel extensional veins, separated by sample; d) fault-perpendicular extensional veins in sample AC19. From Cerchiari et al., submitted.*

Eu anomaly (Fig. 2.20.b). The extensional veins, instead, show more articulate trends of enrichment and depletion and some of their patterns acquire a small positive Eu anomaly (Fig. 2.20.c, d).

2.c.2. Interpretation of the geochemical data

The REE distribution data obtained from mass spectrometry were interpreted to identify the possible sources of vein-crystallizing fluids. In particular, Eu anomalies and REE enrichment/depletion trends were observed as informative of the nature and provenance of the fluids.

Host rock REE values are within the range of comparable shaly sediments, both in terms of abundances and patterns (Fig. 2.17), and in general reflect their mineral content, derived from weathering, erosion and transport of the upper continental crust. In contrast, carbonate veins show that a large variability of REEs can occur within the 1 m-thick thrust-fault-related shear zone, also showing substantial differences between vein types.

The great variability in REE absolute concentrations can be linked to several factors, which include changes in REE concentration in solution, fluid oxidation state, temperature of the fluid, presence of REE-complex species and changes in flow rate (Henderson, 1984). More recently, it has been argued that calcite crystallization mode, in particular crystallization rate, can also influence REE concentration in calcite. Barker et al. (2006) and Barker and Cox (2011) reported the results of LA-ICP-MS elemental analysis on both natural vein samples and experimentally grown calcite crystals, and they noted fine-scale variations in trace element concentrations very similar to those found in Vidiciatico veins: an "oscillatory trace element zoning", that they attributed to differences in calcite precipitation rate. Rapid growth of a crystal promotes the entrapment of ions concentrated in the near-surface region more effectively, while at slower rate there is much time for elements in solution to diffuse through the crystal lattices and prevent the formation of a compositional zoning (Watson, 2004). Anyway, caution should be used in using REE abundances to infer crystallization rate in the case of veins, which formation is influenced strongly also by rate of vein opening, permeability and other structural controls. What is important to notice here, is that fine-scale variations in trace element concentrations are not necessarily indicative of external chemical changes in the fluid prior to crystallization and do not track any specific geological process (Barker and Cox, 2011). Therefore, the variability of the studied veins in terms of REE absolute concentration can be related to a large number of processes that cannot be individually discriminated. Moreover, there is no correlation between REE concentration increase/decrease and vein formation processes or other structural controls, as suggested by the fact that very different absolute values of REE concentration are registered in hybrid shear veins even for multiple spots in the same crack-and-seal increment, that is, for contemporaneous calcite spots (for instance points 17, 18, 19, 20 in Figure 2.11, all disposed along a single crack-and seal increment: as can be seen from correspondent REE values in Table 2.1, points 17, 18 and 19 have more or less similar abundances, but those of point 20 are markedly higher).

REE patterns, whether normalized to chondrite or to the host rock itself, have some distinctive peculiarities between different vein types. Shear veins always exhibit Eu positive anomalies, while most extensional veins, both fault-parallel and fault-perpendicular, are characterized by negative Eu anomalies or do not present an anomaly (Figs. 2.16 and 2.19).

The shear vein REE patterns normalized to wall rocks show the persistence of the Eu positive anomaly, confirming that this is not related to re-equilibrium with the host rock (Fig. 2.20a). Positive Eu anomalies in carbonates are generated by the presence of Eu^{2+} in the fluid, as Eu^{2+} is usually taken into the calcite structure in greater proportion than any other REE^{3+} as a substitute for Ca^{2+}. Divalent Eu is the prevalent oxidation state for Eu in most crustal fluids at temperatures ≥ 200 °C and reducing environments (Bau, 1991; Bau & Möller, 1992). Therefore, positive Eu anomalies registered along the basal thrust front suggest that hybrid shear veins precipitated from a Eu^{2+}-enriched fluid formed in disequilibrium with the fault zone environment, possibly at a temperature markedly higher than the 150 °C maximum of the SVU shallow portion. This is consistent with the structural localization of Vidiciatico shear veins, along thrust surfaces presumably continuous downdip for several kilometers. The larger Eu positive anomaly recorded by AC26 veins relative to those of sample AC15, can be caused by a larger provision of exotic fluid along the AC26 main thrust, when compared to the AC15 minor fault. A similar disequilibrium between the shear veins and the relative wall rocks in this same area has been previously determined through oxygen isotope analyses by Vannucchi et al., (2010). They reported that the general trend for calcite vein isotopes in the fault zone is toward lower $\delta^{18}O$ than in the host rock (Fig. 2.21).

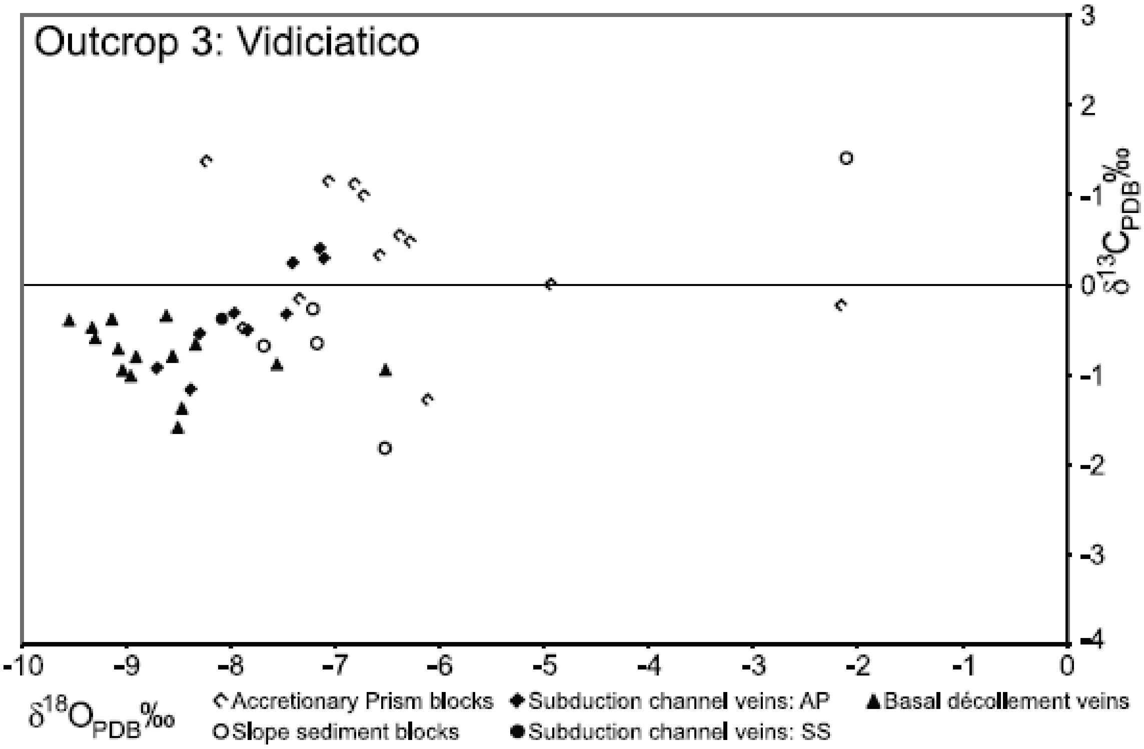

Figure 2.21. *Plot of $\delta^{18}O$ stable isotope data for calcite veins in Vidiciatico outcrop, reported from Vannucchi et al. (2010). The "basal décollement veins" represented by black triangles correspond to the shear veins analised in this study. They show the most negative values, significantly lower with respect to those measured in wall rock components, represented by white circles and rombohedra.*

The progressive decrease goes along with the transition from shallow to deeper portions of the subduction zone, with the most negative values localized along the basal décollement, e.g. in Vidiciatico shear veins (-8.7‰ ± 0.8‰ PDB, where -6.27‰ PDB is a mean value for the host rock and -12‰ to -17‰ PDB are expected values for veins formed in equilibrium with a seawater-like fluid).

tive $\delta^{18}O$ values in fluids at higher T, the disequilibrium between host rock and basal décollement shear vein $\delta^{18}O$, together with the greater proximity between seawater-precipitated veins and Vidiciatico shear veins, suggests that "the basal décollement was a main, rather continuous shear surface that could collect hot modified fluids from depth", derived probably from diagenetic/low metamorphic processes involving footwall rocks.

The small negative Eu anomalies of most of the fault-parallel and fault-perpendicular extensional veins are analogue to those of the wall rock samples, suggesting that calcite crystallized from a fluid in equilibrium with the fault zone environment (including wall rocks and the already crystallized veins) (Figs. 2.16c, d, and 2.17). AC19 veins and some MC3 extensional vein patterns appear to have a small Eu positive anomaly when normalized to their respective host rock (Fig. 2.20c, d). This can reflect a small contribution of carbonate from pressure solution of the shear veins (i. e. extensional veins are in equilibrium with the whole wall-rock + veins ensemble).

LREE enrichments and HREE depletions in calcite veins are due to the different partition of the REE ions depending on their size (Figs. 2.16 and 2.20). In fact, enrichments in LREEs in calcites are mostly controlled by sorption processes, where LREEs are preferentially assimilated in the crystalline lattice than HREEs (Henderson, 1984; Bau, 1991; Bau & Moller, 1992). This process is clearly exemplified by Group 1 extensional veins, which show steep chondrite-normalized REE patterns (Fig. 2.18).

Enrichments in HREEs of the fluids are instead related to preferential complexing of HREEs generally by CO2-bearing fluids, which form stronger complexes with the HREEs than with the LREEs. Some of these fluids could be exemplified by calcites of Group 2 extensional veins (Fig. 2.18). Their HREE enrichment is more evident when normalized to the host rock (Fig. 2.20.c). Some of these HREE-enriched veins are also characterized by LREE enrichments and these complex convex-upward patterns could be related to a combination of sorption and complexation processes. Veins in Vidiciatico have indeed all experienced repeated cycles of pressure solution that might have modified their original REE content, through successive depletions of more incompatible LREEs and additions of fluids coming from other dissolved veins. This is possibly best expressed in MC3 and AC19 veins, for which we have structural evidences of pressure solution processes (Fig.

2.7.c and 2.13) and consequently show LREE and HREE enrichments with respect to their host rock.

Breccia shear veins are very variable in terms of REE enrichments and their patterns are mostly similar to those of crack-and-seal shear veins, but Eu anomaly varies from positive to absent (Figs. 2.16.b, 2.19 and 2.20.b). This indicates that fluid crystallizing breccias may be exotic and travelling along the fault, but possibly also affected by a contribution from a local source with no positive Eu anomaly. This could be related to the mechanism of implosion breccia formation (Sibson, 1985): after a dilational opening along the shear surface, the pressure drop could recall the surrounding locally derived, not Eu-enriched, fluid (see for comparison Peltzer et al, 1998).

In summary, crack-and-seal shear vein trends and Eu positive anomalies point to a source of hot fluid external to the system, which fed the incrementally growing veins repeatedly over time. Conversely, extensional vein Eu negative anomalies and variable trends suggest that their fluid source should have been internal to the system and equilibrated to the host rock, but subsequently modified by sorption and complexation reactions and pressure solution processes. Breccia shear veins instead crystallized from a fluid that may be the result of mixing between the hybrid-shear-type and a local source.

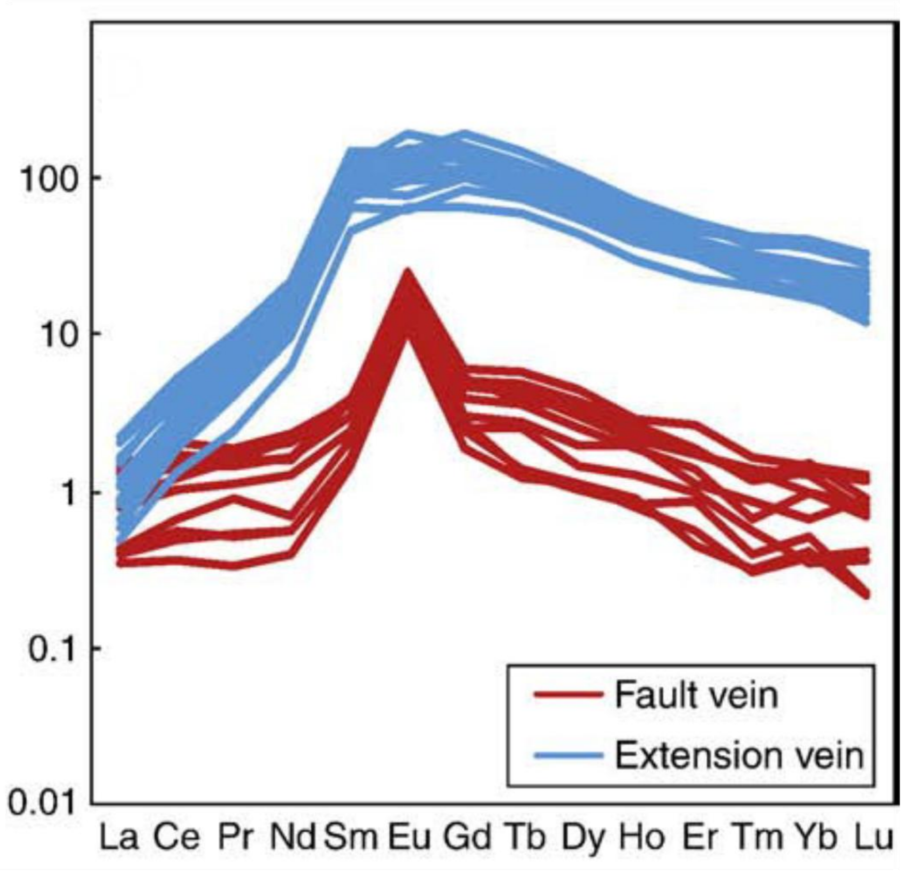

Figure 2.22. *Chondrite-normalized REE distribution patterns for fault veins (veins along shear fractures), in red, and extensional veins, in blue, sampled from the Nobeoka fossil megasplay thrust, Shimanto Belt, Japan. Reported from Yamaguchi et al. (2011). Note the similarity between the fault vein patterns and those of shear crack-and-seal shear veins in Vidiciatico outcrop (Fig.2.16.a).*

Differences in REE patterns between fault (along shear fractures) and extensional veins and the presence of Eu anomalies only in fault veins have been recorded in samples from the Nobeoka Thrust, a fossilized megasplay fault within the Shimanto Accretionary Complex, Japan (Fig. 2.22, Yamaguchi et al., 2011). Integrating REEs and C and O isotopes, the authors suggest the involvement of a large-scale fluid influx, in disequilibrium with the local fluid, in the precipitation of the fault veins. Alternatively, they explain the positive Eu anomaly retained by the fault veins as due to reducing conditions developed locally along the fault plane, through production of hydrogen by co-seismic mechano-chemical reactions (Kita et al., 1982). However, a similar mechanism seems unlikely in Vidiciatico fault zone (Tmax < 150°C), given that at low temperature the generation of a positive Eu anomaly would require an extremely low oxygen fugacity (Bau & Möller, 1992).

Section 2.d. Integration of structural and geochemical data and their implications in the seismic cycle

2.d.1. Analysis of the stress and pore fluid pressure conditions

The data discussed above underline a correlation between the mode of brittle failure, extensional vs shear, and the provenance, local vs exotic, of the fluids infiltrating the fault. Here, a failure diagram in pore fluid factor (λ) - differential stress (σ) space (Fig. 2.21) will be used to evaluate the stress and pore fluid pressure conditions compatible with the structural relations between sets of veins observed in the thrust fault zone (see Section 2.a and 2.b).

The diagram was constructed referring to Cox (2010) and Sibson (1998; 2000; 2013): the formulation of failure criteria in a $\lambda - \sigma$ space is introduced as detailed by Cox (2010), neglecting the effect of the intermediate principal stress σ_2. Brittle shear failure and shear failure along pre-existing faults follow a linear Coulomb criterion (respectively, blue and purple lines in Fig. 2.23). Conditions for hydraulic- and hybrid-extensional fracturing are expressed in the form of Secor (1965) (red lines in Fig. 2.23), and approximated by the parabolic Griffith failure criterion (Griffith, 1924) (green lines in Fig. 2.23), respectively. Following Sibson (2013), the failure criteria for compressive and extensional regimes were combined on the same plot. As a first order approximation, principal stresses are assumed as horizontal and vertical, therefore the differential stress reduces to (σ_h - σ_v), with positive values in compressional regime and negative values in extensional regime (Fig.2.23). The assumption of an Andersonian stress state is coherent with the orientation of the deformation structures observed in Vidiciatico fault zone. As reported in Section 2.a, the original orientation of the main thrust cannot be determined precisely, but its direction parallel to footwall bedding characterizes it as a flat portion of the ramp-and-flat SVU basal thrust so low inclined to the horizontal

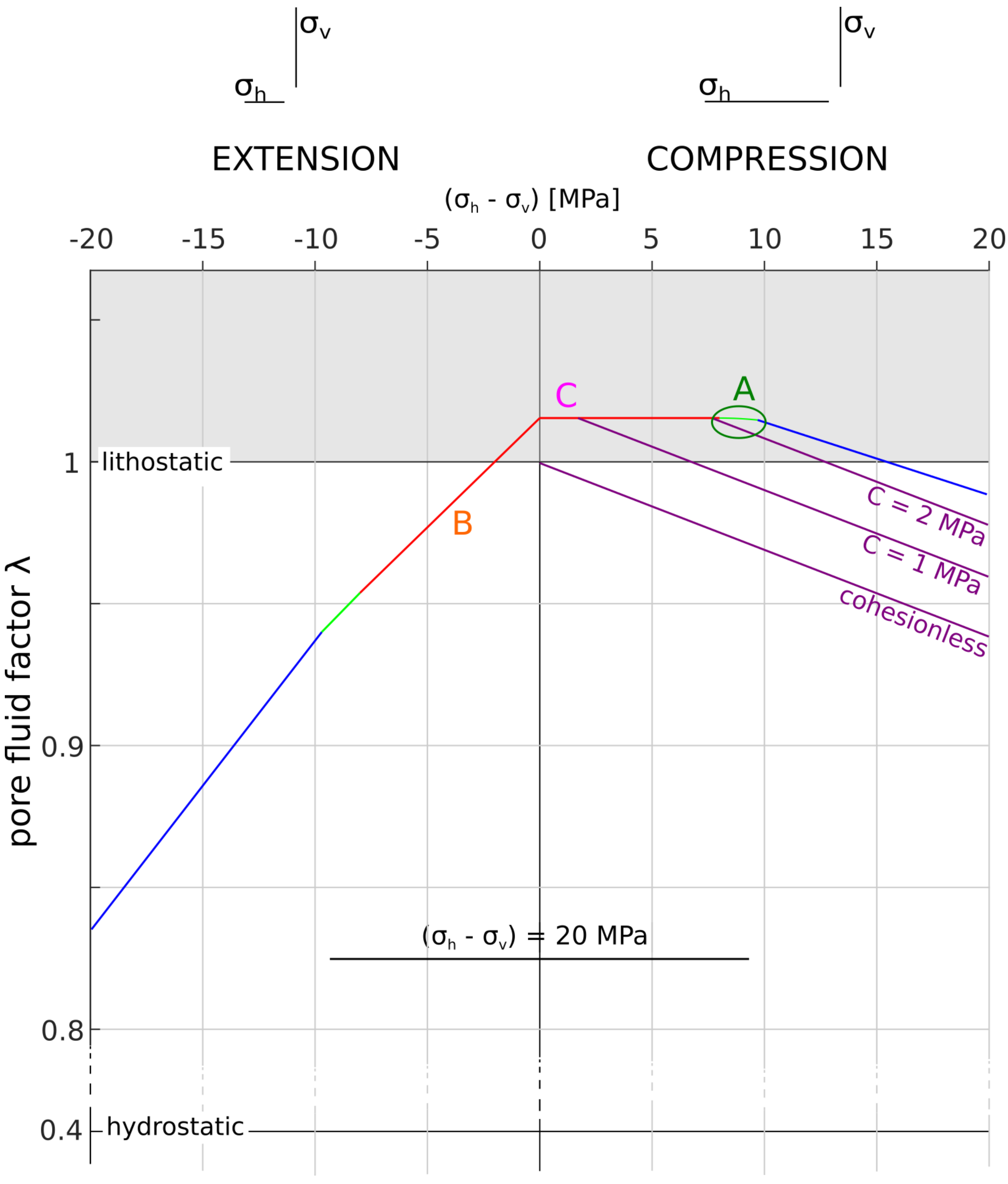

Figure 2.23. *$\lambda - \sigma$ diagram of the state of stress of the Vidiciatico thrust at 5 km depth. See text for explanation. From Cerchiari et al., submitted.*

direction (about 5-10°). The fault-parallel flattening foliation planes and high-angle extensional veins are consistent with a subvertical σ_1, while the low-angle extensional veins are compatible with a subhorizontal σ_1. A low friction coefficient of 0.4 and a low tensional strength of 1 MPa are assumed for the thrust, accounting for its composition of foliated clay-rich rocks (e.g., den Hartog et al., 2012; Collettini et al., 2009; Saffer & Marone, 2003) and the precipitation of calcite in the shear veins, respectively. Extensional veins crosscut both the thrust and the wall rock marls, whose tensional strength has been set to 2 MPa, at the lowest end of published values for limestones/mudstone (Carmichael, 1982), while the coefficient of internal friction, which is relatively constant for weak and strong rocks, has been set to the broadly used value of 0.75 (e.g., Sibson, 2013; Cox, 2010). With a low angle dipping thrust and an Andersonian stress state, fault-parallel extensional veins are expected to

be subhorizontal and fault-perpendicular extensional veins are subvertical (Fig. 2.23). In the $\lambda - \sigma$ failure plot in Figure 2.23, the conditions for opening extensional veins perpendicular to the fault zone are met in extensional regime, with $\sigma_v = \sigma_1$, $(\sigma_v - \sigma_h) < 4T = 8$ MPa, and at supra-hydrostatic to supra-lithostatic fluid pressures ($0.95 < \lambda < 1.015$). In contrast, extensional veins parallel to the fault form in compressive regime, with $\sigma_v = \sigma_3$, $(\sigma_h - \sigma_v) < 4T$ and supra-lithostatic pore pressures ($\lambda = 1.015$). These conditions are similar to those for reactivating the low-cohesion thrust faults in association with hybrid extensional-shear veins, with supralithostatic pore pressure and $4T < (\sigma_h - \sigma_v) < 5.5T$ (Fig. 2.23).

From this simple analysis, it results that, in all its brittle activity, the Vidiciatico basal thrust fault strand worked in conditions of low differential stresses (less than 10 MPa in absolute value) and high pore fluid factors (> 0.95) (Fig. 2.23), similar to the ambient conditions of shallow active subduction megathrusts as imaged by geophysical methods (e.g., Saffer & Tobin, 2011; Hardebeck, 2017).

Fault-perpendicular extensional veins form in an extensional regime with $\sigma_v = \sigma_1$, while fault-parallel extensional veins and shear on the thrust fault both occurr in compressional regime with $\sigma_v = \sigma_{3,}$ as previously outlined also in Section 2.b. Both fault-perpendicular and fault-parallel extensional veins show evidence for shortening and folding, thus suggesting long term fault-perpendicular and fault-parallel compression upon their formation (Figs. 2.7.c, h and 2.14). Long term subvertical shortening has been described also in other field analogues of subduction megathrusts (e.g. the Chrystalls beach Complex in New Zealand, Fagereng, 2013; the Kodiak Islands in Alaska, Fisher and Byrne, 1987; the Shimanto Accretionary Complex in Japan, Ujiie, 2002; Ujiie et al., 2018), where it resulted difficult to reconcile the formation of fault-parallel and fault-normal extensional veins without a cyclical change of stress orientation (see discussion in Ujiie et al., 2018).

Stress switching from a compressional to an extensional regime after large earthquakes has been documented in several active megathrusts, as related to total stress release above the megathrust, which promoted extensional faulting in the wedge and in the outer rise (e.g., Ide et al., 2011). According to Sibson (2013), which proposed a mechanical analysis of the required drop in differential stress for a weak megathrust fault at 20 km depth starting from 40 MPa, in the shallower Vidiciatico basal thrust a drop in differential stress of less than 20 MPa can have caused the switch of the stress state from compressional to extensional (Fig. 2.23). This is confirmed by the low differential stresses constrained by the dominantly dilatant mode of failure.

2.d.2. Stress/fluid interplay during the seismic cycle

The geochemical and structural interpretations are here combined to propose a model accounting for the variations in stress and fluid circulation during the seismic cycle.

The geochemical signatures of vein sets in Vidiciatico are strongly correlated with their structural significance. Shear veins, which are associated with shearing along the thrust, bear evidence for the influx of fluids external to the system, while small-scale extensional veins are cemented by local fluids in equilibrium with the surrounding rocks, independently on their orientation. Brittle failure mode appears thus to be strongly coupled with fluid transport, as expected for low porosity rocks like the tectonized marls hosting the Vidiciatico thrust fault (e.g., Sibson, 2013; Cox, 2010). Based on the above analysis of the differential stress-pore fluid pressure conditions necessary to form the vein sets and considered their mutually crosscutting relations, the activity of the basal thrust may have occurred through the following phases (sketched in Fig. 2.24), which repeated cyclically:

(i). Seismic failure along the thrust. The differential stress-pore fluid factor conditions are likely within the area A in Figures 2.23, 2.24 and 2.25, meeting both the condition for reshear on the recemented main fault and the condition for opening of shear veins inside small dilational jogs (Figs. 2.24.A and 2.25). The earthquake ruptures, which likely nucleated in deeper sectors of the fault, can cause a drop in differential stress able to switch the stress state of the area from a subvertical σ_3 to a subvertical σ_1. This differential stress fall is associated with a drop in pore fluid pressure caused by several factors, namely: -) the poroelastic relaxation due to the drop in mean stress, expressed by the Skempton coefficient (e.g., Sibson, 2013) and -) the increase in fracture permeability due to the expansion of fluid circulation paths caused by the coseismic damage (e.g., Sibson, 1986; Mitchell and Faulkner, 2012). Coseismic fluid drainage agrees with the REE patterns of crack-and-seal shear veins and, on a lesser extent, of implosion breccias, which point to fluids sourced by deeper reservoirs in disequilibrium with the thrust wall rock, partially modified in the postseismic phase for the breccias. After the earthquake, due to the simultaneous drop in both differential stress and pore pressure, the conditions of the faults in $\lambda - \sigma$ space are within the area B in Figures 2.23, 2.24 and 2.25.

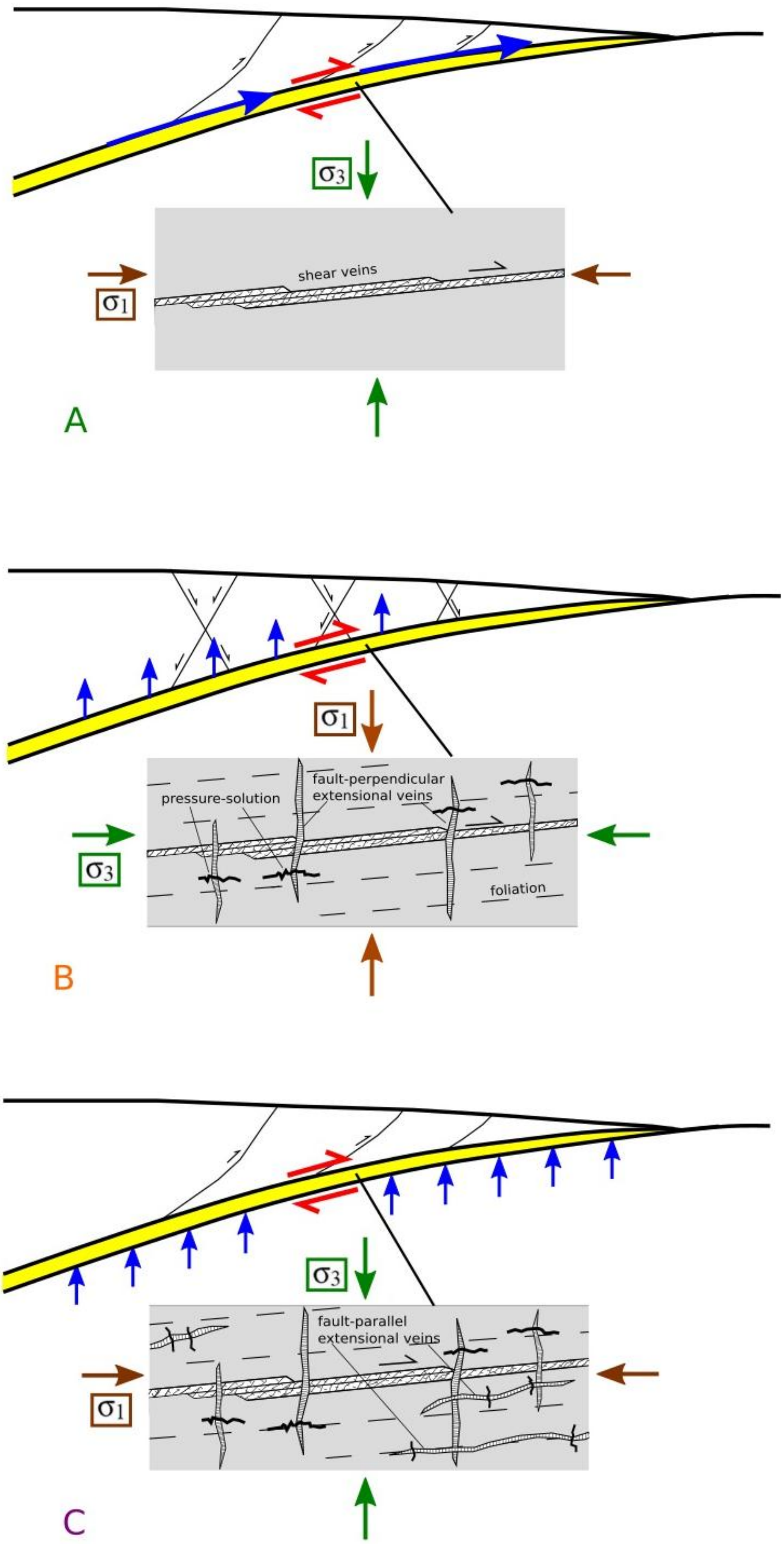

Figure 2.24. Interpretative sketch of the seismic cycle phases at the macro- and meso-scale, with phase labels A, B, C corresponding to those in Figs. 2.23 and 2.25. See text for explanation; blue arrows trace the assumed fluid pathways. From Cerchiari et al., submitted.

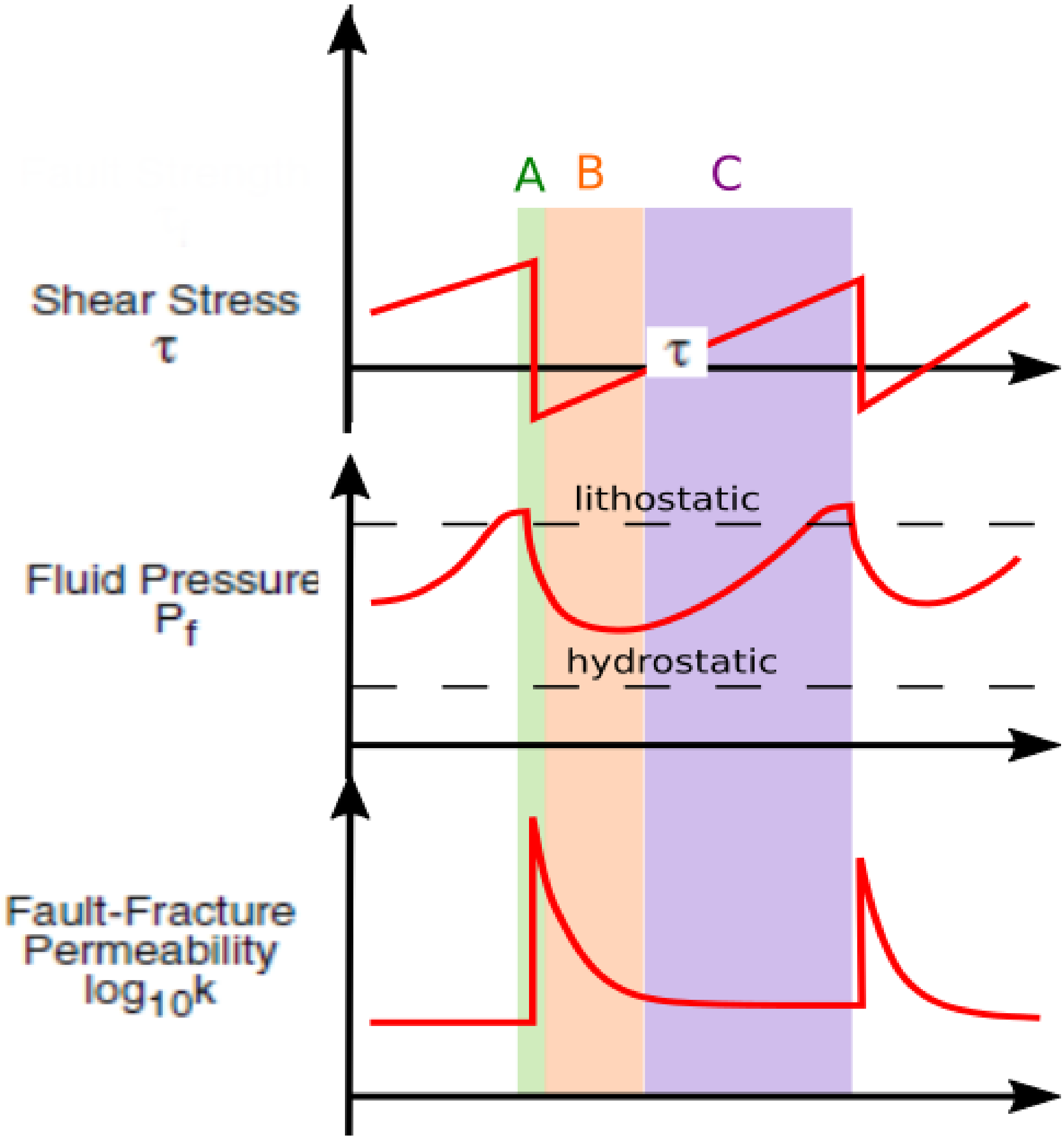

Figure 2.25. *Diagram showing changes in fault strength, fluid pressure and permeability for every cycle phase. See correspondence to Fig. 2.24. Modified from Sibson (2013). From Cerchiari et al., submitted.*

(ii) Postseismic phase. After the earthquake, the fault undergoes compaction, which causes a reduction of porosity and consequent pore fluid pressure increase (e.g., Sleep and Blanpied, 1992). An increase in pore fluid can lead to the onset of extensional failure in extensional regime, thus producing fault perpendicular extensional veins (B in Figs. 2.23, 2.24 and 2.25). The pore pressure excesses are likely to be local and immediately discharged by the formation of the veins, thus limiting the increase in pore fluid pressure. REE patterns of fault perpendicular extensional veins are buffered by the wall rock and affected by pressure solution processes as they drain local fluids in the surroundings of the veins. Strength, pore fluid pressure and stress recover in extensional regime.

(iii) Reloading phase. The increase in σ_h due to tectonic loading allows the differential stress to decrease in absolute value, and subsequently to switch to a compressional regime, with pore fluid

pressure limited by the formation of subhorizontal extensional veins (C in Figs. 2.23, 2.24 and 2.25). Accordingly, subhorizontal extensional veins precipitate calcite from local fluids, in equilibrium with the wall rock (REE patterns buffered by the host rocks) and affected by pressure-solution due to fault-parallel shortening. Strength, pore fluid and stress recover in compressional regime.

(iv) Back to phase (i). The increase in σ_h due to tectonic loading causes an increase in differential stress which leads the thrust to reactivation (A in Figs. 2.23, 2.24 and 2.25).

2.3. Conclusions

The basal thrust incorporated sediments shortly after their deposition, and transported them down to depths typical of the onset of seismicity in active megathrusts, thus it represents a good analogue for investigating the deformation processes of shallow present day megathrusts above the transition to the seismogenic zone.
What reported in this Chapter suggests that:

- Shear deformation started to act in not completely lithified sediments and then gradually evolved to dilatant brittle deformation with the increasing grade of lithification of fault zone rocks. Strain was accommodated based on the competence contrast of the components: clay-rich portions underwent diffuse pressure solution and grain reorientation along S-C shear band. Carbonate-rich portions remained deformed internally but were cut by localized brittle fault and fractures coated by hybrid-shear veins. Progressive lithification went along with further localization of the shear deformation, up to the complete strain concentration onin D3 main thrust fault (Mittempergher et al., 2018).

- The thrust fault zone has a maximum thickness of 4–5 m, similar to present day megathrust fault strands, and, with increasing maturity and depth, the active portion of the fault further localizes in a thinner fault zone, less than 30 cm-thick. The increasing localization of slip with increasing depth is coherent with conditions approaching those estimated for the transition to the seismogenic zone in active megathrusts (Mittempergher et al., 2018).

- The basal thrust fault was active under low differential stress, and the state of stress within the active fault was likely decoupled from that in the footwall, suggesting that the components of the basal thrust fault were weak compared with the footwall (Mittempergher et al., 2018).

- Extensional veins in the fault zone are often unfavourably oriented relative to the stress field required for thrusting, suggesting that faulting was promoted by repeated failures at low effective stress and in presence of fluids in all stages of activity of the thrust and that stress along the fault cyclically switched from a vertical σ_3 to a vertical σ_1 (Cerchiari et al, submitted).

- The switching implies that the stress drop during a seismic event accounts for a complete release of the shear stress along the surface and probably also an overshooting. This has been effectively observed in modern margins (see for instance Lin et al., 2013 and Brodsky et al., 2016). The total stress release is facilitated by the low differential stress inferred from the geometrical relations between the veins (Cerchiari et al., submitted);

- Thrust activity is correlated to changes in permeability, with input of fluid external to the system marked by an Eu positive anomaly, during the main seismic event, and a local fluid source, with no Eu anomaly, in the post-seismic and reloading phases (Cerchiari et al, submitted). A similar explanation has been given by Yamaguchi et al. (2011) to explain the REE signatures on quartz-calcite veins of the Mugi mélange in the Shimanto Belt, Japan. In particular, the shear veins are very similar to those of Vidiciatico in terms of REE distribution.

Therefore, these findings show that the combination of geochemical and structural analyses of veins in megathrust field analogues represents a promising tool towards a deeper understanding of the interplay between stress state and fluids in subduction zones.

Chapter 3. Llŷn shear zone in SW Llŷn Peninsula, NW Wales

This chapter presents the results of a meso- and microstructural study of an accretion-related fault strand belonging to the Gwna Group, the oldest part of the Mona accretionary Complex in northwestern Wales (Fig. 3.1). The whole complex has been studied for many years at the regional scale, given the abundance of coastal exposures, which are much less accessible for direct observation at the outcrop scale. Detailed meso-and microstructural studies of parts of the complex are generally lacking, and this study hopefully will contribute to fill this gap. After a first brief description of the geological setting (paragraph 3.1) and the methods used (paragraph 3.2), Section 3.a describes the internal meso- and microstructure of Llŷn fault strand, at the southwestern tip of Llŷn Peninsula. Section 3.b presents the results of fluid inclusion microthermometry (paragraph 3.b.1) and EBSD analyses (paragraph 3.b.2) on quartz tectonic veins, to better constrain the maximum deformation temperature and related vein quartz rheology. In Section 3.c, based on the observed structures, the fault zone deformation history is reconstructed. Finally, in Section 3.d, possible interpretations are discussed, regarding the involvement and role of fluids in the fault zone deformation processes.

3.1. Geological setting

The Mona Complex in Anglesey Island and Lleyn Peninsula (Fig. 3.1), northern Wales, is interpreted as a fragment of a 600-500 Ma (Precambrian/Cambrian) Pacific-type subduction-accretion system (Greenly, 1919; Wood, 1974; Shackleton, 1975; Barber and Max, 1979; Gibbons and Horák, 1996; Kawai et al., 2006; Strachan et al., 2007), resulting from the overthrusting of the western Iapetus Ocean by the Avalonia Plate.
Since the first study by Greenly (1919), the structure of Anglesey Island and Lleyn Peninsula have been subjected to several interpretations (Shackleton, 1954, 1969; Barber and Max, 1979; Phillips, 1991; Gibbons et al., 1994; McIlroy and Horák, 2006). Here I refer to the most recent ones (Asanuma et al., 2015; Kawai et al., 2006; Maruyama et al., 2010; Sato et al., 2015), that reported how accretion in the Mona Complex has involved lithologies interpreted as a complete ocean plate stratigraphic succession.

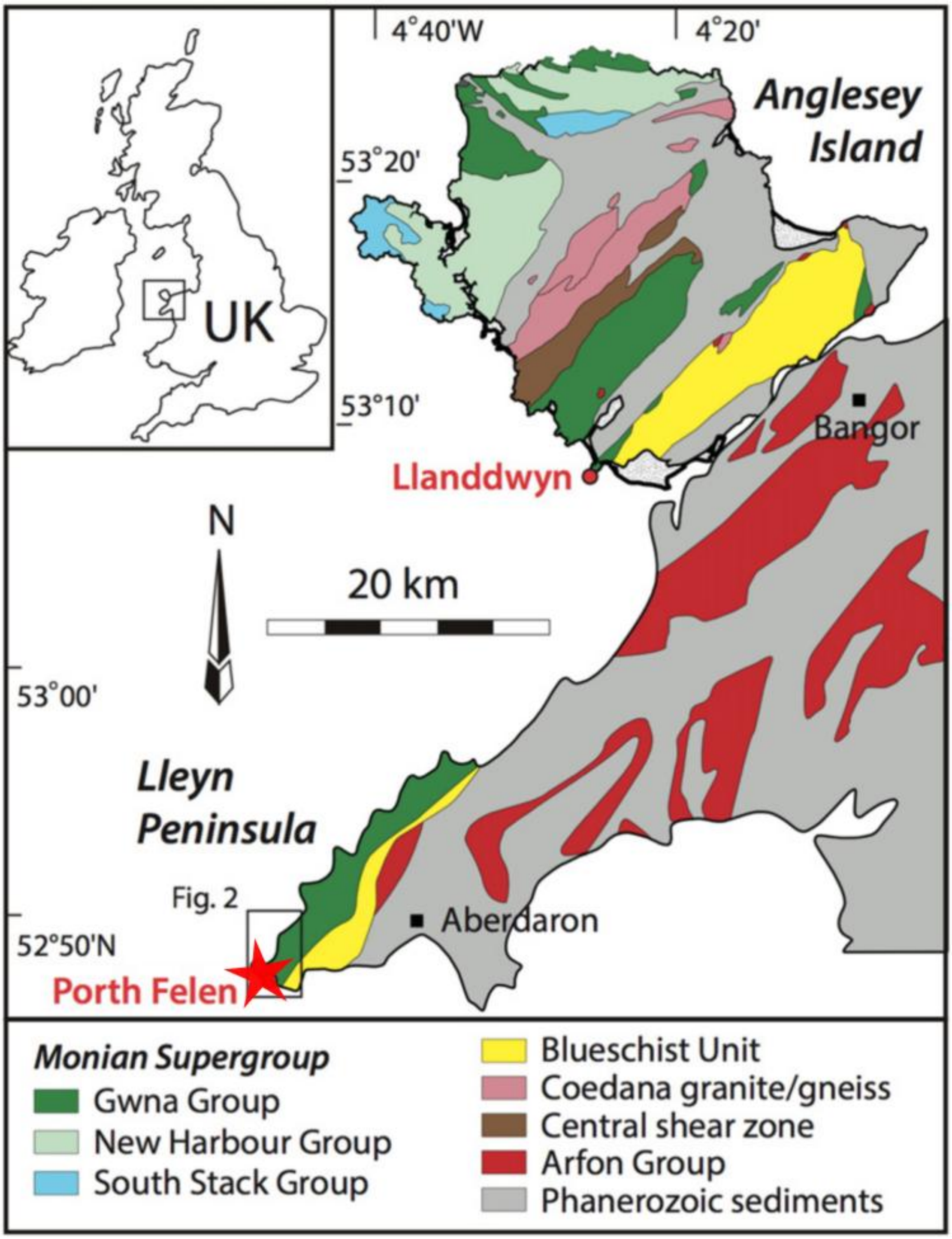

Figura 3.1. *Geological map of Anglesey Island and Llŷn Peninsula, NW Wales (UK), modified from Sato et al. (2015). Red star indicates the location of Llŷn shear zone outcrop, near Porth Felen, southwestern Llŷn Peninsula. "Lleyn" is the English word for the welsh "Llŷn".*

Oceanic plate stratigraphy (OPS) records the travel history of an oceanic plate from a ridge to a trench. At the base of the characteristic sequence, there are MORB basalts spreading from the ridge, then cherts, deposited under deep-sea pelagic conditions at or near the ridge. The cherts can be substituted by limestones if the ridge rises above the carbonate compensation depth. If the plate passes over a plume, OIB basalts can be incorporated in the succession. When the plate reaches a hemipelagic environment near the trench, radiolarian siliceous shales and fine-grained continental-derived mudstones are deposited. Already accreted, water-saturated sediments may slump to form gravitational olistostrome deposits. Finally, at the trench, turbidity currents add clastic shales, sand-stones and conglomerate (Maruyama et al., 2010; Matsuda and Isozaki, 1991).

In the Mona Complex, OPS from structural top to bottom is composed by (see map in Fig. 3.1):

The Coedana granite-gneiss complex. Quartzo-feldspatic gneisses and post-tectonic granites of Pre-cambrian age (666 ± 7 Ma and 613 ± 4 Ma from zircons respectively) cropping out in the centre of Anglesey Island and interpreted as the basement of the Mona Complex (Kawai et al., 2007; Maruyama et al., 2010).

The Gwna Group. It records the ridge-trench transition in OPS, well visible in a series of accreted duplexes on Anglesey northern coast, Llanddwyn Island (SW Anglesey) and in northern and south-western Llŷn Peninsula. The duplex structure is particularly well preserved on Llanddwyn Island (Fig. 3.2). There, two parallel N-S strike-slip faults divide the island into eastern and western units, each subdivided by several bedding-parallel link thrusts into a series of horses separated by two major roof- and floor-thrusts. All the units face downwards to the SE. In each horse, the stratigraphic bottom is a MORB-like, pillow-bearing or massive basaltic flow. Pillows are 30-60 cm in diameter and cemented by a glassy matrix. Then, interpillow cherts or limestones, depending on the different horses, are overlained by mafic mudstones with lenses of pillow breccias and limestone, pelagic carbonates and finally sandstones. The sedimentological changes reflect the gradual change in environment from eruption of basaltic lavas in the deep ocean at or near a ridge, through deposition of pelagic chert or limestone in an ocean far from a continent, hemipelagic mudstone while approaching the trench, to sandy turbidite and conglomerate at the trench. Following calculations of Maruyama et al. (2010), the 300 m-thick accretionary complex on Llanddwyn Island preserves an OPS detached from over 7800 m of subducted lithosphere. On the other hand, the low metamorphic grade (sub-greenschist, zeolite facies) associated with the very low deformation suggests a shallow depth of accretion, correspondent to either offscraping or underplating of < 10 km of lithosphere (Maruyama et al., 2010).

The Blueschist Unit. It corresponds to subducted OPS metamorphosed under blueschist-facies conditions and crops out on western Anglesey and on the SW Lleyn Peninsula (Maruyama et al., 2010). Its variable composition is mainly characterized by meters- to tens of meters-thick lenses of

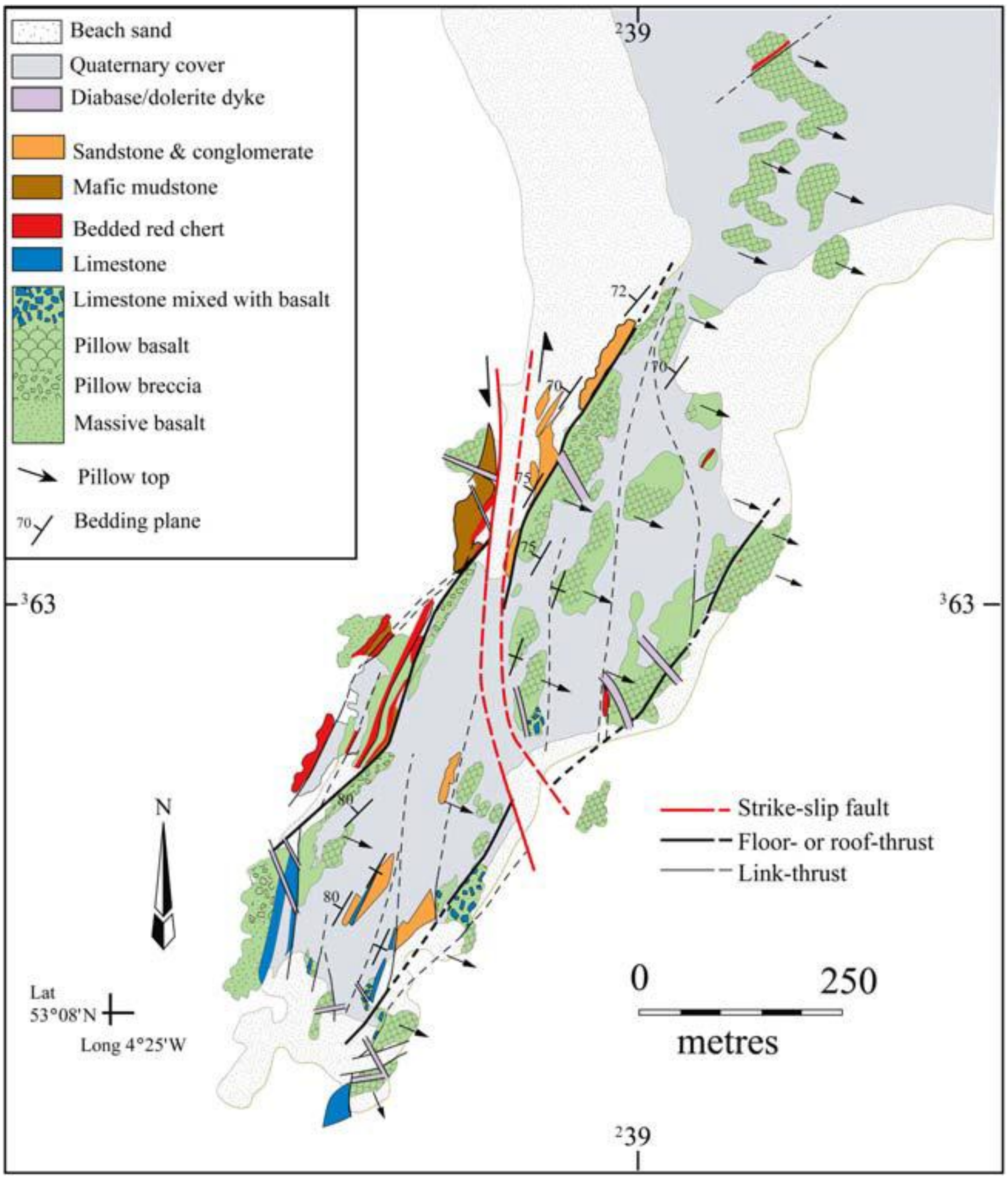

Figure 3.2. *Simplified geological map of Llanddwyn Island, showing the main stratigraphic units and the principal structural features. The two high angle strike-slip faults in the centre (red dashed lines) offset the island, subdividing it in a western and an eastern region, each composed of stacked duplexes, delimited by link and floor-/roof-thrusts (black thin and thick lines, respectively). From: Maruyama et al. (2010).*

quartzite, limestone and greenstone (blueschist or horneblende schists) in a matrix of mica schist or mafic chloritic schist (560-550 Ma $^{40}Ar/^{39}Ar$ mineral age, at the Precambrian/Cambrian limit, following Dallmeyer and Gibbons, 1987). The protolith of the Blueschist Unit is interpreted as trench-fill pelitic sediment. Based on recent interpretations, it could have been emplaced by a wedge extrusion process, resulting from an approaching buoyant mid-ocean ridge that possibly lowered the subduction angle and contributed to the widespread, landward calc-alkaline magmatism of the Arfon Group in NW Wales (Kawai et al., 2007; Maruyama et al., 1996; Maruyama, 1997).

The olistostrome-type accretionary complex. The unmetamorphosed unit lying structurally below the Blueschist Unit on SW Lleyn is interpreted by Kawai et al., 2007 and Maruyama et al., 2010 as an olistostrome-type mélange, in which an already-formed accretion complex had collapsed from the inner wall of a trench to form a gravitational deposit. It contains many centimeters-to meters-long olistoliths (exotic clasts) of quartzite, dolomite, sandstone and basaltic greenschist and slumped packs of strata in a matrix of mafic mudstone. At its base, it is underlain by a unit with well-preserved OPS (sandstone – mudstone - thick red bedded chert - basalt) (Maruyama et al., 2010).

The New Harbour Group. Micaschist with biotite, chlorite and epidote, containing up to 2 km-long lenses of basaltic greenschist with supra-subduction zone arc affinity (Thorpe, 1993) and red cherts (Maruyama et al., 2010).

The South Stack Group. It consists of thick quartzitic psammites interbedded with thin chloritic and mafic pelites, most probably formed on a passive continental margin (Phillips, 1991). With a late Cambrian zircon age (501 ± 10 Ma) is the youngest group in Anglesey-Llŷn (Collins and Buchan, 2004).

The Units described above are juxtaposed in that order by low-angle thrusts, producing a subhorizontal thrust-nappe pile (Maruyama et al., 2010). The underthrusting of crust to NW by the youngest sediments of the South Stack Group should have caused the doming and uplifting of the extruded Blueschist Unit and associated rocks in central Anglesey. The consequent development of high-angle secondary faults has complicated the original structural relationships between the Blueschist Unit, the subduction-accretion complex (the Gwna Group), and the coeval arc (the Arfon Group) (Kawai et al., 2007).
The subduction polarity is inferred to the SE (Iapetus Ocean underthrusting Avalonia), because of the widespread magmatism extending up to England, the sense of younging of the OPS (Kawai et al., 2007), geometry of the duplexes accreted and the sense of shear along thrusts (Maruyama et al., 2010).

Here, one of the accretion-related fault strands within the Gwna Group mélange will be described. The outcrop is located on the SW Llŷn Peninsula, near Porth Felen (Figs. 3.1 and 3.3). As will be discussed below, although the OPS structure and the general tectonic structure is similar and can be linked to that in Llanddwyn (Fig. 3.2), this outcrop presents some peculiarities whose significance will be highlighted in the following sections. The Gwna Group in Llŷn Peninsula does not present a

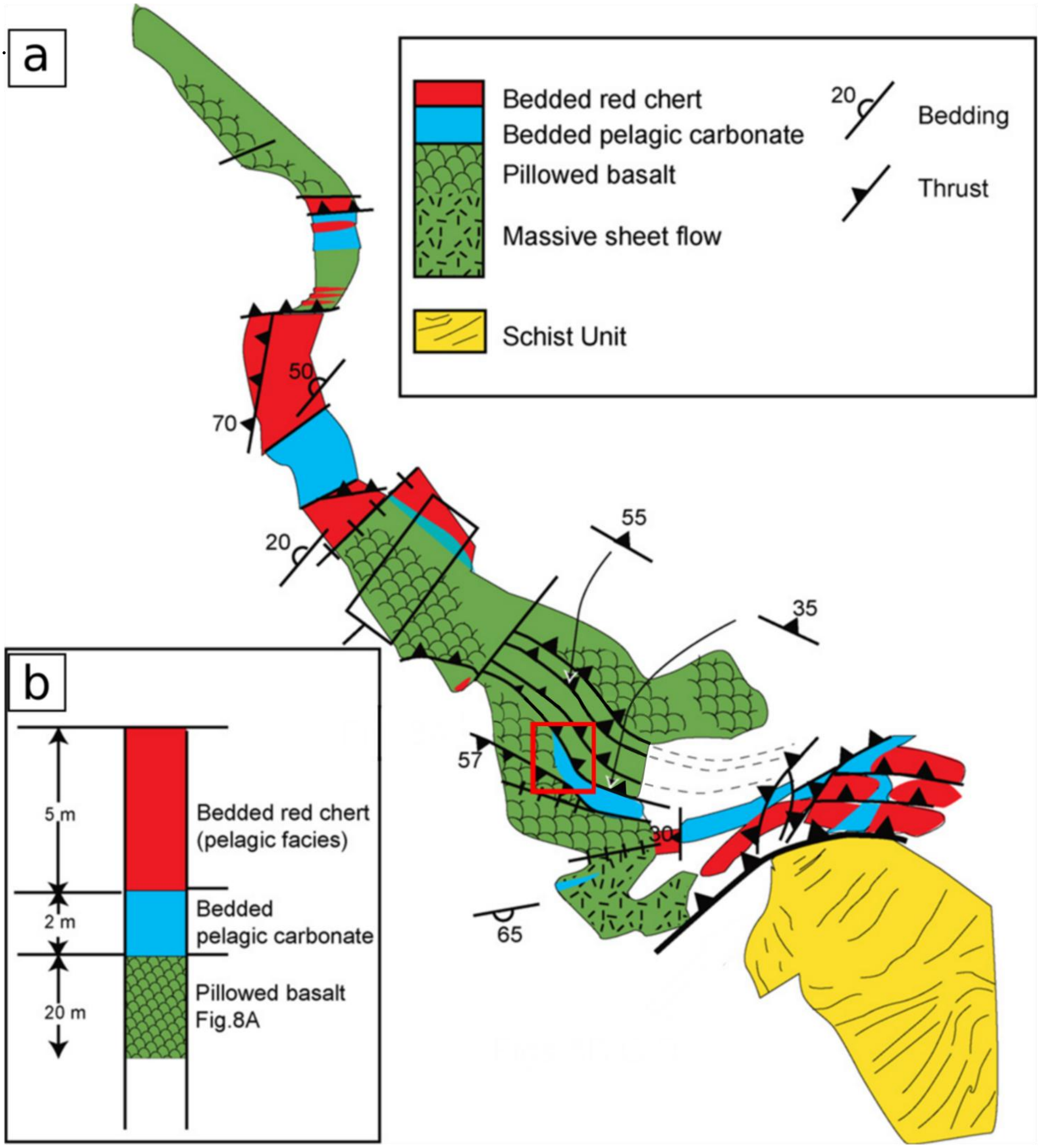

Figure 3.3. Schematic geological map of Porth Felen aerea in SW Llŷn Peninsula, reported from Kawai et al. (2007), with location of the studied fault strand in the red box. b) Geological columnar section of primary ocean plate stratigraphy that has been involved in the Gwna Group accretion-subduction thrusting. In this map, Kawai et al. (2007) did not report hemipelagic mudstone or turbidite sandstone in the fault strand area, but these have instead been observed on the outcrop, as will be explained in Section 3.a.

clear subdivision of duplexes bounded by link and roof thrusts like in Llanddwynn (Fig. 3.2) (despite some recent interpretations, i.e. Sato et al., 2015), but it shows rather the block-in-matrix structure typical of heterogeneous tectonic mélanges, with high internal competence contrasts.

Parallel low-angle thrust faults cut more competent boudins through the matrix, and no high angle thrusts are present (Fig. 3.4).

3.2. Methods

Two main fieldtrips were performed in Summer 2017 and 2019 to conduct an outcrop mesoscale analysis and to collect samples for the realization of thin sections. Structural orientations and the relations between geometrical elements were measured and recorded on sketches and stereoplots (Fig. 3.4 and 3.5). The data were plotted using Stereonet 9 software on an equiareal, lower hemisphere stratigraphic projection (Allmendinger et al., 2012) (Fig. 3.5.b).

From samples collected in the field, 18 polished thin sections with a 30 μm thickness were obtained, for the optical microscope and, with proper gold coating, also for SEM and EDX analyses. The scanning electron microscope is a Field Emission Gun FEI Nova Nano-SEM 450 apparatus, equipped with a Quantax-200 X-Flash 6 detector for EDS and hosted at the Centro Interdipartimentale Grandi Strumenti of Modena University. Three additional thin sections derived from samples of crack-and-seal quartz veins were especially realized, two for the fluid inclusion microthermometry study and one for the Electron BackScattered Diffraction EBSD analysis, respectively (Section 3.b).

For fluid inclusion microthermometry, thin sections were first cut with a 100 μm thickness and well polished on one side, subsequently glued to a glass slide. Then, the thin sections were polished on the other side and put in acetone overnight to let the glue degrade completely. After this, the so-called “double polished wafers” were obtained, carefully detaching manually each thin section from its glass slide. These preparation phases were accomplished at the Department of Chemical and Geological Sciences, University of Modena, then the double-polished thin sections were analyzed with the LINKHAM THM 600 heating/cooling microscope at the Fluid Inclusion Laboratory of the Department of Physics and Earth Sciences, University of Parma, to retrieve the fluid inclusion formation temperatures (homogeneization temperature Th, see paragraph 3.b.1), from which a minimum value of the highest temperature reached in the outcrop can be deduced.

The EBSD thin section was especially superpolished and metalized, then analysed with the Zeiss Sigma HD FEG Analytical SEM (ASEM), equipped with an Oxford Instruments Aztec EBSD detector, at the School of Earth and Ocean Sciences of Cardiff University, Wales, UK. The crystallographic orientation data obtained for quartz were processed with MTEX script for MATLAB software and orientation maps were obtained (see paragraph 3.b.2).

Section 3.a. Meso- and microstructural description

3.a.1. Mesostructures

The accretion-related fault strand studied (Fig. 3.4) crops out at the southwestern tip of Llŷn Peninsula, near Porth Felen (Fig. 3.3). Here, the Gwna Group OPS sequence (see paragraph 3.1) is composed of: pillow basalts (> 4 m-thick), bedded dolostone (2 m-thick), black mudstone (5 m-thick) and sandy and muddy turbidite (15 m-thick) (Sato et al., 2015). Llŷn fault strand promotes the relative movement between reddish bedded dolostone in the footwall and grey sandy/muddy turbidite in the hangingwall, concentrating shear in the black mudstone level (Fig. 3.4). In the fault strand, 30°- to 10°-inclined parallel thrust faults, extended for meters to tens of meters, cut through a tectonic mélange with a block-in-matrix structure (Festa et al., 2019 and references therein).
The footwall dolostones are bedded, with strata 5 to 10 cm thick (Fig. 3.4), folded in at least two roughly perpendicular directions with hinges oriented to the NW and to the NE. In some points folds appear isoclinal and refolded. Extensional veins are present along hinge lines, interconnected with other complex network of quartz veins (Fig. 3.5.f). All the folds and fractures in the dolostones are truncated by one of the main thrust faults, at the base of the fault strand (Fig. 3.4).
In the fault strand mélange, the matrix consists of black mudstones, thinly laminated and varying in colour and percentage of silica, as reported in detail by Sato et al. (2015). A tectonic foliation is well developed in the mudstones, with an average inclination of 45° relative to the main thrusts (Fig. 3.4 and 3.5.a, b). More or less continuous subhorizontal Riedel R shear fractures are present (Figs. 3.4 and 3.5.b). Blocks of chert and quartz-rich sandstone, ranging from tens of cm to a few meters, are aligned on foliation planes or along shear surfaces in the mudstones. They have a lenticular shape with tapered extremities and, especially the chert blocks, display boudinage fractures and extensional veins oriented perpendicular to the mudstone foliation (Fig. 3.5.c).Along the thrust fault surfaces, 1-5 cm-thick quartz shear veins are visible, reaching a few decimeters in dilational jogs (Fig. 3.5.d). Slickenfibers are always clearly detectable and they display multiple directions of shearing, indicating a mean top-to-the-south thrusting (Fig. 3.5.c). Sporadically, thin extensional veins are seen both perpendicular to the shear veins and parallel to foliation planes. Locally, both shear and extensional quartz veins appear as deformed, folded and partially dissolved (Fig. 3.5.a), up to very complex arrangements of vein fragments in a pervasively deformed mudstone matrix.
The decrease in intensity of shear fractures, thrusts and boudinage marks the passage to the merely but intensely foliated hangingwall sandy and muddy turbidite. Hangingwall rocks are scarcely accessible due to the outcrop face steepness, but they display a foliation with the same orientation as in the fault strand mélange.

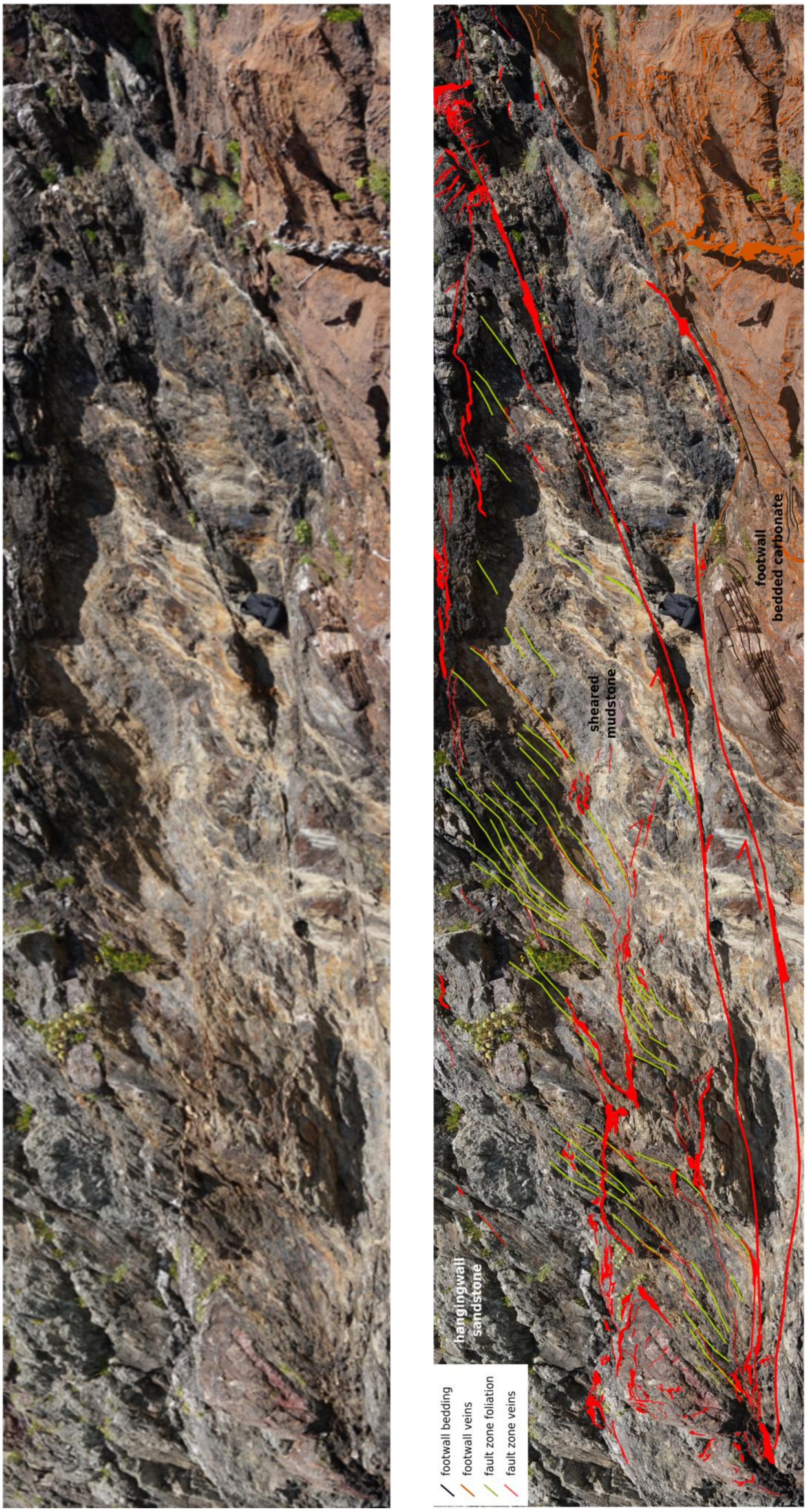

Figure 3.4. *Photocomposition with interpretation of the outcrop scale structures in Llŷn shear zone. Backpack in the middle for scale. Proportions are not always maintained, due to the slight distorsion resulting from the combination of different photographs.*

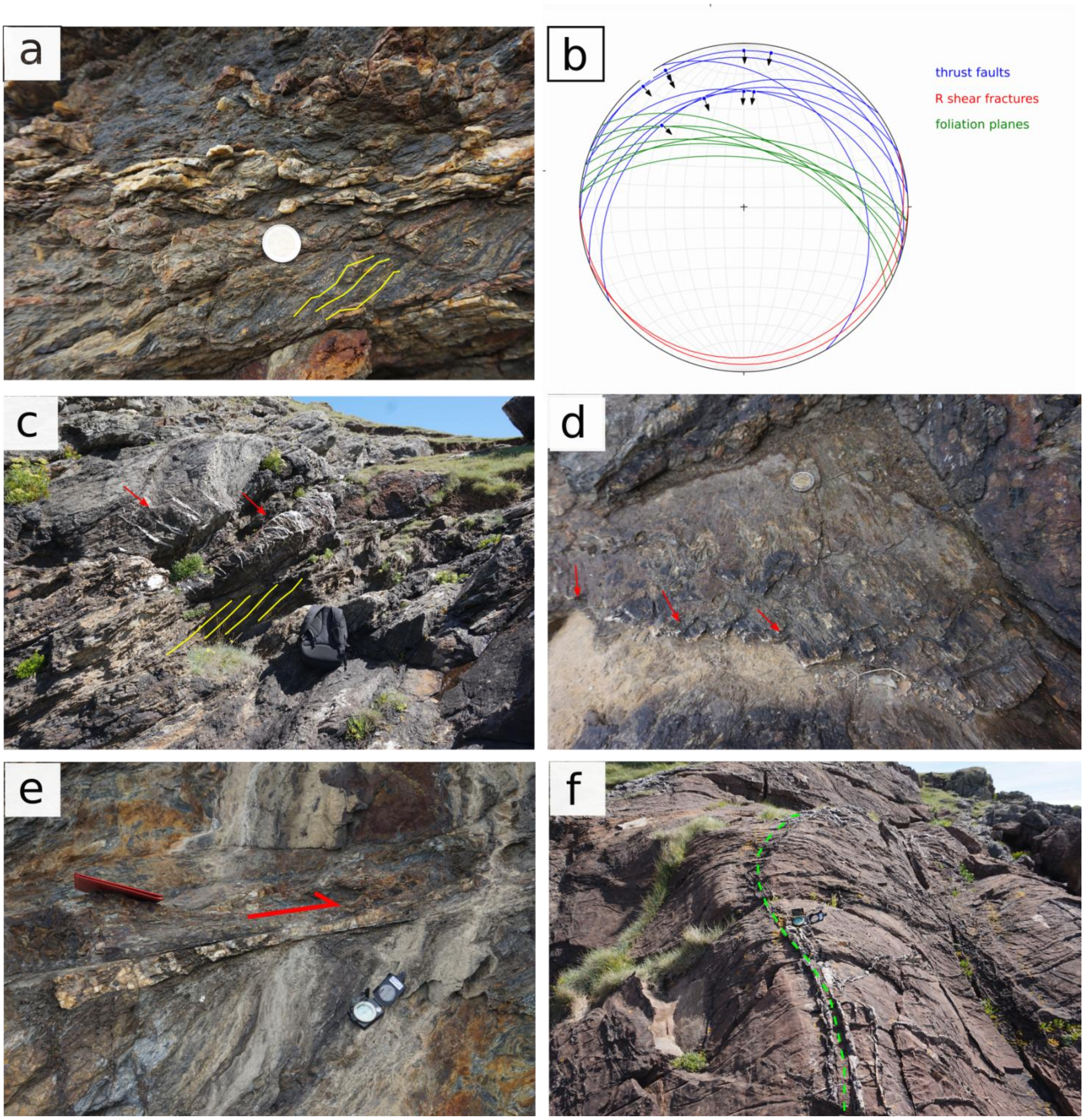

Figure 3.5. *Field pictures of the mesoscopic deformation structures. a) Deformed and partially dissolved quartz shear veins. Yellow lines indicate the orientation of the foliation in the black mudstone. b) Stereoplot of the main structural features. c) Extensional quartz veins in competent boudins, oriented perpendicular to the foliation. d) Scattered slickenfibres (red arrows show directions) on the upper surface of a quartz shear vein. e) Quartz crack-and-seal shear veins in a dilational jog along a thrust. f) Folding in the footwall dolostones, with extensional veins along hinges (green dashed line) and interconnected networks of quartz veins.*

3.a.2. Microstructures

From samples of the fault zone, 17 thin sections were obtained: 1 from the dolomite, 2 from a quartz-rich sandstone portion of the footwall turbidite, 2 from some vein-rich portions in the mudstone and the remaining from different points on the quartz veins coating the thrusts. The thin sections were carefully analyzed at the optical and scanning electron microscope, obtaining EDS data for selected regions. The most suitable quartz vein thin sections further underwent Electron BackScattered Diffraction (EBSD) analysis, to obtain information on quartz recrystallization from grain orientation maps (see paragraph 3.c.2), and a preliminary fluid inclusion microthermometry study, to put some constraints on the temperature range during quartz crystallization (see paragraph 3.c.1).

The dolomite at the base of the fault zone is cut by mm-scale extensional veins of both blocky dolomite and quartz. Cross-cutting relationships are mutual and the latest veins appear as dirty, darkened by a brownish/reddish infilling that penetrates also through the dolomite crystals (Fig. 3.6.a, b). The dolomite crystals in the wall rock are equigranular, with an average dimension of 100-200 μm. In patches, the grain size increases, reaching 0.5-1 mm, similar to crystals of the vein-filling dolomite (Fig. 3.6.b). Dolomite in the vein is associated to either dark brown material or quartz crystals, suggesting a possible interplay of the two through pressure solution processes.

The mélange mudstone hosting the thrusts is characterized by alternating mm-scale laminae, variable in colour, thickness and grain size (Fig. 3.6.f): more coarse silty or sandy intervals are lighter in colour (yellowish/grey) and contains small quartz grains, together with mica and chlorite, whose flaky crystals are especially developed next to quartz veins. Finer laminae are dark/red brown and contain no terrigenous clasts and carbonate minerals. A pressure-solution foliation has developed in the mudstone, at an angle of about 30°/45° to the main thrust faults (Fig. 3.6.f). The pressure solution seams defining the foliation plains are enriched in Fe and Mn oxides, opaque in plain and polarized light. They are anastomosed and deflected, wrapping hard indenters as vein edges or competent layers portions. The coarser intervals are variable in thickness, often boudinaged in clasts with lenticular shape (Fig. 3.6.e).

The hangingwall sandstone is very rich in quartz grains, quite rounded and ranging from 100 μm to 1 mm in average dimension. Also the sandstone is characterized by a lamination (1 mm to 1 cm in thickness) defined by the different abundances of quartz and the variation of its grain size (Fig.3.6.c). Also here pressure solution is developed, producing a foliation subparallel to the depositional lamination, and pressure-solution seams that penetrate between the quartz grains. High angle, up to subvertical fractures in coarser layers are filled with opaque Fe and Mn oxides and affected by dissolution at their intersection with foliation planes (Fig. 3.6.d).

The overall fault zone rocks can be defined, based on the mineral assemblage, as slightly metamorphosed, deformed under subgreenschist facies conditions (at a temperature lower than ~300°C).

The microstructure of quartz veins in the fault zone has been observed in detail. In the mudstone,

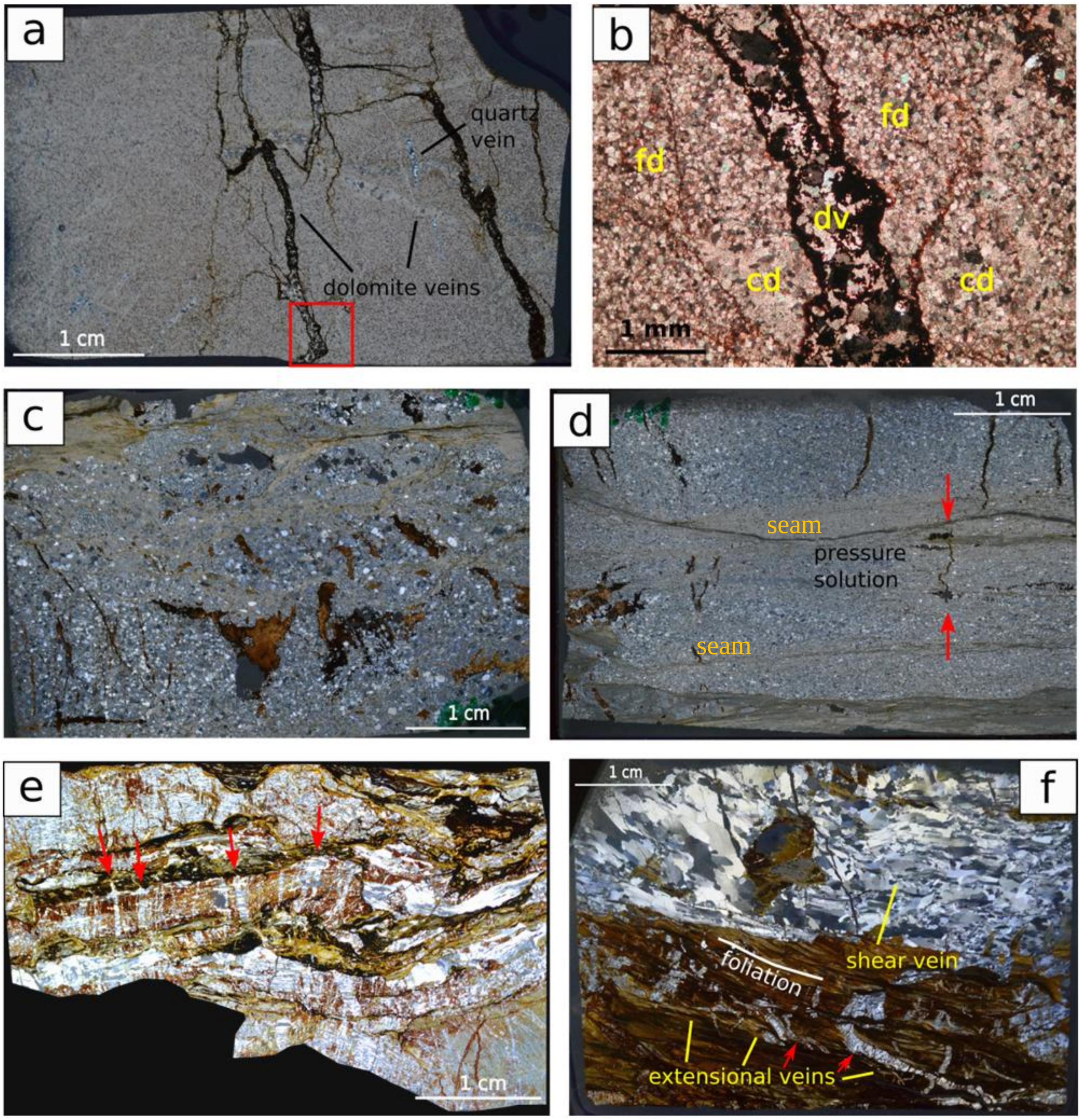

Figure 3.6. *Microstructures. a) Dolomite with extensional veins filled of quartz and coarse dolomite crystals. Red square encompasses photo (b) area. b) Close-up of the red square in (a), with a dolomite vein (dv) showing insoluble material penetrating through the crystals, the fine grained dolomite (fd) and patches of coarser grained dolomite (cd). c) Quartz-rich sandstone layer above mudstone hosting the thrust. d) Pressure solution seams parallel to alternating finer and coarser layers in the sandstone, with perpendicular fractures hosting insoluble material. e) Crack-and-seal extensional veining in the coarsest boudinaged layers of the mudstone. f) Extensional veins parallel and perpendicular to mudstone foliation, affected by pressure solution at the contact with foliation planes and cut by a crack-and-seal shear vein (see text). Red arrows point to extensional veins curved at 90°. All photographs are cross-polarized.*

series of short parallel extensional veins are developed, subperpendicular or subparallel to the foliation (Fig. 3.6.f). In some cases parallel and perpendicular veins correspond to a single bended vein (red arrows in Fig. 3.6.f). The texture of extensional veins is composed by 100-200 μm-thick crack-and-seal stretched crystals (following the definition of Oliver and Bons, 2001), perpendicular to the vein walls, but extensively affected by dissolution and dirty of insoluble material (Fig. 3.7.a). The veins have wavy interfaces with the wall rock and are dissolved at the contact with foliation planes and cut by the shear veins developed along one of the major thrusts (Fig. 3.6.f). These are crack-and-seal shear veins (Ramsay, 1980; Koehn and Passchier, 2000), with thickness ranging from 1 to 10 cm. They have scattered orientations, even on the same thrust surface, but a main dextral sense of shear, consistent with the mesoscale top-to-the-S transport direction, is inferred from the orientation of the crack-and-seal increments and inclusion bands (Fig. 3.7.b). Vein mineralization is always quartz. Crack-and-seal millimetric increments are well defined by fluid and solid (fragments of crystal boundaries and wall rock) inclusion trails, oriented at 70-80° to the vein edges (Fig. 3.7.b, d). Fe and Mn oxides are often found filling fractures parallel to the inclusion bands, or as thin seams penetrating at the boundaries between quartz crystals (Fig. 3.7.f).

Associated to quartz shear veins, there is chlorite: it crystallizes in thin veins (1 mm in thickness) between the shear veins or, more frequently, around quartz vein edges, at the contact with the wall rock. The chlorite crystals have a flaky aspect, blue in colour under crossed Nicols (Fig. 3.7.e). Quartz crystals in all veins show a certain amount of ductile deformation: undulose extinction (Fig. 3.7.b), deformation lamellae, often arranged in subperpendicular strands (Fig. 3.9.a, from upper left to lower right and Fig 3.9.b, subhorizontal), subgrains (Fig. 3.9.b-f) and grain boundary bulging (Fig. 3.9.c-f). In a few thin sections, smaller (<100 μm in diameter) quartz crystals can be seen in patches (Fig. 3.10.a, b) or along fractures inside the crack-and-seal crystals (Fig. 3.10.c, e, f). These fractures frequently exploit the weak planes of the deformation lamellae and often mismatch crystal boundaries, suggesting active shearing (Fig. 3.10.c).

Ductile deformation features are present in all quartz veins, but they are not equally distributed: extensional veins show a strong action of grain boundary bulging, producing irregular serrated vein margins and fiber boundaries (Fig. 3.10.d). Conversely, in the crack-and-seal shear veins, microtransforms delimit some portions that are much less affected by ductile features, their crystals showing only intra-crystalline deformation and limited recovery (Fig. 3.7), and other portions that present instead extensive grain boundary bulging, formations of subgrains and what can be interpreted as recrystallized grains (Fig. 3.10).

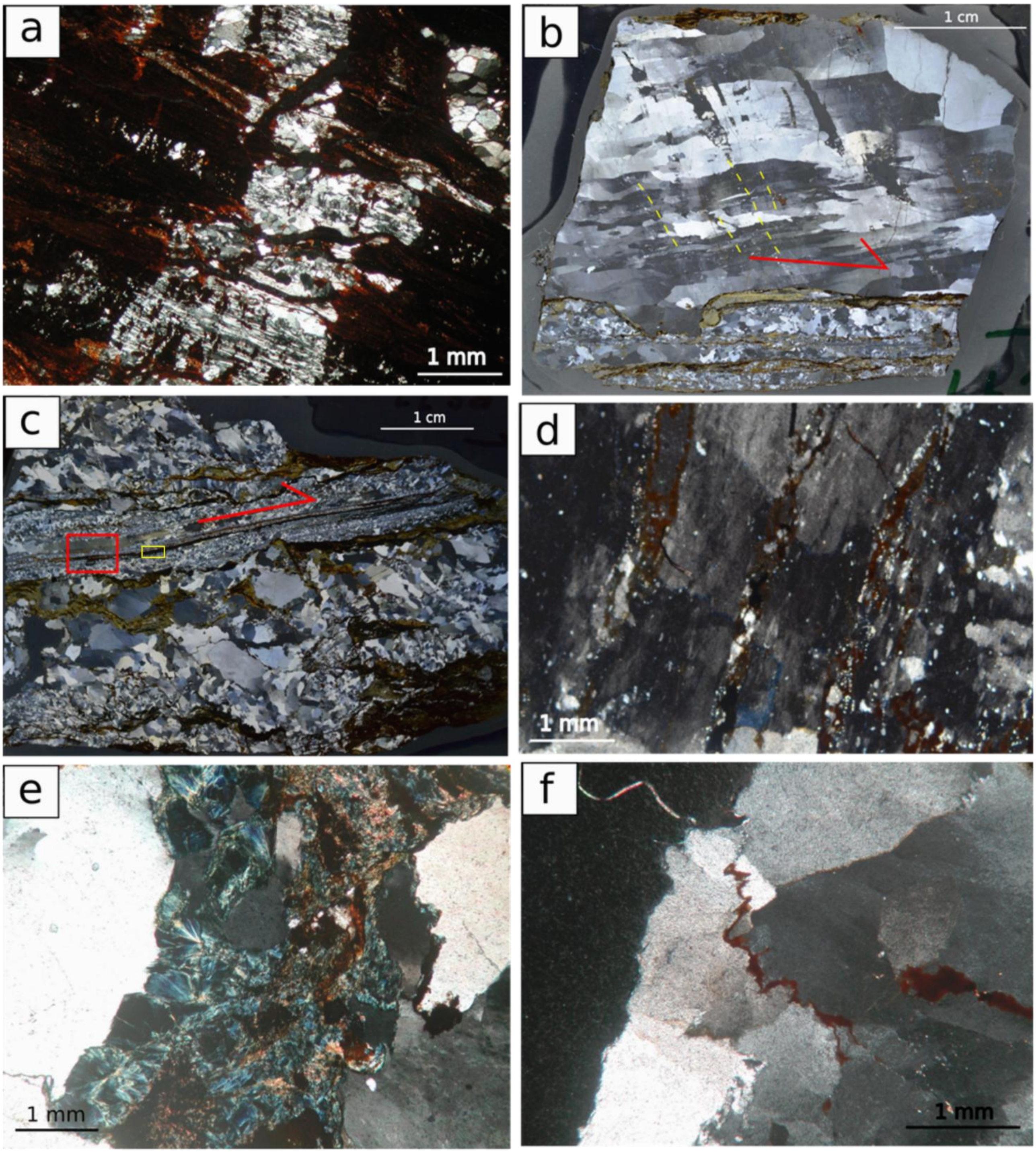

Figure 3.7. *Quartz microstructures in the crack-and-seal veins. a) Crack-and-seal extensional vein, affected by pressure solution at the contact with foliation planes. b) Fluid and solid inclusion trails (marked in yellow). Undulose extinction well visible in the elongated incremental crystals. The upper portion of the vein is less plastically deformed than the lower one. c) Very fine-grained quartz crystallized on shear planes in a crack-and-seal vein, see text for description. The red square marks the localization of the EBSD sample, the area in the yellow is the location of EDX analysis of Fig. 3.8. d) Quartz solid inclusions along trails and crystal fragments with insoluble material in fractures opened along the trails. e) Blue chlorite crystallized on the boundary of a crystal at the edge of a crack-and-seal shear vein. f) Fe and Mn oxides at the boundary between quartz crystals. All photographs are cross-polarized.*

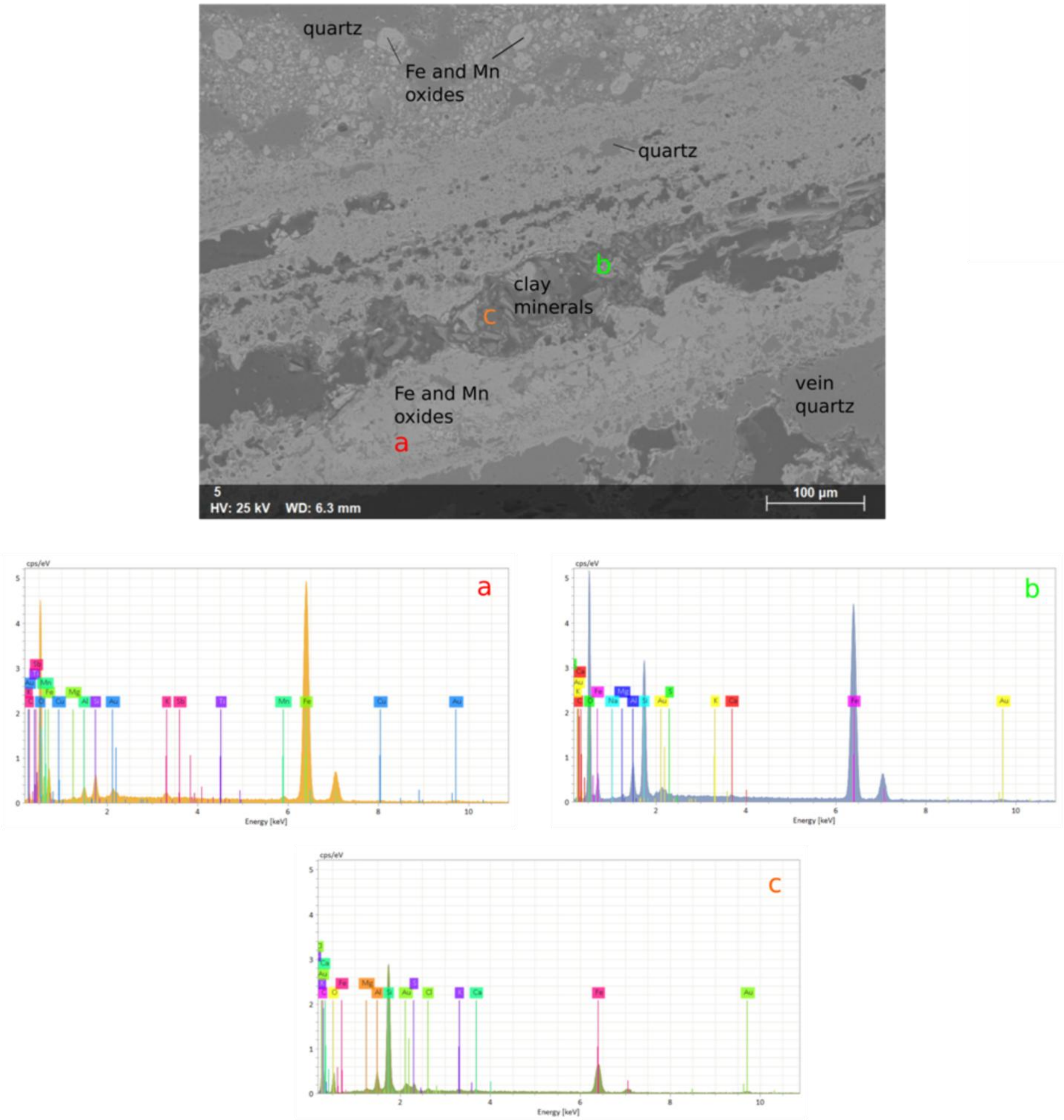

Figure 3.8. *Electron backscattered image of the area in the yellow box of Fig. 3.7.c, showing Fe and Mn oxides associated with clay minerals (mostly kaolinite and chlorite) alternating to quartz microcrystals strands. Blocky crystals of Fe and Mn oxides are also found inside the quartz strands (top of the photograph). EDX spectra for a, b, c points are shown (the presence of Au is due to gold coating).*

Section 3.b. Fluid inclusion microthermometry and EBSD analysis

3.b.1. Fluid inclusion microthermometry

The upper veins in Fig. 3.7.b, where the crack-and-seal-increments are well preserved and appear not particularly affected by ductile deformation, were suitable to put a lower limit on the temperature value of crack-and-seal veins formation and observe if and how this has varied in the lower, more deformed veins.

Following the basic principles of a fluid inclusion study for microthermometry (Goldstein and Reynolds, 1994), the most suitable FIAs (Fluid Inclusion Assemblages) of two-phase gas/liquid fluid inclusions were selected, for instance all the fluid inclusions aligned on a single inclusion band in the crack-and-seal veins. Each FIA was then subjected to repeated heating runs, with the aim to obtain the homogenization temperature (Th) value. This is defined as the temperature at which, during heating, the gas bubble (see Fig. 3.11.c) disappears and the whole inclusion becomes a single homogeneous liquid phase. It corresponds to the minimum estimated temperature of entrapment of the fluid inclusion.

In the studied thin sections, fluid inclusions were well developed in vein quartz, with mean size around 5 microns. They were two-phase aqueous inclusions, with somewhat consistent gas/liquid ratios (Fig. 3.11.c). Total 34 FIAs in the studied thin sections gave reliable data, other were discarded because of the uncertain appearing/disappearing point of the gas bubbles during cooling/heating stages. In fact, freezing runs were performed to obtain values for the final melting temperature of ice Tm and, in this way, assess the composition and salinity of the inclusions, but it was difficult to see any shrinking or sudden change in position of the bubbles during re-heating of the frozen inclusions, so no useful data were obtained. The lack of this information, as well as of an independent constraint for pressure, resulted in the impossibility to obtain the real temperature of entrapment of the fluid inclusions in the crack-and-seal vein, e. g. the temperature of formation of the shear veins themselves. For all these reasons, and since the quality of the fluid inclusion microthermometry results highly depends on the experience of the operator, the following data and their interpretation (see Section 3.c) are a very preliminary contribute, that hopefully could be improved and refined in future.

In the less deformed crack-and seal shear vein, FIAs were: i) aligned on shear inclusion bands, and these should be primary inclusions, formed with the relative crack-and-seal increments; ii) inside the crystals, where they could be either primary, or secondary on healed microfractures: some had indeed negative crystal shapes suggesting necking-down, that is the process of dissolution and reprecipitation of the host mineral at crack interfaces to reduce the surface free energy (Goldstein and Reynolds, 1994).

Anyway, both types of inclusion in the crack-and-seal veins yield pretty consistently a Th value of 160°C (Fig. 3.11.a, b, d), indicating the same minimum T value for the formation of the crack-and-seal increments and the microcracking in crystals.

In the most deformed veins in the lower part of the thin sections, there are very spare fluid inclusion assemblages suitable to be measured, and this is consistent with the extent of ductile deformation, that could be responsible for the decrepitation of most of them. Fluid inclusions still preserved in the samples yield a mean Th value of 270°C (Fig. 3.11a, b, d).

3.b.2. EBSD analysis

Fig. 3.7.c shows a crack-and-seal shear vein cut by another sharp shear zone, about 1 cm-thick and with the appearance of a shear vein, formed by multiple parallel strands of quartz grains. These crystals in places retain what seems to be a former crack-and-seal structure (elongated quartz crystals as in Fig. 3.10.e, f), but more frequently are very fine grained crystals, up to submillimetric ones not visible at the optical microscope (Fig. 3.10.f, yellow lines). The microcrystalline strands in places are encompassed between sharp boundaries, appearing as flat crystal margins or fracture surfaces (Fig. 3.10.e); in other cases, strands are less continuous, they are segments that form elongated patches of micrograins with more irregular, wavy boundaries with larger quartz crystals (Fig. 3.10.b). Dark brown material is accumulated in sharp submillimetric layers alternated to quartz crystals strands, but is also present inside the quartz grains (Fig. 3.10.e). At higher magnification, up to 50 μm sized Fe oxide cubic crystals are visible, identified as Fe and Mn oxides (Fig. 3.9). These crystals could be responsible for the squared blocky appearance of some brown dark inclusions inside the quartz microcrystal strands.
A 3 x 2,5 mm region of these sample (Fig. 3.10.f) has been analyzed with the electron backscattered diffraction (EBSD). Electron backscattered diffraction (EBSD) is a SEM–based microstructural-crystallographic characterization technique commonly used in the study of crystalline or polycrystalline materials. Captured patterns can be used to determine grain morphology, crystallographic orientation and chemistry of present phases, which provide complete characterization of microstructure and strong correlation to both properties and performance of materials. EBSD patterns are obtained by focusing electron beam on a crystalline sample. The sample is tilted to approximately 70 degrees with respect to the horizontal, and in this way more electrons can be scattered and escape towards the detector. The electrons disperse beneath the surface, subsequently diffracting among the crystallographic planes. The diffracted electrons with constructive interference produce a pattern composed of intersecting bands which, properly indexed, can be converted in mappable orientation data (Stojakovic, 2012). Data obtained were processed with MTEX for MATLAB to obtain a map of the quartz crystals orientations, reported in Fig. 3.11. Here, colours vary with the orientations of quartz c-axis [0001]: red indicates a strong preferred orientation parallel to the x direction of the sample (that is, the horizontal margin of the figure). It is clearly visible that the elongated quartz

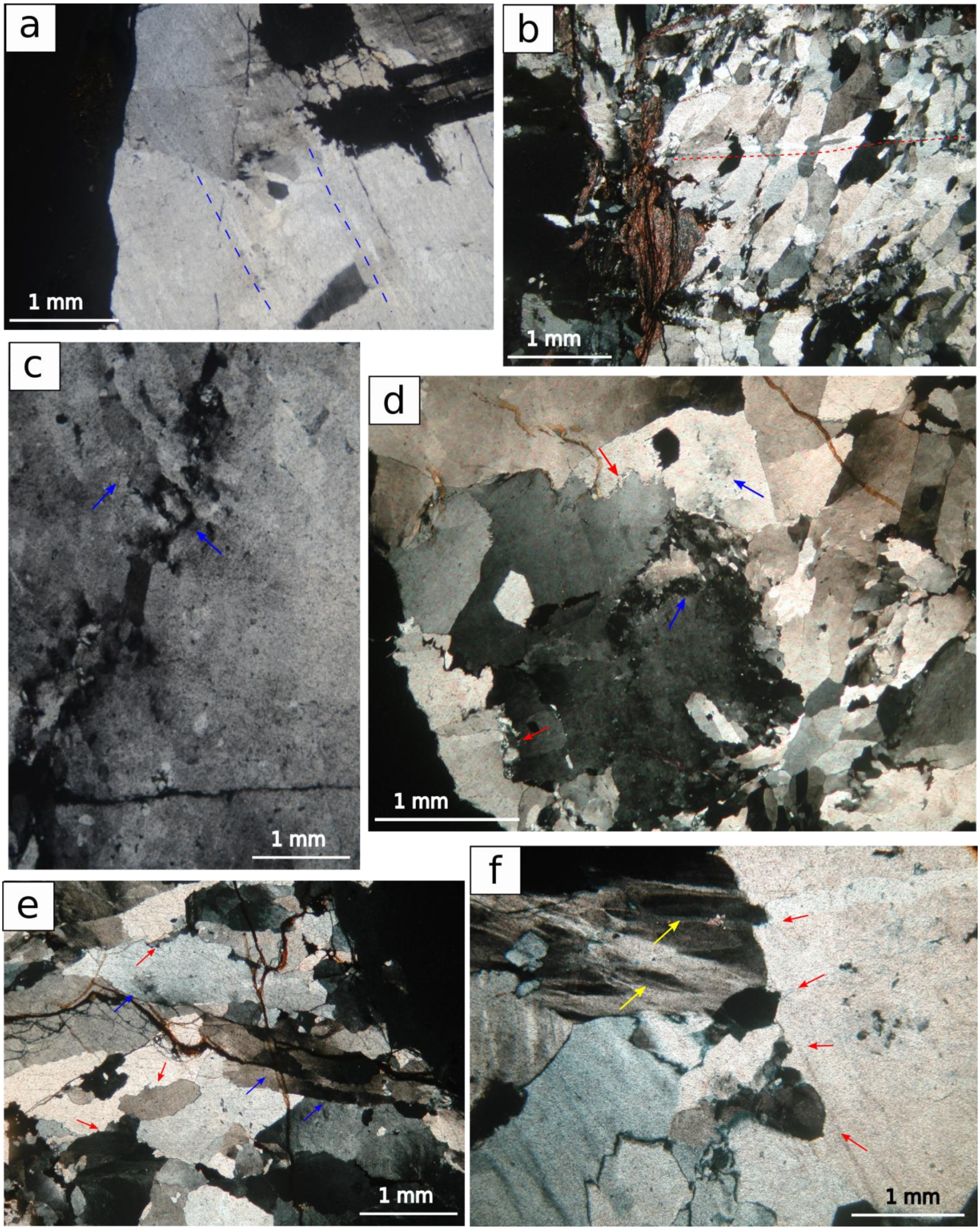

Figure 3.9. *Intra-crystalline deformation in vein quartz crystals. a) and b) Deformation lamellae (trend marked by blue and red line, a) comes from the upper less deformed vein in Fig. 3.7.b. c) Subgrains marked by blue arrows, particulars of the upper vein in Fig. 3.7.b; d), e) and f) Enlargements of portions of the lower more deformed veins of Fig. 3.7.b, where d) extensive formation of subgrains (blue arrows) and grain boundary bulging (red arrows) up to the formation of new grains; e) and f) grain boundary bulging (red arrows) and subgrains (blue and yellow arrows). All photographs are cross-polarized.*

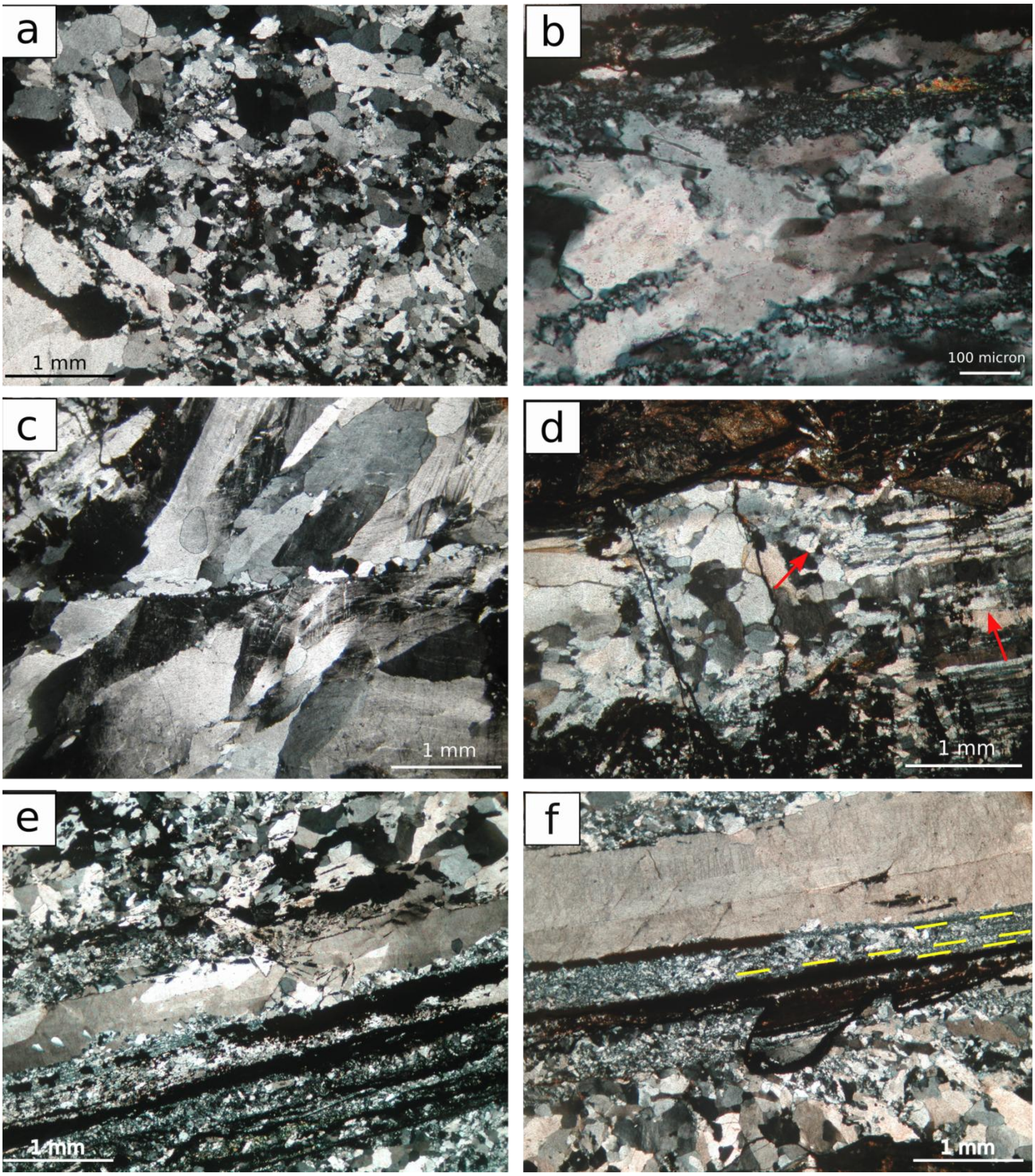

Figure 3.10. *a) and b) Crack-and-seal shear vein showing patches of recrystallized grains. c) Strand of small grains crystallized on a fracture surface developed on a weakness plane. The crack-and-seal crystals are firstly bent by deformation lamellae and then sheared to the right, as indicated by the mismatch of the crystal boundaries from one fracture side to the other; d) Partial recrystallization of an extensional vein (to the right), see serrated vein margins and crystal boundaries. e) Close-up of a portion of the EBSD sample (from the thin sections of Fig. 3.7c), showing brecciation (centre of the figure) and fracturing parallel to the shear direction (to the right) in the crack-and-seal crystals, with quartz micrograins and iron oxides. f) Another close-up of Fig. 3.7.c (the EBSD sample), showing strands of aligned crystals (yellow dashed lines) reaching very small sizes, not visible at the optical microscope, and pressure solution affecting them.*

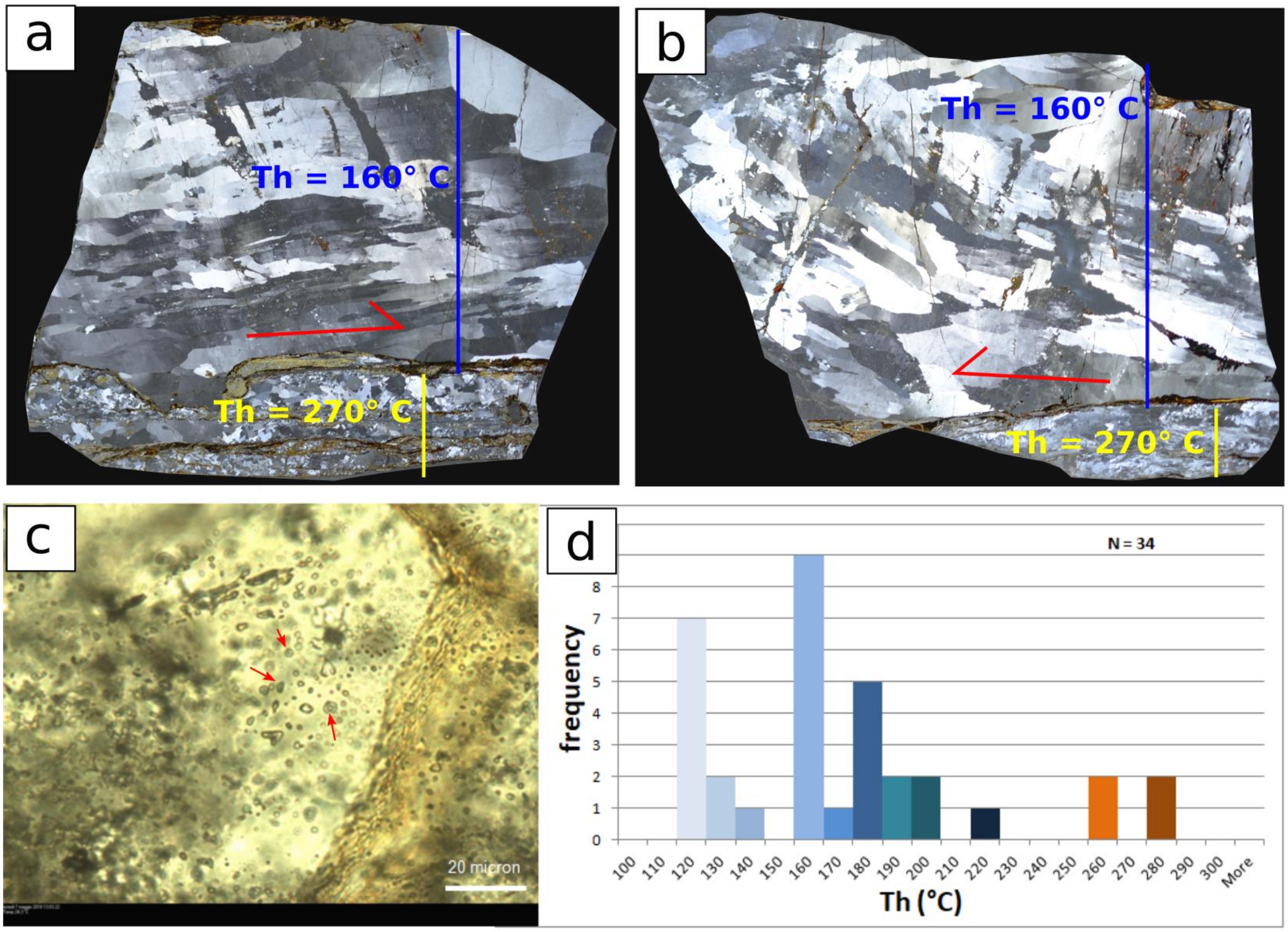

Figure 3.11. *Fluid inclusion microthermometry data. a) and b) Thin sections LL1a and LL1b, cut from samples of the same crack-and-seal shear vein, showing a different mean value of Th in different portions of the veins; c) A small fluid inclusion assemblage in crack-and-seal crystals; d) Frequency histogram of Th distributions.*

crystals are characterized by a quite uniform red colour, that corresponds to a fairly constant horizontal orientation, while the microcrystals show a great variability in colour and consequently in orientation.

Section 3.c. Interpretation of the structural data

The studied fault zone is interpretable as a portion of the Gwna Group subduction tectonic mélange, where the shear deformation is concentrated in the black mudstone level.

The dolostone at the base of the fault zone have a very complex network of quartz, which has no specific relation to the shear direction. Dolomitization of a previous protolith is inferred from the sparse quartz grain relicts, dark brown seams found through the crystal and in the veins, which could represent the insoluble selvage of the Mg-rich fluid that caused dolomitization.

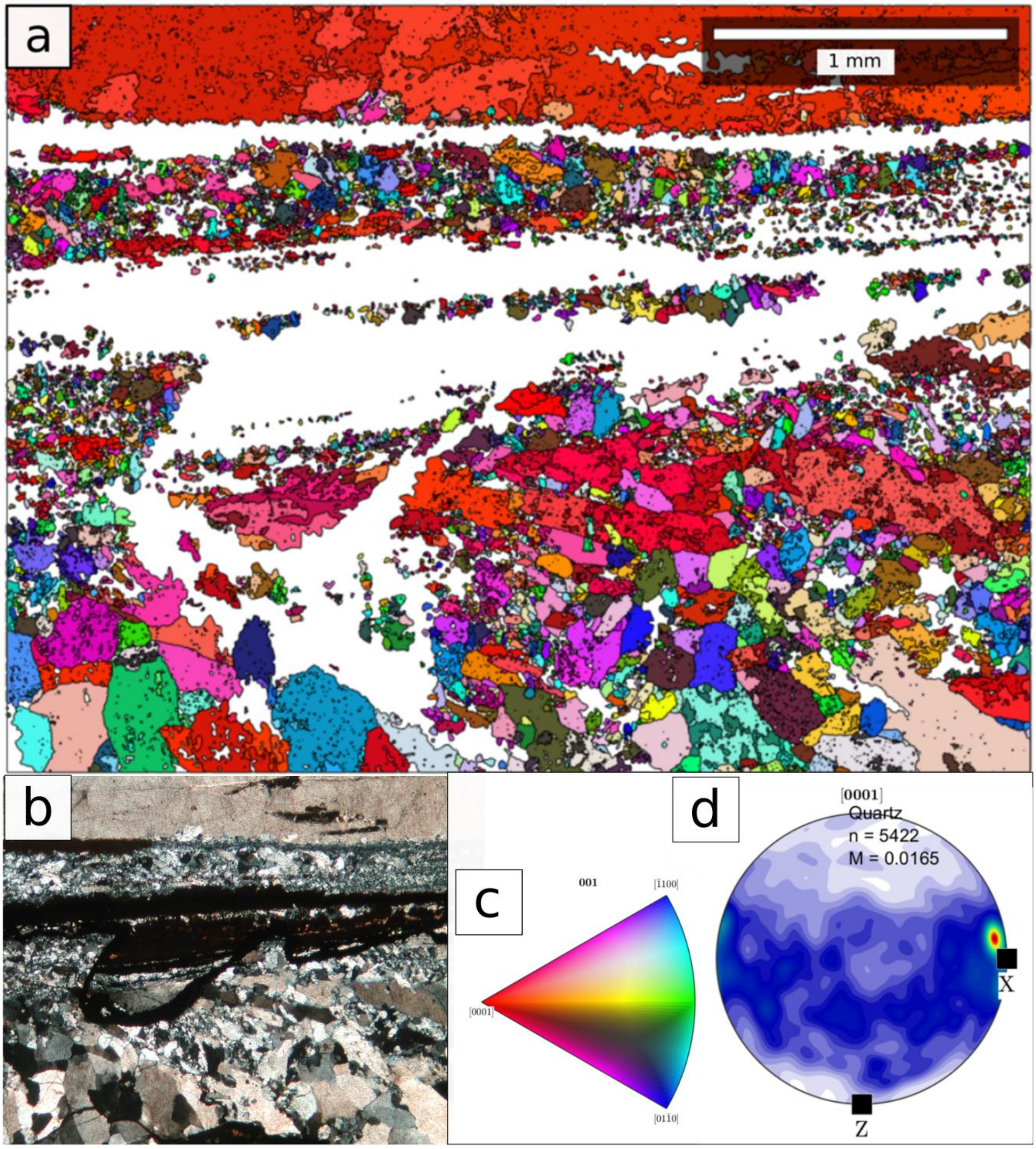

Figure 3.12. *EBSD data for the thin section sample of Fig. 3.9f, shear direction to the right. a) Orientation map of quartz crystals; b) cross-polarized micrograph of the mapped area; b) Inverse pole figure color key; c) Pole figure showing a c-axis CPO only for a small cluster of crystals, the crack-and-seal ones.*

The two different ranges of grain size in wall rock and dolomite veins suggest at least two distinct phases of dolomitization: one producing the wall rock dolomite, and, subsequently, another one responsible for the vein filling and the coarser-grained cement in the patches (that should be also limestone remnants of the firs process of dolomitization, recrystallized during this second stage).

Since vein orientations are not clearly related to shear and since they are cut by one of the main thrusts at the contact with the mudstone, vein forming processes, included dolomitization, should precede the phase of shear deformation.

The slightly deformed aspect of the sandstone above the mudstone level reflects merely layer-parallel shortening, with interplay between pressure solution perpendicular to the sedimentary lamination and high angle fractures. No asymmetric structures suggesting a shear component are developed.

The mudstone represents the weakest level, thus accommodating the most of shear strain. Merging meso- and microstructural data, the deformation sequences related to shear deformation can be reconstructed as following:

- *Syn-lithification phase.* A first step where compaction prevailed on not completely lithified sediment is testified by the pinch-and-swell boudinage of more competent strata of chert and quartz-rich sandstone, producing lenticular blocks by soft sediment particulate flow. These subsequently underwent progressive lithification faster than the surrounding mudstone, being subjected to extensional fracturing and veining. The weaker mudstone matrix deformed by dissolution-precipitation process, forming the pressure solution foliation bounding and wrapping the blocks, with the mean direction of the planes perpendicular to the extensional veins in the blocks. To this phase probably belong also the thin extensional veins developed in the mudstone, both parallel and perpendicular to foliation (Fig. 3.6.f): their irregular margins suggest a not complete lithification of the wall rock and their being dissolved along surfaces parallel to the host rock foliation planes indicates that pressure solution was still active in the matrix after their formation.

Dissolution-precipitation processes could indeed have represented the source of material for the formation of the veins, either perpendicular to σ_1 (veins perpendicular to foliation) or along the discontinuities represented by foliation planes, provided that sufficient overpressure of the fluid phase has been reached to locally overcome σ_1. This can easily occur in impermeable fine-grained mudstone, especially if the differential stress ($\sigma_1 - \sigma_3$) is low. Nevertheless, a shifting of the σ_1 orientation, like that invoked to explain similar structures in other fossil subduction margins (see Chapter 2), is unlikely: indeed, in places the veins are curved at 90° (Fig. 3.6.f), showing portions both parallel and perpendicular to the foliation planes, and no crosscutting between veins with different orientations has been observed. The simplest explanation is that, in presence of low differential stress, veins initially formed parallel to a high angle σ_1, i.e. perpendicular to foliation. Then, following fluid pressure pulses that temporarily overcame σ_1, veins changed direction exploiting the voids between foliation planes.

- *Post-lithification phase*. When the whole fault zone gained a sufficient coherence, brittle mechanisms were activated and thrust faults developed in the weakest fine grained mudstones, at the contact with rigid boudins, together with associated Riedel shear fractures.

Thrust faults, coated by veins, based on geometric relations with pressure solution foliation and extensional veins in the blocks, were oriented at ~45° to σ_1 (Fig. 3.5.b). The crack-and-seal texture of the veins is characteristic of incremental growth in hybrid shear-extensional fractures, by small steps of coupled slip and dilation along the plane, with the opening of small dilational jogs in which the fluid crystallizes (Ramsay, 1980; Koehn and Passchier, 2000). 45° to σ_1 is a slightly bad orientation for the formation of the hybrid-shear extensional fractures. Based on the Mohr-Coulomb failure criterion, 45° to σ_1 is the theoretical upper bound for the orientation of shear fractures, extensional fractures form parallel to σ_1 and hybrid-shear fractures should form at an intermediate angle, typically around 10° (Ramsay and Chester, 2004). It is possible that Llŷn thrusts have been weakened, by both the low friction coefficient of the muddy wall rock and/or fluid overpressures developed along the thrust interfaces, so allowing dilatant shear even at 45° to σ_1. Weakness of the thrust is further implied by the high-angle σ_1 at which crack-and-seal dilatant openings should have formed, ~60° to 80° to the thrusts as inferred from the orientation of wall rock inclusion bands. The crack-and-seal veins cut all the extensional veins, which then can be restricted to the syn-lithification phase.

The crystal-plastic deformation features found in quartz veins may at first sight suggest the onset of a third phase, with an increase in temperature allowing the transition from brittle to ductile deformation. The undulose extinction and the perpendicular sets of deformation lamellae suggest intracrystalline mechanisms active in the crack-and-seal crystals, while a partial recovery is indicated by the presence of subgrains and grain boundary bulging (Passchier and Trouw, 2005). The quartz grains found in patches between the crack-and-seal crystals, and in strands along microfractures, would be interpretable as the product of dynamic bulging recrystallization. The extensively deformed extensional veins, older than the shear ones, may have stored more strain and lattice defects during time and so they could have been even more prone to plastic deformation.
Recrystallization by localized grain boundary migration (referred to as "bulging recrystallization") consists in displacement of the atoms on the boundaries between crystals. They move from crystals with high dislocation density to fit in the lattice of crystals with low dislocation density, resulting in progressive bulging of the boundaries in the more deformed crystals up to the formation of new independent strain-free crystals (Tullis and Yund, 1985; Stipp et al., 2002; Passchier and Trouw, 2005). Stipp et al. (2002) stated that recovery and dynamic bulging recrystallization in naturally de-

formed quartz are dominant above 280° ± 30, marking the frictional-viscous transition (from cataclasite to mylonite). This would be concordant with the minimum estimate of the maximum temperature registered by fluid inclusions in the veins, which is the 270°C value of homogenization temperature found through the fluid inclusion microthermometry. The 160°C Th value registered by fluid inclusions of the other crack-and-seal veins could simply refer to the minimum temperature of vein crystallization and formation of the inclusions, which would have not been re-equilibrated later to the higher temperature of the ductile deformation phase. What the Th data would suggest is that shear veins formed during a brittle phase at a minimum T of 160 °C and then experienced a phase of higher T deformation, with a minimum value of 270 °C, registered in some inclusions that re-equilibrated.

Nevertheless, there are evidences that contrast with this model of a deformation phase at higher temperature. First of all, the fact that the ductile deformation features are not equally distributed in all the veins and in particular they are unevenly present in the different crack-and-seal shear veins superimposing along microtransforms on the same thrust. Younger portions of the veins overlapping older ones are much less deformed in a ductile way (Fig. 3.11.a and b). In other words, what microstructures seem to suggest is that the action of ductile deformation mechanisms has not been constant through time, but rather intermittent.

Moreover, the results of the EBSD analysis indicate that quartz recrystallization might be much less developed than how inferred based on observations at the optical microscope. It is generally accepted that dynamic recrystallization leads to grain-size reduction and consequent strain localization (Drury, 2005; Stipp et al., 2002; Tullis and Yund, 1985; Xia and Platt, 2018). Considering this, the analyzed sample could be easily interpreted as a mylonitic shear zone, where recrystallization in the crack-and-seal shear veins should have produced low grain size quartz, which in turn has localized strain along the shear microtransforms. The spots of dark material between or inside the grains would be relicts of microtransform layers, incorporated by new grains during recrystallization.

Anyway, if the strands of quartz microcrystals were the product of dynamic recrystallization, they should have developed a lattice preferred orientation, caused by the dislocation creep along one or more quartz crystal slip plane (Passchier and Trouw, 2005). The EBSD data (Fig. 3.12) show that quartz microcrystals have a random crystallographic orientation, in contrast with the slightly similar orientations of the residual crack-and-seal crystals (in shades of red in the map), elongated subparallel or at low angle to the shear direction. This suggests microcrystals are not dynamically recrystallized, but rather newly formed.

New grains can be produced by different processes such as cataclasis, static recrystallization or precipitation from a fluid phase in low-stress regions.

Cataclasis, i. e. the mechanical fragmentation accompanying brittle shear, would explain the, brecciation and fracturing in the crack-and-seal crystals, the wide range of grain size of the new crystals and their random orientations, but it would hardly justify the micrograins encompassed between shear surfaces marked by iron oxides, rather than a fragments-in-matrix texture. Cataclasis is facilitated by high fluid pressures but requires a non dilatant shear. In Llŷn shear zone, σ_1 is unfavourably oriented for dilation, but crack-and-seal hybrid dilatants shear veins are nevertheless present, and suggest faults are weak (see above). Cataclasis is a process that generally requires high differential stress and high strain rates (Passchier and Trouw, 2005), while extension veins in the fault zone suggest that at the time of their formation the differential stress was low (see above). Therefore, cataclasis seems not to be the most favoured grain-size reducing process active in the fault zone.

Static recrystallization can be excluded. The process would continue to promote the recrystallization also after deformation has ceased (decelerated or stopped), to minimize the internal free energy of the crystals (Passchier and Trouw, 2005). Being a recrystallization process, it should produce a preferred orientation in the new quartz grains, therefore it does not fit to the random-oriented pattern of the EBSD analysis.

The third mechanism of microcrystal formation could be the precipitation from a Si-enriched fluid phase originated by pressure solution process. This would be concordant with the presence of iron oxides, residual relative to dissolution. The process would need an intergranular fluid phase, as easily suggested also by the presence of fluid inclusions, and low stress regions, where quartz could precipitate. These could be represented by the microtransforms bounding the crack-and-seal shear veins, since shear has a dilatant component that can create space for the microcrystals to grow and produce the final texture of quartz grains arranged in parallel strands. Dissolution-reprecipitation processes operate at low strain rates.

Summarizing, dissolution-reprecipitation mechanisms, in conditions of relatively low temperature, presence of fluids and varying strain rate, could have produced the randomly-oriented quartz microcrystals analyzed with the EBSD technique.

If this interpretation is correct, the extent of ductile deformation of quartz in Lleyn shear veins is actually less than initially inferred. Nevertheless, the unambiguous presence of grain boundary bulging and subgrains in the most deformed parts of the veins suggests that at least incipient recrystallization was taking place there, as, for instance, in the small patches of grains between crystals in Fig. 3.9b. Once again, different parts of the crack-and-seal shear veins on the same thrust surface show
3.9b. Once again, different parts of the crack-and-seal shear veins on the same thrust surface show
an inhomogeneous distribution of the ductile deformation features.

A possible interpretation is that the conditions of the fault zone have changed cyclically from brittle to ductile, so as to produce the observed mutual overprinting between crystallization in fractures and quartz plastic deformation. These repeated variations cannot be explained through a fluctuation of the temperature, which of course must increase monotonically as the shear deformation increases. The repeated shifting between brittle and ductile mechanisms must have happened at a constant value of temperature, likely corresponding to the 270° (minimum estimate) of the microthermometry study.

Brittle-ductile cycling is probably best explained by strain rate variations and overpressured fluid pulses promoting repeated transient embrittlement. At low strain rate, the presence of fluid promoted hydrolitic weakening (Griggs, 1967) in vein crystals, thus facilitating the onset of low temperature (< 300°C) quartz plasticity in high dislocation density regions, for instance older extensional or shear veins that have had much time to accumulate crystal lattice strain. At the same time, the matrix experienced distributed shear deformation by dominant dissolution-precipitation creep (Fagereng, 2011). At higher strain rate, deformation localized in thin shear zones where fluid overpressures counteracted the principal stress, allowing dilatant fracturing to occur more easily and producing new shear veins.

Such a deformation model would take in account the crosscutting relationship observed in Llŷn shear zone, together with the evidences of an active circulation of fluid during deformation represented by veins crystallized in fault-fracture meshes and fluid inclusions in the vein quartz. The transient embrittlement characterizing Llŷn shear zone has not been observed, by now, in other outcrops of the Gwna Group, for example in the already cited Llanddwyn Island (see paragraph 3.1), where shear deformation structures appear to be mostly ductile, probably due to creep at slow strain rate (and at temperatures similar to that in Llŷn, as inferred from petrography). In Llanddwyn outcrop, veins are spare and not continuous, and there are not well developed evidences of fluid circulation. This is another element pointing out for fluids as responsible for the discontinuous brittle deformation characterizing Llŷn shear zone.

Variations in strain rate could also contribute to suggest another different explanation to the shear zone analyzed with the EBSD. Trepmann et al. studied experimental (Trepmann et al., 2007; Trepmann and Stöckhert, 2013) and natural (Trepmann et al., 2017) samples of vein quartz deformed at lower greenschist facies conditions correspondent to the brittle-viscous transition. In particular, the natural samples were taken from two different shear zones in the Alps where a probable active seismicity has been documented by pseudotachylyte occurrences. What Trepmann et al. found is that microfabrics from both shear zones record a switch from low-temperature plasticity (high dislocation density revealed by TEM analysis and correspondent to short-wavelength undulose extinction, see Trepmann et al., 2017) at transient high stress to recrystallization (by subgrain rotation and strain-induced grain boundary migration) at relaxing stresses. What is different between the two shear zones is the microfabrics of the new grains developed by recrystallization and this is attributed to a different relaxation rate, after the transient peak stress: for the first shear zone, relaxation is rapid, the stress becomes suddenly low and new grains develop strain-free and randomly oriented; for the second shear zone, relaxation is slower, thus allowing the new grains to form while the stress is still higher enough to promote dislocation glide and develop a CPO.

Since the P-T conditions and the geological context are similar, it is reasonable to attribute to Lleyn EBSD sample microfabric the same explanation given by Trepmann et al. (2017) to their first shear zone sample: after brittle fracturing at transient peak stress, and provided that the stress falls rapidly to low values, shear deformation in Llŷn veins could have also been promoted by dynamic recrystallization in localized high-strain areas developed during the low-temperature plasticity enhanced by hydrolitic weakening at slow strain rate (Fig 3.13).

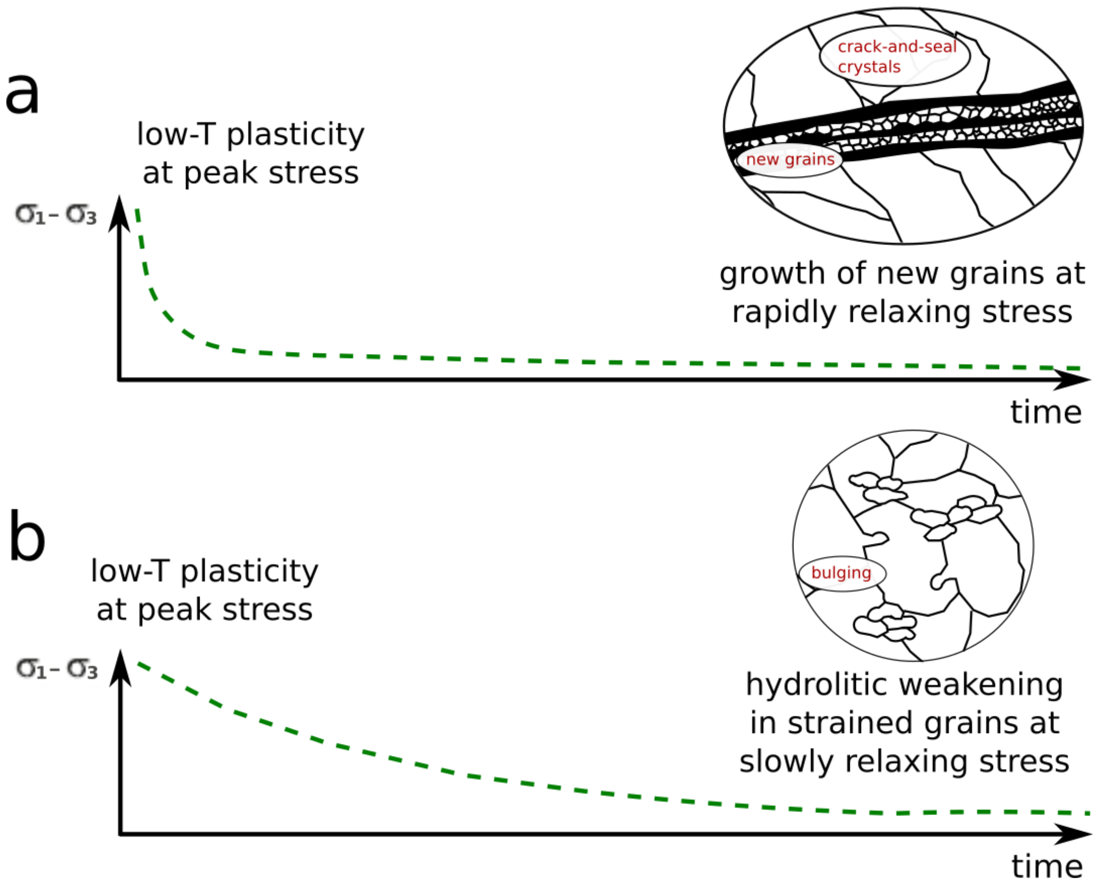

Figure 3.13. *Schematic sketch depicting formation of new grains in quartz crystals after low temperature plasticity at transient peak stresses during (a) fast stress relaxation, with precipiatation of randomly oriented new grains in dilatants fractures, and (b) slow stress relaxation, with hydrolitic weakening promoting bulging and incipient recrystallization at grain boundaries. Redrawn and modified from Trepmann et al., (2017).*

Chapter 4. The Nankai active subduction megathrust

This Chapter reviews some of the most recent findings about one of the better studied active plate boundaries: the Nankai subduction zone megathrust, off southwesternern Japan. First, a brief account will be given of the multistage IODP Nankai Trough Seismogenic Zone Experiment (NanTroSEIZE) Drilling Project, which has been investigating for 12 years the Nankai subduction margin. Following, the main outcomes of the Core-Log-Seismic-Investigation at Sea Workshop, held onboard IODP Expedition 380 NanTroSEIZE Stage 3: Frontal Thrust LTBMS in January and February 2018, will be described.

The workshop allowed an international team of young early-career scientists to directly examine and sample cores drilled in previous NanTroSEIZE project stages and to review the state-of-the-art knowledge about Nankai subduction margin, publishing the workshop findings in Cerchiari et al. (2018). Some of the main elements are reported here, with particular reference to data useful for a comparison with megathrust fossil analogues, such as observed deformation microstructures, the measured or inferred fluid pressures, permeability and state of stress on the plate boundary at different depths.

4.1. Deep ocean drilling and the NanTroSEIZE Project

Scientific ocean drilling is a fundamental tool in contributing to understand earthquake and faulting processes through direct sampling and in situ measurement within active systems, including continuous real-time surveys. Core drilling is essential not only to sample materials for analyses and experiments, but also to provide access to the subseafloor, and allow borehole observatories to be installed. These instruments continuously monitor strain, pore fluid pressure, composition and temperature and enable small earthquakes and transients to be resolved in great detail. They represent one of the advances in deciphering processes controlling the initiation and triggering of fault slip and slope failures, identify potential precursory phenomena, understand slip dynamics and post-failure recovery. Borehole measurements are fundamental in acquiring high-resolution spectra of fault slip behaviors and determine where strain accumulation occurs during the interseismic period.

Observatories are especially developed at particular sites, where transients are likely to be observed, such as fault zones approaching rupture, or faults that have recently failed and are regaining strength. One of the main characteristics of these long-term borehole observatories is the potential for directly investigating fluid circulation in subduction zones. Designed techniques include cross-hole hydrogeologic testing and injection of multiple tracers from a central borehole. In parallel, pressure and temperature conditions are monitored and sampling is carried out in surrounding bore-holes distributed in multiple directions and distances (Fisher et al., 2011). Borehole measurements during active drilling or from long-term observatories acquired by now have revealed links between fluid composition and transient flow rates, suggesting a coupling between hydrology and strain from earthquake events.

Single borehole monitoring systems are linked to cabled seafloor networks, which provide instant access to data, allowing real-time assessment and updating of the survey. One important example is the Dense Ocean Floor Network for Earthquakes and Tsunamis (DONET) (Kaneda, 2014). It is a submarine cabled real-time seafloor observatory network for the precise earthquake and tsunami monitoring through 20 sets of 15-20 km-spaced interfaces, which are currently under deployment off SW Japan at the Nankai subduction zone, as part of the Integrated Ocean Drilling Program (IODP) NanTroSEIZE Project.

The Integrated Ocean Drilling Program (IODP) Nankai Trough Seismogenic Zone Experiment (NanTroSEIZE) is a multiyear project that, since 2007, has involved total 13 expeditions in three stages. Deep drilling operations have been designed to sample and instrument the plate boundary system and have yet been conducted at 22 sites, for a total of 68 holes, off-shore the Kii Peninsula in SW Japan (Fig. 4.1) (Kinoshita et al., 2009). The main objective is to investigate outstanding scientific questions such as, among the many, the processes of earthquake, tsunami, and slow slip generation, the mechanics of strain accumulation and release, and the absolute mechanical strength of the plate boundary fault. Furthermore, a particular primary exploration target is the so-called "megasplay" fault (Fig. 4.1), an out-of-sequence thrust (OOST) which branch from the megathrust and cuts through the accretionary prism, and which represents a source of information about the potential role of a major upper plate fault system in seismogenesis and tsunamigenesis (Expedition 348 Scientists and Scientific Participants, 2014; Kopf et al., 2017).

4.2. The Nankai plate boundary and megasplay investigation

The Nankai Trough has a 1300 years long historical record of recurring tsunamigenic earthquakes,

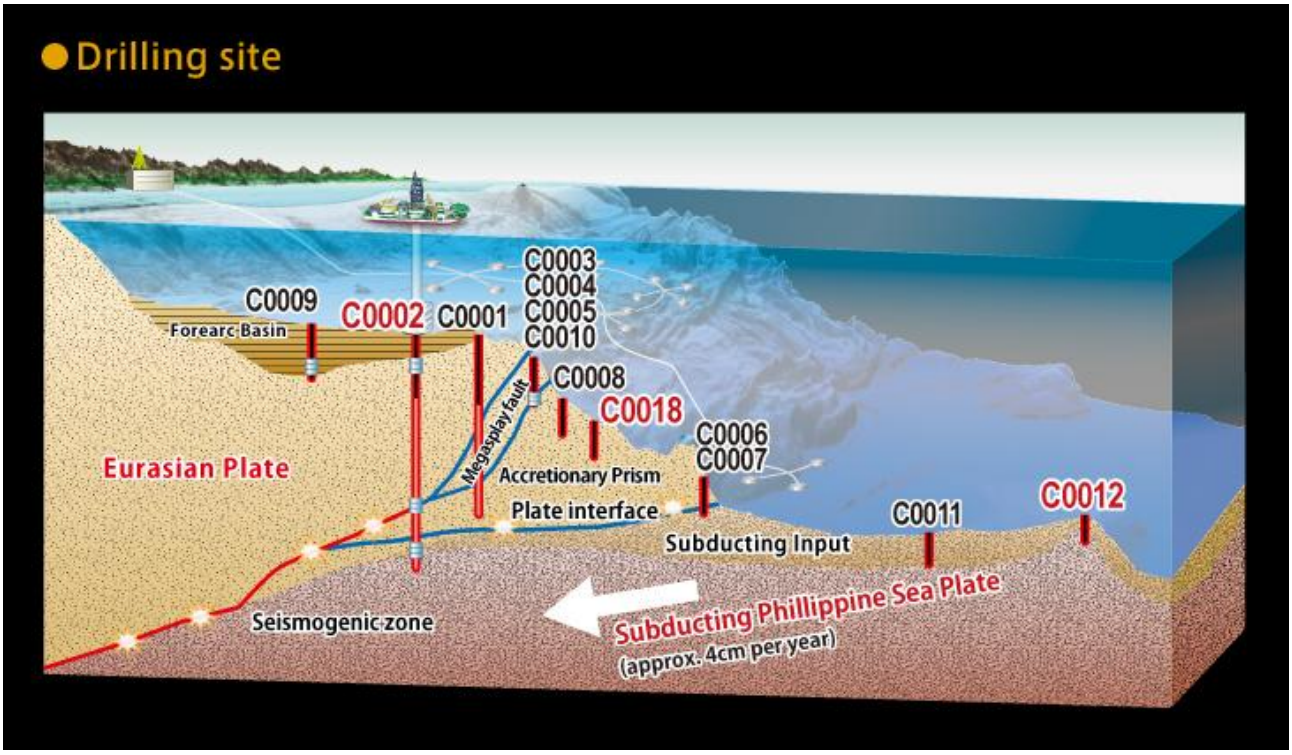

Figure 4.1. Schematic cross section of Nankai subduction margin, with location of the NanTroSEIZE Project drilling sites. C0011 and C0012 cross the input hemipelagic deposits of the Shikoku Basin on the incoming plate. C0006 and C0007 cut through the main frontal thrust at the prism toe. C0002 penetrates in the Kumano Basin deposits in the forearc and the accretionary prism below. The site C0002 portion colored in red represents the deepening of the hole as intended in the IODP EXP. 358, which aimed to reach both the megasplay and the megathrust at a ~5000 m b.s.f. This objective has unfortunately not been reached during the expedition, due to challenging drilling condition, but the record depth of ~3300 m b.s.f. has however been achieved. From: https://www.jamstec.go.jp/chikyu/e/nantroseize/science.html.

which includes the 1944 Tonankai Mw 8.2 and 1946 Nankaido Mw 8.3 earthquakes (Ando, 1975; Hori et al., 2004). It results from subduction of the Philippine Sea plate below the SE Eurasian plate, at a rate of ~40–60 mm/y (Figs. 4.1 and 4.2) (Seno et al., 1993; Miyazaki and Heki, 2001; DeMets et al., 2010). The convergence direction is slightly oblique to the trench, and trench wedge turbidites and hemipelagic sediments of the Shikoku Basin are actively accreting at the deformation front. The complex geodynamic evolution of the Shikoku Basin, including the migration of the boundaries of the Amurian, Pacific and Philippine plates over time (e.g., Moore et al., 2015), has resulted in large lateral variations in basement relief, with associated variations in the nature and thickness of sediments, resulting in structures highly variable laterally within the accretionary prism.

In cross section (Fig. 4.2), the deformation front is located at the toe of the prism, at the boundary with the deepest part of the trough. Upslope from the prism toe, landward-dipping imbricated

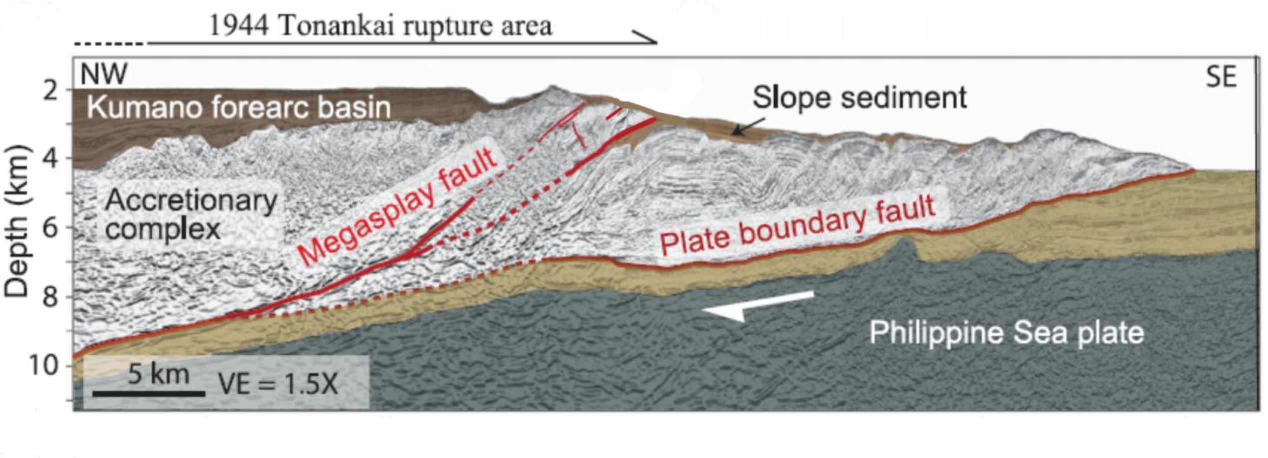

Figure 4.2. Schematic cross section of Nankai subduction zone, with indication of the two major fault systems: the plate boundary megathrust and the megasplay fault. Modified from Sakaguchi et al. (2011).

thrusts with associated anticlines and back-thrusting branches form together the Imbricate Thrust Zone (ITZ; Park et al., 2002; Moore et al., 2009).

The thrusts of the ITZ sole into the basal décollement, corresponding to a strong continuous positive polarity reflection on the seismic reflection data. Beneath the upper slope, two distinctive branches of a first-order thrust correspond to the so-called "Mega-Splay Fault" (MF) (Fig. 4.2) (Park et al., 2002, 2010). The MF cuts across the older part of the accretionary prism and can be traced ~10 km deep toward the top of the subducting plate. The MF extends more than 120 km along strike (Moore et al., 2007; Park et al., 2010) close to the updip limit of inferred coseismic rupture in the 1944 Tonankai Mw 8.2 earthquake (Fig. 4.2). Landward of the MF, the oldest parts of the prism are overlain by marine sediments accumulated in the Kumano forearc basin, bounded to the southeast by a topographic valley at the limit between the basin and the upper part of the trench slope (Fig. 4.2).

Geological studies at the Nankai margin (Sakaguchi et al., 2011; Screaton et al., 2009), direct observational evidences from the 2011 Tohoku earthquake (e.g., Fujiwara et al., 2011; Ito et al., 2013), and new results from the long-term borehole monitoring system (LTBMS) installations (Wallace et al., 2016; Araki et al., 2017) suggest that both the décollement and the megasplay are capable of storing and releasing elastic strain and may be involved in tsunamigenic megathrust earthquakes (Kimura et al., 2011; Sakaguchi et al., 2011).

Land-based offshore geodetic studies suggest that the plate boundary thrust is currently strongly locked (Miyazaki and Heki, 2001; Yokota et al., 2016). Consistently, a significant strain accumulation on the megathrust during the interseismic phases can be deduced also by the relatively low level of microseismicity near the updip limits of the 1940s earthquakes (Obana et al., 2001).

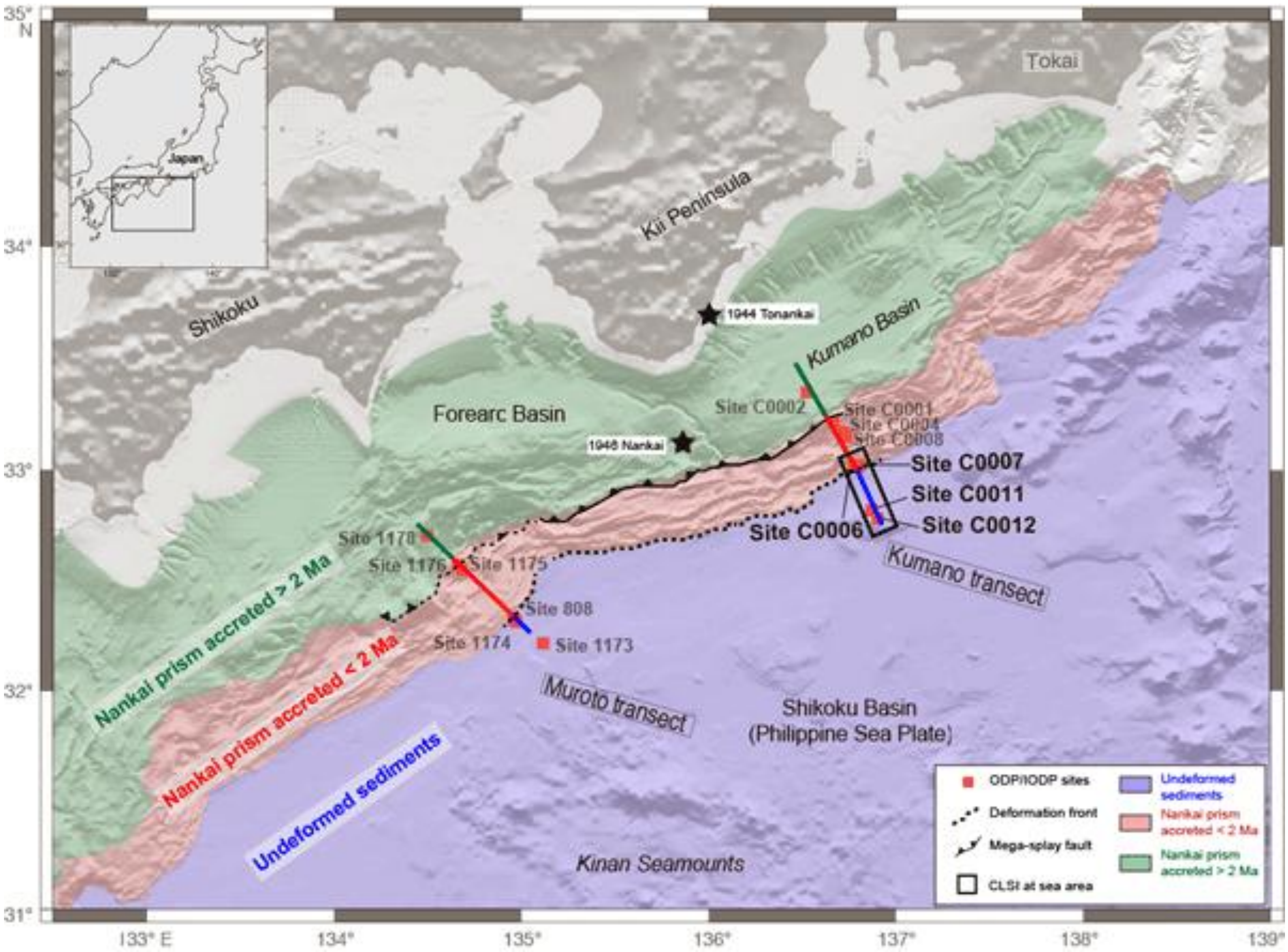

Figure 4.3. *Synthesis map of the Nankai Trough offshore southwestern Japan. The locations of the actual area of investigation of the IODP NanTroSEIZE project and the previous area of the former ODP, Ocean Drilling Program, are shown. The area of investigation of the CLSI@Sea workshop corresponds to the black frame, including Site C0006, the target of IODP Expedition 380. The colors show the stage of evolution of the deformation within the Nankai Trough. From Cerchiari et al. (2018).*

Nevertheless, this interseismic strain is complex and not restricted only to slow elastic strain accumulation, as demonstrated by very low frequency earthquakes (VLFE) recently registered within or prism (Obara and Ito, 2005 just below the accretionary; Ito and Obara, 2006; Obana and Kodaira, 2009; Sugioka et al., 2012), or episodic slow slip events and nonvolcanic tremor occurring in the downdip part of the rupture zone (Ito et al., 2007). SSEs have been observed extending up to less than 25 km from the trench and recurring every 12-18 months (Araki et al., 2017). Seismicity in the subducting Philippine Sea below the rupture zone is weak (Obana et al., 2005), while the incoming ocean crust is affected by microearthquakes, as documented by ocean-bottom seismometer (OBS) studies (Obana et al., 2005).

The NanTroSEIZE Project investigations focuses on a trench–normal transect across the Nankai Trough subduction zone offshore the Kii Peninsula of southwest Honshu Island. This transect runs from the Kumano Basin in the fore-arc region ~60 km landward of the trench axis to the Kashinosaki Knoll seamount on the downgoing plate ~40 km seaward (Fig. 4.3) (Becker et al., 2018). This particular region was selected for several reasons, first of all because the coseismic rupture area of the 1944 Tonankai M8.2 event (the most recent great earthquake, here) in this region clearly extends shallow enough for drilling (the seismogenic zone lies ~4700–6000 m beneath the seafloor) and an updip zone of large slip has been identified and targeted (Nakanishi et al., 2002; Ichinose et al., 2003; Baba and Cummins, 2005). Furthermore, this transect is generally typical of the Nankai margin in terms of heat flow and sediment on the incoming plate, in contrast with the area offshore Cape Muroto, the location of previous scientific ocean drilling where both varying basement topography and anomalously high heat flow have been documented (Moore et al., 2001, 2005; Moore and Saffer, 2001).

During the last 12 years, the NanTroSEIZE Project has been articulated in three Stages, during which drilling, coring, logging and installation of borehole monitoring systems have been accomplished at multiple sites by the Japanese Drilling Vessel Chikyu (Kopf et al., 2017).

NanTroSEIZE Stage 1, conducted in 2007–2008, performed three riserless drilling operations in incoming sediments and ocean crust of the subducting plate to characterize their physical properties, composition, pore pressure and temperature conditions.

Stage 2, in the time-span 2009–2011, included the first riser drilling in the Integrated Ocean Drilling Program at Site C0009 in the Kumano Basin, observatory installations and additional riserless coring of subduction inputs and mass wasting deposits on the continental slope (Expedition 319 Scientists, 2010; Kopf et al., 2011; Underwood et al., 2010; Henry et al., 2012).

Stage 3 started from 2010 and, by now, has focused on riser drilling with the ultimate objective of penetrating both the megasplay fault and the plate boundary thrust at ~5000 m b.s.f., to sample the hangingwall, the fault zone and into the footwall (Tobin et al., 2018). In March 2018, last IODP Expedition 358 "NanTroSEIZE Plate Boundary Deep Riser 4: Nankai seismogenic/slow slip megathrust" drilling operations have ended at a shallower depth than the intended plate boundary fault target, due to geological and structural conditions more complex than foreseen. Nevertheless, this expedition reached 3,262.5 meters below sea floor (1,939 m water depth) at Site C0002 (Fig. 4.1), a new depth record in scientific ocean drilling. Furthermore, core samples of 2.5 meters in total length were recovered from 2,836.5 to 2,848.5 meters below sea floor, also a new depth record in scientific ocean coring (*https://www.jamstec.go.jp/e/about/press_release/20190329/*, IODP –

JAMSTEC Press Release, 1 March 2019). Research using the data and samples collected by this expedition are currently ongoing, carried out by international scientific teams.

4.3. The CLSI@Sea Workshop

From 12 January to 7 February 2018, as part of the NanTroSEIZE Project Stage 3, the Core-Log-Seismic Integration at Sea (CLSI@Sea) Workshop was held onboard the Drilling Vessel Chikyu in the Nankai Trough subduction zone. This workshop was developed to enhance multidisciplinary research in addressing the role of accretionary prism frontal deformation in tsunamigenic earthquakes and slow slip in the shallow portion of the subduction interface. The CLSI@Sea Workshop was designed to leverage existing archives of IODP cores, logging data and associated seismic datasets previously acquired as part of the NanTroSEIZE program. Re-investigation of the available is particularly interesting in the light of the recent evidence of very shallow seismic and tsunamigenic slip provided by the 2011 Tohoku-Oki earthquake (Chester et al., 2013) and inferred as possible also for the the shallow portion of the Nankai subduction zone (Kinoshita et al., 2009; Sakaguchi et al., 2011; Ito et al., 2013).

The CLSI@Sea workshop represented an original approach in several aspects (Cerchiari et al., 2018). First, CLSI@Sea was an unprecedented opportunity to examine legacy data from multiple former expeditions in the context of a mission not dedicated to core recovery. CLSI@Sea workshop was in fact held concurrently with IODP Expedition 380, which installed a long-term borehole monitoring system (LTBMS) at Site C0006, above the deformation front of the Nankai accretionary prism, thus allowing workshop participants to investigate archived data from the site where the IODP expedition was focused and interact with the expedition science party. Second, a challenging aspect of the workshop was to connect a group of science mentors with extensive experience in the Nankai margin with early-career researchers from diverse research backgrounds, to work on common research questions. Third, workshop participants were given the opportunity to pursue new research while onboard Chikyu, thanks to full access to shipboard laboratory facilities to re-investigate the IODP archived data. Well-preserved sedimentary cores were brought onboard Chikyu from the Kochi Core Center and made available for laboratory analyses. Seismic reflection, log, and drilling parameter data were also kindly provided to all workshop participants onboard. The international team of workshop participants was then able to develop interdisciplinary discussions and organize both individual and collaborative research plans to address outstanding questions regarding seismogenic, tsunamigenic and slow slip processes in the Nankai subduction zone.

One of these projects aims to characterize the frictional properties and the seismic behavior of subduction input material, cored at site C0012 oceanward of the deformation front, envisaging high-velocity friction experiments on core samples set up in collaboration with the Istituto Nazionale di Geofisica e Vulcanologia (INGV) in Rome, Italy. The tests will be performed with SHIVA, the Slow to High Velocity Apparatus hosted at INGV. This is a rotary shear apparatus that can impose on cohesive and non- cohesive rocks large normal stresses (up to 50 MPa), high slip velocities (up to 9 m/s) and displacements (tens of meters). SHIVA is then especially designed to simulate very large coseismic slips, like the one occurred during the 2011 Tohoku earthquake and inferred as possible also for the Nankai frontal thrust. In particular, samples coming from the first interval of C0012 core (0-150 m core depth below seafloor) will be tested, with material belonging to the Pliocenic Unit of Upper Shikoku Basin Facies, mainly hemipelagic mud with pyroclastic interlayers (Expedition 322 Scientists, 2010), similar to mudstones that host the principal thrust surface (C0007 Site, Expedition 316 Scientists, 2009). Samples will be tested at increasing normal stresses up to 10 MPa, 1.3 m/s slip rate and up to 10 m displacement under room humidity and water dampened conditions. Additional experiments will be performed under water-saturated conditions, to observe coseismic weakening at very short displacements (< 0.03 m). Fault rock materials produced through experiments will be then analyzed at the microscale (through optical microscope and SEM) and compared to natural core samples materials, with a continuous feedback to constrain the shear-related deformation and mechanisms in detail. First tests have been set up in April 2019, but no useful data were collected due to problems in the operative functioning of the instrumental apparatus. The friction experiments are currently under rescheduling.

4.4. Main NanTroSEIZE Project findings

Although too recent to have brought experimental results, the participation in the CLSI@Sea Workshop and related research projects design have provided the opportunity to review some of the recent outstanding findings about the structural architecture, geophysical conditions and parameters controlling the seismogenic behavior of the megathrust, with particular reference to Sites C0006 and C0007, corresponding to the frontal plate boundary thrust, and C0011 and C0012, located ahead of the prism, offshore the deformation front, in the sediment input of subdcution. Here, a brief summary can be found, integrated with data from literature reviews (for more details, Cerchiari et al., 2018; Saffer, 2015).

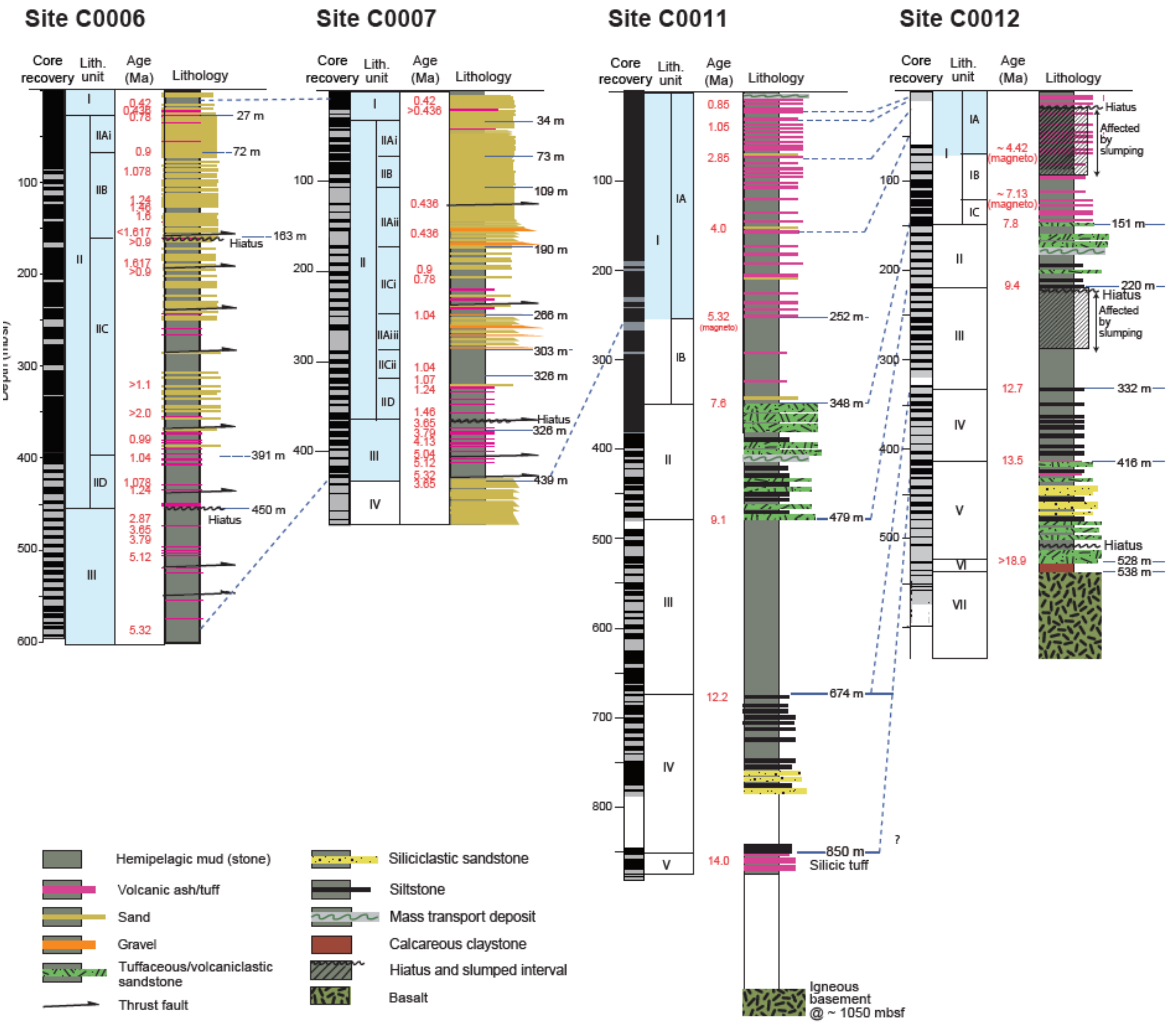

Figure 4.4. *Lithological sections across the Nankai frontal prism (Sites C0006 and C0007) and the input sites (C0011 and C0012). The columns at each site show core recovery, lithologic units, sedimentary ages, and lithology distribution. From Cerchiari et al. (2018), modified from Kinoshita et al. (2009), Strasser et al. (2014) and references therein.*

4.4.1 Lithostratigraphy

The workshop resulted in a new synthesis of the lithostratigraphy and chronostratigraphy for reference subduction input frontal thrust zone sediments (Figs. 4.4 and 4.5).

Sites C0011 and C0012 transect the entire incoming sediment sequence of the Shikoku Basin to basaltic ocean crust (Fig. 4.4) (Underwood et al., 2010; Strasser et al., 2014). Unit I corresponds to late Pleistocene to late Miocene Upper Shikoku Basin deposits and contains silty clays with minor ash. Unit II is marked by the occurrence of volcaniclastic sandstones in silty claystone and

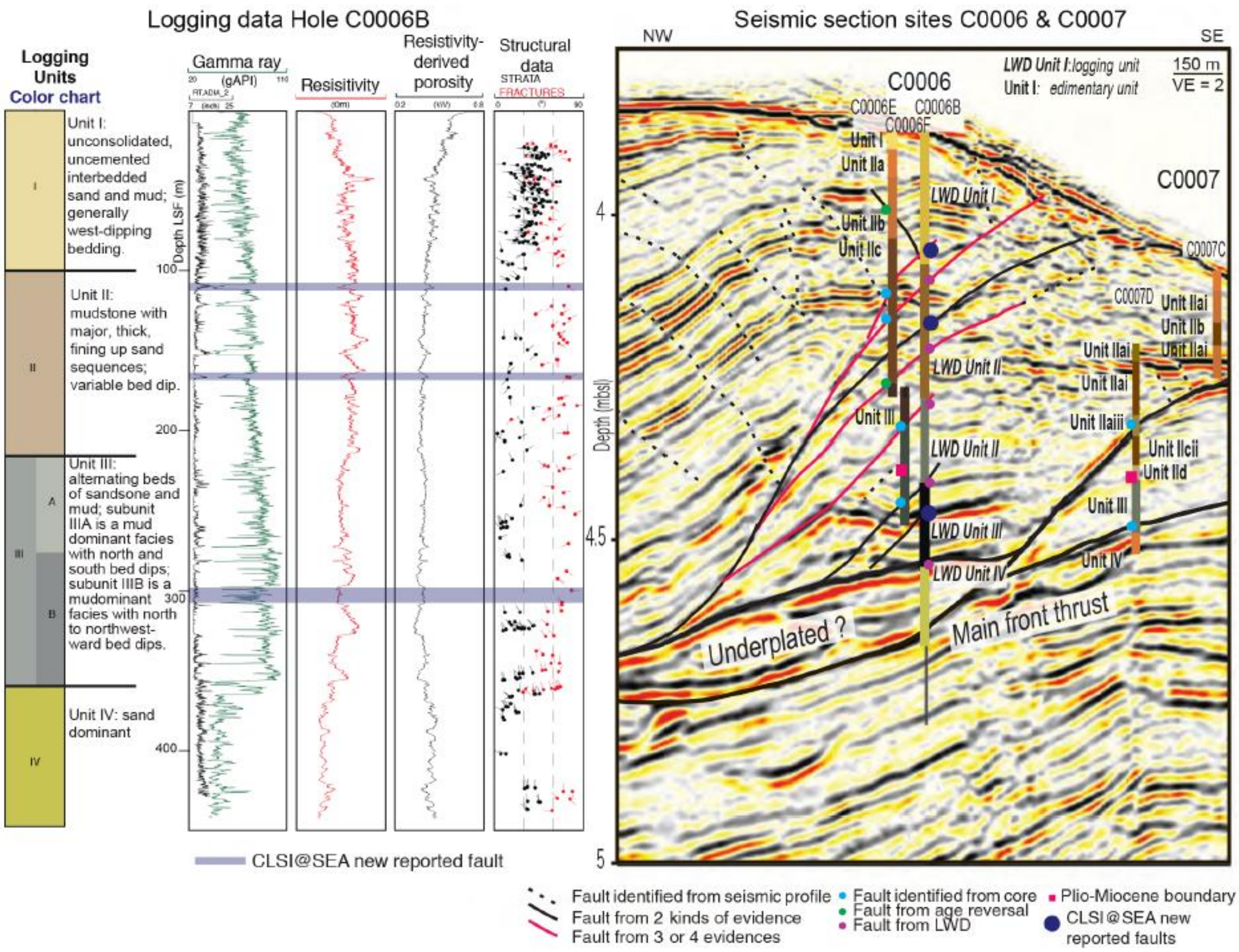

Figure 4.5. *Sedimentary, logging and seismic data at the deformation front of the Nankai prism (Sites C0006 and C0007). Dark blue markers (strips, dots) are additions provided by the CLSI@Sea workshop. The figure shows (from left to right) the logging data at Hole C0006B, the interpreted seismic section (IL 2435) across the Nankai 3-D volume illustrating the structures at the deformation front, and the lithological and logging units identified at both Sites C0006 and C0007. Some structures (dark blue) have been identified by integration of the Core-Logging-Seismic data. From Cerchiari et al. (2018), after Kimura et al. (2008) and Kinoshita et al. (2008, 2009).*

corresponds to late Miocene Middle Shikoku Basin deposits. Units III to V correspond to middle-late Miocene Lower Shikoku Basin deposits. Unit III is a succession of uniform silty claystone and lime mudstone; Unit IV contains silty claystone/clayey siltstone comprising fine-grained, turbiditic sand layers; Unit V contains tuffaceous sandy siltstone with some silty claystone and tuff. The oldest units recovered include calcareous mudstone (Unit IV) overlying oceanic basement basalts (Unit VII). The dominant mineral assemblages are quartz, feldspar, clay minerals and calcite. No major trends in mineral content are observed within Units I and V, but Unit VI has an overall higher clay content and lower quartz and feldspar contents compared to overlying units.

Sites C0006 and C0007 cores sampled accreted Shikoku basin deposits and overlying wedge slope deposits (Fig. 4.4) (Kinoshita et al., 2009). Unit I contains unconsolidated hemipelagic mud and turbidites deposited in a wedge slope environment (Kinoshita et al., 2009). Unit II contains alternating sequences of Pleistocene hemipelagic muds and turbidites deposited in a transitional trench–wedge environment. Unit II, which directly overlies the décollement at Sites C0006 and C0007, is made up of accreted sediments correlated with the Pliocene to Upper Miocene in the Shikoku Basin. Unit IV, recovered below the décollement at Site C0007, consists of a small (~15 cm) section of dark, medium to coarse-grained sands. As in Site C0012, the dominant mineral assemblage is feldspar, clay minerals and calcite, and does not display major trends in mineral content.

4.4.2 Tectonic structure of the frontal thrust

The workshop resulted in a new synthesis of structural features observed in core, log, and seismic data from the incoming plate and frontal wedge of the Nankai prism, including identification of new faulted intervals in the formal prism. The structures examined are at the deformation front of the Nankai prism, where the thrust–fault activity is the youngest (Fig. 4.5) and the compressional deformation propagates oceanward (Moore et al., 2009; Underwood and Moore, 2012).

Site C0012 is located seaward of the deformation front. Bedding orientations at this site are dominantly subhorizontal, with intervals of higher angle bedding resulting from gravitational slumping, and high angle fractures resulting from subvertical compaction. Sites C0006 and C0007 penetrated the first two imbricate thrusts at the deformation front, including the main frontal thrust at ~700 m LWD depth below seafloor (LSF) (Fig. 4.5) (Kinoshita et al., 2008, 2009). Bedding at Site C0007 is dominantly subhorizontal, but a major lithologic inversion at ~400–450 m b.s.f. places moderately consolidated hemipelagic mudstones over poorly consolidated trench turbidite sands. Site C0006 can be divided into four log units corresponding to distinct structural domains (Fig. XXX). Unit I (0–100 m LSF) has generally westdipping bedding resulting from northwestward tilting driven by plate convergence and southwestward tilting driven by gravitational slumping. Unit II (100–220 m LSF) is a thrust zone that contains several faults identified in core, log and seismic data (Fig. 4.5). Units III and IV (below 220 m LSF) contain northwestward-dipping beds and fractures, consistent with north-northwestward-directed shortening driven by plate convergence.

Cores from Sites C0006 and C0007 intersect several major faults, including the plate boundary interface intersected at Site C0006 at ~700 m LSF and Site C0007 at ~400 m LSF (Kinoshita et al., 2008, 2009). In the cores, faults largely occur as breccias, gouges, and zones with striated fractures, in which the sense of displacement is often difficult to observe directly. The décollement is characterized by a similar pattern of brecciation within an approximately 30- to 40-m-thick damage zone, composed of mm- to cm scale overconsolidated mudstone fragments bounded by striations (e.g., Mikada et al., 2002; Ujiie et al., 2003). A black gouge-bearing fault zone recovered in the core from Site C0007 at 438 m LSF exhibits a vitrinite reflectance anomaly interpreted to reflect shear heating during past seismic slip to the trench (Sakaguchi et al., 2011). In log data, faults can be identified by simultaneous decreasing of the gamma ray and resistivity values. Cross-comparison of core and log data with 3-D seismic reflection data across the Kumano transect allowed observation of the persistent lateral continuity of the main thrusts across the seismic volume, whereas secondary and tertiary branches of the thrusts show important lateral variations in three dimensions. Resistivity images and logging also confirmed the presence of the 30-m-thick plate boundary fault zone containing abundant electrically conductive fractures (Bourlange et al. 2003; Ienaga et al. 2006), suggesting the presence of an increased pore fluid pressure (Saffer, 2015).

4.4.3 Permeability, pore fluid pressure and stress state

Saffer and Bekins (1998) conducted a detailed study at the Nankai margin, which, investigating the pore pressure distribution and patterns of pore-water freshening, showed for the steady-state décollement permeability values from 10^{-17} to 10^{-15} m^2 in the outermost 50 km of the accretionary complex. Models coupling loading, sediment consolidation and fluid flow predict that the décollement permeability must decrease systematically from approximately 6 to 8.2 x 10^{-14} m^2 near trench to 7 x 10^{-16} m^2 by 40 km landward (Skarbek and Saffer, 2009). This is required to accommodate the dewatering flux from underthrusting sediments while also sustaining pore pressures able to match both large-scale mechanical constraints from critical taper theory and those values inferred along the wedge base from porosity and seismic waves velocities. Modeling efforts at different locations yield steady-state décollement permeabilities in a strikingly similar range (10^{-15} to 10^{-13} m^2), despite the fact that the geometries, rates of accretion and dewatering, and sediment matrix permeabilities differ substantially between margins (Saffer, 2015).
Recent studies have revealed fluid geochemical and thermal anomalies centered at the décollement in drilled boreholes at Nankai subduction margin (Henry et al., 1992; Henry et al., 2002). To explain geochemical anomalies like pore water freshening, fluids must necessary flow from zones of mineral dehydration at depth to the near-trench region where boreholes have been drilled, and flow must be rapid enough to preserve a chemical signature of the deeply seated fluids (Bekins et al., 1995; Spinelli et al., 2006). This is consistent with those models that predict pressure and permeability 'fronts' migrating up-dip, generating periodic pulses of near lithostatic pore pressures (Shipley et al., 1994; Henry, 2000; Bourlange et al., 2003). Moreover, transient pulses of pore fluid pressure at shallower depths are required to satisfy mechanical constraints at the Nankai subduction zone (e.g., Henry, 2000; Skarbek and Saffer 2009), where measured or inferred present-day pres-

sures near the trench are approximately 0.5-3 MPa lower than is needed for sliding along the décollement. Parallel, also fault permeability is inferred to be transient and/or discontinuous (Stauffer and Bekins, 2001; Bekins and Screaton, 2007), as demonstrated by measured or modeled flow rates at the margin, that are approximately 10–500 times greater than the inventory of fluids: they imply that increased permeability is present only approximately 0.2–10% of the time or that permeable channels occupy only a fraction of the fault surface at any given time (e.g., Le Pichon et al., 1990; Brown et al., 1994; Saffer and Bekins, 1999; Spinelli et al. 2006).

Kitajima et al. (2017) gave a quantification of the in situ pore pressure and stress conditions, using data obtained during drilling and logging operations and from sediment core and cuttings sampled at Site C0002, from the upper Kumano forearc Basin to the lower accretionary prism. They first defined the in situ porosity from the Vp logging data, and used this datum as a proxy of the sediment compression state, in turn directly related to the in situ stress state. Based on parameters retrieved for the specific sediments from laboratory deformation experiments, they estimated the differential stress, effective mean stress, in situ stress tensors and pore pressure for the end-member loading conditions of one-dimensional vertical consolidation and critical state loading causing shear of the sediment.

The resulting pore pressure is nearly hydrostatic in the Kumano Basin, whereas the prism is modestly overpressured. The pore pressure ratios within the prism ($\lambda = 0.58$ in average) are lower than the value of $\lambda = \sim 0.85$ at greater depth near the megathrust fault at the location of Site C0002 estimated from regional seismic velocity data sets (e.g., Kitajima and Saffer, 2012; Tsuji et al., 2014) and suggest that the pore pressure ratio varies significantly with depth, both above and beneath the décollement.

Also the stress state varies, accordingly to Kitajima et al. (2017) results: their analysis suggests that at Site C0002, the maximum horizontal stress SH is smaller than the maximum vertical stress Sv in the Kumano Basin, thus corresponding to a normal faulting regime (Sv ≥ SH ≥ Sh, where Sh is the minimum horizontal stress). Within the prism, SH becomes close to or greater than Sv, marking the transition to a strike-slip fault regime (SH ≥ Sv ≥ Sh). In the inner prism the differential stress, though greater than in Kumano basin, has always a low magnitude (<~25 MPa) and the prism is in a strike-slip faulting regime to at least 3 km b.s.f. To reconcile the strike-slip regime within the inner prism with active thrust faulting and consequent slip on the megathrust, the authors discuss alternative hypothesis necessarily implying that the horizontal stresses SH and Sh vary with time or depth and/or that the shear stress along the megathrust is low (Kitajima et al., 2017).

Lin et al. (2016) compared the stress state in the hangingwall of the frontal plate-interface between Site C0006 in the Nankai and Site C0019 in the Japan Trench subduction zone drilled after the 2011

Mw 9.0 Tohoku-oki earthquake. A similar current stress state with trench parallel extension was recognized at both C0006 and C0019 sites, which appear to be in the early stages of the interseismic cycle with vertical σ_1 and that Sh_{max} (interpreted to be σ_2) is generally parallel to the plate convergence vector. Hypothetically this may indicate that the Nankai Trough is still in an early stage of the interseismic cycle of a great earthquake, supposed to occur on the décollement and to be capable of propagating to the toe (around site C0006).

Chapter 5. Discussion

In this Chapter, a comparison between the two fossil analogue fault strands chosen (Llŷn fault zone in Northern Wales and the SVU basal thrust in the Northern Apennines of Italy) and the active megathrust at the Nankai subduction margin will be presented, as a first attempt to answer to the outstanding questions highlighted at the beginning of this work (see Chapter 1, paragraph 1.5). Specifically, this work is aimed at contributing to:

- better constrain the updip and downdip limits of the seismogenic zone, from a geological point of view (paragraph 5.1);
- assess if megathrust faults are weak (paragraph 5.2);
- consider the interplay between the strain accumulation/release and fluids circulating in megathrust fault zone (paragraph 5.3);

The studied examples represent fault strands (*sensu* Rowe et al., 2013) which can be correlated to three different megathrust portions, located at progressively shallowing depth:

- Llŷn fault zone is interpreted as compatible to the downdip limit of the seismogenic zone, at the brittle-ductile transition, with temperature of 300-350 °C (see Chapter 3);
- the Vidiciatico fault zone reached a depth of a few kilometers (4-5 km) and maximum temperatures of 120-150 °C, compatible with the "classical" updip limit of the seismogenic zone (see Chapter 2);
- the Nankai active frontal megathrust and megasplay represent the shallowest portion, cored and studied from the trench to about 3 km depth (see Chapter 4).

5.1. The geologic updip and downdip limits of the seismogenic zone

Both Llŷn and SVU fossil analogues record superimposing progressive deformation phases, from pre-lithification to post-lithification (Chapter 2, Section 2.b; Chapter 3, Section 3.c): pre-lithification continuous "ductile" (*sensu* Fagereng et al., 2018) mechanisms start in unconsolidated sediments and subsequently evolve in a progressively lithifying rock assemblage. In Vidiciatico, pre-lithification deformation is expressed in D1 by the ductile realignment of mica and clay lamellae by particulate flow along shear bands, and by the formation of discontinuous anastomosing crack-and-seal extensional veins, with dirty calcite and fuzzy boundaries suggesting vein opening in not completely lithified sediment (Chapter 2, paragraph 2.b.1, Fig. 2.6). The syn-lithification deformation structures, overprinting the pre-lithification ones, include tectonic foliations formed by pressure solution in less competent lithologies (siltstone in D1 and clay-rich portions of D2 marls) and brittle boudinage, extensional fracturing and/or veining in more competent lithologies (D2 carbonate-rich marls), or at discontinuities (for example the contact between D1 and D2 layers, marked by a shear vein) (Chapter 2, paragraph 2.b.2, Figs. 2.5, 2.6 and 2.7). D3 main thrust, with its S-C' shear bands, shear and extensional veins, intensely folded and boudinaged, all cut by sharp and tens-of-meters long shear vein, is the main brittle surface accommodating shear and truncating all the structures below it (Chapter 2, paragraph 2.b.3) This suggests that, as the shear zone lithification becomes more homogeneous, the activation of discontinuous brittle mechanisms is progressively more favoured: shear fractures, thrusts (and, in presence of fluid overpressure, veining) gradually pass from being dispersed, cutting through the more competent portions in the fault zone, to be very continuous and sharp, localized along discrete thin thrust surfaces, capable to accommodate slip efficiently (Chapter 1, paragraph 1.1), like Vidiciatico D3 layer. Localization to a thin slipping zone is, in fact, generally associated with seismic slip (e.g., Sibson, 2003).

Therefore, the lithologies involved in a fault zone, their relative competence contrast and degree of lithification are all factors greatly influencing the onset of brittle discontinuous deformation mechanisms and the potential to generate seismic ruptures. This lithology-controlled deformation style during the first stages of thrust activity is consistent with observations of many other fossil analogues worldwide. Similar fault zone evolutions have been described for the Chrystalls Beach Complex in New Zealand (Fagereng et al., 2013); the Shimanto Belt in Japan (Ujiie et al., 2002; Hashimoto and Yamano, 2014); the Alps in Northern Italy (Dielforder et al., 2015) and the Kodiak Islands in Alaska (Fisher and Byrne, 1987). This recurrent evolutionary pattern in which progressive lithification corresponds to further localization of the deformation on thin individual faults in active strands suggests that lithologies involved in the fault zone and the relative proportion of competent and incompetent material changing through time are primary controls on the transition to the seismogenic zone of a megathrust. Since lithification is gradual, depending also on the competence of lithologies involved, the rheologic state homogeneous enough to undergo brittle failure and slip (and ultimately seismogenesis) can be reached at different depths depending on the starting lithological assemblage. In this perspective, the updip limit of the seismogenic zone would not correspond to fixed P/T (and related depth) conditions, it would be rather gradual and lithology-controlled. A similar transition implies a significant mixing of slip styles, from continuous and slow to progressively more transient and rapid, as long as the fault zone has not reached a homogeneous mechanical behavior: each component accommodates slip based on its rheological properties, such as cohesion and cementation, fluid content etc. This is consistent with the range of slip modes, from episodic slow slip and tremor to low- or very-low-frequency earthquakes, observed along the shallow part of active megathrust, from the trench to the inferred updip limit of the seismogenic zone (Chapter 1, paragraph 1.1), as also highlighted for Nankai margin (Chapter 4, paragraph 4.2).

Transient slip events like SSEs and tremors registered at the base of the seismogenic zone suggest that a similar varying character can be attributed also to the downdip passage from brittle (potentially seismic) to high-temperature ductile (aseismic) deformation. This information is supported by what can be observed in Llŷn fault strand, where the onset of ductile deformation by crystal plasticity of quartz shear veins at temperatures around 300 °C occurs coincident with dissolution-precipitation creep in phyllosilicate fault matrix, and alternated cyclically with new brittle shear on the same faults (Chapter 3, Section 3.c). The interpreted factors determining this repeated strain partitioning and brittle/ductile intermittence in Llŷn veins are transient fluid overpressures and variations in strain rate, which could reflect the different loading rates that accompany and follow a seismic event. Low strain rates, in presence of inter-crystalline fluids, activate plastic mechanisms at crystal boundaries in quartz shear veins. High strain rates and fluid pressures cause embrittlement and renewed slip on the fault surfaces coated by the already plastically deformed veins. This interpretation is consistent with the strain partitioning observed on other field analogues for the downdip end of the seismogenic zone, for instance the Damara Belt in Namibia (Fagereng et al., 2014), the Central Alps in Northern Italy (Bachmann et al., 2009) and the Franciscan Complex in California, USA (Wassmann and Stöckhert, 2012), where a background diffuse ductile creep is accompanied by transient veining along foliation planes.

5.2. Thrust weakness and the role of fluid pressure

Both in Llŷn and Vidiciatico, the thickness of the actively deforming faults in the post-lithification phase does not exceed 20–30 cm. In Llŷn, the fault zone footwall dolomites do not record the shear deformation phase, whose strain has been accommodated entirely by the fault mélange (Chapter 3, Section 3.b). In Vidiciatico, the localization of the deformation to D3 main thrust is associated with the deactivation of the structural domains below it, where the shear component of strain is overprinted by thrust-parallel flattening: in D1, subperpendicular extensional veins are folded and dissolved at the contact with planes of the mm spaced foliation subparallel to the thrust (Chapter 2, paragraph 2.a.1, Fig. 2.6.e). Also in D2, fault-perpendicular extensional veins are affected by pressure solution (Chapter 2, paragraph 2.a.2, Fig. 2.6.c), and the microscopic shear bands both synthetic and antithetic to the main thrust shear sense (Fig. 2.7.e, f), even in D3 (Fig 2.8.a, b) are compatible with fault-normal flattening. Shear seems to have migrated from the base of the fault zone to the final localization in D3 main thrust surface, with D1 and D2 layers continuing to accommodate only fault-parallel extension.

A similar strain decoupling across actively shearing décollements has been measured in magnetic susceptibility studies on cores from the basal décollement of active megathrusts, as the one of the Barbados accretionary prism (Housen et al. 1996) and of the Japan Trench prism (Yang et al. 2013). Strain decoupling, likely responding to stress decoupling, suggests that the studied faults are weak and capable to accumulate only low shear stress.

Low shear stress is necessary also for stress switching in consequence of a seismic event, as hypothesized for the Vidiciatico fault zone, where a very low differential stress, not exceeding 10 MPa, is implied (Chapter 2, Section 2.c). The modeled σ_1 and σ_3 switching during the seismic cycle seem to fit well with the results of several stress tensor inversion studies conducted on active megathrusts, e.g. at the Japan Trough after the Tohoku-oki earthquake (Ide et al., 2011; Hasegawa et al., 2011; Hasegawa et al., 2012; Lin et al., 2013; Brodsky et al., 2016) or at the Nankai Trough (Lin et al., 2016; Kitajima et al., 2017; Chapter 4, paragraph 4.4.3).

Though both working at low differential stress, the interpreted migration of the main thrust fault with progressive strain decoupling of the lower portions of the fault zone and the repeated stress switching along thrust faults in Vidiciatico fault strands, can be coherent if seen as expressions of processes active at different time scales: the stress switching corresponds to the timing of the single seismic cycle phases, while the strain decoupling across the whole fault strand is mediated on a geological time scale. The low differential stress inferred for stress switching and strain decoupling is also required to open the hybrid-shear and breccia veins observed both in Llŷn and Vidiciatico. It is needed also to form the high-angle extensional veins found in Vidiciatico, which must match the hydrofracture criteria: differential stress must be less than four times the tensile strength (Etheridge, 1983) and fluid pressure must exceed the least principal stress. Even more, the low-angle foliation-parallel extensional veins seen both in Llŷn and Vidiciatico, need a fluid pressure high enough to counteract $\sigma1$, reaching supra-lithostatic values in Vidiciatico reloading phase (Chapter 2, paragraph 2.d.2), where $\sigma1$ is coincident with the lithostatic load. Similar veins have been found in many fossil analogues of megathrust at different depths (Fisher et al., 1995; Labaume et al. 1997;

Meneghini and Moore, 2007; Meneghini et al., 2007; Fagereng et al., 2010; Dielforder et al., 2015; Ujiie et al., 2018). Extensional veins parallel to the foliation are frequent also down to the interpreted base of the seismogenic zone (Bachmann, 2009; Fagereng et al., 2014). Several qualitative geophysical data from active margins (high amplitude seismic reflectivity, e.g., Ranero et al. 2008; anomalously low P-wave velocity, e.g., Park et al. 2010; high Pto S-wave velocity ratios, Moreno et al. 2014), suggest higher than hydrostatic fluid pressures in the shallowest portion of active megathrusts. Thrust-parallel extensional veins in geological examples lead to infer also episodic locally higher than lithostatic fluid pressures.

All these evidences suggest that cyclical fluid over-pressuring plays a major role in keeping the stress on the fault low and the fault itself weak. The dilatant character of crack-and-seal hybrid-shear veins, accommodating incremental slip both in Llŷn and Vidiciatico, implies that friction on the fault surface is not high. Strain localization is not accompanied by significant cataclasis or brecciation on fault surfaces in the studied field analogues, even in quite competent marls hosting Vidiciatico main fault. This suggests that fluid over-pressuring can help weakening a fault even if wall rock lithologies are not inherently weak (e.g. the material friction coefficient is not low, see Chapter 1, paragraph 1.3). Actually, as reported in Chapter 4, paragraph 4.4.2, the cored plate boundary at Nankai Site C0007 is characterized by 30- to 40-m-thick damage zone composed of mudstone mm- to cm-scale brecciated and striated fragments and by a black gouge-bearing fault zone with vitrinite reflectance anomaly possibly indicating shear heating, all elements that suggest high friction on the fault. These small scale observations are limited to the few centimeters width of the core diameter, thus they are not representative of the deformation style for the whole length of the fault considered. They can nevertheless at least suggest that high friction fault patches can be present even in a décollement area where seismic imaging and logging have revealed intense fluid flow (Chapter 4, paragraph 4.4.2). Heterogeneous distributions of overpressured fluid pockets have indeed been mapped along the décollement zone by several authors (Brown et al., 1994, Shipley et al., 1994, Shipley et al., 1995, Moore et al., 1995a, Moore et al., 1995b, Moore and Klaus, 1998, Bangs et al., 1999, Screaton et al., 2000, Bourlange et al., 2003). This can be a consequence of the transient character of high fluid pressure pulses, related to both fluid source availabilities and the discontinuity in time and space of fault permeability patterns, which therefore need to be better investigated and described.

5.3. Interplay between fluid, stress and strain

In Llŷn fault strand, deformation mechanisms operating at different strain rates seem to be linked to distinct fluid sources and circuits (Chapter 3, section 3.c): the low-strain rate bulging recrystallization in little vein patches is enhanced by the presence of thin fluid films at the boundaries, probably the product of local dissolution-reprecipitation mechanisms. The high-strain rate dilational opening along thrust faults can instead be promoted by high pressure pulses of fluids exploiting wider fault surface permeability, based on the classic fault-valve effect (Sibson, 1998).

Similarly, in the stress analysis reconstructed for Vidiciatico fault (Chapter 2, Section 2.c), distinct successive deformation phases are linked to the development of veins with characteristic orientations and crystallizing from different fluids. In particular, the switching of the stresses interpreted as consequent to seismic slip along the fault appears to be tightly related to the activation of fluid circuits with different extensions, permeability geometry and drawing from different sources (Chapter 2, paragraph 2.c.2). The rapid shifting of the maximum principal stress orientation from low angle to subperpendicular to the margin, caused by the reset of the shear stress on the fault plane with seismic slip, annihilates the potential for fault-parallel dilation and, consequently, leads to the temporary deactivation of fault-parallel permeability and fluid flow from depth. Dilational opening is, in this way, promoted by the vertical lithostatic load and produces fractures at high angle to the fault, capable to drain only the local host rock. The same local circuit feeds the new fault-parallel extension fractures produced as the low angle shear stress is rebuilt, until new failure on the main fault strands reactivate the wider circuit of fluid flow along fault.

The preservation of geochemical anomaly in the exotic fluid crystallized on the fault surfaces indicates that not only the fluid influx, but also the crystallization, should be rapid enough to not re-equilibrate to the local host rock (Saffer, 2015; Bekins et al., 1995; Spinelli et al., 2006), as instead happens for the highly rock-buffered extensional veins. This can be further evidence that seismic slip is intimately related to transient pulses of high fluid pressures.

In Llŷn, the more local dissolution-reprecipitation fluid circuit possibly produces concentrated intergranular film of fluids in vein quartz, slowly promoting hydrolitic weakening at the crystal boundaries. The wide-traveling hybrid-shear vein fluid is pumped at higher pressure, transiently exceeding lithostatic values to produce fault-parallel dilation. Geochemical analyses on Llŷn quartz veins would be particularly useful to further confirm this hypothesis.

This interpretation of a cyclical coupled alternation of different fluid circuits and seismic cycle phases would reconcile the observations made on many fossil analogues, where layer-parallel extension along plate boundary mélanges has been widely documented (Fisher and Byrne, 1987; Cowan, 1985; Needham, 1995), and data coming from seismic and logging-while-drilling studies of modern convergent margins (included Nankai, Chapter 4), which led to model the décollement as a site of concentrated and episodic fluid flow (e.g. Brown et al., 1994, Shipley et al., 1994, Moore et al., 1995a, Moore et al., 1995b, Bangs et al., 1999, Bourlange et al., 2003).

Conclusions

The aim of this work was to describe the deformation of two fossil thrust fault strands, compatible with different depths along a megathrust, and to compare the results between them and with what is observed in active subduction plate margins.

The studied fault strand zones preserve the structural evolution from soft-sediment pre-lithification ductile deformation to brittle fluid-assisted shear faulting, showing also incipient high-temperature ductile deformation features in the case of the deepest outcrop. Hybrid-shear veins with a dilatants character coat all low-angle thrust surfaces in both outcrops, and extensional veins subperpendicular and subparallel to the thrusts are systematically present.

The observed meso- and microstructures and the interpreted evolution mechanisms in the two fossil analogues are concordant with analyses of many other field examples (Byrne and Fisher, 1990; Meneghini and Moore, 2007; Meneghini et al., 2007; Bachmann et al., 2009; Fagereng et al., 2010, 2011, 2014; Yamaguchi et al., 2012; Dielforder et al., 2015; Ujiie et al., 2018) and active megathrusts studies (Bourlange et al., 2003; Hasegawa et al., 2012; Brodsky et al., 2016; Lin et al., 2013, 2016; Kitajima et al., 2017), and altogether suggest that:

- The updip transition to the seismogenic zone is gradual, can vary in depth and is strongly controlled by the lithification state depending on lithologies involved. The downdip limit is similarly transitional, influenced by strain rate variations and the developing of fluid overpressures.

- Along shallow megathrusts and possibly down to the brittle-ductile transition, shear occurs on localized weak faults sustaining low shear stress, low differential stress and cyclical high (up to supra-lithostatic) fluid pressures.

- Cyclical intermittent slip along megathrust faults is strongly related to the alternating activation of fluid circuits with different amplitude, geometry and source.

The results of this study confirm that multidisciplinary studies of tectonic veins in fossil analogues can reveal a great deal of information about chemistry, source and circulation patterns of fluids flowing at plate boundaries and about how they are involved in the seismic cycle.

References

Allman, B. P. and Shearer, P. 2009. Global variations of stress drop for moderate to large earthquakes. *Journal of Geophysical Research*, **114**, B01310. doi: 10.1029/2008JB005821.

Allmendinger, R. W., Cardozo, N. C. and Fisher, D. 2012. *Structural Geology Algorithms: Vectors & Tensors*. Cambridge, England: Cambridge University Press, 289 pp.

An, M., Zhang, F., Zhang, L. and Fang, Y. 2018. Effects of Normal Stress and Clay Content on the Frictional Properties of Reservoir Rocks Under Fully Saturated Conditions. In: Zhang, L. et al. (eds.). GSIC 2018, Proceedings of GeoShangai 2018 International Conference: Rock Mechanics and Rock Engineering, pp. 220-231.

Anderson, E.M. 1905. The dynamics of faulting. *Trans. Edinb. Geol. Soc.*, **8**, 387–402. doi: https://doi .org /10 .1144 /transed .8 .3 .387.

Ando, M. 1975. Source mechanisms and tectonic significance of historical earthquakes along the Nankai Trough, Japan. *Tectonophysics*, **27** (2), 119–140. doi:10.1016/0040-1951(75)90102-X.

Araki, E., Saffer, D. M., Kopf, A. J., Wallace, L. M., Kimura, T., Machida, Y., Ide, S., Davis, E. and IODP Expedition 365 shipboard scientists. 2017. Recurring and triggered slow-slip events near the trench at the Nankai Trough subduction megathrust. *Science*, **356** (6343), 1157-1160. doi: 10.1126/science.aan3120.

Asanuma, H., Okada, Y., Fujisaki, W., Suzuki, K., Sato, T., Sawaki, Y., Sakata, S., Yamamoto, S., Hirata, T., Maruyama, S. and Windley, B. F. 2015. Reconstruction of ocean plate stratigraphy in the Gwna Group, NW Wales: Implications for the subduction–accretion process of a latest Proterozoic trench-forearc. *Tectonophysics*, **662**, 195-207.

Baba, T., Cummins, P.R. and Hori, T. 2005. Compound fault rupture during the 2004 off the Kii Peninsula earthquake (M 7.4) inferred from highly resolved coseismic sea-surface deformation. *Earth, Planets and Space*, **57** (3), 167–172. doi: http://www.terrapub.co.jp/journals/EPS/pdf/2005/5703/57030167.pdf.

Bachmann, R., Oncken, O., Glodny, J., Seifert, W., Georgieva, V. and Sudo, M. 2009. Exposed plate interface in the European Alps reveals fabric styles and gradients related to an ancient seismogenic coupling zone. *Journal of Geophysical Research*, **114** (B05402). doi: 10.1029/2008JB005927.

Bangs, N. L. B., Shipley, T. H., Moore, J. C. and Moore, G. F. 1999. Fluid accumulation and channeling along the northern Barbados Ridge décollement thrust. *Journal of Geophysical Research,* **104** (B9), 20.399e20.414.

Barber, A.J. and Max, M. D. 1979. A new look at the Mona Complex, Anglesey, North Wales. *Journal of the Geological Society of London*, **136**, 407–432.

Barker, S.L.L. and Cox, S.F. 2011. Oscillatory zoning and trace element incorporation in hydrothermal minerals: insights from calcite growth experiments. *Geofluids*, **11**, 48–56. doi: https://doi.org/10.1111/j.1468-8123.2010.00305.x.

Barker, S.L.L., Cox, S.F., Eggins, S.M. and Gagan, M.K. 2006. Microchemical evidence for episodic growth of antitaxial veins during fracture-controlled fluid flow. Earth and Planetary Science Letters, **250**, 331–344. doi: https://doi.org/10.1016/j.epsl.2006.07.051.

Bau, M. 1991. Rare-earth element mobility during hydrothermal and metamorphic fluid-rock interaction and the significance of the oxidation state of europium. *Chemical Geology*, **93**, 219–230.

Bau, M. and Möller, P. 1992. Rare Earth Element Fractionation in Metamorphogenic Hydrothermal Calcite , Magnesite and Siderite. *Mineralogy and Petrology*, **45**, 231–246.

Becker, K, Fisher, A.T, and Davis, E.E. 1997. The CORK experiment in hole 949C: long-term observations of pressure and temperature in the Barbados accretionary prism. *Proc. Ocean Drill. Program Sci. Results*. In: Shipley, T.H., Ogawa, Y. and Bahr, J.M. (eds.), 156, 247–252. College Station, TX: Ocean Drill. Program.

Becker, K., Kinoshita, M., Toczko, S. and the Expedition 380 Scientists. 2018. NanTroSEIZE Stage 3: Frontal Thrust Long-Term Borehole Monitoring System (LTBMS). *Proceedings of the Integrated Ocean Discovery Program, 380*. College Station, TX (International Ocean Discovery Program). doi: https://doi.org/10.14379/iodp.proc.380.2018.

Bekins, B. A. and Screaton, E. J. 2007. Pore pressure and fluid flow in the northern Barbados accretionary complex. In: Dixon, T. (ed.). *The Seismogenic Zone of Subduction Thrust Faults*, pp. 148–70, Columbia University Press, New York.

Bekins, B. A., McCaffrey, A. M., Dreiss, S. J. 1995. Episodic and constant flow models for the origin of low-chloride waters in a modern accretionary complex. *Water Resource Research*, **31**, 3205–3215.

Bettelli, G. 2002. Note illustrative della Carta Geologica d'Italia alla scala 1:50.000, Foglio 236 "Pavullo nel Frignano", ed. Servizio Geologico d'Italia, S.EL.CA., Firenze.

Bettelli, G. and Boccaletti, M. 2002. Note illustrative della Carta Geologica d'Italia alla scala 1:50.000, Foglio 252 "Barberino del Mugello", ed. Servizio Geologico d'Italia, S.EL.CA., Firenze.

Bettelli, G. and Panini, F. 1992. Liguridi, mélanges e tettoniti nel complesso caotico lungo la ‘‘linea del Sillaro’’ (Appennino Settentrionale, Province di Firenze e Bologna). *Memorie Descrittive della Carta Geologica d'Italia*, **46**, 387–415.

Bettelli, G., Panini, F. and Capitani, S. 2002. Carta Geologico-Strutturale dell'Appennino emiliano sudorientale. In: *Atti del terzo seminario sulla cartografia geologica, 26–27 February 2002, Bologna*, p. 47-52. Servizio Geologico Sismico e dei Suoli RER.

Bilek, S. L. and Lay, T. 2002. Tsunami earthquakes possibly widespread manifestations of frictional conditional stability. *Geophysical Research Letters*, **29** (14). doi:10.1029/2002GL015215.

Bilek, S. L. and Lay, T. 2018. Subduction zone megathrust earthquakes. *Geosphere* , **14** (4): 1468–1500. doi: https://doi.org/10.1130/GES01608.1.

Bird, P. Initiation of intracontinental subduction in the Himalaya. *Journal of Geophysical Research: Solid Earth*, **83** (B10), 4975-4987.

Bizzarri, A. and Cocco, M. 2006. A thermal pressurization model for the spontaneous dynamic rupture propagation on a three-dimensional fault: 1. Methodological approach. *Journal of Geophysical Research*, **111**, B05303. doi: https://doi.org/10.1029/2005JB003862.

Blanpied, M.L., Lockner, D.A. and Byerlee, J.D. 1995. Frictional slip of granite at hydrothermal conditions. *Journal of Geophysical Research*, **100**, 13045–13064. doi:10.1029/95JB00862.

Boccaletti, M., Elter, P. and Guazzone, G. 1971. Plate Tectonic Models for the Development of the Western Alps and Northern Apennines. *Nature Physical Science*, **234**, 108–111. doi: https://doi.org/10.1038/physci234108a0.

Bons, P.D., Elburg, M.A. and Gomez-rivas, E. 2012. A review of the formation of tectonic veins and their microstructures. *Journal of Structural Geology*, **43**, 33–62.

Borradaile, J. G. 1981. Particulate flow of rock and the formation of cleavage. *Tectonophysics*, **72**, 305–21.

Bortolotti, V., Principi, G. and Treves, B. 2001. Ophiolites, Ligurides and the tectonic evolution from spreading to convergence of a Mesozoic Western Tethys segment. In: Vai G. B. and Martini I. P. (eds.) *Anatomy of an Orogen: The Apennines and adjacent Mediterranean*, p. 151–164. Kluwer Academic Publishers, Great Britain, UK.

Botti, F., Aldega, L. and Corrado, S. 2004. Sedimentary and tectonic burial evolution of the Northern Apennines in the Modena-Bologna area: constraints from combined stratigraphic, structural, organic matter and clay mineral data of Neogene thrust-top basins. *Geodinamica Acta*, **17**, p. 185–203. doi: https://doi.org/10.3166/ga.17.185-203.

Botti, F., Daniele, G., Baldacci, F., Palandri, S., Ribolini, A.,Ungari, A. and Molli, G. 2011. Note illustrative della Carta Geologica d'Italia alla scala 1:50.000 – Foglio 251 Porretta Terme. Available at: http://www. isprambiente.gov.it/Media/carg/note_illustrative/251_Porretta_Terme.pdf.

Bourlange, S., Henry, P., Moore, J. C., Mikada, H. and Klaus, A. 2003. Fracture porosity in the décollement zone of Nankai accretionary wedge using Logging While Drilling resistivity data. *Earth and Planetary Science Letters*, **209** (1-2), 103-112. doi: 10.1016/S0012-821X(03)00082-7.

Brace, W. F. and Byerlee, J. D. 1966. Stick-Slip as a Mechanism for Earthquakes. *Science*, **153**, (3739), 990-992. doi: 10.1126/science.153.3739.990.

Brodsky, E. E., Saffer, D., Fulton, P., Chester, F., Conin, M., Huffman, K. and Moore, J. C. 2016. The post-earthquake stress state on the Tohoku megathrust as constrained by reanalysis of the JFAST breakout data. Geophysical Research *Letters*, **44** (16), 8294-8302.

Brown, K. M., Bekins, B. A., Clennell, B., Dewhurst, D., Westbrook, G. K. 1994. Heterogeneous hydrofracture development and accretionary fault dynamics. *Geology*, **22**, 259–262.

Brown, K. M., Saffer, D. M. and Bekins, B. A. 2001. Smectite diagenesis, pore-water freshening, and fluid-flow at the toe of the Nankai wedge. *Earth Planetary Science Letters*, **194** (1/2), p. 97-109.

Byerlee, J. 1978. Friction of rocks. *Pure and Applied Geophysics*, **116**, 615–626.

Byrne, T. and Fisher, D. 1990. Evidence for a weak and overpressured decollement beneath sediment-dominated accretionary prisms. *Journal of Geophysical Research*, **95**, 9081–9098.

Carmichael, R. S. 1982. Handbook of Physical Properties of *Rocks*. **2** Boca Raton, FL: CRC Press.

Carson, B., and Screaton, E.J. 1998. Fluid flow in accretionary prisms: Evidence for focused, time-variable discharge. *Reviews of Geophysics*, v. **36**, p. 329–351. doi:10.1029/97RG03633.

Cerchiari, A., Fukuchi, R., Gao, B., Hsiung, K.-H, Jaeger, D., Kaneki, S., Keller, J., Kimura, G., Kuo, S.-T., Lymer, G., Maison, T., Motohashi, G., Regalla, C., Singleton, D. and Yabe, S. 2018. IODP workshop: Core-Log Seismic Investigation at Sea - Integrating legacy data to address outstanding research questions in the Nankai Trough Seismogenic Zone Experiment. Scientific Drilling, 24, 93-107. doi: 10.5194/sd-24-93-2018.

Cerchiari, A., Remitti, F., Cipriani, A., Mittempergher, S., Festa, A. and Lugli, F. Structural and geochemical evidences of stress/fluid interplay during a seismic cycle in a tectonic mélange. *Journal of the Geological Society*, submitted.

Chester, F. M., Mori, J., Eguchi, N., Toczko, S. and the Expedition 343/343T Scientists. 2013. Proceedings of the Integrated Ocean Drilling Program, 343/343T. Tokyo (Integrated Ocean Drilling Program Management International, Inc.). doi: https://doi.org/10.2204/iodp.proc.343343T.2013.

Cibin, U., Spadafora, E., Zuffa, G. G. and Castellarin, A. 2001. Continental collision history from arenites of episutural basins in the Northern Apennines, Italy. *Geol. Soc. Am. Bull*., **113**, 4–19.

Collettini, C., Niemeijer, A.,Viti, C. and Marone, C. 2009. Fault zone fabric and fault weakness. *Nature*, **462**, 907–10.

Collins, A.S. and Buchan, C., 2004. Provenance and age constraints of the South Stack Group, Anglesey, UK: U–Pb SIMS detrital zircon data. *J. Geol. Soc. Lond*., **161**, 743–746.

Cowan, D.S. 1978. Origin of blueschist-bearing chaotic rocks in the Franciscan Complex, San Simeon, California. *Geological Society of America Bulletin*, **89**, 1415–1432. doi: 10.1130/0016-7606(1978)89<1415:OOBCRI.>2.0.CO;2.

Cowan, D.S. 1985. Structural style in Mesozoic and Cenozoic mélanges in the Western Cordillera of North America. *Geological Society of America Bulletin*, **96**, 451-462.

Coward, M. and Dietrich, D. 1989. Alpine tectonics - an overview. In: Coward, M. P., Dietrich, D. and Park, R. G. (eds), *Alpine Tectonics*, p. 1-29. Geological Society Special Publication.

Cox, S.F. 2010. The application of failure mode diagrams for exploring the roles of fluid pressure and stress states in controlling styles of fracture-controlled permeability enhancement in faults and shear zones. *Geofluids*, **10**, 217–233. doi: https://doi.org/10.1111/j.1468-8123.2010.00281.x.

Currie, C. A., Hyndman, R. D., Wang, K. and Kostoglodov, V. 2002. Thermal models of the Mexico subduction zone: Implications for the megathrust seismogenic zone. *Journal of Geophysical Research*, **107** (B12), 2730. doi: 10.1029/2001JB000886.

Dallmeyer, R. D. and Gibbons, W. 1987. The age of blueschist metamorphism in Anglesey, North Wales: evidence from ^{40}Ar/^{39}Ar mineral dates of the Penmynydd schists. *Journal of the Geological Society, London*, **144**, 843–852.

DeMets, C., Gordon, R. G. and Argus, D. F. 2010. Geologically current plate motions. *Geophysical Journal International*, **181** (1), 1–80. doi: https://doi.org/10.1111/j.1365-246X.2009.04491.x.

den Hartog, S. A. M., Peach, C., de Winter, D. A. M., Spiers, C. J. and Shimamoto, T. 2012. Frictional properties of megathrust fault gauges at low sliding velocities: New data on effects of normal stress and temperature. *Journal of Structural Geology*, **38**, 156-171.

Dielforder, A., Berger, A. and Herwegh, M. 2016. The accretion of foreland basin sediments during early stages of continental collision in the European Alps and similarities to accretionary wedge tectonics. *Tectonics*, **35,** 2216–2238.

Dielforder, A.,Vollstaedt, H.,Vennemann, T.,Berger, A. and Herwegh, M. 2015. Linking megathrust earthquakes to brittle deformation in a fossil accretionary complex. *Nature Communications*, **6**, 7504.

Dieterich, J.H. 1979. Modeling of rock friction: 1. Experimental results and constitutive equations. *J. Geophys. Res.*, **84** (B5), 2161. http://dx.doi.org/10.1029/JB084iB05p02161.

Dixon T. H. and Moore J. C. (eds), 2007. *The Seismogenic Zone of Subduction Thrust Faults*. 680 pp. New York, Columbia University Press.

Drury, M. R. 2005. Dynamic recrystallization and strain softening of olivine aggregates in the Laboratory and the Lithosphere. *Geological Society London Special Publications*, **243** (1).

Duarte, J.C., Schellart, W.P. and Cruden, A.R. 2015. How weak is the subduction zone interface? *Geophysical Research Letters*, **42**, 2664–2673. doi: https://doi.org/10.1002/2014GL062876.

Expedition 316 Scientists. 2009. Expedition 316 Site C0007. In: Kinoshita, M., Tobin, H., Ashi, J., Kimura, G., Lallemant, S., Screaton, E. J., Curewitz, D., Masago, H., Moe, K. T. and the Expedition 314/315/316 Scientists, *Proceedings of the Integrated Ocean Discovery Program*, **314/315/316**. Washington, DC (Integrated Ocean Drilling Program Management International, Inc.). doi: 10.2204/iodp.proc.314315316.135.2009.

Expedition 319 Scientists. 2010. Expedition 319 summary. In: Saffer, D., McNeill, L., Byrne, T., Araki, E., Toczko, S., Eguchi, N., Takahashi, K. and the Expedition 319 Scientists. *Proceedings of the Integrated Ocean Drilling Program*, **319**. Tokyo (Integrated Ocean Drilling Program Management International, Inc.). doi: http://dx.doi.org/10.2204/iodp.proc.319.101.2010.

Expedition 322 Scientists. 2010. Site C0011. In: Saito, S., Underwood, M. B., Kubo, Y. and the Expedition 322 Scientists. *Proceedings of the Integrated Ocean Drilling Program*, **322**. Tokyo (Integrated Ocean Drilling Program Management International, Inc.). doi: 10.2204/ iodp.proc.322.103.2010.

Fagereng, Å. 2011. Geology of the seismogenic subduction thrust interface. In: Fagereng, Å., Toy, V. G. e Rowland, J. V. (eds). Geology of the Earthquake Source: A Volume in Honour of Rick Sibson. *Geological Society of London*, Special Publication **359**, p. 319-331.

Fagereng, Å. 2013. On stress and strain in a continuous-discontinuous shear zone undergoing simple shear and volume loss. *Journal of Structural Geology*, **50**, 44-53.

Fagereng, Å. and Ellis, S. 2009. On factors controlling the depth of interseismic coupling on the Hikurangi subduction interface, New Zealand. *Earth and Planetary Science Letters*, **278** (1–2), 120-130. doi: https://doi.org/10.1016/j.epsl.2008.11.033.

Fagereng, Å and Sibson, R.H. 2010. Mélange rheology and seismic style. *Geology*, **38**, p. 751-754. doi: 10.1130/G30868.1.

Fagereng, Å, Diener, J.F.A., Ellis, S., and Remitti, F. 2018. Fluid-related deformation processes at the up- and downdip limits of the subduction thrust seismogenic zone: What do the rocks tell us? In: Byrne, T., Underwood, M.B., Fisher, D., McNeill, L., Saffer, D., Ujiie, K., and Yamaguchi, A. (eds.). Geology and Tectonics of Subduction Zones: A Tribute to Gaku Kimura. *Geological Society of America Special Paper*, **534**, p. 187–215. doi: https://doi.org/10.1130/2018.2534(12).

Fagereng, Å., Hillary, G.W. and Diener, J.F. 2014. Brittle-viscous deformation, slow slip, and tremor. *Geophysical Research Letters*, **41**, 4159–4167. doi: 10.1002/2014GL060433.

Fagereng, Å., Remitti, F. and Sibson, R.H. 2010. Shear veins observed within anisotropic fabric at high angles to the maximum compressive stress. *Nature Geoscience*, **3**, 482–485. doi: https://doi.org/10.1038/ngeo898.

Fagereng, A., Remitti, F. and Sibson, R. H. 2011. Incrementally developed slickenfibers - Geological record of repeating low stress-drop seismic events? *Tectonophysics*, **510**, 381–386.

Faulkner, D. R., Sanchez-Roa, C., Boulton, C., and den Hartog, S. A. M. 2018. Pore fluid pressure development in compacting fault gouge in theory, experiments, and nature. Journal of Geophysical Research. *Solid Earth*, **123**, 226–241. doi: https://doi.org/10.1002/2017JB015130.

Festa, A., Pini, G. A., Ogata, K. and Dilek, Y. 2019. Diagnostic features and field-criteria in recognition of tectonic, sedimentary and diapiric mélanges in orogenic belts and exhumed subduction-accretion complexes. *Gondwana Research*, **74**, 7–30. doi: https://doi.org/10.1016/j.gr.2019.01.003.

Fisher, A.T., Cowen, J., Wheat, C. G. and Clark J. F. 2011. Preparation and injection of fluid tracers during IODP Expedition 327, eastern flank of Juan de Fuca Ridge. In: Fisher A. T., Tsuji T., Petronotis K. and the Expedition 327 Scientists. Proceedings of the Integrated Ocean Drilling Program, 327, Tokyo (Integrated Ocean Drilling Program Management International, Inc.). doi:10.2204/iodp.proc.327.108.2011.

Fisher, D.M. and Byrne, T. 1987. Structural evolution of underthrusted sediments, Kodiak Islands, Alaska. *Tectonics,* **6**, p. 775-793. doi: https://doi.org/10.1029/TC006i006p00775.

Fisher, D. M., Brantley, S.L., Everett, M. and Dzvonik, J. 1995. Cyclic fluid flow through a regionally extensive fracture network within the Kodiak accretionary prism. *Journal of Geophysical Research*, **100**, 12881–12894.

Frank, W. B., Shapiro, N. M., Husker, A. L., Kostoglodov, V., Bhat, H. S., and Campillo, M. 2015. Along-fault pore-pressure evolution during a slow-slip event in Guerrero, Mexico. *Earth and Planetary Science Letters,* **413**, 135–143. doi: https://doi.org/10.1016/j.epsl.2014.12.051.

Fujiwara, T., Kodaira, S., No, T., Kaiho, Y., Takahashi, N. and Kaneda, Y. 2011. The 2011 Tohoku-oki earthquake: displacement reaching the trench axis. *Science*, **334**, 1240.

Gao, X. and Wang, K. 2014. Strength of stick-slip and creeping subduction megathrusts from heat flow observations. *Science*, **345** (6200), 1038-41. doi: 10.1126/science.

Gao, S. and Wedepohl, K. H. 1995. The negative Eu anomaly in Archean sedimentary rocks: Implications for decomposition, age and importance of their granitic sources. *Earth and Planetary Science Letters*, **133**, 81-94.

Garagash, D. I. 2012. Seismic and aseismic slip pulses driven by thermal pressurization of pore fluid. Journal of Geophysical Research, 117, B04314. doi: https://doi.org/10.1029/2011JB008889.

Gibbons, W. and Horák, J. 1990. Contrasting metamorphic terranes in northwest Wales. In: D'Lemos, R.S., Strachan, R.A. and Topley, C.G. (eds.). The Cadomian Orogeny. *Geological Society of London, Special Publication*, **51**, 315–327.

Gibbons, W., Tietzsch-Tyler, D., Horák, J.M. and Murphy, F.C. 1994. Precambrian rocks in Anglesey, southwest Llŷn and southeast Ireland. In: Gibbons, W. and Harris, A.L. (eds.). *A Revised Correlation of Precambrian Rocks in the British Isles: Special Report 25, London*. Geological Society of London, pp. 75–84.

Goldstein, R. H. and Reynolds, T. J. 1994. Systematics of fluid inclusions in diagenetic minerals. SEPM Short Course 31. Society for Sedimentary Geology.

Gomberg, J., Bodin, P., Larson, K. and Dragert, H. 2004. Earthquake nucleation by transient deformations caused by the M ¼ 7.9 Denali, Alaska, earthquake. *Nature*, **427**, p. 620-624.

Greenly, E. 1919. *The Geology of Anglesey, Memoir Geological Survey of Great Britain*, vol. 2. HMSO, London, 980 pp.

Griffith, A. A. 1924. The theory of rupture. *Proc. 1st Intern. Congr. Appl. Mech.*, Delft, 55-63.

Griggs, D. 1967, Hydrolytic Weakening of Quartz and Other Silicates. Geophysical Journal of the Royal Astronomical Society, **14**, 19-31. doi:10.1111/j.1365-246X.1967.tb06218.x.

Gromet, L. P., Dymek, R. F., Haskin, L. A. and Korotev, R. L. 1984. The "North American shale composite": Its compilation, major and trace element characteristics. *Geochimica et cosmochimica acta*, **48**, 2469-2482.

Haines, S.H., van der Pluijm, B. A., Ikari, M. J., Saffer, D. M. and Marone, C. 2009. Clay fabric intensity in natural and artificial fault gouges: implications for brittle fault zone processes and sedimentary basin clay fabric evolution. *Journal of Geophysical Research*, **114**, B05406

Hardebeck, J. L. 2017. The spatial distribution of earthquake stress rotations following large subduction zone earthquakes. *Earth, Planets and Space*, **69**, 69.

Hasegawa, A., Yoshida, K. and Okada, T. 2011. Nearly complete stress drop in the 2011 M w 9.0 off the Pacific coast of Tohoku Earthquake. *Earth Planets Space*, **63**, 703–707. doi: https://doi.org/10.5047/eps.2011.06.007.

Hasegawa, A., Yoshida, K., Asano, Y., Okada, T., Iinuma, T. and Ito, Y. 2012. Change in stress field after the 2011 great Tohoku-Oki earthquake. *Earth and Planetary Science Letters*, **355–356**, 231–243 doi: https://doi.org/10.1016/j.epsl.2012.08.042

Henderson, P. 1984. Rare earth element geochemistry. *Developments in Geochemistry*, vol. **2**, Elsevier, Oxford.

Henry, P. 2000. Fluid flow at the toe of the Barbados accretionary wedge constrained by thermal, chemical, and hydrogeologic observations and models. *Journal of Geophysical Research*, **105**, 25855–25872.

Henry, P., Foucher, J.-P., Le Pichon, X., Sibuet, M., Kobayashi, K., Tarits, P., Chamot-Rooke, N., Furuta, T. and Schultheiss, P. 1992. Interpretation of temperature measurements from the Kaiko-Nankai cruise: modeling of fluid flow in clam colonies. *Earth and Planetary Science Letters*, **109**, 355–71.

Henry, P., Kanamatsu, T., Moe, K. and the Expedition 333 Scientists. 2012. *Proceedings of the Integrated Ocean Drilling Program, 333*. Tokyo (Integrated Ocean Drilling Program Management International, Inc.). doi: http://dx.doi.org/10.2204/iodp.proc.333.2012.

Henry, P., Lallemant, S., Nakamura, K., Tsunogai, U., Mazzotti, S. and Kobayashi, K. 2002. Surface venting at the toe of the Nankai wedge and implications for flow paths. *Marine Geology*, **187**, 119–43.

Hori, T., Kato, N., Hirahara, K., Baba, T., and Kaneda, Y. 2004. A numerical simulation of earthquake cycles along the Nankai Trough in southwest Japan: lateral variation in frictional property due to the slab geometry controls the nucleation position. *Earth and Planetary Science Letters*, **228** (3–4), 215–226. doi:10.1016/j.epsl.2004.09.033.

Housen, B.A., Tobin, H. J., Labaume, P., Leitch, E.C., Maltman, A. J. and Ocean Drilling Program Leg 156 Shipboard Science Party 1996. Strain decoupling across the decollement of the Barbados accretionary prism. *Geology*, **24**, 127–130.

Hyndman, R. D. 2007. The Seismogenic Zone of Subduction Thrust Faults: What We Know and Don’t Know. In: Dixon T. H. and Moore J. C. (eds.) *The Seismogenic Zone of Subduction Thrust Faults*. 680 pp. New York, Columbia University Press.

Hyndman, R. D. and Wang, K. 1993. Thermal constraints on the zone of major thrust earthquake failure: The Cascadia Subduction Zone. *Journal of Geophysical Research: Solid Earth*, **98** (B2), 2039-2060. doi: https://doi.org/10.1029/92JB02279.

Hyndman, R. D., Wang, K., and Yamano, M. 1995. Thermal constraints on the seismogenic portion of the southwestern Japan subduction thrust. *Journal of Geophysical Research*, **100** (B8), 15373– 15392. doi:10.1029/95JB00153.

Hyndman, R. D., Yamano, M. and Oleskevich, D. A. 1997. The seismogenic zone of subduction thrust faults. *Island Arc*, **6**, 244-260. doi:10.1111/j.1440-1738.1997.tb00175.x.

Ichinose, G.A., Thio, H.K., Somerville, P.G., Sato, T. and Ishii, T. 2003. Rupture process of the 1944 Tonankai earthquake (Ms 8.1) from the inversion of teleseismic and regional seismograms. *Journal of Geophysical Research: Solid Earth*, **108** (B10), 2497. doi: http://dx.doi.org/10.1029/2003JB002393.

Ide, S., Baltay, A. and Beroza, G. C. 2011. Shallow dynamic overshoot and energetic deep rupture in the 2011 Mw 9.0 Tohoku-Oki earthquake. *Science,* **332** (6036), 1426-1429.

Ienaga, M., McNeill, L. C., Mikada, H., Saito, S., Goldberg, D. and Moore, J. C. 2006. Borehole image analysis of the Nankai Accretionary Wedge, ODP Leg 196: Structural and stress studies. *Tectonophysics,* **426** (1-2), 207-220. doi: 10.1016/j.tecto.2006.02.018.

Ikari, M. J., Ito, Y., Ujiie, K. and Kopf, A.J. 2015a. Spectrum of slip behaviour in Tohoku fault zone samples at plate tectonic slip rates. *Nature Geoscience*, **8**, p. 870–874. doi: https://doi.org/10.1038/ngeo2547.

Ikari, M.J., Kameda, J., Saffer, D.M. and Kopf, A.J. 2015b. Strength characteristics of Japan Trench borehole samples in the high-slip region of the 2011 Tohoku-oki earthquake. *Earth and Planetary Science Letters,* **412**, p. 35–41. doi: https://doi.org/10.1016/j.epsl.2014.12.014.

Ito, Y. and Obara, K. 2006. Very low frequency earthquakes within accretionary prisms are very low stress-drop earthquakes. *Geophys. Res. Lett*., **33** (9), L09302. doi: 10.1029/2006GL025883.

Ito, Y., Hino, R., Kido, M., Fujimoto, H., Osada, Y., Inazu, D., Ohta, Y., Iinuma, T., Ohzono, M., Miura, S., Mishina, M., Suzuki, K., Tsuji, T. and Ashi, J. 2013. Episodic slow slip events in the Japan subduction zone before the 2011 Tohoku-Oki earthquake. *Tectonophysics*, **600**, 14–26. doi: https://doi.org/10.1016/j.tecto.2012.08.022.

Ito, Y., Obara, K., Shiomi, K., Sekine, S. and Hirose, H. 2007. Slow earthquakes coincident with episodic tremors and slow slip events. *Science*, **315** (5811), 503–506. doi: 10.1126/science.1134454.

Jochum, K.P., Hofmann, A.W., Herwig, K., Lammel, E., Stoll, B. & Nohl, U. 2007. GeoReM: A New Geochemical Database for Reference Materials and Isotopic Standards. Geostandards and Geoanalytical Research, **29**, 333–338. doi: https://doi.org/10.1111/j.1751-908x.2005.tb00904.x.

Kaneda, Y. 2014. Introduction to ocean floor networks and their scientific application. *Marine Geophysical Research*, **35**, 177. doi: https://doi.org/10.1007/s11001-014-9232-x.

Kawai, T., Windley, B.F., Terabayashi, M., Yamamoto, H., Maruyama, S. and Isozaki, Y. 2006. Mineral isograds and zones of the Anglesey blueschist belt, UK: implications for the metamorphic development of a subduction–accretion complex. *Journal of Metamorphic Geology*, **24**, 591–602.

Kawai, T., Windley, B. F., Terabayashi, M., Yamamoto, H., Maruyama, S. and Isozaki, Y. 2007. Geotectonic framework of the blueschist unit on Anglesey–Lleyn, UK, and its role in the development of a Neoproterozoic accretionary orogeny. *Precambrian Research,* **153**, 11–28.

Kimura, G., Moore, G.F., Strasser, M., Screaton, E., Curewitz, D., Streiff, C. and Tobin, H. 2011. Spatial and temporal evolution of the megasplay fault in the Nankai Trough. *Geochem., Geophys., Geosyst.*, **12** (3), Q0A008. doi:10.1029/2010GC003335.

Kimura, G., Screaton, E. J., Curewitz, D. and the Expedition 316 Scientists: NanTroSEIZE Stage 1A: NanTroSEIZE shallow megasplay and frontal thrusts. *IODP Preliminary Reports*, **316**. doi: https://doi.org/10.2204/iodp.pr.316.2008.

Kimura, G., Yamaguchi, A., Hojo, M., Kitamura, Y., Kameda, J., Ujiie, K., Hamada, Y., Hamahashi, M. and Hina, S. 2012. Tectonic mélange as fault rock of subduction plate boundary. *Tectonophysics*, **568–569**, p. 25-38. doi: https://doi.org/10.1016/j.tecto.2011.08.025

Kinoshita, M., Tobin, H., Ashi, J., Kimura, G., Lallemant, S., Screaton, E.J., Curewitz, D., Masago, H., Moe, K.T. and the Expedition 314/315/316 Scientists, 2009. *Proceedings IODP, 314/315/316*. Washington, DC (Integrated Ocean Drilling Program Management International, Inc.). doi:10.2204/iodp.proc.314315316.2009.

Kinoshita, M., Tobin, H., Moe, K. T. and the Expedition 314 Scientists. NanTroSEIZE Stage 1A: NanTroSEIZE LWD transect. *IODP Preliminary Reports*, **314**. doi: https://doi.org/10.2204/iodp.pr.314.2008.

Kirkpatrick, J. D., et al. 2015. Structure and lithology of the Japan Trench subduction plate boundary fault. *Tectonics*, **34**, 53–69, doi: 10.1002/2014TC003695.

Kita, I., Matsuo, S. and Wakita, H. 1982. H_2 Generation by reaction between H_2O and crushed rock: an experimental study on H_2 degassing from the active fault zone. *Journal of Geophysical Research*, **87**, B13.

Kitajima, H. and Saffer, D. M, 2012. Elevated pore pressure and anomalously low stress in regions of low frequency earthquakes along the Nankai Trough subduction megathrust. *Geophysical Research Letters*, **39** (L23301).

Kitajima, H., Saffer, D., Sone, H., Tobin, H. and Hirose, T. 2017. In situ stress and pore pressure in the deep interior of the Nankai accretionary prism, integrated Ocean Drilling Program Site C0002. *Geophysical Research Letters*, **44**, 9644–9652. doi: https://doi.org/10.1002/2017GL075127.

Knipe, R. J. 1986. Deformation mechanism path diagrams for sediments undergoing lithification. In: Moore, J. C. (ed.) *Structural Fabric in Deep Sea Drilling Project Cores from Forearcs*, Geological Society of America Memoires no. 166, p. 151–160.

Kodaira, S., No, T., Nakamura, Y., Fujiwara, T., Kaiho, Y., Miura, S., Takahashi, N., Kaneda, Y., and Taira, A., 2012. Coseismic fault rupture at the trench axis during the 2011 Tohoku-oki earthquake. *Nature Geoscience*, v. **5**, p. 646–650. doi:10.1038/ngeo1547.

Koehn, D. and Passchier, C.W. 2000. Shear sense indicators in striped bedding-veins. *Journal of Structural Geology*, **22**, 1141–1151, doi: https://doi.org/10.1016/S0191-8141(00)00028-6.

Kopf, A., Araki, E., Toczko, S. and the Expedition 332 Scientists, 2011. *Proceedings of the Integrated Ocean Drilling Program, 332*. Tokyo (Integrated Ocean Drilling Program Management International, Inc.). doi: http://dx.doi.org/10.2204/iodp.proc.332.2011.

Kopf, A., Saffer, D., Toczko, S., Araki, E., Carr, S., Kimura, T., Kinoshita, C., Kobayashi, R., Machida, Y., Rösner, A., and Wallace, L.M. 2017. Expedition 365 summary. With contributions by S. Chiyonobu, K. Kanagawa, T. Kanamatsu, G. Kimura, and M.B. Underwood. In: Saffer, D., Kopf, A., Toczko, S., and the Expedition 365 Scientists. *NanTroSEIZE Stage 3: Shallow Megasplay Long-Term Borehole Monitoring System.* Proceedings of the International Ocean Discovery Program, **365**: College Station, TX (International Ocean Discovery Program). doi: https://doi.org/10.14379/iodp.proc.365.101.2017.

Labaume, P., Berty, C. and Laurent, P. H. 1991. Syndiagenetic evolution of shear structure in superficial nappes: an example from the Northern Apennines (NW Italy). *Journal of Structural Geology*, **13**, 385–98.

Labaume, P., Kastner, M., Trave, A. and Henry, P. 1997. Carbonate veins from the décollement zone at the toe of the northern Barbados accretionary prism: microstructure, mineralogy, geo-chemistry, and relations with prism structure and fluid regime. In: Shipley, T. H., Ogawa, Y., Blum, P. and Bahr, J. M. (eds.) *Proceedings of the Ocean Drilling Program Scientific Results*. p. 79–96. Ocean Drilling Program no. 156, College Station, Texas.

Lacroix, B., Travé, A., Buatier, M., Labaume, P., Vennemann, T. and Dubois, M. 2014. Syntectonic fluid- flow along thrust faults: Example of the South-Pyrenean fold-and-thrust belt. *Marine and Petroleum Geology*, **49**, 84–98. doi: https://doi.org/10.1016/j.marpetgeo.2013.09.005

Lamb, S. 2006. Shear stresses on megathrusts: Implications for mountain building behind subduction zones. *Journal of Geophysical Research*, **111**, 1–24. doi: https://doi.org/10.1029/2005JB003916.

Landuzzi, A. 2004. *Syn-Depositional emplacement of the Liguride allochton in the Miocene foredeep of the Western Romagna Apennines in Mapping Geology in Italy* (eds. Pasquaré, G. and Venturini, C.), 220-226. APAT.

Le Pichon, X., Henry, P., Lallemant, S. 1990. Water flow in the Barbados accretionary complex. *Journal of Geophysical Research*, **95**, 8945–67.

Lin, W., Byrne, T. B., Kinoshita, M., McNeill, L. C., Chang, C., Lewis, J. C., Yamamoto, Y., Saffer, D. M., Moore, J. C., Wue, H.-Y., Tsuji, T., Yamada, Y., Conin, M., Saito, S., Iton, T., Tobin, H. J., Kimura, G., Kanagawa, K., Ashi, J., Underwood, M. B. and Kanamatsu, T. 2016. Distribution of stress state in the Nankai subduction zone, southwest Japan and a comparison with Japan Trench. *Tectonophysics*, **692**, 120–130. doi: http://dx.doi.org/10.1016/j.tecto.2015.05.008.

Lin, W., Faure, M., Chen, Y., Ji, Wenbin., Wang, F., Wu. L., Charles, N., Wang, J. and Wang, Q. 2013. Late Mesozoic compressional to extensional tectonics in the Yiwulüshan massif, NE China and its bearing on the evolution of the Yinshan-Yanshan orogenic belt: Part I: Structural analyses and geochronological constraints. *Gondwana Research*, **23** (1), 54-77.

Lockner, D. A. and Byerlee, J. D. 1994. Dilatancy in hydraulically isolated faults and the suppression of instability. *Geophysical Research Letters*, **21**, 2353–2356. doi: https://doi.org/10.1029/94GL02366.

Logan, B.W. and Semeniuk, V. 1976. Dynamic metamorphism: processes and products in Devonian carbonate rocks, Canning Basin, Western Australia. *Geological Society of Australia*, vol. **6**.

Logan, J. M., Dengo, C.A., Higgs, N.G. and Wang, Z. Z. 1992. Fabrics of experimental fault zones: their development and relationship to mechanical behavior, In: Evans, B. and Wong, T.-F. (eds.) *Fault Mechanics and Transport Properties of Rocks*, p. 33–67. San Diego, Calif. Academic.

Lucente, C.C. and Pini, G. A. 2008. Basin-wide masswasting complexes as markers of the Oligo-Miocene foredeep-accretionary wedge evolution in the Northern Apennines, Italy. *Basin Research*, **20**, 49–81.

Maltman, A. (Ed.) 1994. *The Geological Deformation of Sediments*, Springer, 307 p.

Marone, C. and Saffer, D. Fault Friction and the Upper Transition from Seismic to Aseismic Faulting. In: Dixon T. H. and Moore J. C. (eds), 2007. *The Seismogenic Zone of Subduction Thrust Faults*. 680 pp. New York, Columbia University Press.

Marroni, M., Meneghini, F. and Pandolfi, L. 2010. Anatomy of the Ligure-Piemontese subduction system: Evidence from Late Cretaceous-middle Eocene convergent margin deposits in the Northern Apennines, Italy. *International Geology Review*, **52**, 1160–92.

Maruyama, S. 1997. Pacific-type orogeny revisited: Miyashiro-type orogeny proposed. *Island Arc*, **6**, 91–120.

Maruyama, S., Kawaii, T. and Windley, B. F. Ocean plate stratigraphy and its imbrication in an accretionary orogen: the Mona Complex, Anglesey–Lleyn, Wales, UK. In: Kusky, T. M., Zhai, M.-G. and Xiao, W. (eds). *The Evolving Continents: Understanding Processes of Continental Growth*. Geological Society, London, Special Publications, **338**, 55–75.

Maruyama, S., Liou, J.G. and Terabayashi, M. 1996. Blueschists and eclogites of the world and their exhumation. *Int. Geol. Rev.*, **38**, 485–594.

Matsuda, T. and Isozaki, Y. 1991. Well-documented travel history of Mesozoic pelagic chert in Japan: from remote ocean to subduction zone. *Tectonics*, **10**, 475–499.

McCann, W.R., Nishenko, S.P., Sykes, L.R. and Krause, J. 1979. Seismic gaps and plate tectonics: Seismic potential for major boundaries. *Pure and Applied Geophysics*, **117** (6): 1082. doi: https://doi.org/10.1007/BF00876211

McGinty, P., Reyners, M. and Robinson, R. 2000. Stress directions in the shallow part of the Hikurangi subduction zone, New Zealand, from the invertion of earthquake first motions. *Geophys. J. Int.*, **142**, 339-350.

McIlroy, D. and Horák, J. 2006. Neoproterozoic: the late Precambrian terranes that formed Eastern Avalonia. In: Brenchley, P. and Rawson, P. (eds.). *The Geology of England and Wales*. Geological Society of London, pp. 9–23.

McLennan, S.M. 1989. Rare Earth Elements in Sedimentary Rocks: Influence of Provenance and Sedimentary Process. *Review of Mineralogy*, **21**, 169-200.

McNally, K. C. and Minster, J. B. 1981. Nonuniform seismic slip rates along the Middle America Trench. *Journal of Geophysical Research*, **86** (B6), 4949– 4959. doi: 10.1029/JB086iB06p04949.

Meneghini, F. and Moore, J.C. 2007. Deformation and hydrofracture in a subduction thrust at seismogenic depths: The Rodeo Cove thrust zone, Marin Headlands, California. *GSA Bulletin*, **119**, 174–183. doi: https://doi.org/10.1130/B25807.1

Meneghini, F., Marroni, M. and Pandolfi, L. 2007. Fluid flow during accretion in sediment-dominated margins: Evidence of a high-permeability fossil fault zone from the Internal Ligurian accretionary units of the Northern Apennines, Italy. *Journal of Structural Geology*, **29**, 515-529

Mikada, H., Becker, K., Moore, J. C. and Klaus, A. 2002. ODP Leg 196: Logging-while-drilling and advanced CORKS at the Nankai trough accretionary prism. *JOIDES Journal*, **28** (2), 8-12.

Mitchell, T. M. and Faulkner, D. M. 2012. Towards quantifying the matrix permeability of fault damage zones in low porosity rocks. *Earth and Planetary Science Letters*, **339**, 24-31.

Mittempergher, S., Cerchiari, A., Remitti, F. and Festa, A. 2018. From soft sediment deformation to fluid assisted faulting in the shallow part of a subduction megathrust analogue: the Sestola

Vidiciatico tectonic Unit (Northern Apennines, Italy). *Geological Magazine*, **155** (2), p. 438–450. doi: https://doi.org/10.1017/S0016756817000668

Miyazaki, S. and Heki, K. 2001. Crustal velocity field of southwest Japan: subduction and arc-arc collision. *Journal of Geophysical Research: Solid Earth*, **106** (B3), 4305–4326. doi:10.1029/2000JB900312.

Moore, J.C., Klaus, A. and the ODP Shipboard Scientific Party. 1998. Proceedings of the ODP, Initial Reports, 171A, College Station, TX (Ocean Drilling Program).

Moore, J. C. and Saffer, D. 2001. Updip limit of the seismogenic zone beneath the accretionary prism of southwest Japan: An effect of diagenetic to low-grade metamorphic processes and increasing effective stress. *Geology*, **29** (2), p. 183–186. doi: https://doi.org/10.1130/0091-7613(2001)029<0183:ULOTSZ>2.0.CO;2

Moore, G. F., Bangs, N. L., Taira, A., Kuramoto, S., Pangborn, E. and Tobin, H. J. 2007. Three-dimensional splay fault geometry and implications for tsunami generation. *Science*, **318**, 1128–1131.

Moore, G. F., Boston, B. B., Strasser, M., Underwood, M. B. and Ratliff, R. A. 2015. Evolution of tectono-sedimentary systems in the Kumano Basin, Nankai Trough forearc. *Mar. Petrol. Geol.*, **67**, 604–616. doi: https://doi.org/10.1016/j.marpetgeo.2015.05.032.

Moore, G.F., Mikada, H., Moore, J.C., Becker, K. and Taira, A. 2005. Legs 190 and 196 synthesis: deformation and fluid flow processes in the Nankai Trough accretionary prism. In: Mikada, H., Moore, G.F., Taira, A., Becker, K., Moore, J.C., and Klaus, A. (eds.). *Proceedings of the Ocean Drilling Program, Scientific Results, 190/196.* College Station, TX (Ocean Drilling Program), 1–25. doi: http://dx.doi.org/10.2973/odp.proc.sr.190196.201.2005.

Moore, J.C., Moore, G.F., Cochrane, G.R. and Tobin, H.J., 1995a. Negative polarity seismic reflections along fault of the Oregon accretionary prism: Indicators of overpressuring. *Journal of Geophysical Research,* **100** (B7). doi: 12.895e12.906.

Moore, G. F., Park, J.-O., Bangs, N. L., Gulick, S. P., Tobin, H. J., Nakamura, Y., Sato, S., Tsuji, T., Yoro, T., Tanaka, H., Uraki, S., Kido, Y., Sanada, Y., Kuramoto, S., and Taira, A. 2009. Structural and seismic stratigraphic framework of the NanTro-SEIZE Stage 1 transect. In: Kinoshita, M., Tobin, H., Ashi, J., Kimura, G., Lallement, S., Screaton, E. J., Curewitz, D., Masago, H., Moe, K.

T. and the Expedition 314/315/316 Scientists (eds.). *Proceedings of the International Ocean Drilling Program, 314/315/316.* Washington DC (Integrated Ocean drilling Program Management International, Inc.). doi: https://doi.org/10.2204/iodp.proc.314315316.102.2009.

Moore, J.C., Shipley, T., Goldberg, D., et al., 1995b. Abnormal fluid pressures and fault-zone dilation in the Barbados accretionary prismdevidence from logging while drilling. *Geology,* **23**, 605-608.

Moore, G.F., Taira, A., Klaus, A., Becker, L., Boeckel, B., Cragg, B.A., Dean, A., Fergusson, C.L., Henry, P., Hirano, S., Hisamitsu, T., Hunze, S., Kastner, M., Maltman, A.J., Morgan, J.K., Murakami, Y., Saffer, D.M., Sánchez-Gómez, M., Screaton, E.J., Smith, D.C., Spivack, A.J., Steurer, J., Tobin, H.J., Ujiie, K., Underwood, M.B. and Wilson, M. 2001. New insights into deformation and fluid flow processes in the Nankai Trough accretionary prism: results of Ocean Drilling Program Leg 190. *Geochemistry, Geophysics, Geosystems*, **2** (10), 1058. doi: http://dx.doi.org/10.1029/2001GC000166.

Moreno, M., Haberland, C., Oncken, O., Rietbrock, A., Angiboust, S. & Heidbach, O. 2014. Locking of the Chile subduction zone controlled by fluid pressure before the 2010 earthquake. *Nature Geoscience*, **7**, 292–6. doi:10.1038/ngeo2102.

Nakamura, M. and Sunagawa, N. 2015. Activation of very low frequency earthquakes by slow slip events in the Ryukyu Trench. *Geophysical Research Letters*, **42**, 1076–1082.

Nakanishi, A., Takahashi, N., Park, J.-O., Miura, S., Kodaira, S., Kaneda, Y., Hirata, N., Iwasaki, T. and Nakamura, M. 2002. Crustal structure across the coseismic rupture zone of the 1944 Tonankai earthquake, the central Nankai Trough seismogenic zone. *Journal of Geophysical Research: Solid Earth*, **107** (B1). doi: http://dx.doi.org/10.1029/2001JB000424.

Needham, D.T., 1995. Mechanisms of me´lange formation: examples from SW Japan and Southern Scotland. Journal of Structural Geology, **17**, 971-985.

Noda, H. 2016. Implementation into earthquake sequence simulations of a rate- and state-dependent friction law incorporating pressure solution creep. *Geophysical Journal International*, **205** (2), 1108–1125. doi: http://dx.doi.org/10.1093/gji/ggw058.

Noda, H. and Lapusta, N. 2010. Three-dimensional earthquake sequence simulations with evolving temperature and pore pressure due to shear heating: Effect of heterogeneous hydraulic diffusivity. *Journal of Geophysical Research*, **115**, B12314. doi: https://doi.org/10.1029/2010JB007780.

Noda, H. and Shimamoto, T. 2010. A rate- and state-dependent ductile flow law of polycrystalline halite under large shear strain and implications for transition to brittle deformation. *Geophysical Research Letters*, **37** (9). doi: http://dx.doi.org/10.1029/2010GL042512.

Norabuena, E., Dixon, T. H., Schwartz, S. Y., DeShon, H., Newman, A., Protti, M., Gonzalez, V., Dorman, L., Flueh, E. R., Lundgren, P., Pollitz, F. and Sampson, D. 2004. Geodetic and seismic constraints on some seismogenic zone processes in Costa Rica. *Journal of Geophysical Research*, **109** (B11403). doi: 10.1029/2003JB002931.

Norabuena, E., Leffler-Griffin, L., Mao, A., Dixon, T., Stein, S., Sacks, S. I., Ocola, L. And Ellis, M. 1998. Space Geodetic Observations of Nazca-South America Convergence Across the Central Andes. *Science*, **279** (5349), 358-362. doi: 10.1126/science.279.5349.358.

Obana, K. and Kodaira, S. 2009. Low-frequency tremors associated with reverse faults in a shallow accretionary prism. *Earth and Planetary Science Letters*, **287** (1), p. 168-174. doi: 10.1016/j.epsl.2009.08.005.

Obana, K., Kodaira., S. and Yoshiyuki, K. 2005. Seismicity in the incoming/subducting Philippine Sea plate off the Kii Peninsula, central Nankai Trough. *Journal of Geophysical Research: Solid Earth*, **110** (B11), B11311. doi: 10.1029/2004JB003487.

Obana, K., Kodaira, S., Mochizuki, K. and Shinohara, M. 2001. Micro-seismicity around the seaward updip limit of the 1946 Nankai earthquake dislocation area. Geophysical Research Letters, **28** (12), 2333–2336. doi: http://dx.doi.org/10.1029/2000GL012794.

Obara, K. 2002. Nonvolcanic deep tremor associated with subduction in southwest Japan. *Science*, **296**, p. 1679–1681.

Obara, K. and Ito, Y. 2005. Very low frequency earthquakes excited by the 2004 off the Kii peninsula earthquakes: A dynamic deformation process in the large accretionary prism. Earth, *Planets and Space*, **57**, BF03352570.

Okubo, P.G. 1989. Dynamic rupture modeling with laboratory-derived constitutive relations. *J. Geophys. Res.*, **94** (B9), 12321. doi: http://dx.doi.org/10.1029/JB094iB09p12321.

Oleskevich, D.A., Hyndman, R.D. and Wang, K. 1999. The updip and downdip limits to great subduction earthquakes: Thermal and structural models of Cascadia, south Alaska, SW Japan, and Chile. *Journal of Geophysical Research,* **104**, p. 14,965–14,991. doi: https://doi.org/10.1029/1999JB900060

Oliver, N.H.S. and Bons, P.D. 2001. Mechanisms of fluid flow and fluid–rock interaction in fossil metamorphic hydrothermal systems inferred from vein–wallrock patterns, geometry and microstructure. *Geofluids*, **1**, 137-162.

Park, J.O., Fujie, G., Wijerathne, L., Hori, T, Kodaira, S., Fukao, Y.,Moore, G. F.,Bangs, N. L.,Kuramoto, S. and Taira, A. 2010. A low velocity zone with weak reflectivity along the Nankai subduction zone. *Geology*, **38**, 283–286.

Park, J.-O., Tsuru, T., Kodaira, S., Cummins, P. R. and Kaneda, Y. 2002. Splay Fault Branching Along the Nankai Subduction Zone. *Science*, **297**, 1157–1160.

Passchier, C.W. and Trouw, R.A. 2005. *Microtectonics*, vol. **1**. Springer Science & Business Media.

Peacock, S.M. 1996. Thermal and Petrologic Structure of Subduction Zones. In: Bebout, G. E., Scholl, D. W., Kirby, S. H. and Platt, J. P. (eds.) *Subduction: top to bottom.* Geophysical Monograph Series, vol. 96. The American Geophysical Union. doi:10.1029/GM096p0119.

Peacock, S.M and Hyndman, R.D. 1999. Hydrous minerals in the mantle wedge and the maximum depth of subduction thrust earthquakes. *Geophys. Res. Lett.*, **26**, 2517-2520.

Peltzer, G., Rosen, P., Rogez, F. and Hudnut, K. 1998. Poroelastic rebound along the Landers 1992 earthquake surface rupture. *Journal of Geophysical Research: Solid Earth*, **103**, 30131–30145. doi: https://doi.org/10.1029/98jb02302.

Peng, Z. and Gomberg, J. 2010. An integrated perspective of the continuum between earthquakes and slow slip phenomena. *Nature Geoscience*, **3**, p. 599–607.

Phillips, E. 1991. The lithostratigraphy, sedimentology and tectonic setting of the Monian Supergroup, western Anglesey, North Wales. *Journal of the Geological Society of London*, **148**, 1079–1090.

Pini, G. A. 1999. Tectosomes and Olistostromes in the Argille Scagliose of the Northern Apennines, Italy. *Geological Society of America Special Papers*, **335**, 70 pp.

Plank, T. and Langmuir, C.H. 1998. The chemical composition of subducting sediment and its consequences for the crust and mantle. *Chemical Geology*, **145**, 325–394. doi: https://doi.org/10.1016/S0009-2541(97)00150-2.

Plesi, G. 2002. *Foglio 235 Pievepelago e Note illustrative della carta geologica d'Italia alla scala 1:50.000.* S.EL.CA., Firenze.

Plesi, G., Daniele, G., Botti, F. and Palandri, S. 2002. Carta strutturale dell'alto Appennino tosco-emiliano (scala 1:100000) fra il Passo della Cisa e il Corno alle Scale. In: *Atti del terzo seminario sulla cartografia geologica, Bologna 2002*. SELCA Firenze.

Principi, G. and Treves, B. 1984. Il Sistema corsoappenninico come prisma di accrezione. Riflessi sul problema generale del limite Alpi-Appennini. *Memorie della Società Geologica Italiana*, **28**, 549–76.

Ramsay, J. G. 1980. The crack-seal mechanism of rock deformation. *Nature*, **284**, 135–139.

Ramsay, J.G. and Huber, M.I. 1984. *The Techniques of Modern Structural Geology*, *Vol. 1: Strain Analysis*. Academic Press, 307 pp.

Ramsay, J. M. and Chester, F. M. 2004. Hybrid fracture and the transition from extension fracture to shear fracture. *Nature*, **428** (6978), 63-66.

Ranero, C.R., Grevemeyer, I., Sahling, H., Barckhausen, U., Hensen, C., Wallmann, K.,m Weinrebe, W., Vannucchi, P., von Huene, R. and McIntosh, K. 2008. Hydrogeological system of erosional convergent margins and its influence on tectonics and interplate seismogenesis. *Geochemistry Geophysics Geosystems*, **9**, Q03S04.

Remitti, F., Balestrieri, M.L., Vannucchi, P. and Bettelli, G. 2013. Early exhumation of underthrust units near the toe of an ancient erosive subduction zone: a case study from the Northern Apennines of Italy. *Geological Society of America Bulletin*, **125**, 1820–32.

Remitti, F., Bettelli, G., Panini, F., Carlini, M. and Vannucchi, P. 2012. Deformation, fluid flow, and mass transfer in the forearc of convergent margins: a two-day field trip in an ancient and exhumed erosive convergent margin in the Northern Apennines. *Geological Society of America Field Guides*, **28**.

Remitti, F., Bettelli, G. and Vannucchi, P. 2007. Internal structure and internal evolution of an underthrust tectonic mélange: the Sestola-Vidiciatico tectonic unit of the Northern Apennines, Italy. *Geodinamica Acta*, **20**, 37–51.

Reutter, K. J. 1981. A trench-forearc model for the Northern Apennines. In: Wezel, F. C. (eds.), *Sedimentary Basins of Mediterranean Margins*, p. 435-443. Tecnoprint, Bologna.

Rimstidt, J.D. and Barnes, H.L. 1980. The kinetics of silica-water reactions. *Geochimica et Cosmochimica Acta*, **44**, 1683–1699. doi:10.1016/0016-7037(80)90220-3.

Rogers, G. C. and Dragert, H. 2003. Episodic tremor and slip on the Cascadia subduction zone: the chatter of silent slip. *Science*, **300**, p. 1942–1943.

Rowe, C.D., Moore, J.C. and Remitti, F. 2013. The thickness of subduction plate boundary faults from the seafloor into the seismogenic zone. *Geology,* **41**, p. 991–994.

Rubin, A. M. 2008. Episodic slow slip events and rate-and-state friction. *Journal of Geophysical Research*, **113**, B11414. doi: https://doi.org/10.1029/2008JB005642.

Ruina, A. 1983. Slip instability and state variable friction laws. *J. Geophys. Res. Solid Earth*, **88** (B12). doi: http://dx.doi.org/10.1029/JB088iB12p10359.

Sagy, A., Brodsky, E. E. and Axen, G. J. 2007. Evolution of fault-surface roughness with slip. *Geology*, **35**, 283–286.

Saffer, D.M. 2003. Pore pressure development and progressive dewatering in underthrust sediments at the Costa Rican subduction margin: Comparison with northern Barbados and Nankai. *Journal of Geophysical Research*, **108**, 2261. doi:10.1029/2002JB001787.

Saffer, D. M. 2015. The permeability of active subduction plate boundary faults. *Geofluids*, **15**, 193-215.

Saffer, D.M. and Bekins, B.A. 1998. Episodic fluid flow in the Nankai accretionary complex: Timescale, geochemistry, flow rates, and fluid budget. *Journal of Geophysical Research*, v. **103**, p. 30,351–30,370. doi:10.1029/98JB01983.

Saffer D. M. and Bekins B. A. 1999. Fluid budgets at convergent plate margins: implications for the extent and duration of fault zone dilation. *Geology*, **27**, 1095–1098.
Saffer, D. M. and Marone, C. 2003. Comparison of smectite-and illite-rich gouge frictional properties: application to the updip limit of the seismogenic zone along subduction megathrusts. *Earth and Planetary Science Letters*, **215** (1-2), 219-235.

Saffer, D.M. and Tobin, H.J. 2011. Hydrogeology and mechanics of subduction zone forearcs: Fluid flow and pore pressure. *Annual Review of Earth and Planetary Sciences*, **39**, p. 157-186. doi: https://doi.org/10.1146/annurev-earth-040610-133408.

Sakaguchi, A., Chester, F., Curewitz, D., Fabbri, O., Goldsby, D., Kimura, G., Li, C.-F., Masaki, Y., Screaton, E. J., Tsutsumi, A., Ujiie, K. and Yamaguchi. 2011. A. Seismic slip propagation to the updip end of plate boundary subduction interface faults: Vitrinite reflectance geothermometry on Integrated Ocean Drilling Program NanTroSEIZE cores. Geology, 39, 395–398. doi: https://doi.org/10.1130/G31642.1.

Samuelson, J., Elsworth, D. and Marone, C. 2009. Shear-induced dilatancy of fluid-saturated faults: Experiment and theory. *Journal of Geophysical Research*, **114**, B12404. doi: https://doi.org/10.1029/2008JB006273.

Sato, T., Sawaki, Y., Asanuma, H, Fujisaki, W., Okada, Y., Maruyama, S., Isozaki, Y., Shozugawa, K., Matsuo, M. and Windley, B. F. 2015. Redox condition of the late Neoproterozoic pelagic deep ocean: ^{57}Fe Mössbauer analyses of pelagic mudstones in the Ediacaran accretionary complex, Wales, UK. *Tectonophysics*, **662**, 472-480.

Scholz, C.H., 1991. Earthquakes and friction laws. *Nature*, **391** (6662), 37-42. doi: 10.1038/34097.

Scholz, C.H. and Campos, J. 1995. On the mechanism of seismic decoupling and back arc spreading at subduction zones. *Journal of Geophysical research*, **100** (Bll), 22103-22115.

Schwartz, S.Y. and Rokosky, J. M. 2007. Slow slip events and seismic tremor at Circum-Pacific subduction zones. *Reviews of Geophysics*, **45**, RG3004.

Screaton, E., Carson, B., Davis, E., 2000. Permeability of a décollement zone: results from a two-well experiment in the Barbados accretionary complex. *Journal of Geophysical Research*, **105**, 21403-21410.

Screaton, E., Kimura, G., Kurewitz, D., Moore, G., Chester, F., Fabbri, O., Fergusson, C., Girault., F., Goldsby, G., Harris, R., Inagaki, F., Jiang, T., Kitamura, I., Knuth, M., Li, C.-F., Claesson Liljedhal, L., Louis, L., Milliken, K., Nicholson, U., Riedinger, N., Sakaguchi, A., Solomon, E., Strasser, M., Su, X., Tsutsumi, A., Yamaguchi, A., Ujiie., K. and Zhao, X. 2009. Interactions between deformation and fluids in the frontal thrust region of the NanTroSEIZE transect offshore the Kii Peninsula, Japan: Results from IODP Expedition 316 Sites C0006 and C0007. *Geochem. Geophys. Geosyst.*, **10**, Q0AD01. doi:10.1029/2009GC002713.

Screaton, E., Saffer, D., Henry, P., and Hunze, S. 2002. Porosity loss within the underthrust sediments of the Nankai accretionary complex: Implications for overpressures. *Geology*, **30**, p. 19–22. doi:10.1130/0091-7613(2002)030<0019:PLWTUS>2.0.CO;2.

Secor, D.T. 1965. Role of fluid pressure in jointing. *American Journal of Science*, **263** (8), 633-646.

Segall, P. and Rice, J. R. 1995. Dilatancy, compaction, and slip instability of a fluid-infiltrated fault. *Journal of Geophysical Research*, **100**, 22155–22171. doi: https://doi.org/10.1029/95JB02403.

Seno, T. 2009. Determination of the pore fluid pressure ratio at seismogenic megathrusts in subduction zones: Implications for strength of asperities and Andean-type mountain building. *Journal of Geophysical Research*, **114**, B5. doi: https://doi.org/10.1029/2008JB005889

Seno, T., Stein, S. and Gripp, A.E. 1993. A model for the motion of the Philippine Sea plate consistent with NUVEL-1 and geological data. *Journal of Geophysical Research: Solid Earth*, **98** (B10), 17941–17948. doi:10.1029/93JB00782.

Shackleton, R.M. 1954. The structure and succession of Anglesey and the Lleyn Peninsula. *Adv. Sci.*, **11**, 106–108.

Shackleton, R.M. 1969. The Precambrian of North Wales. In: Woods, A. (ed.). *The Precambrian and Lower Palaeozoic Rocks of Wales*. University of Wales Press, Cardiff, pp. 1–22.

Shackleton, R.M. 1975. Precambrian rocks of Wales. In: Harris, A.L. (ed.). A Correlation of Precambrian Rocks in the British Isles. *Geological Society of London, Special Publications*, **6**, 76–82.

Shapiro, N. M., Campillo, M., Kaminski, E., Vilotte, J.-P., and Jaupart, C. 2018. Low-frequency earthquakes and pore pressure transients in subduction zones. *Geophysical Research Letters*, **45**. https://doi.org/10.1029/2018GL079893.

Shelly, D. R. 2010. Migrating tremors illuminate complex deformation beneath the seismogenic San Andreas fault. *Nature*, **463**, 648–652.

Shelly, D. R., Beroza, G. C. and Ide, S. 2007. Non-volcanic tremor and low-frequency earthquake swarms. *Nature*, **446**. doi:10.1038/nature05666.

Shibazaki, B. and Iio, Y. 2003. On the physical mechanism of silent slip events along the deeper part of the seismogenic zone. *Geophysical Research Letters*, **30** (9), 1489. doi: http://dx.doi.org/10.1029/2003GL017047.

Shipley, T. H. and the ODP Leg 156 Scientific Party. 1994. Seismically inferred dilatancy distribution, northern Barbados Ridge décollement: implications for fluid migration and fault strength. *Geology*, **22**, 411–414.

Shipley, T.H., Moore, G.F., Bangs, N.L., Moore, J.C. and Stoffa, P.L., 1994. Seismically inferred dilatancy distribution, Northern Barbados Ridge décollement - implication for fluid migration and fault strength. *Geology*, **22**, 411-414.

Sibson, R. H. 1984. Roughness at the base of the seismogenic zone: Contributing factors. *Journal of Geophysical Research*, **89** (B7), 5791– 5799. doi:10.1029/JB089iB07p05791.

Sibson, R. H. 1985. Stopping of earthquake ruptures at dilatational jogs. *Nature*, **316** (6025), 248-251. doi: 10.1038/316248a0.

Sibson, R.H. 1986. Brecciation processes in fault zones: Inferences from earthquake rupturing. *Pure and Applied Geophysics*, **124** (1), 159-175.

Sibson, R.H. 1987. Earthquake rupturing as a mineralizing agent in hydrothermal systems. *Geology*, **15**, 701–704. doi: https://doi.org/10.1130/0091-7613(1987)15<701:ERAAMA>2.0.CO;2

Sibson, R.H. 1992. Implications of fault-valve behaviour for rupture nucleation and recurrence. *Tectonophysics*, **211**, 283–293.

Sibson, R.H. 1998. Conditions for fault-valve behavior. *Geological Society of London Special Publications*, **54** (1), 15-28. doi: 10.1144/GSL.SP.1990.054.01.02.

Sibson, R.H. 2000. Fluid involvement in normal faulting. *Journal of Geodynamics*, **29** (3), 469-499. doi: 10.1016/S0264-3707(99)00042-3.

Sibson, R. H., 2003. Thickness of the Seismic Slip Zone. *Bulletin of the Seismological Society of America*, **93**, 1169–1178.

Sibson, R.H. 2013. Stress switching in subduction forearcs: Implications for overpressure containment and strength cycling on megathrusts. *Tectonophysics*, **600**, 142–152. doi: https://doi.org/10.1016/j.tecto.2013.02.035

Sibson, R.H. 2017. Tensile overpressure compartments on low-angle thrust faults. *Earth, Planets and Space*, **69**, 1–15. doi: https://doi.org/10.1186/s40623-017-0699-y

Skarbek, R. M. and Saffer, D. M. 2009. Pore pressure development beneath the decollement at the Nankai subduction zone: implications for plate boundary fault strength and sediment dewatering. *Journal of Geophysical Research*, **114** (B07401).

Sleep, N. H. and Blanpied, M. L. 1992. Creep, compaction and the weak rheology of major faults. *Nature*, **359** (6397), 687.

Spinelli, G., Saffer, D. M., Underwood, M. B. 2006. Effects of alongstrike variability in temperature on the hydrogeology of the Nicoya margin subduction zone, Costa Rica. *Journal of Geophysical Research*, **111** (B04403).

Stauffer, P. and Bekins, B. A. 2001. Modeling consolidation and dewatering near the toe of the northern Barbados accretionary complex. *Journal of Geophysical Research*, **106**, 6369–6383.

Stipp, M., Stünitz, H., Heilbronner, R. and Schmid, S. M. 2002. The eastern Tonale fault zone: a "natural laboratory" for crystal plastic deformation of quartz over a temperature range from 250 to 700 °C. *Journal of Structural Geology*, **24**, 1861-1864.

Stojakovic, D. 2012. Electron backscatter diffraction in materials characterization. *Processing and Application of Ceramics*, **6** (1), 1-13.

Strachan, R. A., Collins, A. S., Buchan, C., Nance, R. D., Murphy, J. B. and D'Lemos, R. S. 2007. Terrane analysis along a Neoproterozoic active margin of Gondwana: insights from U–Pb zircon geochronology. *Journal of the Geological Society, London*, **164**, 57–60.

Strasser, M., Dugan, B., Kanagawa, K., Moore, G. F., Toczko, S., Maeda, L., Kido, Y., Moe, K. T., Sanada, Y., Esteban, L., Fabbri, O., Geersen, J., Hammerschmidt, S., Hayashi, H., Heirman, K., Hüpers, A., Jurado Rodriguez, M. J., Kameo, K., Kanamatsu, T., Kitajima, H., Masuda, H., Milliken, K., Mishra, R., Motoyama, I., Olcott, K., Oohashi, K., Pickering, K. T., Ramirez, S. G., Rashid, H., Sawyer, D., Schleicher, A., Shan, Y., Skarbek, R., Song, I., Takeshita, T., Toki, T., Tudge, J., Webb, S., Wilson, D. J., Wu, H.-Y., and Yamaguchi, A. 2014. Expedition 338 summary. In: Strasser, M., Dugan, B., Kanagawa, K., Moore, G. F., Toczko, S. and Maeda, L. (eds.). *Proceedings of the Integrated Ocean Drilling Program*, **338**. Yokohama, Japan, Integrated Ocean Drilling Program, 47 pp. doi: https://doi.org/10.2204/iodp.proc.338.101.2014.

Sugioka, H., Okamoto, T., Nakamura, T., Ishihara, Y., Ito, A., Obana, K., Kinoshita, M., Nakahigashi, K., Shinohara, M. and Fukao, Y. 2012. Tsunamigenic potential of the shallow subduction plate boundary inferred from slow seismic slip. *Nat. Geosci.*, **5** (6), 414–418. doi: 10.1038/ngeo1466.

Sun, T., Wang, K., Fujiwara, T., Kodaira, S. and He, J. 2017. Large fault slip peaking at trench in the 2011 Tohoku-oki earthquake. *Nature Commuications*, **8**, 14044. doi: 10.1038/ncomms14044.

Taylor, S.R. and McLennan, S.M. 1985. *The Continental Crust: Its Composition and Evolution*. Blackwell, Oxford, p. 1-312.

Tesei, T., Collettini, C., Carpenter, B. M., Viti, C. and Marone, C. 2012. Frictional strength and healing behavior of phyllosilicate-rich faults. *Journal of Geophysical Research*, **117**, B09402.

Tesei, T.,Lacroix, B. and Collettini, C. 2015. Fault strength in thin skinned tectonic wedges across the smectite-illite transition: Constraints from friction experiments and critical tapers. *Geology*, **43**, 923–926.

Thomson, S.N., Brandon, M.T., Reiners, P.W., Zattin, M., Isaacson, P.J. and Balestrieri, M.L. 2010. Thermochronologic evidence for orogen-parallel variability in wedge kinematics during extending convergent orogenesis of the northern Apennines, Italy. *GSA Bulletin*, **122**, p. 1160–1179. doi: https://doi.org/10.1130/B26573.1.

Thorpe, R.S. 1993. Geochemistry and eruptive environment of metavolcanic rocks from the Mona Complex of Anglesey. North Wales, U. K. *Geol. Mag.*, **130**, 85–91.

Tichelaar, B.W. and Ruff, L.J. 1993. Depth of seismic coupling along subduction zones. *Journal of Geophysical Research*, **98** (B2), 2017– 2037. doi:10.1029/92JB02045.

Tobin, H. and Saffer, D.M. 2009. Elevated fluid pressure and extreme mechanical weakness of a plate boundary thrust, Nankai Trough subduction zone. *Geology*, **37** (8), 679–682. doi: https://doi.org/10.1130/G25752A.1

Tobin, H., Hirose, T., Saffer, D.M., Toczko, S., Maeda, L., Kubo, Y., Boston, B., Broderick, A., Brown, K., Crespo-Blanc, A., Even, E., Fuchida, S., Fukuchi, R., Hammerschmidt, S., Henry, P., Josh, M., Jurado, M.J., Kitajima, H., Kitamura, M., Maia, A., Otsubo, M., Sample, J., Schleicher, A., Sone, H., Song, C., Valdez, R., Yamamoto, Y., Yang, K., Sanada, Y., Kido, Y., and Hamada, Y. 2015. Expedition 348 summary. In: Tobin, H., Hirose, T., Saffer, D., Toczko, S., Maeda, L., Kubo, Y. and the Expedition 348 Scientists. *Proceedings of the Integrated Ocean Discovery Program, 348.* College Station, TX (Integrated Ocean Drilling Program). doi:10.2204/iodp.proc.348.101.2015.

Tobin, H., Kimura, G., Kinoshita, M., Toczko, S. and Maeda, L. 2018. *Expedition 358 Scientific Prospectus: NanTroSEIZE Plate Boundary Deep Riser 4: Nankai Seismogenic/Slow Slip Megathrust.* Integrated Ocean Discovery Program. doi: https://doi.org/10.14379/iodp.sp.358.2018.

Trepmann, C.A. and Stöckhert, B., 2013. Short-wavelength undulatory extinction in quartz recording coseismic deformation in the middle crust e an experimental study. *Solid Earth*, **4**, 263-276.

Trepmann, C.A., Hsu, C., Hentschel, F., Döhler, K., Schneider, C., Wichmann, V., 2017. Recrystallization of quartz after low-temperature plasticity - the record of stress relaxation below the seismogenic zone. *Journal of Structural Geology*, **95**, 77-92. doi: https://doi.org/10.1016/j.jsg.2016.12.004.

Trepmann, C.A., Stöckhert, B., Dorner, D., Küster, M., Röller, K., and Moghadam, R.H., 2007. Simulating coseismic deformation of quartz in the middle crust and fabric evolution during postseismic stress relaxation e an experimental study. *Tectonophysics*, **442**, 83-104.

Tse, S. T. and Rice, J. R. 1986. Crustal earthquake instability in relation to the depth variation of frictional slip properties. *Journal of Geophysical Research*, **91** (B9), 9452– 9472. doi:10.1029/JB091iB09p09452.

Tsuji, T., Kawamura, K., Kanamatsu, T., Kasaya, T., Fujikura, K., Ito, Y., Tsuru, T. and Kinoshita, M. 2013. Extension of continental crust by anelastic deformation during the 2011 Tohoku-oki earthquake: the role of extensional faulting in the generation of a great tsunami. *Earth and Planetary Science Letters*, **364**, 44–58.

Tullis, J. and Yund, R. A. 1985. Dynamic recrystallization of feldspar: A mechanism for ductile shear zone formation. *Geology*, **13** (4), 238-241.

Ujiie, K. 2002. Evolution and kinematics of an ancient décollement zone, mélange in the Shimanto accretionary complex of Okinawa Island, Ryukyu Arc. *Journal of Structural Geology*, **24**, 937–952.

Ujiie, K., Hisamitsu, T., and Taira A. 2003. Deformation and fluid pressure variation during initiation and evolution of the plate boundary décollement zone in the Nankai accretionary prism. *Journal of Geophysical Research*, **108**, 2398. doi: 10.1029/2002JB002314, B8.

Ujiie, K., Saishu, H., Fagereng, Å., Nishiyama, N., Otsubo, M., Masuyama, H. and Kagi, H. 2018. An Explanation of Episodic Tremor and Slow Slip Constrained by Crack-Seal Veins and Viscous Shear in Subduction Mélange. *Geophysical Research Letters*, **45**, 1–9. doi: https://doi.org/10.1029/2018GL078374

Ujiie, K., Tanaka, H., Saito, T., Tsutsumi, A., Mori, J.J., Kameda, J., Brodsky, E.E., Chester, F.M., Eguchi, N., and Toczko, S. 2013. Low coseismic shear stress on the Tohoku-Oki megathrust determined from laboratory experiments. *Science*, v. **342**, p. 1211–1214. doi:10.1126/science.1243485.

Underwood, M. B. and Moore, G. F. 2012. Evolution of sedimentary environments in the subduction zone of southwest Japan: recent results from the NanTroSEIZE Kumano transect. In: Busby, C. and Azor, A. (eds.). *Tectonics of Sedimentary Basins: Recent Advances*. Blackwell Publishing Ltd.

Underwood, M. B., Saito, S., Kubo, Y. and the Expedition 322 Scientists. 2010. Expedition 322 summary. In: Saito, S., Underwood, M.B., Kubo, Y. and the Expedition 322 Scientists. *Proceedings of the Integrated Ocean Drilling Program, 322*. Tokyo (Integrated Ocean Drilling Program Management International, Inc.). doi: http://dx.doi.org/10.2204/iodp.proc.322.101.2010.

Vai, G. B. and Martini, I. P. 2001. *Anatomy of an orogen: the Apennines and the Adjacent Mediterranean Basins*. Dordrecht/Boston/London: Kluwer Academic Publishers, 632 pp.

van den Ende, M. P. A., Chen, J., Ampuero, J.-P. and Niemeijer, A. R. 2018. A comparison between rate-and-state friction and microphysical models, based on numerical simulations of fault slip. *Tectonophysics*, **783**, 273-295.

Vannucchi, P., Remitti, F. and Bettelli, G. 2008. Geological record of fluid flow and seismogenesis along an erosive subducting plate boundary. *Nature*, **451**, 699–703. doi: https://doi.org/10.1038/nature06486

Vannucchi, P., Remitti, F., Bettelli, G., Boschi, C. and Dallai, L. 2010. Fluid history related to the early Eocene - middle Miocene convergent system of the Northern Apennines (Italy): Constraints from structural and isotopic studies. *Journal of Geophysical Research*, **115**, 1–23. doi: https://doi.org/10.1029/2009JB006590.

Vannucchi, P., Sage, F., Phipps Morgan, J., Remitti, F. and Collot, J.-Y. 2012. Toward a dynamic concept of the subduction channel at erosive convergent margins with implications for interplate material transfer. *Geochemistry Geophysics Geosystems*, **13**, Q02003. doi:10.1029/2011GC003846

Vrolijk, P. 1990. On the mechanical role of smectite in subduction zones. *Geology*, **18**, p. 703–707. doi: https://doi.org/10.1130/0091-7613(1990)018<0703:OTMROS>2.3.CO;2.

Wakabayashi, J. 2011. Mélanges of the Franciscan Complex, California: Diverse structural settings, evidence for sedimentary mixing, and their connection to subduction processes. In: Wakabayashi, J. and Dilek, Y. (eds.). Mélanges: Processes of formation and societal significance. *Geological Society of America Special Paper*, **480**, 117–141. doi:10.1130/2011.2480(05).

Wallace, L.M., Araki, E., Saffer, D., Wang, X., Roesner, A., Kopf, A., Nakanishi, A., Power, W., Kobayashi, R., Kinoshita, C., Toczko, S., Kimura, T., Machida, Y. and Carr, S. 2016. Near-field observations of an offshore Mw 6.0 earthquake from an integrated seafloor and subseafloor monitoring network at the Nankai Trough, southwest Japan. *Journal of Geophysical Research: Solid Earth*, **121** (11), 8338–8351. doi: http://dx.doi.org/10.1002/2016JB013417.

Wallace, L. M., Reyners, M. et al. 2009. Characterising the seismogenic zone of a major plate boundary subduction thrust: the Hikurangi Margin, New Zealand. *Geochemistry Geophysics Geosystems*, **10**, Q10006.

Wang, K. 2000. Stress–strain ‘paradox’, plate coupling, and forearc seismicity at the Cascadia and Nankai subduction zones. *Tectonophysics*, **319**, 321-338.

Wang, K., Mulder, T., Rogers, G.C. and Hyndman, R.D. 1995. Case for very low coupling stress on the Cascadia Ssubduction Fault. *J. Geophys. Res.*, **100** (B7), 12907–12918. doi:10.1029/95JB00516.

Wassmann, S. and Stöckhert, B. 2012. Matrix deformation mechanisms in HP-LT tectonic mélanges—Microstructural record of jadeite blueschist from the Franciscan complex, California. *Tectonophysics*, **568–569**, 135–153. doi: 10.1016/j.tecto.2012.01.009.

Wei, M., McGuire, J. J. and Richardson, E. 2012. A slow slip event in the south central Alaska Subduction Zone and related seismicity anomaly. *Geophysical Research Letters*, **39**, L15309. doi:10.1029/2012GL052351.

Wood, D.S. 1974. Ophiolites, mélanges, blueschists, and ignimbrites: early Caledonian subduction in Wales? In: Dott, R.H. and Shaver, R.H. (eds.). Modern and Ancient Geosynclinal Sedimentation. *Soc. Econ. Paleontol. Mineral., Spec. Publ.*, **19**, 334–344.

Xia, H. and Platt, J.P., 2018. Quartz grainsize evolution during dynamic recrystallization across a natural shear zone boundary. *Journal of Structural Geology*, **109**, p. 120-126. doi: https://doi.org/10.1016/j.jsg.2018.01.007.

Yamaguchi, A., Cox, S.F. and Kimura, G. 2011. Dynamic changes in fluid redox state associated with episodic fault rupture along a megasplay fault in a subduction zone. *Earth and Planetary Science Letters*, **302**, 369–377. doi: https://doi.org/10.1016/j.epsl.2010.12.029.

Yamaguchi, A., Ujiie, K., Nakai, S. and Kimura, G. 2012. Sources and physicochemical characteristics of fluids along a subduction-zone megathrust: A geochemical approach using syn-tectonic mineral veins in the Mugi mélange, Shimanto accretionary complex. *Geochemistry, Geophysics, Geosystems*, **13**, 1–227. doi: https://doi.org/10.1029/2012GC004137.

Yamamoto, Y., Obana, K., Kodaira, S., Hino, R. and Shinohara, M. 2014. Structural heterogeneities around the megathrust zone of the 2011 Tohoku earthquake from tomographic inversion of onshore and offshore seismic observations. *Journal of Geophysical Research–Solid Earth*, **119**, p. 1165-1180. doi: https://doi.org/10.1002/2013JB010582.

Yang, T.,Mishima, T.,Ujiie, K.,Chester, F. M.,Mori, J. J., Eguchi, N., Toczko, S. and Expedition 343 Scientists. 2013. Strain decoupling across the décollement in the region of large slip during the 2011 Tohoku-Oki earthquake from anisotropy of magnetic susceptibility. *Earth and Planetary Science Letters*, **381**, 31–8.

Yokota, Y., Ishikawa, T., Watanabe, S., Tashiro, T. and Asada, A. 2017. Seafloor geodetic constraints on interplate coupling of the Nankai Trough megathrust zone. *Nature*, **534**, 374–377.

Yoshihiro Ito, Y and Obara, K. 2006. Very low frequency earthquakes within accretionary prisms are very low stress-drop earthquakes. Geophysical Research Letters, 330 (9), doi: 10.1029/2006GL025883.